

MODELLING ICE-SHELF/OCEAN INTERACTION

Benjamin Keith Galton-Fenzi

B. Sc. (Hons Env. Sc.), Grad. Cert. Mar. Sci.

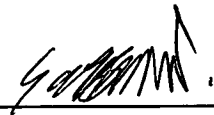
**Submitted in fulfilment of the requirements for a
Doctor of Philosophy in Quantitative Marine Science**

**A joint program between the
Commonwealth Science and Industry Research Organisation
and the University of Tasmania
November 2009**

STATEMENT OF DECLARATION

I declare that this thesis contains no material which has been accepted for a degree or diploma by the University or any other institution, except by way of background information and duly acknowledged in the thesis, and to the best of my knowledge and belief no material previously published or written by another persona except where due acknowledgement is made in the text of the thesis, nor does the thesis contain any material that infringes copyright.

This thesis may be made available for loan and limited copying in accordance with the *Copyright Act of 1968*



Benjamin Keith Galton-Fenzi

2009

CONTENTS

ABSTRACT	v
ACKNOWLEDGEMENTS	vii
LIST OF SYMBOLS	ix
CHAPTER 1. INTRODUCTION	1
1.1 Interaction of Ice Shelves with the Ocean	4
1.2 Modelling Ice Shelf-Ocean Interaction	7
1.3 Thesis Aims: Testable Objectives	7
1.4 Thesis Overview	8
CHAPTER 2. ICE-OCEAN THERMODYNAMICS	11
2.1 Ice Shelf-Ocean Dynamics	11
2.2 Frazil Ice-Ocean Dynamics	13
2.3 Concluding Remarks	26
CHAPTER 3. ADAPTATION OF AN OCEAN MODEL	27
3.1 The Regional Ocean Modeling System	27
3.2 The Pressure Gradient Force	28
3.3 Equation of State for Seawater in Polar Regions	40
3.4 Frazil Settling Scheme	41
3.5 Concluding Remarks	44
CHAPTER 4. SIMPLIFIED MODELS OF ICE-OCEAN INTERACTION	45
4.1 The Plume Model of Jenkins & Bombosch (1995)	45
4.2 With Rotation: Variations on Grosfeld (1997)	52
4.3 Concluding Remarks	57

CHAPTER 5. THE AMERY ICE SHELF OCEAN MODEL: SETUP	59
5.1 Geometry and Location	59
5.2 General Model Configuration	68
5.3 Forcing and Initial Conditions	68
5.4 Concluding Remarks	78
CHAPTER 6. THE AMERY ICE SHELF-OCEAN MODEL	79
6.1 General Circulation and Water Mass Properties	79
6.2 Antarctic Bottom Water Formation	85
6.3 Mass Balance of the Amery Ice Shelf	89
6.4 Seasonal Cycles of Melt/Freeze and Circulation	96
6.5 Sensitivity Studies	104
6.6 Concluding Remarks	107
CHAPTER 7. COASTAL ANTARCTIC RESPONSE TO CLIMATE CHANGE	113
7.1 Recent Climate Change	113
7.2 Experiments	116
7.3 Results and Discussion	117
7.4 Concluding Remarks	125
CHAPTER 8. CONCLUSIONS	127
8.1 Summary and Main Findings	127
8.2 Caveats and Future Work	129
APPENDIX 1. EQUATION OF STATE POLYNOMIALS	133
REFERENCES	137

ABSTRACT

The effect of climate change on the mass balance of ice shelves and bottom water formation is investigated using a terrain-following three-dimensional numerical ocean model. The Regional Ocean Modeling System was modified to simulate the thermodynamic processes beneath ice shelves, including direct basal processes and frazil ice dynamics. Process-orientated studies of simplified ice-shelf-ocean cavities investigate the sensitivity of the melting/freezing to the various parametrisations which describe the internal physics of the models. The Amery Ice Shelf/ocean model is forced with tides, seasonal winds and relaxation to seasonal lateral boundary climatologies. The open ocean surface fluxes are modified by an imposed climatological sea-ice cover that includes the seasonal effect of polynyas.

The circulation and basal melting and freezing show good agreement with glaciological and oceanographic observations that have been collected from beneath the Amery Ice Shelf via boreholes through the ice and in the adjacent area of Prydz Bay. Strong horizontal and thermohaline (“ice-pump”) circulation is primarily driven by melting and refreezing of the ice shelf. The net basal melt rate is $\sim 45 \text{ Gt year}^{-1}$ ($\sim 0.7 \text{ m year}^{-1}$), which represents 67 % of the total mass loss of the Amery Ice Shelf. The total amount of refreezing is $\sim 5.3 \text{ Gt year}^{-1}$, of which 70 % is due to frazil accretion. The seasonal variability of the basal melt/freeze (up to $\pm 1 \text{ m year}^{-1}$) within 100 km of the open ocean is the same magnitude as the area-averaged melt rates. The annual averaged bottom water formation rates are $\sim 1.2 \text{ Sv}$ to the west of the Amery, in the vicinity of Cape Darnley.

The Amery Ice Shelf/ocean model is used to investigate the sensitivity of the basal melt/freeze and bottom water formation to the inclusion of various physical mechanisms and changes in forcing. Direct comparison with glaciological observations shows that ice-shelf models that include frazil processes improve the simulated pattern of marine ice accretion. Simulations without ice-shelf/ocean thermodynamic processes overestimate bottom water formation by up to 2.8 times as much as simulations with ice-shelf/ocean thermodynamic processes, due to the missing buoyant freshwater from the melting ice shelf. Climate change sensitivity studies suggest that an ocean warming of 1°C above present day temperatures can potentially remove the Amery Ice Shelf in ~ 500 years, solely due to increased basal melting, and can also lead to a significant decrease in the formation of bottom water. This research contributes to understanding how interaction between ice shelves and various forcing mechanisms can lead to changes in basal melt/freeze and dense water formation, which has major implications for the stability of ice shelves, sea level rise, and the salt budget of the global oceans.

ACKNOWLEDGEMENTS

The completion of this thesis would not have been possible without the help of many people. I would like to acknowledge the complementary guidance, inspiration, resources and support of my supervisors Richard Coleman, John Hunter, Simon Marsland and John Church.

I would also like to thank, in no particular order, Claire Maraldi ; Dave Rasch for a great time on the Amery Ice Shelf; Neal Young (ACE CRC); Helen Fricker (Scripps Institution of Oceanography); Hugh Tassell (Geoscience Australia) and Kath McMahon (Macquarie University); Rachael Hurd (ACE CRC) and Mike Craven (AAD); Mark Hemer; Andreas Klocker; Michael Schlodlock (NASA-JPL); Takeshi Tamura and the Hokaido group (Low Temperature Institute, Hokaido); Roland Warner (AAD); Jason Roberts (AAD); Trevor McDougall (CSIRO); Chris Sherwood (USGS); Robin Robertson (ADFA, Canberra); The Society of Sub-professional Oceanographers (SoSO) and last but not least, Ben Joseph (UTas) for fantastic computing support. Special thanks must also go to Benoit Legresy (LEGOS, Toulouse) for hosting me during two visits to LEGOS; Mike Dinniman (ODU, Norfolk) and Paul Holland (BAS, Cambridge) for allowing me to examine specific parts of their code for development of the model presented here. Thanks also to my examiners Adrien Jenkins (BAS) and Chris Sherwood (UGS) for their constructive comments.

This research was supported by a scholarship jointly provided by the Commonwealth Science and Industry Research organisation and the University of Tasmania as part of the Quantitative Marine Science PhD program, and a stipend from the Antarctic Climate and Ecosystems Cooperative Research Centre. Supercomputing resources were kindly provided by the Tasmanian Partnership for Advanced Computing, Hobart and under two separate grants from the National Computing Infrastructure (formally known as the Australian Partnerships for Advanced Computing) located in Canberra.

I am especially indebted to Bill Scott for sharing with me his love for science. Second last is a thanks to my friend and office mate Andrew Meijers. Finally, to Wenneke ten Hout, my eternal gratitude.

*Niet zonder je liefde, vriendschap, steun, geduld en begrip
dat je hebt gegeven aan me tijdens deze laatste jaren.
Bedankt, mijn kleine prinsesje*

LIST OF SYMBOLS

Latin Symbols

a	Slope of liquidus for seawater (T_f decrease with S)
a_r	Aspect ratio of frazil discs
A	Tidal amplitude
\mathcal{A}	Area
b	Offset of liquidus for seawater (T_f at $S=0$, z =surface)
c	Freezing temp change with depth (T_f decrease with z)
c_d	Drag coefficient
c'_d	Frazil crystal drag coefficient
c_i	Specific heat capacity of ice
c_w	Specific heat capacity of seawater
C	Frazil concentration
D	Diameter of frazil crystal
\mathcal{E}	Kinetic energy
$\bar{\mathcal{E}}$	Barotropic Kintetic energy
f'	Rate of change of frazil ice volume
\mathbf{F}	Tracer flux
\mathcal{F}	Barotropic Kinetic Energy Fraction
g	Acceleration due to gravity
h	Thickness of a sigma layer
He	Heaviside function
\bar{H}	Total average depth
HC	Haney criteria
\mathcal{HC}	Ocean heat content
H_i	Ice draft
i	Frazil size class
k	Thermal conductivity
k_T	Molecular thermal diffusivity of seawater
k_S	Molecular haline diffusivity of seawater
K	Tracer eddy diffusion
$K_{x,y}$	Horizontal tracer eddy diffusion
K_z	Vertical tracer eddy diffusion
l	Turbulent length scale
L	Latent heat of ice fusion
m	Basal melt rate
m^*	Ratio between frazil radius and Kolmogorov length scale
\mathcal{M}	Mass of seawater fraction and frazil

n	Unit vector normal to area
\overline{N}	Cap on number of crystals for secondary nucleation
\mathcal{N}	Total number of frazil size classes
Nu	Nusselt number
p'	Frazil precipitation rate
P	Pressure
P_b	Pressure at ice shelf base
Pr	Molecular Prandtl number of seawater
Re	Frazil disc reynolds number
q_c	Rate of conductive heat transfer
q_i	Rate of conductive heat transfer from ice to freshwater
Q	Surface heat flux
r	Radius of major frazil ice surface
s	Bottom slope
S	Salinity of mixed layer
S	Tracer source
S_b	Salinity of boundary layer
S_i	Salinity of shelf (salt trapped in ice during freezing)
Sc	Molecular Schmidt number of seawater
Sh	Sherwood number
Sv	Sverdrup
t	Time
T	Temperature of mixed layer
T_b	Temperature of boundary layer
T_f	Thermodynamic freezing point temperature
T_i	Temperature of ice
u	Mixed layer velocity
u', v'	Wind speed
$\overline{u}, \overline{v}$	Depth averaged velocities in the x and y directions
u_i	Critical erosion velocity at ice shelf base
u_d	Friction velocity
\mathbf{v}	Advection velocity
$< V >$	Maximum baroclinic velocity
\mathcal{V}	Volume
w'	terminal velocity
w_{turb}	Turbulent motions of frazil crystals
x, y	Horizontal coordinates
z	Vertical coordinate

Greek Symbols

α	Direction of the axis of principal variability
γ_S	Salt transfer coefficient at ice shelf base
γ_T	Heat transfer coefficient at ice shelf base
γ'_S	Salt transfer coefficient for frazil ice
γ'_T	Heat transfer coefficient for frazil ice
ρ	Density of seawater
ρ_a	Density of air
ρ_1	Density at the first level of the ocean model
ρ_i	Density of ice
ρ_0	Reference density of seawater
ρ_s	Density of seawater fraction
τ	Stress at ice base or sea floor
σ	Vertical sigma coordinate
σ_{maj}	Major axis of an ellipse
σ_{min}	Minor axis of an ellipse
ϵ	Turbulent dissipation rate (Chapter 2) or Complex error (Chapter 5)
η	Kolmogorov length scale
θ	Potential temperature
Θ	Basal “two equation” scaling factor
Θ'	Frazil “two equation” scaling factor
ν	Kinematic viscosity of seawater
τ	Surface stress or Relaxation time (Chapter 3)
ϕ	Tidal phase

CHAPTER ONE

INTRODUCTION

Much of the uncertainty in climate change projections and their impacts on sea level rise and ocean salt budgets is due to limited understanding of the dynamical processes in the cryosphere between grounded ice sheets and the ocean [IPCC, 2007]. Ice shelves are a major part of the global climate system and are an important interface between the grounded ice sheet and the oceans. Most of the snowfall on inland Antarctica drains, via large ice streams, to the sea where it floats seaward of the grounding line forming ice shelves (Fig. 1.1).

About 50% of the Antarctic continental margin [Fox and Cooper, 1994] is framed by ice shelves

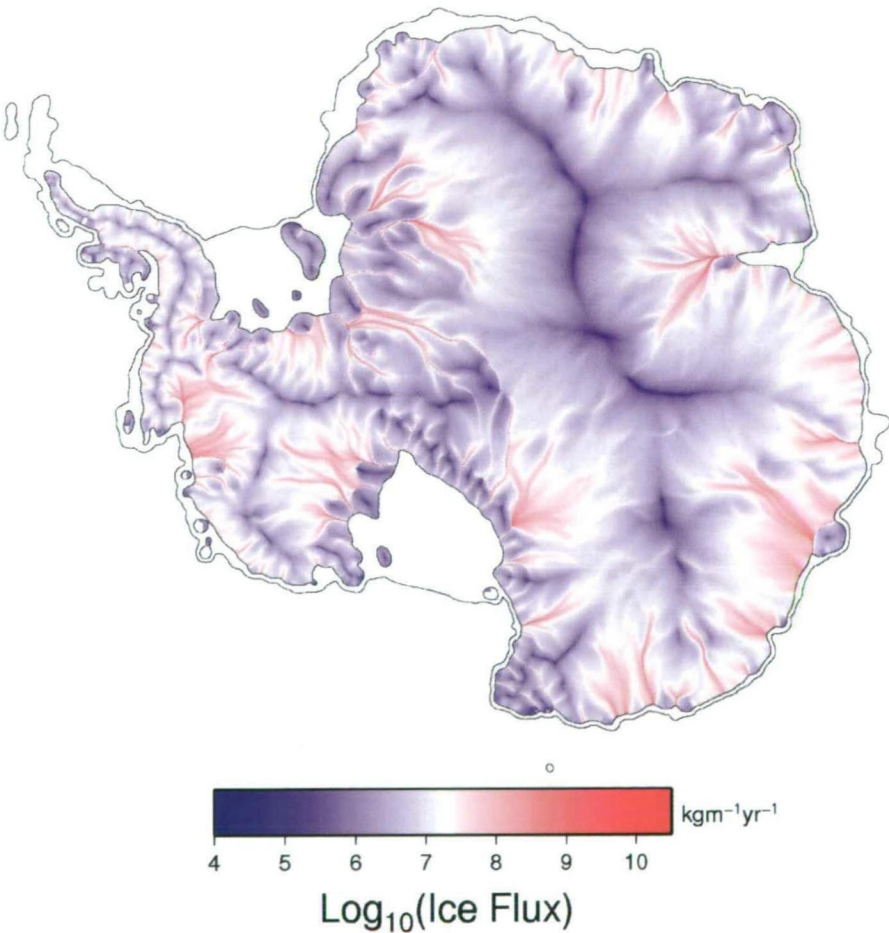


Figure 1.1: Slow moving ice (blue) drains from the Antarctic interior to the coast via fast moving glaciers (red). The image is produced using Lagrangian balance ice flux estimates from the *Arthern et al. [2006]* accumulation data set, mapped to 1 km Eulerian grid for visualisation. (Personal communication: Jason Roberts, AAD).

in coastal embayments, such as the Filchner, Ronne, Ross and Amery, and fringing shelves on the periphery of the ice sheet, such as the Shackleton, Fimbulisen, West, and Larsen shelves (see Fig. 1.2).

Assuming that the Antarctic ice sheet is in approximate steady state, then accumulation over the ice sheet must be balanced by the major outputs. The net average accumulation rate over the Antarctic ice sheet has been estimated at $1811 \text{ Gt year}^{-1}$ [Vaughan *et al.*, 1999], which represents $\sim 57 \text{ mSv}$ of fresh water that is added to the Southern Ocean. The freshwater contribution is primarily due to melting of ice shelves and the melting of icebergs that have calved from the front of ice shelves. The basal melt water contributions from ice shelves have been estimated using numerical models to be 28 mSv ($1 \text{ mSv} = 10^3 \text{ m}^3 \text{ s}^{-1}$) of freshwater to the Southern Ocean [Hellmer, 2004]. Earlier estimates of iceberg calving suggest a mass loss of $\sim 70 \text{ mSv}$ [$2016 \text{ Gt year}^{-1}$, Jacobs *et al.*, 1992]. Although these estimates are subject to considerable uncertainty

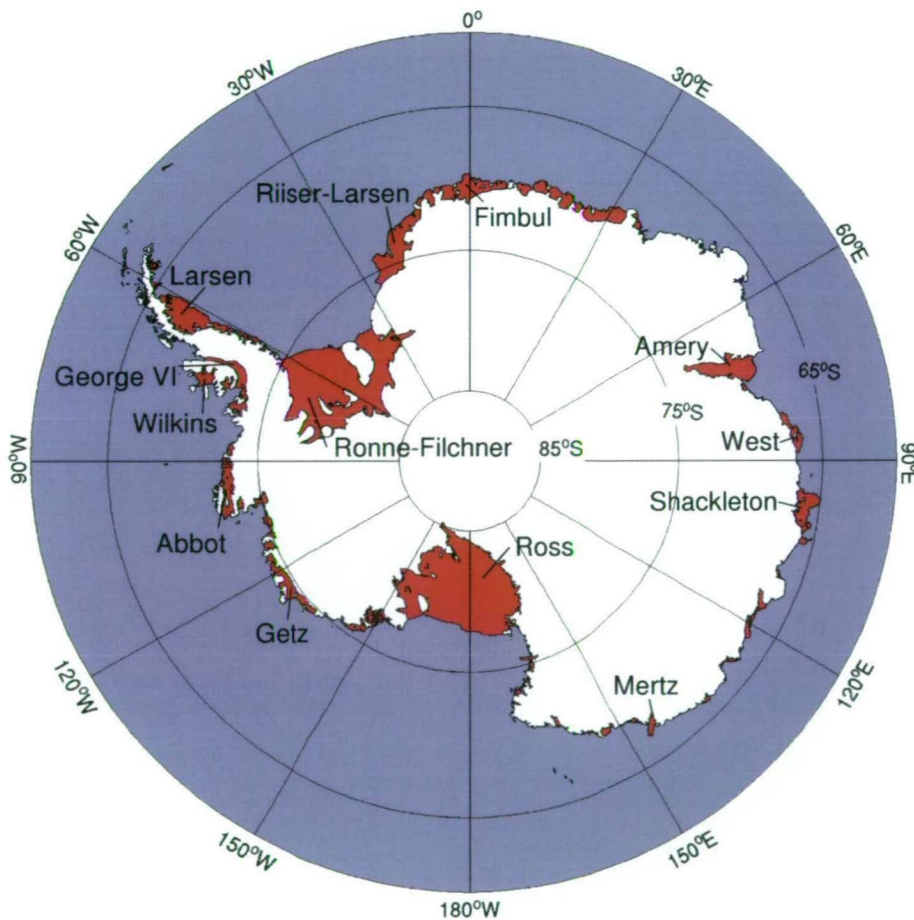


Figure 1.2: Ice shelves (red) are the floating part of the Antarctic Ice Sheet. Ice shelves connect the ice that is grounded on the Antarctic continent (white) to the waters of the Southern Ocean (blue). The coastline and grounding line data used to make this figure come from the MODIS-based Mosaic of Antarctica [Scambos *et al.*, 2007].

they imply that the Antarctic continent is currently in negative mass balance. The imbalance of the ice sheet's mass-budget can effect sea level and the heat and salt tracer budgets of the oceans. As such, the ice flux from the major ice sheets into the ocean is strongly controlled by the mass loss processes that occur beneath the ice shelves.

Ice shelves are similarly assumed to be maintained in a dynamic equilibrium that depends on the flow of the feed glacier, snowfall and ablation on the upper surface, basal melting and freezing, and the calving of icebergs (Fig. 1.3).

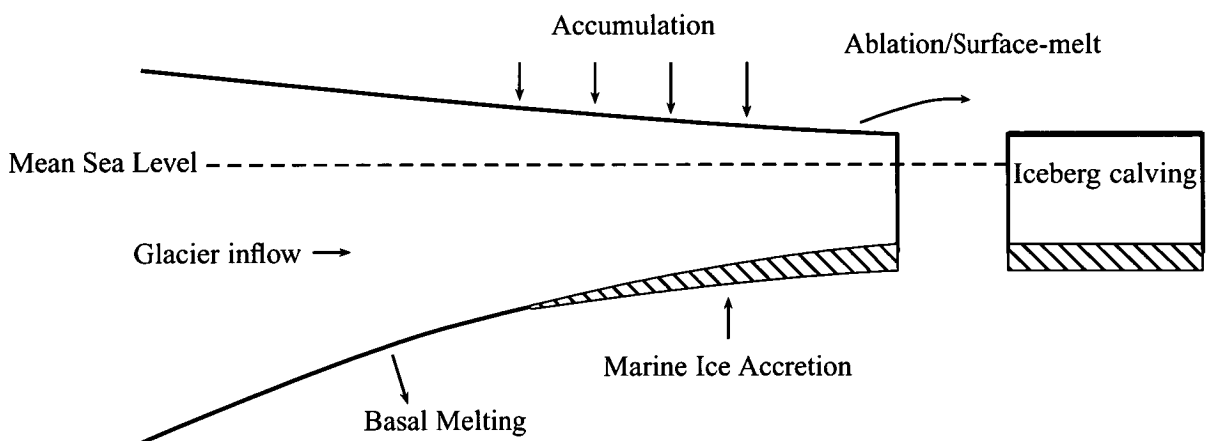


Figure 1.3: Ice shelf mass balance schematic. Ice shelves are maintained by being in a dynamic balance between the addition of 'ice' via inflowing glaciers, net snow accumulation and marine ice accretion and the removal of ice via basal melting and iceberg calving. The net basal mass loss is equal to the basal melting minus marine ice accretion.

The dynamics (and hence the response time) of upstream inland Antarctic ice is now known to be influenced by ice shelves. Removal of mass from an ice shelf leads to an acceleration and thinning of tributary ice streams and can hence indirectly influence sea level [Dupont and Alley, 2005]. This process is known as the buttressing effect [Thomas, 1979]. For example, Larsen A and B Ice Shelves on the Antarctic Peninsula disappeared in 1995 and 2002 respectively. The collapse of the Larsen B ice shelf and the subsequent speed-up of grounded ice behind [De Angelis and Skvarca, 2003], led to an increase of about 4 % in the rate of sea level rise [Scambos *et al.*, 2004].

Satellite observations of the Antarctic ice sheet fringing the Amundsen Sea have confirmed that various ice streams there are thinning [Wingham *et al.*, 2006], accelerating [Joughin *et al.*, 2003], and experiencing retreat of their associated grounding lines, at which the ice stream goes afloat [Rignot, 1998]. These processes lead to a transfer of mass from the ice sheet to the oceans, though it is unclear whether Antarctica as a whole has a negative mass balance at present [Allison *et al.*, 2006; Wingham *et al.*, 2006]. The ice streams observed to be thinning are glaciologically distinct, but all share similar behaviour, leading to suspicion that the thinning results from a common change in external forcing rather than internal glacier dynamics [Holland *et al.*, 2008]. Increased

ocean temperature (and hence basal melting) has been implicated in the thinning of Pine Island Glacier in West Antarctica and the collapse of parts of the Larsen Ice Shelf on the Antarctic Peninsula [Shepherd *et al.*, 2003, 2004]. Limitations in our understanding of these processes present a fundamental barrier to accurate predictions of sea level rise [IPCC, 2007].

The current rate of sea level rise from 1961 to 2003 is about 1.5 ± 0.4 mm yr⁻¹ [Domingues *et al.*, 2008]. The contribution due to the melting of continental ice (glaciers, ice caps and ice sheets) is a substantial source of current sea level rise, and one that is accelerating more rapidly than was predicted a few years ago. The most recent report from the IPCC [2007] highlights that the uncertainty in projections of future sea level rise is dominated by uncertainty concerning continental ice. Understanding of the key processes that can lead to loss of continental ice must be improved before reliable projections of sea level rise can be made. The direct basal melting of ice shelves can also cause a small but significant change in the rate of sea level rise [Noerdlinger and Brower, 2007; Jenkins and Holland, 2007] due to the density differences between the ice shelf, primarily composed of glacial ice, and the oceans.

Recent estimates suggest an accelerating mass loss from the Antarctic ice sheet, which is thought to manifest itself as a freshening signal in the Antarctic bottom water and Antarctic surface waters. Possible reasons for the Southern Ocean freshening include changes in winds and precipitation, evolving sea-ice volume, and increased melting of the Antarctic ice sheet [Jacobs, 2004]. Much of the observed freshening in the upper part of the Southern Ocean can be explained by an increase in net precipitation, north of 60 °S chosen as the southern data limit due to the low numbers of Argo profiles in the polar region [Helm, 2008]. However, freshening of the deep ocean near the Antarctic continent can only partially be explained by this mechanism suggesting the source is due to enhanced ice shelf melt [Rintoul, 2007].

1.1 Interaction of Ice Shelves with the Ocean

In most cases, the major forcing on ice shelf evolution is the basal melt/freezing rate. Ice shelves largely isolate the ocean below from the effects of the atmosphere. The interaction between the ice shelves and the ocean is mainly thermodynamic with heat and freshwater exchanged between the ice shelf and the ocean. The major physical processes of an ice shelf-ocean system are shown in Fig. 1.4.

The freezing point temperature of seawater decreases with increasing pressure and therefore depth. Most water that enters ice shelf cavities is either at or near the surface freezing temperature, such as High Salinity Shelf Water (HSSW). Water masses from the ocean can enter the cavity and become warmer than the local freezing temperature by moving deeper in the water column. Interaction of these waters with the base of the ice shelf causes melting. The meltwater can mix with the ambient water forming Ice Shelf Water (ISW), which is colder than the surface freezing temperature. Although the ISW is colder, it is fresher and more buoyant than the ambient water and can rise under the ice shelf. The circulation associated with these processes is known as the ice-pump [Lewis, 1985].

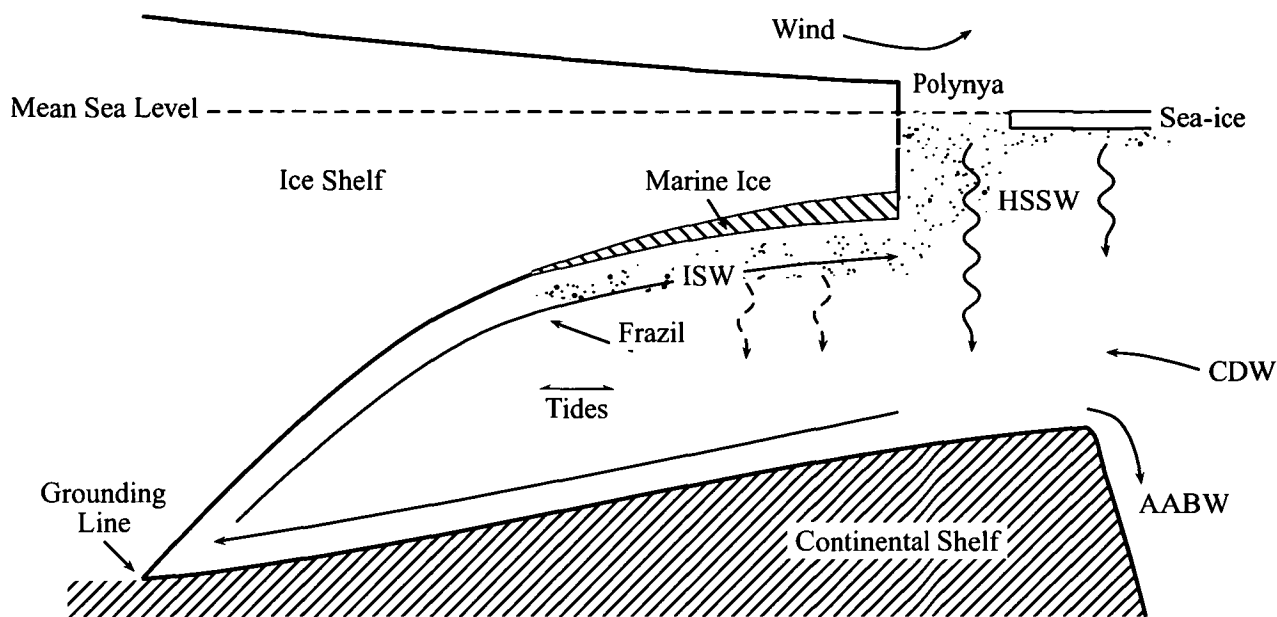


Figure 1.4: Schematic of an ice shelf and the 'ice-pump' mechanism (illustrated using the straight and curved lines). An inflow of Circumpolar Deep Water (CDW) can mix with the product of sea-ice formation (solid curved lines), such as High Salinity Shelf Water (HSSW), which can sink (typically poleward) down the continental shelf and can melt the ice sheet. Buoyant freshwater that is released during the melting process rises along the underside of the ice shelf as Ice Shelf Water (ISW) and can become locally supercooled at a shallower depth, leading to the formation of frazil ice (shown by the dots) and basal accretion of marine ice. The water that is created by the re-freezing process is analogous to that created by sea-ice formation (dashed curved lines). These processes are important for deep water formation processes – such as Antarctic Bottom Water (AABW) – that ventilate the abyssal oceans. The grounding line is the region where the ice shelf is in contact with the sea floor.

1.1.1 Marine ice formation

The increase in the local freezing temperature may then cause the ISW to become supercooled where it can freeze directly at the ice shelf base and also (much more effectively) as small frazil ice crystals in the water column that can later accrete to the base of the ice shelf. These two re-freezing processes act to remove the supercooling from the ISW and are important to sub-ice ocean dynamics and overall glacial ice mass balance.

Marine ice has been shown to occupy distinct areas under the Amery Ice Shelf [Fricker *et al.*, 2001]. Recent observations suggest marine ice accretion can act to 'cement' adjacent ice streams together, thereby enhancing the ice shelf stability [Holland *et al.*, 2009; Craven *et al.*, 2009]. It is thought that a large component of the refrozen marine ice is due to accreted frazil ice. Frazil ice is thought to be important to sub-ice ocean dynamics and overall glacial ice mass balance for a number of reasons described by Smedsrud and Jenkins [2004]:

- Frazil ice growth is thought to be a more effective sink for supercooling than is the growth

of columnar ice directly onto the ice shelf base

- The presence of suspended ice crystals makes the ISW more buoyant. The formation of frazil ice thus modifies the forcing on the overturning circulation within the cavity, which determines the location and rate of marine ice accumulation at the ice shelf base [*Jenkins and Bombosch, 1995*].

With its own set of unique thermal and mechanical properties the presence of marine ice has important ramifications for the dynamic modelling of ice shelf processes and interaction with seawater in the ocean cavities beneath them.

1.1.2 Dense water formation

Ocean interaction beneath the ice shelves is important because they are a major component of the Antarctic mass budget and because they modify the characteristics of the surrounding ocean. Water that circulates onto the continental shelf is modified through sea-ice formation processes and interaction with the base of the ice shelves [*Williams et al., 2008*]. The resulting dense shelf water, with sufficient negative buoyancy and an export pathway to the continental slope, can mix downslope and supply the deep and bottom layers of the global ocean with nutrients and oxygen, as well as with indicators of recent anthropogenic activity, such as chlorofluorocarbons [*Meredith et al., 2001*] and increased concentrations of carbon dioxide [*Sabine et al., 2004*]. Moreover, the temperature and salinity changes that have been observed for Antarctic water masses may influence circulation patterns and lead to modification of Antarctic ice shelves [*Jacobs et al., 2002; Aoki et al., 2005*].

The densest waters in the world's ocean thermohaline circulation are formed in the Southern Ocean, primarily along the Antarctic continental margin. Several interrelated mechanisms involve the addition of 'negative buoyancy' by cooling and salinisation of partially ventilated surface and shelf waters, and by enhancement of mixing with warmer and saltier deep water. Mixing of modified Circumpolar Deep Water (CDW) near the continental shelf break with locally-formed HSSW may contribute to the formation of Antarctic Bottom Water (AABW) which is a key driver in the global thermohaline circulation [*Jacobs, 2004*]. Heat exchange at the ice-ocean interface has a major impact on the global ocean heat and freshwater budget as water masses are formed and modified in the sub-ice shelf cavity [*Wong et al., 1998; Williams et al., 2001*].

Many coupled climate models tend to have too much ventilation of the deep Southern Ocean [*Dutay et al., 2002*]. Perturbation experiments showed that models without ice shelf cavities and the freshwater flux associated with them both underestimated sea-ice thicknesses and increased the rate of bottom water formation and overturning *Hellmer [2004]*. However, both the formation rate of dense water and melting of ice shelves are not well constrained. Furthermore, the effect of the melting of ice shelves on the formation of AABW is poorly known. It is thought that the formation of bottom water can be suppressed due to increased entrainment of fresh glacial melt water. The mixing with freshwater decreases the buoyancy of the dense water formation to a point where it cannot penetrate to the ocean floor.

1.2 Modelling Ice Shelf-Ocean Interaction

Numerical modelling studies are crucial to improve our understanding of the impact of climate change on floating ice shelves and ice sheet mass balance. Understanding the physical mechanisms between ice shelves and the ocean relies on numerical simulations because observations in the polar regions are logistically difficult. Numerical simulations can also be used to predict the response of these mechanisms to climate change. However, most global climate models poorly resolve the continental shelf surrounding the Antarctic continent. As such, understanding the impacts of climate change on ice-ocean interaction relies on using high resolution regional models.

Three-dimensional numerical ocean models have been applied to cavities under several theoretical ice shelves [*Determann and Gerdes, 1994*] and more recently with some success to the Filchner-Ronne Ice Shelf [*Gerdes et al., 1999; Jenkins and Holland, 2002; Jenkins et al., 2004; Grosfeld et al., 2001; Grosfeld and Sandhager, 2004*], the Ross Ice Shelf [*Holland et al., 2003*], and the Amery Ice Shelf [*Williams et al., 2001, 2002*]. The local nature of the basal heat and freshwater fluxes are largely understood and can be reasonably well characterised [for example *Hellmer and Olbers, 1989; Grosfeld et al., 1997; Holland and Jenkins, 1999*]. However, frazil ice dynamics remain a complication to the processes of marine ice formation and the effect of the thermohaline circulation beneath ice shelves.

The dynamics of ISW plumes have been the focus of many specialised modelling studies [for example, *MacAyeal, 1985; Hellmer and Olbers, 1989; Jenkins, 1991*]. Frazil ice dynamics in ISW plumes have been studied in one-dimensional averaged models by *Jenkins and Bombosch [1995; Sherwood [2000]; Smedsrud and Jenkins [2004]* and most recently in two-dimensions by *Holland and Feltham [2005]*. However, these models are deficient for two reasons: (1) The path that each plume follows must be known beforehand to determine the pressure at the ice shelf base, and (2) the plume is introduced between the ambient fluid and the ice shelf base and so must stay in contact with the base of the ice shelf.

1.3 Thesis Aims: Testable Objectives

There are a number of studies that have investigated the interaction of the oceans with ice shelves [for example, *Jenkins, 1991*], dense water processes on the shelf seas around Antarctica [for example, *Marsland et al., 2004*] and the influence of ISW on the formation of sea-ice [*Hellmer, 2004*]. However, to the knowledge of the author, there are no studies that have yet investigated the mechanisms whereby shelf sea processes can influence both the ice shelf evolution and dense water production and the sensitive feedbacks that can exist between these processes. Furthermore, insofar as the author is aware, in the context of AABW formation and ice shelf mass balance, none has included a three-dimensional model of the formation or deposition of frazil ice, which accounts for the majority of marine ice deposition and influences ISW plume thermodynamics [*Foldvik and Kvinge, 1974; Smedsrud and Jenkins, 2004*]. Here, the aim of this thesis is to explore the mechanisms by which climate change can affect ice shelves, sea level rise and the salt budgets of the ocean by using high resolution regional ice-ocean models.

For this study, a three-dimensional ice shelf ocean cavity model, based on the Regional Ocean Modelling System [ROMS, *Shchepetkin and McWilliams*, 2005], has been developed, which represents the state-of-the-art in ice shelf cavity ocean modelling. The thesis will apply the ice shelf/ocean model to the Amery Ice Shelf/Prydz Bay system. Since 2002/03 there has been a concerted program of data collection on and under the Amery Ice Shelf and in the adjacent area of Prydz Bay. These data, not available to previous studies, are used to evaluate the model.

As well as for our understanding of the impacts of climate change, understanding the mechanisms that drive the circulation and water mass formation in the vicinity of the AIS are important for sediment studies [*Hemer and Harris*, 2003], biological studies [*Craven et al.*, 2006; *Riddle et al.*, 2007] and paleo-climate studies of past grounding line positions [*O'Brien et al.*, 2007]. Marine ice has been shown to occupy distinct areas under the Amery Ice Shelf [*Fricker et al.*, 2001] which are thought to be important for ice shelf stability [*Craven et al.*, 2009]. Furthermore, some sparse ocean observations suggest that the region is an important source of AABW formation [*Yabuki et al.*, 2006; *Meijers et al.*, 2009]. This is a result of the combined effects of features such as the presence of a large ice shelf cavity, recurring polynyas, and a wide and abruptly sloping continental shelf over which the densest shelf waters in Antarctica are formed [*Ohshima et al.*, 2009].

The objectives of this thesis are summarised as follows:

- To extend the present equations of ice-ocean thermodynamics, including frazil dynamics to be used in a three-dimensional terrain following ocean model.
- To establish the validity of using terrain following models for the study of ice shelf/ocean interaction.
- To quantify the interaction between the ocean and the Amery Ice Shelf with a model that incorporates the physical components outlined in Fig. 1.4. These interactions include describing the general circulation and patterns, and rates of melt/freeze in the vicinity of the ice shelf over a seasonal cycle.
- To make projections about the state of ice shelves and deep water formation under different climate forcing regimes.

1.4 Thesis Overview

The outline of the remainder of this thesis is as follows:

Chapter 2 reviews previous formulations of the thermodynamic processes that occur beneath ice shelves. The chapter identifies some key discrepancies related to frazil ice dynamics that are explored in later chapters.

Chapter 3 describes the base modifications that have been made to the use of sigma models as applied to the sub-ice shelf ocean cavities. A section is devoted to addressing concerns with

errors that occur with the pressure gradient force calculation in sigma-coordinate models, due to the non-orthogonality of the vertical coordinate.

Chapter 4 examines the results from some simplified ice shelf ocean cavity studies. The results are evaluated against previous simplified studies, including the Ice Shelf - Ocean Model Inter-comparison Project (ISOMIP) and shows some of the first modelling that includes frazil ice dynamics in a three-dimensional ocean model.

Chapter 5 describes the set-up used for the Amery Ice Shelf ocean model. Particular attention is given to the development of the cavity geometry and seasonal boundary conditions.

Chapter 6 evaluates the response of the Amery Ice Shelf ocean system to present day forcing and tests the sensitivity of some physical parameters.

Chapter 7 tests the sensitivity of the Amery Ice Shelf ocean system to climate change with a range of experiments that examine both the combined and separate effects that changing air-sea forcing and lateral boundary warming can have on the mass balance of the Amery Ice Shelf and the formation of AABW.

Chapter 8 presents the major conclusions of the thesis and discusses some caveats related to using ocean models for ice/ocean interaction studies and briefly discusses the potential for future research.

Two fundamentally different ways are used to evaluate the model, as discussed in the *IPCC* [2001]. In the first, an attempt has been made to quantify model errors, to consider the causes for those errors (where possible) and to understand the nature of interactions within the model. In the second, the important issues are the degree to which a model is physically based and the degree of realism with which essential physical and dynamical processes and their interactions have been modelled. It should be emphasised that, within this context, evaluation is a more appropriate term than the commonly-used term validation. Validation implies an affirmation that a model is a complete and accurate representation of the system which is being simulated; however, this is impossible in practice, given that such an affirmation requires a complete and accurate understanding of that system [Oreskes *et al.*, 1994].

The evaluation considers:

- Component-level evaluation: the model is evaluated against the results of other models that have contributed to ISOMIP [Hunter, 2006] and against the two-dimensional overturning model first described by Jenkins and Bombosch [1995] in Chapters 3 and 4.
- System-level evaluation: focused on the outputs of the “full” model. The model is evaluated against published oceanographic and glaciological observations done in the region of the Amery Ice Shelf and Prydz Bay in Chapter 6. The model presented here is also compared against previous models of the Amery Ice Shelf region, where appropriate.

It should be noted that during the final stages of the writing of this thesis the author discovered an error in the base ROMS model code. It was found that the u-component of the quadratic surface stress beneath ice was calculated incorrectly. An investigation revealed that the error was introduced into the ROMS code by the developers during a major rewrite sometime around 2004/05. A re-run of the simulations with the correct surface stress algorithm showed the error affected the spatial pattern of melt/freeze by $\sim 12\%$ for the Amery run with present day forcing. The general circulation and water mass properties were generally unaffected. However, as Chapter 6 is primarily concerned with spatial comparisons with observations all the runs were redone. The simplified Jenkins and Bombosch cavity runs (Chapter 4) are unaffected as they are without rotation and are long and narrow in the v-direction. Due to pressure on time and resources, the runs for Chapter 7 were not redone for the thesis. This was deemed acceptable because Chapter 7 is primarily concerned with investigating net differences between models and the comparison run showed that it is the spatial pattern of melt/freeze that is primarily affected. This means that the “reference” model used in Chapter 6 differs from the “reference” model used in Chapter 7 in the calculation of the u-component of surface stress. All the affected runs are presently being rerun for submission to journals.

CHAPTER TWO

ICE-OCEAN THERMODYNAMICS

The major forcing on ice shelf evolution that is considered here is the melting and freezing processes that occur beneath the ice shelf. Processes that occur internally to the ice shelf, such as strain thinning and ice shelf calving, are not considered in this thesis. As such, the purpose of this chapter is to develop a set of equations to describe ice-ocean thermodynamics to be used as a basis for the rest of the thesis. The well defined ice shelf-ocean thermodynamics are briefly summarised before a longer review of the current state of frazil ice-ocean thermodynamics. The formulations for the ice-ocean parametrisations that are shown in this chapter are tested in simplified cavities (Chapter 4) and for the Amery Ice Shelf cavity (Chapters 5, 6 and 7).

All known published forms of ice-ocean interactions are derived from Fourier's Law, where the conductive heat transfer rate q_c for a given surface area \mathcal{A} , is given by [Pitts and Sissom, 1977]:

$$\frac{q_c}{\mathcal{A}} = -k \frac{\partial T}{\partial n}, \quad \text{W m}^{-2} \quad (2.1)$$

Here, $\frac{\partial T}{\partial n}$ is the temperature gradient in the direction normal to the area \mathcal{A} . The thermal conductivity k is an empirically determined constant for the medium, and may depend on other properties such as temperature and pressure. The minus sign in Fourier's law is required by the second law of thermodynamics that is thermal energy transfer resulting from a thermal gradient must be from a warmer to a colder region. Eqn 2.1 is appropriate for ice growth in *freshwater* and care must be given when examining ice growth rates in *saltwater*.

2.1 Ice Shelf-Ocean Dynamics

At the ice-ocean shelf interface, a parameterisation with a viscous sub-layer model is used (see Fig. 2.1). Three equations represent the conservation of heat and salt and a linearised version of the equation of freezing point of seawater as a function of salinity and pressure [Holland and Jenkins, 1999]. The free variables that are found by solving the three equations simultaneously are temperature, T_b , salinity, S_b , at the ice shelf base, and the melt rate, m . The parameterization of the fluxes of heat and freshwater that occur at the ice shelf-ocean interface is effective due to the difference in time-scales between the slowly flowing ice shelf (for example, $1 \times 10^{-5} \text{ m s}^{-1}$) and the faster sub-ice shelf ocean current (for example, $1 \times 10^{-1} \text{ m s}^{-1}$). This approach allows the spatial pattern of melting and freezing at an ice shelf base to be simulated. The assumption is that the ice shelf is in a steady-state balance with respect to sources and sinks of mass and heat.

The conservation of heat and salt are:

$$\rho_i(L - c_i \Delta T)m = \rho c_w \gamma_T (T_b - T) \quad (2.2a)$$

$$\rho_i(\Delta S)m = \rho \gamma_S (S_b - S) \quad (2.2b)$$

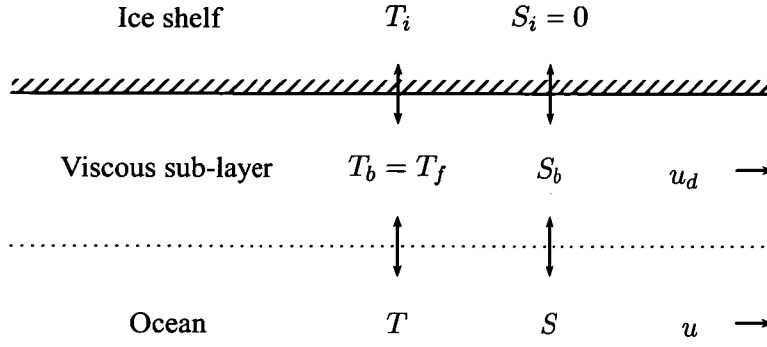


Figure 2.1: Schematic showing the ice shelf-ocean thermodynamic processes. T and S are the water temperature and salinity, with subscript b indicating the condition at the boundary and subscript i in the ice. The free variables are T_b , which is the temperature at the ice shelf base, S_b , which is the salinity at the ice shelf base, and m , which is the melting ($m < 0$) or freezing ($m > 0$) rate (m s^{-1}). The symbols are further described in-text.

where, ρ_i is the density of ice (assumed to be 916 kg m^{-3}), ρ is the density of ocean water, L is the latent heat of ice fusion (3.35×10^5), c_i and c_w are the specific heats of ice ($2009 \text{ J kg}^{-1} \text{ K}^{-1}$) and water ($3974 \text{ J kg}^{-1} \text{ K}^{-1}$), respectively. ΔT is the temperature difference between the ice shelf interior, T_i (-20°C), and the freezing temperature at the base of the ice shelf, T_f . T is the temperature and S the salinity of the water away from the base of the ice shelf base. The assumption is that no salt is present in the ice shelf, which simplifies eqn 2.2b to,

$$\rho_i S_b m = \rho \gamma_S (S_b - S) \quad (2.3)$$

The parameters γ_T and γ_S are coefficients that represent the transfer of heat and salt across the boundary layer. *Jenkins* [1991] used a molecular sub-layer approximation to formulate expressions for γ_T and γ_S as:

$$\gamma_T = \frac{u_d}{2.12 \ln(u_d h / \nu) + 12.5 Pr^{2/3} - 9} \quad (2.4a)$$

$$\gamma_S = \frac{u_d}{2.12 \ln(u_d h / \nu) + 12.5 Sc^{2/3} - 9} \quad (2.4b)$$

where, the molecular Prandtl number (Pr) is the ratio of viscosity to thermal diffusivity and the molecular Schmidt number (Sc), is the ratio of viscosity to salinity diffusivity. The kinematic viscosity of seawater, ν ($1.95 \times 10^{-6} \text{ m}^2 \text{ s}^{-1}$), is considered constant [*Holland and Jenkins*, 1999] over the thickness of the boundary layer, h . The friction velocity, u_d , is defined in terms of the shear stress at the ice-ocean interface:

$$u_d^2 = c_d u^2 \quad (2.5)$$

where c_d is a dimensionless drag coefficient (0.0025) and u is the velocity of the ocean. Note that the ice is considered to be stationary.

The linearised version of the freezing point of seawater as a function of salinity and pressure is:

$$T_f = aS_b + b + cP \quad (2.6)$$

where, T_f is the freezing point at the ice-ocean interface, a is the slope of liquidus for seawater ($-5.73 \times 10^{-2} \text{ }^\circ\text{C psu}^{-1}$), b is the offset of liquidus for seawater ($8.32 \times 10^{-2} \text{ }^\circ\text{C}$), c is the change in freezing temperature with pressure ($-7.61 \times 10^{-4} \text{ }^\circ\text{C dbar}^{-1}$), and P is the pressure at the ice shelf base.

Eqns 2.2a, 2.3 and 2.6 can be solved simultaneously (using known mixed layer and ice properties) to calculate heat and freshwater (salt) fluxes into the ocean [Scheduikat and Olbers, 1990; Hellmer *et al.*, 1998; Holland and Jenkins, 1999]. This has been done previously for several simulations of the flow beneath ice shelves [for example, Beckmann *et al.*, 1999; Timmermann *et al.*, 2002; Holland *et al.*, 2003]. The calculation of the actual heat and salt fluxes into the top model layer of the ocean includes the meltwater advection term that can be important in long simulations or with high basal melt rates [Jenkins *et al.*, 2001]. Simplifications of these equations can be made by assuming that the melt/freeze rates is only driven by the temperature gradient; that is, by setting $S = S_b$ in eqn 2.2b. This assumption reduces the equations to the “two equation” parametrisation as has been discussed in Holland and Jenkins [1999].

2.2 Frazil Ice-Ocean Dynamics

Frazil is important to sub-ice ocean dynamics and overall glacial ice mass balance for two reasons described by Smedsrud and Jenkins [2004]: (1) Frazil ice growth is thought to be a more effective sink for supercooling than is the growth of columnar ice directly onto the ice shelf base. (2) The presence of suspended ice crystals makes the ISW more buoyant. The formation of frazil ice thus modifies the forcing on the overturning circulation within the cavity, which determines the location and rate of marine ice accumulation at the ice shelf base [Jenkins and Bombosch, 1995].

2.2.1 Fundamental equations

Frazil laden water is considered to be a two-component mixture of ice and seawater that is treated as a homogeneous fluid with spatially-averaged properties. The total mass of frazil ice crystals within a fluid parcel is,

$$d\mathcal{M}_C = (d\mathcal{M})C, \quad (2.7)$$

where $d\mathcal{M} = \rho dV$ is the total mass of the parcel of seawater (mass of water plus mass of frazil ice), and C is the mass fraction of frazil ice. For a unit volume of mixture the mass of the seawater fraction is $\rho_s/(1 - C)$ and the mass of the frazil ice fraction is ρ_i/C . For a Boussinesq ocean model, the bulk density of the seawater is,

$$\rho = \rho_s + \rho\mathcal{C}(1 - \frac{\rho_s}{\rho_i}) \quad (2.8)$$

where ρ_s is the density of the seawater without the ice fraction and $\rho\mathcal{C}$ is the mass of frazil ice per unit volume of seawater mixture.

There are two ways in which the mass of frazil ice within a seawater parcel can change:

1. There can be sources and sinks of frazil ice mass within the fluid domain due to melting/freezing, nucleation and precipitation.
2. There can be irreversible molecular or turbulent mixing events that move frazil ice mass between fluid parcels.

For Boussinesq fluid, the time tendency for frazil concentration takes the form,

$$\mathcal{C}_{,t} = -\nabla \cdot (\mathcal{C}\mathbf{v}) - \nabla \cdot (\mathbf{F}) + \mathcal{S} \quad (2.9)$$

where the changes to the frazil ice mass can be mathematically represented by the convergence of tracer flux \mathbf{F} and tracer source \mathcal{S} .

For frazil ice that is suspended in the water column, \mathbf{F} has properties that allow for (1) frazil ice buoyant rising and (2) the turbulent mixing of frazil ice crystals, which yields,

$$\underbrace{\frac{\partial \mathcal{C}}{\partial t}}_{\text{Transient}} + \underbrace{\nabla \cdot (\mathcal{C}\mathbf{v})}_{\text{Advection}} + \underbrace{\mathbf{w}' \frac{\partial \mathcal{C}}{\partial z}}_{\text{Buoyant rising}} = \underbrace{\nabla \cdot (K \nabla \mathcal{C})}_{\text{Mixing}} + \underbrace{\mathcal{S}}_{\text{Source/Sink}} \quad (2.10)$$

where \mathbf{w}' is the vertical buoyancy rising velocity of frazil ice, z is the vertical coordinate (positive upwards), and K is the turbulent exchange coefficient (eddy diffusivity). The model used for the majority of the modelling in this thesis is the Regional Ocean Modeling System that allows the addition of extra tracers, which then handles the advection and diffusion as part of its routines. The mixing term in eqn 2.10 (first term on R.H.S) is separated into horizontal and vertical components, such that,

$$\nabla \cdot (K \nabla \mathcal{C}) = \nabla \cdot (K_{x,y} \nabla_{x,y} \mathcal{C} + K_z \nabla_z \mathcal{C}) \quad (2.11)$$

The horizontal component $K_{x,y}$ is not explicit in the model ($K_x = K_y = 0 \text{ m}^2\text{s}^{-1}$), since the Smolarkiewicz advection scheme used in ROMS is implicitly dissipative [Shchepetkin and McWilliams, 1998]. Vertical eddy diffusion for tracers (K_z) is determined using the K-profile parametrisation (KPP) by Large *et al.* [1994], unless specified to be otherwise.

ROMS solves each term independently using a common numerical technique known as the “Method of Fractional steps” [Yanenko, 1971]. The terms in eqn 2.10 are solved in the sequence: buoyant rising, source/sink, horizontal advection, vertical advection, vertical diffusion, and finally horizontal diffusion. For the purpose of this thesis, the components that have been developed are the sources and sinks (melting and freezing; nucleation; and precipitation) and vertical rise velocity, which are now handled in turn.

Melting and freezing

The process of freezing onto ice crystals that are suspended in the ocean is analogous to that of freezing that can occur directly onto the ice shelf base. In both cases, the temperature of the water that is in contact with the ice will be at the local freezing point (see Fig. 2.2).

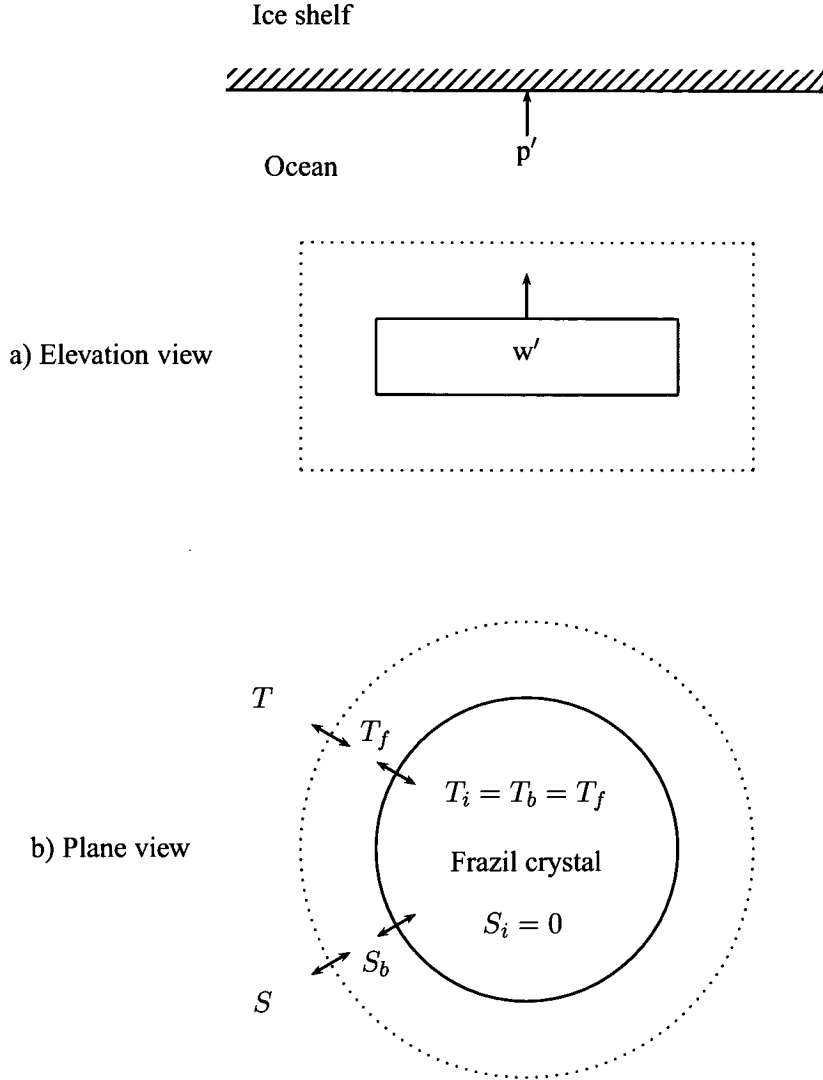


Figure 2.2: Schematic of a frazil ice crystal showing exchanges of temperature T and salinity S across the viscous sub-layer, represented by the dotted circle. The frazil crystal has a vertical settling velocity w' and can precipitate onto the base of the ice shelf at a rate p' . The system is simplified here by making $S_b = S$, which is analogous to the ‘two equation’ basal ice-ocean interaction formulation described in *Holland and Jenkins* [1999].

The source sink terms for heat, salt and ice in the water are related to the melting and freezing of ice particles. This means that ice volume changes in the water are controlled by the flux of heat from crystals already present in the water column. An expression for the heat flux from ice

crystals to surrounding *freshwater* (per unit crystal area) from Fourier's Law (eqn 2.1), is:

$$\frac{q_i}{\mathcal{A}} = \frac{Nuk}{l}(T_i - T) \quad (2.12)$$

where Nu is the Nusselt number, describing the ratio of total heat transfer to conductive heat transfer, $k = k_T \rho c_p$ ($\sim 0.564 \text{ W m}^{-1} \text{ K}^{-1}$) is the thermal conductivity across the ice-water interface, l is characteristic turbulence length scale and $k_T \sim 1.4 \times 10^{-7}$ is the molecular thermal diffusivity of seawater.

Jenkins and Bombosch [1995] state that, as the Nusselt number does not vary significantly from unity, then the transfer of heat from the crystal to the surrounds is solely by molecular diffusion [*Drazin and Reid*, Second Edition, 2004; *Hammar and Shen*, 1995]¹. However, *Holland et al.* [2007] found that the Nusselt number formulation developed by *Hammar and Shen* [1995] incorrectly shows Nu increases as the crystal radius decreases, rather than decreases as the crystal radius decreases, once eddies that move heat away from the crystals surface become smaller than the crystal radius.

Defining an appropriate l is crucial for determining the boundary-layer mixing. The choice of l should match the length scale over which the relevant temperature gradient is taken. Previous authors have chosen a variety of quantities to use for l . Most authors use the crystal disc radius r [*Daly*, 1984; *Hammar and Shen*, 1995; *Sherwood*, 2000; *Holland and Feltham*, 2005; *Smedsrud*, 2002; *Smedsrud and Jenkins*, 2004], but the length $\sqrt{3/8}r$ (based on the crystals total surface area), the disc thickness and half of the disc thickness [*Jenkins and Bombosch*, 1995] have also been used. *Holland et al.* [2007] argue that l is the scale beneath which eddies mix the frazil crystal's boundary layer rather than moving the crystal; whether any such eddies exist is established by comparing l to the Kolmogorov length scale, $\eta = (\nu/\epsilon)^{1/4}$, where ϵ is the turbulent dissipation rate. Using any of the smaller lengths mentioned above will overestimate the influence of these relatively small eddies on the particles relative velocity and thus underestimate their effect on mixing of its thermal boundary layer [*Holland et al.*, 2007].

The formulation of frazil boundary layers in the scientific literature make use of the assumption that the entire crystal is at the local freezing point: that is, there is a zero internal temperature gradient between the edge of the crystal in contact with the water and the centre of the crystal (see Fig. 2.2). However, the analysis is complicated by the fact that the growth and melting of frazil is influenced by transfer of both heat and salt between the ocean and the surface of the ice crystals.

Three equations

The conservation equations for heat and salt due to frazil ice growth and melting are analogous to eqns 2.2a and 2.3. With the assumption that heat diffusion into the crystals are negligible

¹ Nu can also be defined as the ratio of convective to conductive heat transfer [*Incropera and DeWitt*, 1990], which would require Nu in eqn 2.12 to be written as, $(Nu + 1)$. The convention used in-text conveniently utilises the actual transfer of heat, composed of both convective and conductive modes of heat transfer.

($\Delta T = 0$) they can be written as:

$$\rho_i L f' = \rho c_w \gamma'_T \mathcal{A} (T_b - T) \quad (2.13a)$$

$$\rho_i S_b f' = \rho \gamma'_S \mathcal{A} (S_b - S) \quad (2.13b)$$

where, f' is the rate of change of frazil ice volume and the coefficients for heat γ'_T and salt γ'_S are defined in terms of the Nusselt Nu and Sherwood Sh numbers, respectively,

$$\gamma'_T = \frac{Nu k_T}{r} \quad (2.14a)$$

$$\gamma'_S = \frac{Sh k_S}{r} \quad (2.14b)$$

where r is the radius of a disk shaped frazil crystal.

The formulas for the exchange coefficients presented here are different to those in previous literature [for example, *Jenkins and Bombosch*, 1995]. Here, γ'_S is scaled by the Sherwood number Sh (the mass transfer analogy of the Nusselt number), which is the ratio of turbulent mass transfer to mass diffusion. In the course of this review, it was found that *Jenkins and Bombosch* [1995] incorrectly scale both γ'_T and γ'_S only by Nu . Also, the exchange coefficients are scaled by the radius of the frazil disk, r [*Holland et al.*, 2007] and not the half-disk thickness, ra_r [*Jenkins and Bombosch*, 1995], where a_r is the disk aspect ratio.

As such, the growth of frazil ice crystals in *saltwater* depends on the heat transfer rate that is limited by the rate that salt can move away from the ice crystal and water molecules can move toward the ice crystal. An alternate method of calculating the conservation of heat and salt due to frazil growth/melt might, instead, utilise the Sherwood number to calculate the exchange of water molecules from (to) the face of a melting (freezing) ice crystal.

Here, a version of Nu is used that has been truncated for a reasonable range of crystal radii [*Holland and Feltham*, 2006; *Hammar and Shen*, 1995]:

$$Nu_i = \begin{cases} 1 + 0.17 m_i^* Pr^{1/2} & m_i^* \leq \frac{1}{Pr^{1/2}} \\ 1 + 0.55 m_i^{*2/3} Pr^{1/3} & m_i^* > \frac{1}{Pr^{1/2}} \end{cases} \quad (2.15)$$

where $m_i^* = r/\eta$ is the ratio between the frazil radius, r , of size class i and the Kolmogorov length scale, $\eta \sim 1$ mm. The Sherwood number can be calculated, utilising the well known mass-heat transfer analogy [*Drazin and Reid*, Second Edition, 2004], by exchanging Sc for Pr in eqn 2.15, as:

$$Sh_i = \begin{cases} 1 + 0.17 m_i^* Sc^{1/2} & m_i^* \leq \frac{1}{Sc^{1/2}} \\ 1 + 0.55 m_i^{*2/3} Sc^{1/3} & m_i^* > \frac{1}{Sc^{1/2}} \end{cases} \quad (2.16)$$

The effect of salt diffusion, as with that for heat, is strongly dependent on crystal radius. However, the frazil crystal critical radii that determine the turbulent transition points of heat transfer are different to those for mass transfer with discontinuities for Nu at $m^* = 1/Pr^{1/2}$

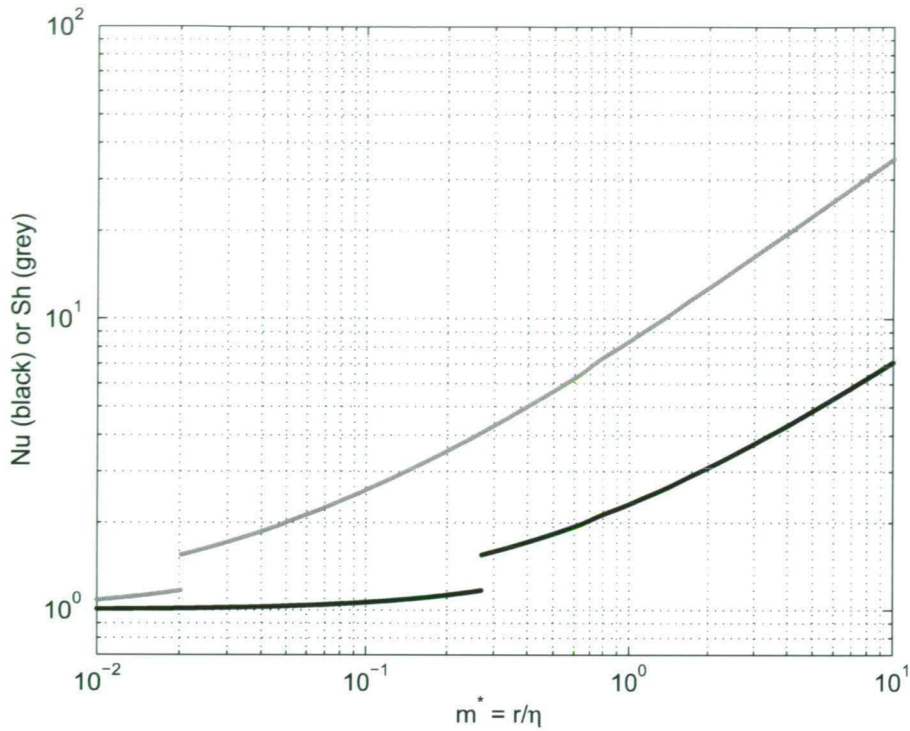


Figure 2.3: Comparing the Nusselt number (Nu; black line) and Sherwood number (Sh; grey line) over a range of m^* , where $\eta \sim 1$ mm. The Nu curve is plotted for $Pr = 13.8$ and the Sh curve is plotted for $Sc = 2432$. Discontinuities occur for Nu at $m^* = 1/Pr^{1/2}$ and for Sh at $m^* = 1/Sc^{1/2}$.

and for Sh at $m^* = 1/Sc^{1/2}$ (see Fig. 2.3).

This section has outlined a set of equations (eqns 2.13a–2.16), that together with knowledge of the local freezing point (eqn 2.6), ambient water properties and the concentrations and size of frazil already present in the water, can be used to calculate heat and freshwater (salt) fluxes into the ocean.

Two equations

It is beneficial to reduce the set of equations outlined above to a simpler ‘two equation’ to reduce the computational overhead that would be required to solve the set of three equations for each frazil size class. This section outlines a set of equations describing frazil melt/freeze that have been implemented into the three-dimensional ocean model used for the remainder of this thesis.

The set of three equations can be simplified by assuming that the growth/melt of frazil ice is driven purely by the heat exchange; that is, $S_b = S$ [for example, *Holland and Feltham*, 2005; *Smedsrud*, 2002]. *Holland and Feltham* [2006] state that since the concern is about the turbulent transfer of heat, which is much larger than the molecular heat exchange, we can regard the diffusion of salt and heat to be equal and the possible effects of salinity are therefore negligible. However, the finite salinity diffusivity supports a salinity difference across the boundary layer and reduces the effectiveness of the thermal driving [*Holland and Jenkins*, 1999]. The assumption in

Holland and Feltham [2006] that the boundary salinity is equal to the ocean salinity will lead to melt/freeze rates that are too large.

To correct for the overestimate of frazil melt/growth, *Smedsrud and Jenkins* [2004] suggested that the Nusselt number can be scaled to consider the effects of salt, based on the scaling factor that was considered for the ‘two equation’ formulation of the ice shelf-ocean boundary conditions [*Holland and Jenkins*, 1999]. That is, as the melt rate of frazil crystals is approximately a linear function of the thermal driving under typical conditions, the impact of salt rejection can be accounted for by simply dividing the heat transfer coefficient, γ'_T by 1.6 to 5.7, depending on the value assumed for the salt transfer coefficient.

However, it has been shown here that the salt transfer coefficient actually depends on the Sherwood number and not the Nusselt number. So, as with the Nusselt number, the exchange of salt between the crystal surface and the ocean scales with the size of the crystal. The ratio of salt transfer coefficient to the heat transfer coefficient is:

$$\left[\frac{\gamma'_S}{\gamma'_T} \right]_i = \frac{Sh_i k_S}{Nu_i k_T} \quad (2.17)$$

The effect of salt diffusion, as with that for heat is strongly dependant on crystal radii. However, the critical frazil crystal radius that determines the turbulent transition points of heat transfer are different to those for mass transfer with discontinuities at $m^* = 1/Pr^{1/2}$ and $m^* = 1/Sc^{1/2}$. The critical radii can be calculated for $m^* = r/\eta$ where $\eta \sim 1$ mm to occur at the turbulent mass transfer point when $r \sim 0.0203$ mm and at the turbulent heat transfer point when $r \sim 0.2692$ mm (Fig. 2.4). The solid horizontal line in Fig. 2.4 is the ratio of salt transfer coefficient to the heat transfer coefficient when $Sh = Nu$, as is implicit in the forms of the exchange coefficients expressed in *Jenkins and Bombosch* [1995]. The effect of frazil radii on the exchange of salt and heat between the frazil crystals and the ocean is clear from Fig. 2.4.

Utilising the similarities in the equations between the ice growth rate at the base of an ice shelf and at the surface of an ice crystal, the scaling factor Θ in *Holland and Jenkins* [1999, eqn 35],

$$\Theta = 1 - \frac{aS_b c_p \gamma'_T}{L \gamma'_S} \quad (2.18)$$

can be modified for frazil to include the formulations of γ'_T and γ'_S , presented here as,

$$\Theta'_i = 1 - \frac{aS_b c_p Nu_i k_T}{L Sh_i k_S} \quad (2.19)$$

Fig. 2.5 shows the scaling factor for a range of frazil radii, where $S_b = 34.4$. The scaling factor for heat transfer is important across all crystal radii and increases towards smaller frazil radii. Provided this factor is approximately constant, a two equation formulation with an effective transfer coefficient of γ'_T/Θ' should yield appropriate melt rates.

Multiple size classes

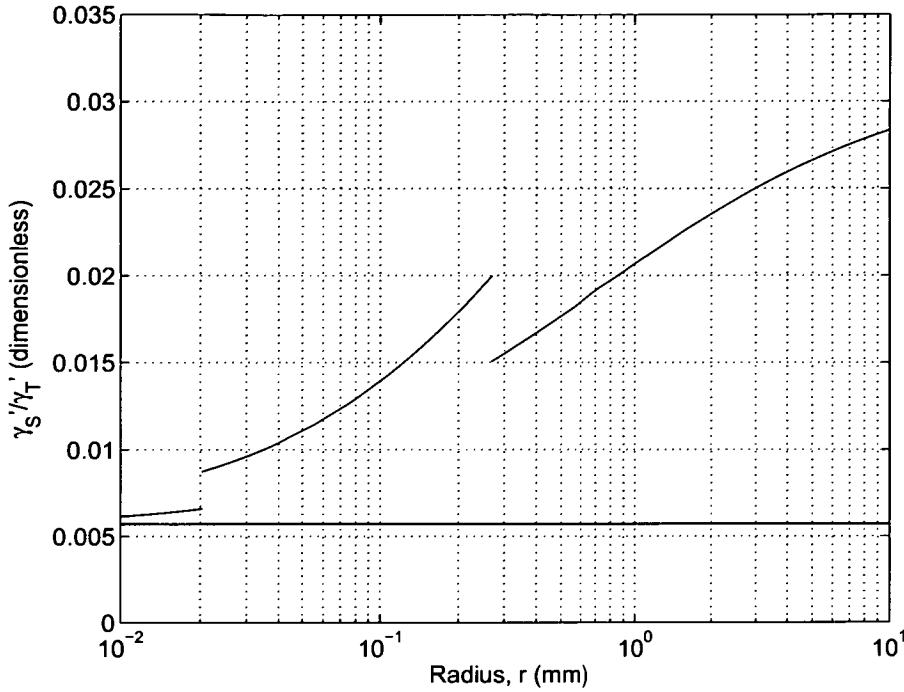


Figure 2.4: The ratio of the salinity (γ'_S) to thermal (γ'_T) exchange velocities plotted against a range of frazil ice sizes. γ'_S and γ'_T were calculated using eqns 2.14a and b. Discontinuities occur for frazil radii, when $m^* = r/\eta$ where $\eta \sim 1$ mm, at the turbulent mass transfer point $r \sim 0.02$ mm and at the turbulent heat transfer point $r \sim 0.27$ mm. The solid horizontal line is $k_S/k_T = 8 \times 10^{-10}/1.4 \times 10^{-7} = 1/175$.

The analysis is complicated by the fact that crystal size (and shape) influences the processes of salt and heat transfer, and in reality a spectrum of frazil crystals can exist within the plume at any one time. See *Daly [1984]* and *Morse and Richard [2009]* for a more thorough review of the problem. The development of a multiple size class frazil model allows that the source of ice is adjusted for the volume concentration of the i -th class [*Smedsrud and Jenkins, 2004; Holland and Feltham, 2005*]. The frazil ice concentration C is distributed between N size classes such that:

$$C = \sum_{i=1}^N C_i \quad (2.20)$$

Melting and freezing of frazil is modelled by the transfer of a certain number of frazil crystals from class n to the larger size class ($n + 1$) in the case of freezing, or smaller size class ($n - 1$) in the case of melting. Therefore, the rate change of frazil concentration in each class is determined by the difference in growth (melting) rates between that class and the one above (below). Transfer processes between classes must also be consistent with the movement of the appropriate volume [*Smedsrud and Jenkins, 2004*].

The melt/freeze of ice crystals is asymmetric: growth occurs at the ice edges and melting occurs

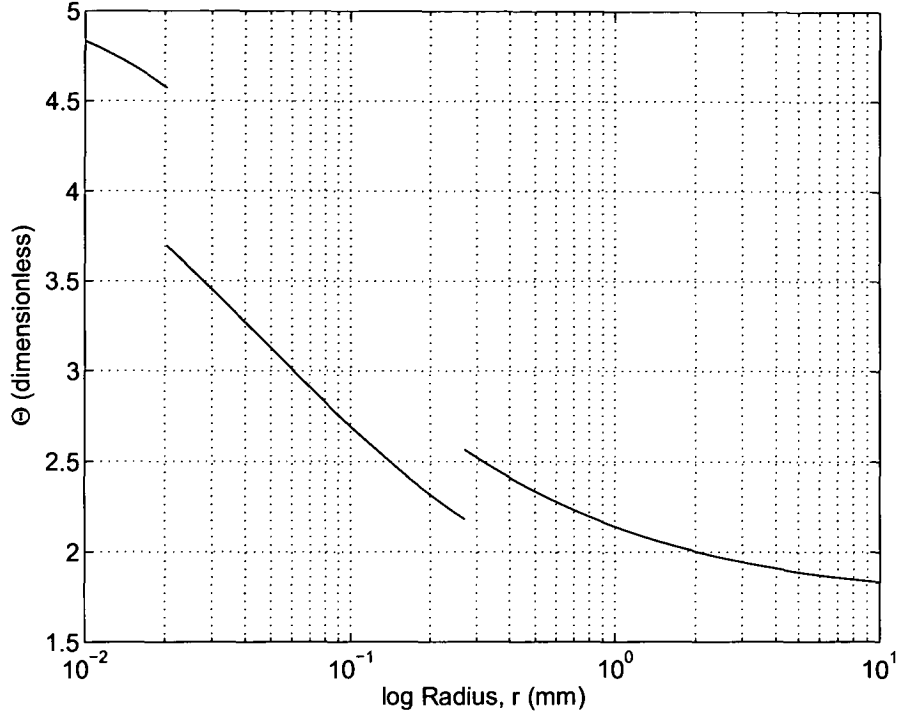


Figure 2.5: Scaling factor plotted against frazil size. The effective exchange based on two equations should include this approximate scaling factor that accounts for the effect of salt.

over the entire crystal. This formulation assumes that the growth of frazil in turbulent seawater only occurs at the edge of the disk and melting occurs over the entire disk to give:

$$G_i = \frac{c_p Nu_i k_t}{L \Theta'_i} (T_f - T) \frac{2}{r_i^2} C_i \quad (2.21a)$$

$$M_i = \frac{c_p Nu_i k_t}{L \Theta'_i} (T_f - T) \frac{2}{r_i} \left(\frac{1}{r_i} + \frac{1}{2a_r r_i} \right) C_i \quad (2.21b)$$

In these expressions Nu_i is the turbulent Nusselt number for each size class, i , which is calculated using eqn 2.15, following *Holland et al.* [2007] and Θ'_i is calculated using eqn 2.19 for each size class. Note that, for $\Theta'_i = 1$, the expressions are those used in previous studies [*Smedsrud and Jenkins, 2004; Holland and Feltham, 2005*].

Nucleation

Formulations of the melt/freeze of frazil rely on the assumption that the growth and melting of frazil is limited by the turbulent diffusion of heat to and from the area of crystals that are *already* in the water. So, the first step that is required when the water becomes locally supercooled is to ‘seed’ the water with a small number of crystals to provide an initial surface area that can be used to calculate the growth rates of ice at the next time-step.

The plume studies that have included frazil [for example, *Holland and Feltham, 2005; Jenkins*

and Bombosch, 1995] have all used strategies of introducing a small concentration of frazil ice crystals when the water becomes supercooled. Frazil seeding is due to dendrite-like platelet ice crystals growing on the ice shelf base that may be detached by eddies and suspended in the water column, providing frazil nuclei of various sizes. As such, the seeding process used by these models makes no adjustment to the temperature and salinity when adding frazil seeds to the water column. If a model cell becomes supercooled and does not contain frazil ice crystals, then the concentration of crystals in that cell is set to 10^{-7} , following the strategy of *Holland and Feltham* [2005]. The assumptions here are:

- There are always sufficient nuclei in the water to grow frazil ice;
- They are distributed evenly over the range of sizes; and
- The initial seed has no impact on the final frazil ice concentrations.

Using a three-dimensional ocean model it is possible that supercooling can occur away from the surface boundary and, as such, frazil nucleation sites are likely at all points in the water column. Seeding is thus allowed to occur at any cell in the model that becomes supercooled.

Secondary nucleation is the process whereby frazil crystals can spawn new “seed” crystals; crystals of the largest size class can fragment into the smallest size class. The main processes thought to give rise to secondary nucleated seed crystals are collisions between frazil and detachment of surface irregularities by fluid shear [*Daly*, 1984]. The formulation used here follows that outlined in *Holland and Feltham* [2005] and allows for secondary nucleation process that include turbulent motions to create new seed crystals. The process is limited to produce a maximum number of seed crystals ($\bar{N} = 1 \times 10^3$) [*Smedsrud*, 2002].

Precipitation, p'

The precipitation of frazil onto the base of an ice shelf borrows from studies of sedimentation in the approach used by *Jenkins and Bombosch* [1995]. Each frazil size class, i will precipitate at a rate:

$$p'_i = \frac{\rho_i}{\rho} w'_i C \left(1 - \frac{|u|^2}{u_i^2} \right) \text{He} \left(1 - \frac{|u|^2}{u_i^2} \right) \quad (2.22)$$

where He is the Heaviside function, which prevents erosion from occurring, and u_i is a critical velocity above which no precipitation can occur, and w'_i is the vertical rise velocity of the frazil crystal (discussed below). This assumes that the flux of crystals that can precipitate out of the water column due to buoyancy is reduced by turbulence in the boundary layer adjacent to the ice shelf base. The critical velocity is expressed as,

$$u_i^2 = \frac{0.05(\rho - \rho_i)g2r_i}{\rho C_d} \quad (2.23)$$

Precipitation starts as soon as the velocity at the base of the ice shelf becomes lower than the

critical velocity. The total precipitation rate is,

$$p' = \sum_{i=1}^N p'_i \quad (2.24)$$

2.2.2 Buoyant “terminal” rise velocity, w'

A frazil ice crystal in still water will rise at its terminal velocity when gravitational forces and drag forces are equal. The formulation choice for the rise velocity w_b relative to the moving fluid is approximated by the rise velocity for frazil ice in still water, following *Holland and Feltham* [2005]:

$$w_b^2 = \frac{4(\rho - \rho_i)ga_r r}{\rho c'_d} \quad (2.25)$$

where, c'_d is a frazil crystal drag coefficient that is calculated using the Newton-Rhapson method from the disc Reynolds number $Re = (w_b 2r)/\nu$. c'_d and can be formulated using either of the below equations:

$$\log(c'_d) = 1.386 - 0.892 \log(Re) + 0.111 \log(Re)^2 \quad (2.26a)$$

$$c'_d = \frac{24}{Re} + \frac{6}{1 + \sqrt{Re}} + 0.4 \quad (2.26b)$$

Eqn 2.26a uses an empirical relationship between rise velocity [*Gosink and Osterkamp*, 1983] and eqn 2.26b is a theoretical formulation of the drag on a sphere [*White*, 1974]. Note that the calculation of the Reynolds number, and hence drag coefficient is only valid for frazil ice crystals larger than 100 μm .

A recent empirical relationship between frazil size and rise velocity has been devised by *Morse and Richard* [2009] based on field observations of frazil ice formation in rivers (sample size = 26470). By fitting power laws to the data they developed a piecewise function:

$$w' = \begin{cases} 2.025D^{1.621} & \text{if } D \leq 1.27\text{mm} \\ -0.103D^2 + 4.069D - 2.024 & \text{if } 1.27 < D \leq 7\text{mm} \end{cases} \quad (2.27)$$

where, $D = 2r$ is the diameter of a frazil ice crystal.

Fig. 2.6 compares the three different methods for calculating w' . Two different aspect ratios, a_r were used to calculate w' from *Gosink and Osterkamp* [1983] and *White* [1974]. $a_r = 1/25$ is the ‘standard’ ratio used in the frazil modelling literature and $a_r = 1/15$ was observed in the studies of *Morse and Richard* [2009]. It is interesting to see that the commonly used $a_r = 1/25$ matches the empirical fit proposed by *Morse and Richard* [2009] better than $a_r = 1/15$. The discrepancy might be due to turbulent motions that are implicit in *Morse and Richard* [2009]. A comparison of the effects of the different rise velocities on frazil ice dynamics are presented in Chapter 4.

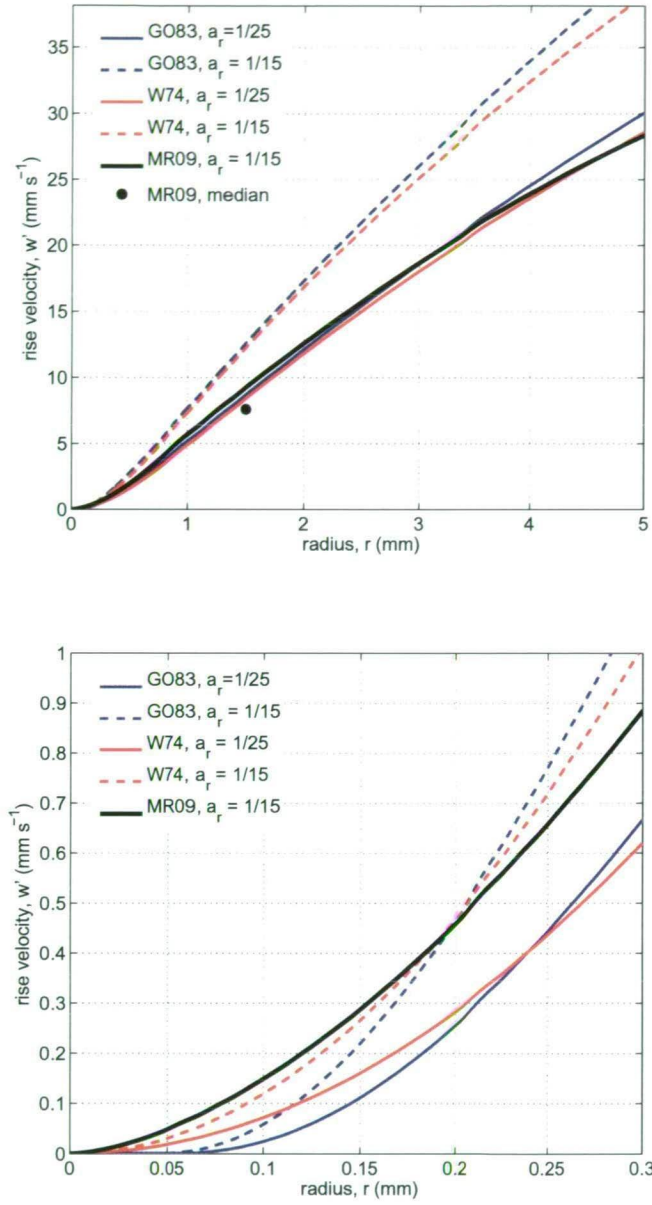


Figure 2.6: Three different formulations for the frazil rise velocity. The formulations follow Gosink and Osterkamp [1983, blue lines, eqn 2.26a], White [1974, red lines, eqn 2.26b] and Morse and Richard [2009, black line, eqn 2.27].

2.2.3 Frazil model stability

During the course of this review and the subsequent simulations (see Chapter 4), it became apparent that a number of stability criterion must be satisfied, which are analogous to the Courant, Friedrichs, and Lewy (CFL) criterion. These are:

1. Frazil crystals should not rise vertically through a grid-level in one time-step.

2. The growth/melt of frazil should not exceed the amount of supercooling/superheating in one time-step, with one related constraint.
3. The amount of frazil that is melted should not exceed the amount of frazil present in the cell; that is, $C' = \max(0, C + \Delta C)$, where C' is the frazil concentration at an incremented time-step and ΔC is the amount of frazil melt (negative).

Thermodynamic rate conditions

As melting occurs over the whole surface of a crystal and is therefore much faster than freezing which only occurs at the edges of a crystal, a violation is more likely to occur because of excessive melting rather than excessive freezing. The rate of transfer between size classes due to melting depends on both the surface area, \mathcal{A} , of crystals available for melting and the thermal driving, ΔT . It is difficult to predict the ΔT or \mathcal{A} that will be present in a given model cell before a model is run to be able to 'estimate' the growth-rate and so ensure that the time-step constraint is not violated. Also, the difference between the volumes of the two smallest size classes is the greatest [see eqns 17 and 19, *Holland and Feltham*, 2006]. During melting the transfer of volume between the classes is proportional to $\Delta T(1/r_{i+1}^2 - 1/r_i^2)$. The uptake of superheating (in the case of melting) is due (non-linearly) to the difference between size class radii, rather than the radii themselves. So, stability can be enhanced by reducing the difference between the two smallest size classes by increasing the size of the smallest size class, and/or increasing the number of size classes ².

The violation of this criterion can be avoided by:

1. Using a smaller time-step.
2. Increasing Θ to reduce the frazil growth/melt rates. Given the uncertainty and assumptions with many aspects of our understanding of frazil dynamics, in the context of ice-ocean modelling, Θ represents a parameter that can be used to 'tune' the frazil model.
3. Bound the maximum growth of frazil in one step to a maximum value pre-calculated from ΔT . The maximum melting of frazil can be bounded by both the limit due to the amount of heat present in the water and the amount of ice that is available for melting.

In the sense of an overall modelling strategy, the time-step ideally needs to be a fraction of the frazil growth and melting. Coupled climate models often use an ice-ocean condition in which only the freezing point at the upper level of the ocean model is diagnosed. At each time-step, the computed temperature is reset to the freezing point and an appropriate amount of ice melted or frozen. In the case of frazil modelling, removing the thermal driving in less than one time-step means that the frazil dynamics is parametrised rather than modelled, which is what is done in most sea-ice models [for example, *Schmidt et al.*, 2004]. However, several time-steps are required during the thermal driving take-up, so that the frazil dynamics can be used to accurately determine

² Personal communications with Paul Holland, British Antarctic Survey, Cambridge, UK.

the ice distribution, hence precipitation. This suggests that the optimum methods to avoid violation are to use a smaller time-step or to tune the rate dependence of the melt/freeze.

2.3 Concluding Remarks

This chapter has outlined the basic ice-ocean thermodynamics that have been included in a three-dimensional ocean model for the purpose of this thesis. There still exist major uncertainties and assumptions in the description of frazil/ocean dynamics. For example, components of the understanding of frazil dynamics come from studies of frazil growth in freshwater [Daly, 1984] and have been borrowed from studies of sedimentation [McCave and Swift, 1976].

Here, key improvements to our understanding of the theory of frazil ice dynamics in ocean water have been made. It has been shown that frazil growth/melting depends on *both* the rate of heat transfer and the rate of mass (salt) transfer. Appropriate exchange coefficients for salt can be defined in terms of the Sherwood number, which describes the ratio of the actual mass transfer rate and the mass transfer rate through diffusion alone. A scaling factor Θ'_i that corrects the *freshwater* approximation of frazil growth in *saltwater* has been introduced for two equation formulations, which depends on crystal size.

CHAPTER THREE

ADAPTATION OF AN OCEAN MODEL

In this chapter modifications that have been made to terrain-following models are presented. In the first section we provide a general description of the Regional Ocean Modeling System (ROMS) that was used for the majority of the modelling studies presented here. This is followed by a section that is designed to alleviate the primary concern expressed in the ice-ocean cavity modelling community about the use of models with terrain-following coordinates. The pressure gradient force error in ice shelf ocean cavity models is addressed by comparing two different terrain-following models; namely, the Australian version of the Princeton Ocean Model (OzPOM) and ROMS. A discussion of the Equation of State (EOS) of seawater and some numerical developments particular to modelling frazil ice follows.

3.1 The Regional Ocean Modeling System

The Rutgers version of ROMS, used for this study, is a coarse grain parallel primitive equation ocean circulation model derived from the serial SCoordinate Rutgers University Model [SCRUM, see *Hedstrom*, 1997]. The model has a free-surface and uses a vertical coordinate, which is terrain-following [*Shchepetkin and McWilliams*, 2005].

ROMS solves the hydrostatic primitive equations for momentum using a split-explicit time-stepping scheme requiring special treatment and coupling between barotropic (fast) and baroclinic (slow) modes. A finite number of barotropic time-steps, within each baroclinic step, are carried out to evolve the free-surface and vertically integrated momentum equations. In order to avoid the errors associated with the aliasing of frequencies resolved by the barotropic time-steps but unresolved by the baroclinic time-step, the barotropic fields are time averaged before they replace those values obtained with a longer baroclinic step. In addition, the separated time-stepping is constrained to maintain exactly both volume conservation and consistent preservation properties which are needed for the tracer equations. Currently, all 2D and 3D equations are time-discretised using a third-order accurate predictor (Leap-Frog) and corrector (Adams-Molton) time-stepping algorithm which is very robust and stable.

In the vertical, the primitive equations are discretised over variable topography using stretched terrain-following coordinates. The stretched coordinates allow increased resolution in areas of interest, such as thermocline and bottom boundary layers. The default stencil uses centred, second-order finite differences on a staggered vertical grid. Options for higher order stencil are available via a conservative, parabolic spline reconstruction of vertical derivatives. The numerical algorithm in ROMS is designed to reduce pressure-gradient errors.

In the horizontal, the primitive equations are evaluated using boundary-fitted, orthogonal curvilinear coordinates on a staggered C-grid [*Arakawa and Lamb*, 1977]. The general formulation of curvilinear coordinates includes both Cartesian (constant metrics) and spherical (variable

metrics) coordinates. All models discussed here use a spherical coordinate. As in the vertical, the horizontal stencil utilizes a centred, second-order finite difference scheme. Further detail can be found in *Shchepetkin and McWilliams [2005]*.

3.1.1 Mechanical surface conditions

The most important consideration of the model numerics is that of incorporating the large mass of ice that is floating on the ocean's surface. The thickness and extent of the ice shelf does not change over the time covered by the simulations presented here. Under the ice, the upper boundary of the model is no longer at sea level but conforms to the ice shelf base. The pressure gradient force calculation accounts for the possibility that the top surface of the water may have a significant slope due to the ice shelf. The hydrostatic pressure at the base of the ice shelf is computed by assuming that the ice is in isostatic equilibrium. This pressure can be calculated by the integral over depth (from mean sea level to the base of the ice shelf) of the density of the water replaced by the ice. Instead of assuming that the density in the integral can be approximated by the density at the first level of the ocean model directly beneath the ice [for example, *Grosfeld et al., 1997*] or a constant average density for every location [for example, *Beckmann et al., 1999*], the density at the first level of the ocean model ρ_1 minus an assumed constant linear dependence of the density with depth $\delta\rho/\delta z$ is used to give a pressure of:

$$P = g(\rho_1 - 0.5 \frac{\delta\rho}{\delta z} H_i) H_i \quad (3.1)$$

where g is the gravitational acceleration and H_i is the ice shelf draft. The change in density with pressure for water near freezing and salinities in the range 34 to 35 psu is relatively constant for the first few hundred meters from the surface and an average over this range ($\delta\rho/\delta z = 4.78 \times 10^{-3} \text{ kg m}^{-4}$) was used [*Dinniman et al., 2007*].

Below the ice shelf, the atmospheric contributions to the momentum and buoyancy flux are set to zero. At the sea bed and at the base of the ice shelf the stress is described by the quadratic friction law:

$$\tau = \rho c_d u_d |u_d| \quad (3.2)$$

where τ is the stress, ρ is the water density, c_d is a drag coefficient (prescribed as 0.0025), and u_d is the water velocity in the model cell adjacent to the sea bed or ice shelf base.

3.2 The Pressure Gradient Force

Terrain-following coordinate models are chosen to model the oceans beneath ice shelves due to their ability to simulate interactions between flows and topography, such as the important buoyant ISW plumes that can rise under ice shelves in a narrow outflow region. Such behaviour is essential to recreate when modelling ice shelf ocean interactions. Terrain following models are well recognised to provide the best method for regional studies of oceanographic processes. However, terrain-following coordinate models are strongly criticised for their inability to handle the pressure gradient calculation [for example, *Losch, 2008*].

Discretisation of the horizontal pressure force is a source of errors for several classes of primitive equation models [summarised in *Adcroft et al.*, 2008]. The most well known problems with pressure gradient force calculations are in terrain-following coordinates which have been the focus of many studies with the aim to minimize these errors [for example, *Haney*, 1991; *Shchepetkin and McWilliams*, 2003]. However, discretisation difficulties are also found in layered (isopycnal) models that include a non-linear equation of state where thermobaric effects (compressibility) can lead to spurious numerical instabilities [*Hallberg*, 2005]. These problems can be alleviated by using a linear equation of state (which is obviously unrealistic), or alternative methods of isolating the compressibility effects [*Adcroft et al.*, 2008]. Pressure gradient errors are also present in the bottom-most cells of the shaved cell or partial step representation of topography in geopotential coordinate (z) models, if poorly handled [*Pacanowski and Gnanadesikan*, 1998]. Small pressure gradient errors can also be present in other coordinate systems, such as stretched geopotential (z^*) or pressure coordinates (p^*) [*Adcroft and Campin*, 2004]. Topographical restrictions occur in other vertical coordinate systems. For example, in z -coordinate models, bottom topography is usually smoothed to eliminate grid scale noise.

Ice shelf processes can be included in terrain-following models with little technical effort: the surface layers subduct beneath the ice shelf and all ice-ocean interactions are applied to the surface level. However, the front of an ice shelf is a cliff face and this means that terrain-coordinates ‘jump’ vertically about 200 m over the horizontal resolution of the model (see Fig. 3.1). It is well known in the literature that the numerical error in the pressure gradient calculation is amplified over steep topography [for example, *Mellor et al.*, 1998; *Ezer et al.*, 2002]. These internal pressure areas are often divided into sigma errors of the first kind (SEFK) and sigma errors of the second kind (SESK) [see *Mellor et al.*, 1998]. SEFK decay to zero and SESK can create artificial flow that does not decay with time. The source of the problem is that in s -coordinates, the horizontal component of the internal density gradient is written:

$$\left. \frac{\partial \rho}{\partial x} \right|_z = \left. \frac{\partial \rho}{\partial x} \right|_\sigma - \frac{\sigma}{H} \frac{dH}{dx} \frac{\partial \rho}{\partial \sigma} \quad (3.3)$$

where x is the horizontal coordinate, z the vertical coordinate, H , the depth, $\sigma \equiv z/H$ and ρ is the seawater density. Near steep topography the two terms on the right hand side may be large and comparable in magnitude. This may cause large errors in the estimates of the internal pressure. The hydrostatic inconsistency condition is essentially the failure of the discretised PGF term to disappear when density surfaces are aligned with geopotential surfaces. The Hydrostatic Condition (HC) can be written as [*Haney*, 1991]:

$$\left| \frac{\sigma}{H} \frac{\partial H}{\partial x} \right| \frac{\Delta x}{\Delta \sigma} \leq 1 \quad (3.4)$$

or, by defining a bottom slope parameter, s , that is the ratio of the change in slope Δh over the

total average depth \overline{H} [Beckmann and Haidvogel, 1993]:

$$s = \frac{\Delta h}{2\overline{H}} \quad (3.5)$$

However, simulations have been run with parameters much higher than suggested by theory with little effect on model performance; up to $HC = 5$ [eqn 3.4, Ciappa, 2006] and up to $s = 0.5$ [eqn 3.5, Ezer *et al.*, 2002]).

For this reason, Beckmann *et al.* [1999] modified the ice shelf edge topography to allow the s -coordinates to vary smoothly across this discontinuity. In a different approach, Grosfeld *et al.* [1997] introduced hybrid coordinates (z -coordinates near the surface and s -coordinates beneath the ice shelves) to resolve the steep topography at the ice shelf front, which requires an ice front that is of a uniform depth across the model domain. Studies by Williams *et al.* [2001, 2002] located the lateral domain boundary at the ice front edge, thereby avoiding the problem entirely. However, with this approach, the model can only be forced at the lateral boundary and atmospheric surface forcing conditions cannot be included.

The numerical error in terrain following coordinate models can be significantly reduced by using methods that involve, for example, higher order schemes [Chu and Fan, 1997], z -level interpolation schemes [Fortunato and Baptista, 1996] or parabolic reconstruction schemes [Shchepetkin and McWilliams, 2003]. These schemes are commonly tested using a steep sided seamount case and have been shown to reduce this error to the level of other numerical errors. An up-to-date review and discussion of the various schemes used to calculate the horizontal pressure gradient force in terrain-following models can be found in Shchepetkin and McWilliams [2003]. The worst performer is considered to be the standard density-Jacobian method of handling the discretised pressure gradient force calculation [Shchepetkin and McWilliams, 2003].

The purpose of this section is to alleviate the concern expressed in the ice-ocean cavity modelling community about the use of models with terrain-following coordinates [for example, Losch, 2008]. In this perspective the behaviour of ROMS is evaluated by comparing its pressure gradient scheme with OzPOM, based on the Princeton Ocean Model of Blumberg and Mellor [1987]. In OzPOM, the standard Jacobian scheme and the sixth order Chu and Fan [1997] scheme are used, and in ROMS the default Shchepetkin and McWilliams [2003] scheme is used in two different configurations. ROMS and OzPOM have been applied to ice shelf ocean cavities [ROMS: Galton-Fenzi *et al.*, 2008a; Dinniman *et al.*, 2007] and [OzPOM: Hunter *et al.*, 2004] and are participating models in the Ice Shelf Ocean Model Inter-comparison Project (ISOMIP). Each model is tested with three different surface forcing experiments.

3.2.1 Experiments

The models

Four pressure gradient algorithms – two each from the two models – are evaluated for the same model configurations:

1. OzPOM-J is OzPOM with the standard density-Jacobian scheme [Mellor *et al.*, 1998];
2. OzPOM-H is OzPOM with the higher sixth order combined compact difference scheme [Chu and Fan, 1997];
3. ROMS-J is ROMS with a standard density-Jacobian; and
4. ROMS-H is ROMS with a density-Jacobian scheme using monotonised cubic polynomial fits [Shchepetkin and McWilliams, 2003].

For a complete evaluation of these schemes for various parameters and detailed numerical descriptions the reader should refer to the appropriate references given above. The differences between these schemes have been tested using a range of seamounts with different gradients [Ezer *et al.*, 2002]. Note that the default scheme in ROMS is the higher order scheme (ROMS-H). The standard Jacobian scheme (ROMS-J) is obtained by setting an internal parameter in the calculation of the pressure gradient algorithm, *OneFifth* = 0. The modified ROMS scheme, with *OneFifth* = 0 is then equivalent to the standard Jacobian scheme used in OzPOM-J. It is expected that the higher order schemes used in OzPOM-H and ROMS-H will perform better than the standard schemes used in OzPOM-J and ROMS-J.

Configuration

The basic model follows the geometry and conditions of ISOMIP [Hunter, 2006]. The geometry of the experiments is similar to "Experiment 1" of Grosfeld *et al.* [1997] but with the 200-metre deep section of ice shelf replaced by open water, as shown in Fig. 3.1.

It is a closed basin of uniform depth 900 m, spanning 15° of longitude, and latitudes 80°S to 70°S. The ice draft rising linearly from 700 m at 80°S to 200 m at 76°S, with open water from 76°S to 70°S. The geometry is uniform in the east-west direction and includes a steep ice front which provides a test of the pressure-gradient problems often associated with terrain-following coordinate models. For comparison with other ISOMIP experiments and that of Grosfeld *et al.* [1997] the basal melt rates are shown at quasi-steady state. Both models use stretched vertical coordinates which allows higher resolution at the ice shelf base and at the seafloor (Fig. 3.1.a). Mixing under stably stratified conditions employs constant horizontal (along s-surfaces) mixing coefficients outlined in Hunter [2006]. In the case of unstable conditions, vertical convection is parametrised by a simple convective adjustment scheme that increases the background vertical mixing coefficients by a factor of 100. Other schemes are available (e.g., the so-called implicit diffusion, and KPP [Large *et al.*, 1994]) but do not alter the present results significantly¹. The cavity described here has a hydrostatic consistency at the upper limit of those described in the literature: $HC = 5.6$ and $s = 0.5$.

¹ Personal communications: Mike Dinniman, Centre for Coastal Physical Oceanography, Old Dominion University, Virginia, U.S.A.

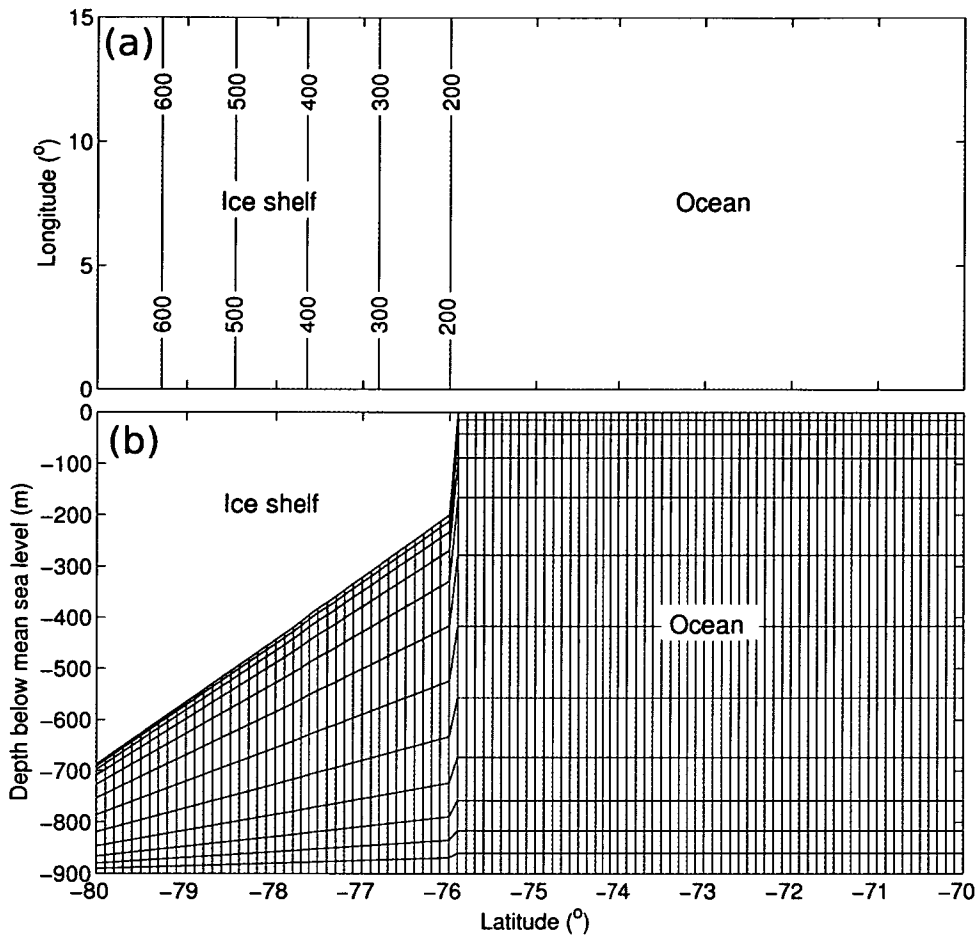


Figure 3.1: Plane (top) and elevation (bottom) views of model basin used for experiments in this section. The s-coordinates can be seen in the lower panel to follow the sloping ice shelf bottom.

3.2.2 Surface forcing conditions

The easiest method of detecting spurious eddy formation due to the PGF calculation is to run the models without forcing. A comparison of the residual currents between models can provide an estimate of the amount of spurious mixing that can occur. As such, experiment 1 is without any forcing at the surface boundary. Experiments 2 and 3 have the same ice-ocean boundary conditions but different prescriptions of the air-sea boundary conditions.

Experiment 1 This experiment has no forcing at all. This test follows seamount test cases to detect spurious mixing due to finite differencing of model domains. Since, ideally, the fluid should remain at rest, non-zero velocity should be interpreted as being due to numerical errors. The water is initially at rest and has uniform potential temperature (-1.9°C) and salinity (34.4).

Experiment 2 This experiment is forced by melting and refreezing underneath the ice shelf, and relaxation to steady prescribed values of temperature and salinity over the open ocean [Model 2.01

of the ISOMIP test cases, *Hunter, 2006*]. The prescribed surface thermodynamic temperature and salinity, T_p and S_p are -1.7°C and 34.4 PSU, respectively, which are annual average temperature and salinities. The relaxation time, τ , is 30 days.

Experiment 3 For this experiment a more realistic seasonal cycle of salt and heat fluxes is prescribed to the open ocean (see Fig. 3.2). The timings and magnitude of the seasonal cycle are based on observations made in Prydz Bay, East Antarctica, which is adjacent to the Amery Ice Shelf [*Gibson and Trull, 1999*]. The growth of sea-ice occurs when the slope of the line describing the salinity is positive and melting occurs when the slope of the line describing the salinity is negative. Note that this forcing is similar to ISOMIP Model 2.02 but uses different values.

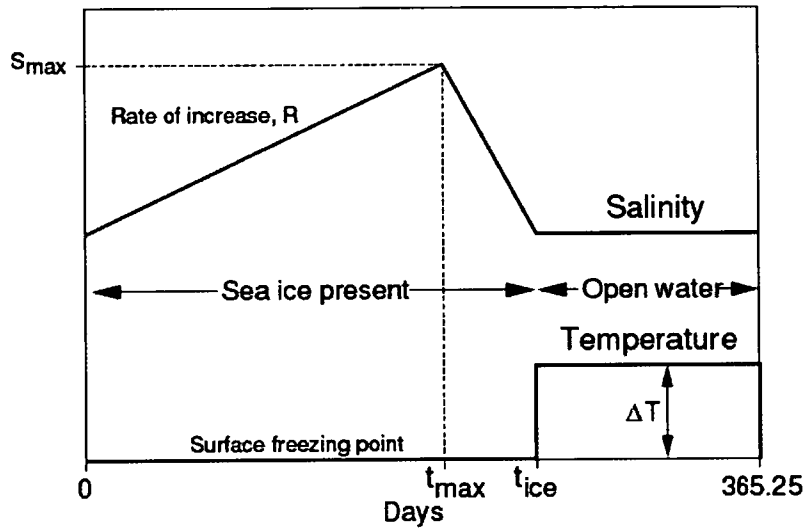


Figure 3.2: Seasonal variation of air-ocean surface salinity and temperature, which are typical of those for the seasonal variation of temperature and salinity in Prydz Bay, East Antarctica [*Gibson and Trull, 1999*], are $S_{max} = 35.0$, $R = 0.01 \text{ day}^{-1}$, $\Delta T = 1^\circ\text{C}$, $t_{max} = 230$ days and $t_{ice} = 290$ days.

Thermodynamic ice shelf-ocean boundary conditions

Freezing and melting form a boundary layer between the ice shelf and ocean which is parametrised following *Grosfeld et al. [1997]*. This parametrisation yields an effective heat flux and a virtual salt flux (i.e., a freshwater flux without volume change in the ocean) between ice shelf and water, that can be conveniently applied at the base of the ice shelf, that is, as a tendency term in the ocean at the appropriate depth.

For experiments 2 and 3, the upward heat flux Q at the interface is parametrised in a bulk formulation proportional to the temperature difference between the ice shelf base and the seawater:

$$Q = \rho c_p \gamma_T (T - T_b) \quad (3.6)$$

where ρ is the density of seawater, $c_p = 3974 \text{ J kg}^{-1}$ is the specific heat capacity of water, and $\gamma_T = 10^{-4} \text{ m s}^{-1}$ is the turbulent exchange coefficient. T_W is the temperature of the model cell adjacent to the ice-water interface. The temperature at the interface T_b is assumed to be the local freezing point of seawater T_f which is computed from a linearised version of the equation for the freezing point of seawater [Foldvik and Kvinge, 1974]:

$$T_f = -0.0573S_b + 0.0939 + 0.0007641P_b, \quad (3.7)$$

from the salinity S_b and the pressure P_b (in dBar) in the cell at the ice-water interface [Gill, 1982].

Neglecting the heat flux through the ice, all heat is used for basal melting and freezing. The associated upward freshwater flux (negative melt rate, in units of freshwater mass per time) can be computed by:

$$q = -\frac{Q}{L} \quad (3.8)$$

with the latent heat of fusion $L = 3.34 \times 10^5 \text{ J kg}^{-1}$. Upward heat flux implies basal melting therefore a downward freshwater flux, hence the minus sign. From the freshwater flux a virtual salt flux is computed using a constant reference salinity of 34.4, according to the ISOMIP specifications.

Thermodynamic air-ocean boundary conditions

The surface boundary conditions for temperature and salinity are prescribed using surface fluxes, rather than the actual temperature or salinity values. This is done by firstly defining an effective vertical transport velocity as the ratio of the thickness of the top model cell to the relaxation time. The surface flux of temperature (say) is then derived from the product of this transport velocity and the difference between the temperature of the top cell and the prescribed relaxation temperature.

At the air/water interface, the inter-facial stress is zero and the thermodynamic temperature and salinity are relaxed to prescribed values, T_p and S_p , using a relaxation time, τ . Therefore, to a first approximation the following is effectively performed each time-step, δt :

$$T_s = T_s + (\delta t/\tau)(T_p - T_s) \quad (3.9a)$$

$$S_s = S_s + (\delta t/\tau)(S_p - S_s) \quad (3.9b)$$

where T_s is the surface thermodynamic temperature, and S_s is the surface salinity.

Diagnostic variables

The experiments are compared using the time histories of the following diagnostic variables [see Shchepetkin and McWilliams, 2003; Thiem and Bernstein, 2006]: Kinetic energy (K.E.),

$$\mathcal{E} = \frac{1}{2\mathcal{V}} \sum_{i,j,k} \left[\Delta \mathcal{V}_{i+\frac{1}{2},j,k} u_{i+\frac{1}{2},j,k}^2 + \Delta \mathcal{V}_{i,j+\frac{1}{2},k} v_{i,j+\frac{1}{2},k}^2 \right]; \quad (3.10)$$

barotropic K.E. fraction,

$$\mathcal{F} = \frac{\bar{\mathcal{E}}}{\mathcal{E}}, \quad (3.11)$$

where $\bar{\mathcal{E}}$ is barotropic kinetic energy,

$$\bar{\mathcal{E}} = \frac{1}{2\mathcal{V}} \sum_{i,j} \left[\Delta \bar{\mathcal{V}}_{i+\frac{1}{2},j} \bar{u}_{i+\frac{1}{2},j}^2 + \Delta \bar{\mathcal{V}}_{i,j+\frac{1}{2}} \bar{v}_{i,j+\frac{1}{2}}^2 \right]; \quad (3.12)$$

maximum velocity,

$$V_{max} = \max \left\{ u_{i+\frac{1}{2},j,k}, v_{i,j+\frac{1}{2},k} \right\}; \quad (3.13)$$

and maximum baroclinic velocity,

$$\langle V \rangle = \max \left\{ u_{i+\frac{1}{2},j,k} - \bar{u}_{i+\frac{1}{2},j}, v_{i,j+\frac{1}{2},k} - \bar{v}_{i,j+\frac{1}{2}} \right\}. \quad (3.14)$$

In eqns 3.10–3.14 above, $\Delta \mathcal{V}_{i,j,k}$, $\Delta \mathcal{V}_{i+\frac{1}{2},j,k}$ and $\mathcal{V}_{i,j+\frac{1}{2},k}$ are control volumes of ρ and velocity component grid boxes, respectively, and

$$\mathcal{V} = \sum_{i,j,k} \Delta \mathcal{V}_{i,j,k} \quad (3.15)$$

is the total volume of the domain,

$$\bar{u}_{i+\frac{1}{2},j} = \frac{1}{\Delta \bar{\mathcal{V}}_{i+\frac{1}{2},j}} \sum_{k=1}^N \Delta \mathcal{V}_{i+\frac{1}{2},j,k} u_{i+\frac{1}{2},j,k} \quad (3.16a)$$

$$\bar{v}_{i,j+\frac{1}{2}} = \frac{1}{\Delta \bar{\mathcal{V}}_{i,j+\frac{1}{2}}} \sum_{k=1}^N \Delta \mathcal{V}_{i,j+\frac{1}{2},k} v_{i,j+\frac{1}{2},k} \quad (3.16b)$$

are the barotropic velocity components, and

$$\Delta \bar{\mathcal{V}}_{i+\frac{1}{2},j} = \sum_{k=1}^N \Delta \mathcal{V}_{i+\frac{1}{2},j,k}, \quad (3.17a)$$

$$\Delta \bar{\mathcal{V}}_{i,j+\frac{1}{2}} = \sum_{k=1}^N \Delta \mathcal{V}_{i,j+\frac{1}{2},k} \quad (3.17b)$$

are the barotropic control volumes.

3.2.3 Assessment of the ROMS PGF algorithm

Experiment 1

The results show a major sensitivity to the choice of PGF algorithm. The four quantities shown in Fig. 3.3 lead to the following observations:

- The overall level of error is judged using the level of maximum velocity as an indicator of

spurious movement after long-runs [Ezer *et al.*, 2002], and determines that best performing model is ROMS-H, closely followed by OzPOM-H. The worst performing model is OzPOM-J.

- The long-term error across all models is predominantly baroclinic. Compared to baroclinic energy, the barotropic energy component (not shown) and maximum barotropic velocity error show little sensitivity to the choice of model or PGF algorithm. The baroclinic component for the ROMS models quickly adjusts (within a few years) and reaches equilibrium. The same is not true of OzPOM which shows strong variability during the runs.

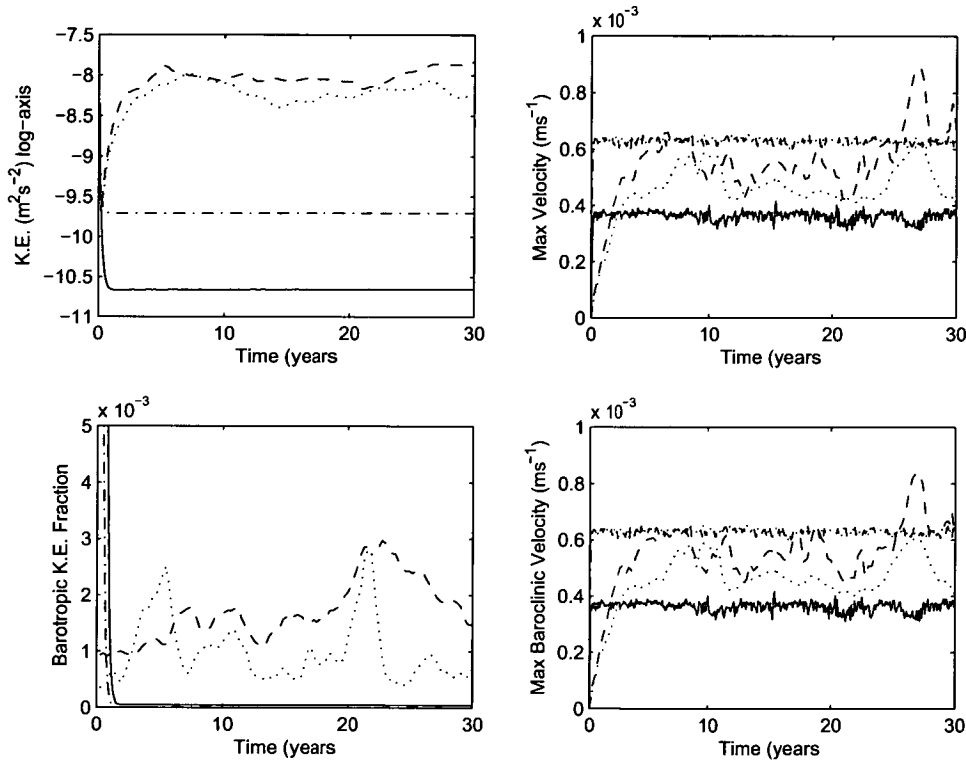


Figure 3.3: Time histories of net kinetic energy (top-left), fraction of barotropic kinetic energy (bottom-left), maximum velocity (top-right) and maximum baroclinic velocity (bottom-right) for experiment 1. These experiments were done on a $102 \times 52 \times 11$ grid for different formulations of the pressure gradient algorithm in two different models: OzPOM-J (dashed line), OzPOM-H (dotted line), ROMS-J (dot-dashed line) and ROMS-H (solid line).

The remaining velocities are primarily attributed to SESK, which can create artificial flow that does not decay with time. The spurious flow is created at the ice front where the sigma layers sharply subduct beneath the ice shelf.

Experiments 2 and 3

Time histories of the area averaged melt rates for experiment 2 are presented in Fig. 3.4. The choice of pressure gradient force for OzPOM shows a clear difference in the melt rate. The same

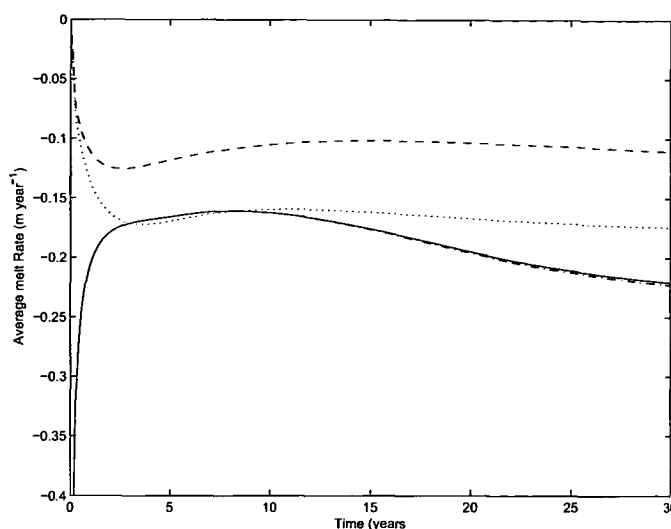


Figure 3.4: Time histories of the area averaged melt rate for experiment 2 for OzPOM-J (dashed line), OzPOM-H (dotted line), ROMS-J (dot-dashed line) and ROMS-H (solid line). Note that the two different ROMS models have a very similar spin-up. The final results are summarised in Columns 1 and 2 of Table 3.1.

is not true of ROMS where both models are in very close agreement with each other.

Fig.3.5 shows a comparison of OzPOM-J (left column), OzPOM-H (middle column) and ROMS-H (right column). Shown are the spatial pattern of the melting (red) and freezing (blue), superimposed with depth averaged current vectors for Experiments 2 (upper row) and Experiment 3 (bottom row). The spatial pattern of melt/freeze and magnitude of the currents agrees well with ROMS for both experiments 2 and 3. For experiment 3, the eddies and spatial pattern of melt/freeze formed in OzPOM-J are very different to those in experiment 2 and as compared to ROMS.

In both experiment 2 and experiment 3, ROMS-H and ROMS-J (not shown) show melting of approximately 1 m year^{-1} in the south-east corner of the domain occurs where warm water from the interior is brought into contact with the ice shelf, and freezing of approximately 1 m year^{-1} along the western boundary current, where cold water rises and refreezes because of the pressure-dependent freezing point of seawater. The magnitude of melt rates for ROMS-H are comparable to other published results of ISOMIP-type cavities and in the closed Grosfeld cavity reported in *Holland et al.* [2007], using an isopycnic-coordinate ocean general circulation model that was adapted to the study of sub-ice shelf cavities by *Holland and Jenkins* [2001] and the closed cavity case, using a z-coordinate model, reported in *Losch* [2008].

Surprisingly, OzPOM-J and ROMS-H both have an area of strong refreezing in the north-west corner, unlike OzPOM-H which uses a higher order scheme. This is unexpected as OzPOM-J was shown to be a worse performer than OzPOM-H in experiment 1. However, it's clear that spurious currents that form across the ice front in OzPOM-J are enhanced by strong seasonal forcing typical

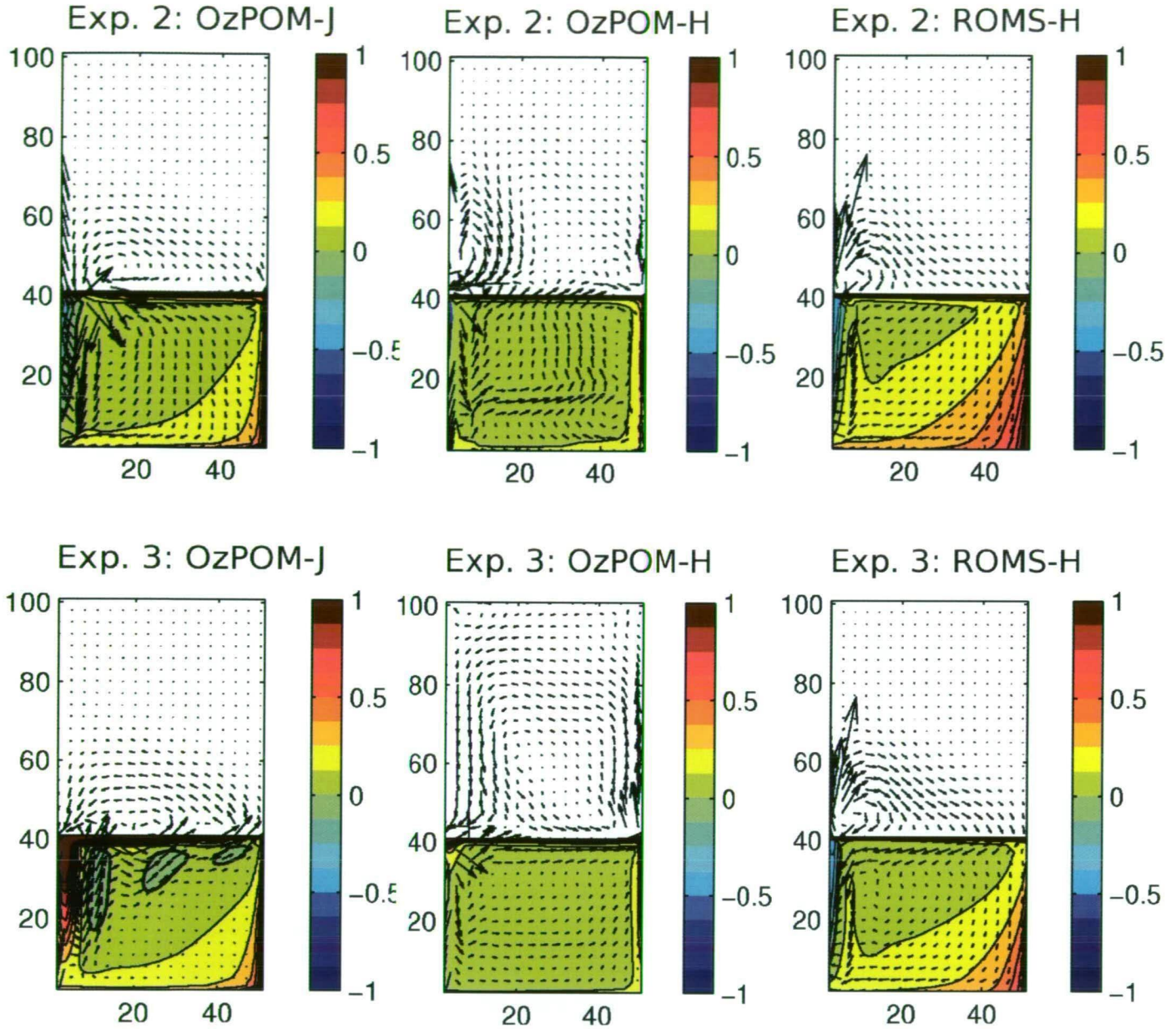


Figure 3.5: Barotropic currents and melt/freeze rates (m year^{-1}) for experiment 2 (top row) and time averaged barotropic currents and melt/freeze for experiment 3 (bottom row), for OzPOM-J (left), OzPOM-H (middle) and ROMS-H (right). The largest currents are about 20cm s^{-1} .

of the Antarctic, with seasonal sea-ice growth and associated brine rejection.

The results of OzPOM-J in experiment 3 show that strong currents become eddying features that drastically alter the pattern of melting and freezing that can occur (see Table 3.1). The effect of using a higher order pressure gradient algorithm in OzPOM is dramatic. Eddies are not present in OzPOM-H at the ice front; however, the main circulation in the open ocean is stronger and in the opposite direction than that shown in ROMS-H.

Table 3.1: Comparing the area averaged melt rates for experiment 2 (constant forcing) and experiment 3 (seasonal forcing) for various pressure gradient force schemes.

Model	Melt rates (m year ⁻¹)	
	Exp 2.	Exp 3.
OzPOM-J	0.152	0.183±0.003
OzPOM-H	0.110	0.107±0.006
ROMS-J	0.255	0.164±0.047
ROMS-H	0.254	0.164±0.047

The smallest error is obtained using a high order accurate density-Jacobian scheme with monotonised cubic polynomial fit as is used in ROMS-H. The ROMS-H scheme is supposedly comparable with the sixth order scheme used in OzPOM-H [Ezer *et al.*, 2002]. However, it is clear from the results that there are other differences between the models which means ROMS performs better overall. Furthermore, ROMS-J and ROMS-H require about the same number of cpu hours and are computationally less expensive than the sixth order scheme used in OzPOM-H. OzPOM-H requires approximately 25% more CPU time than OzPOM-J.

SESK are further enhanced when the open ocean is forced with a seasonal cycle. During winter, the formation of dense water sets up a strong density gradient between the water in the cavity beneath the ice shelf and the open ocean. Fig. 3.5 shows the effect that winter brine formation has on the formation of SESK in OzPOM-J (experiment 3 compared to experiment 2). The SESK are apparent in the velocity fields that show a number of eddies at the ice front in experiment 3: OzPOM-J. However, it is also found that the main component is baroclinic, which is in disagreement with the findings presented by *Shchepetkin and McWilliams* [2003]. The major differences between the experiments of *Shchepetkin and McWilliams* [2003] and those presented here are that SESK are created by truncation errors in the PGF due to the large *surface* slope rather than in the *bottom* slope.

Pressure gradient errors over steep topography in terrain-following ocean models have been an issue of concern for a long time. The comparison with previous modelling studies and the coherence of the spatial pattern of melt/freeze and currents between experiments 2 and 3 show that ROMS-H presents the correct solution. SESK can produce spurious eddies along the ice shelf front in models with inferior PGF algorithms. The magnitude of spurious current and mixing can dramatically change the amount and pattern of melting that can occur. These eddies are due to the rotational component of spurious PGF terms and are analogous to the seamount eight-lobed pattern described in *Chu and Fan* [1997], *Mellor et al.* [2002] and *Tiem and Berntsen* [2006]. Here, it is shown that ROMS handles the effect of a steep sloping ice shelf remarkably well.

This similarity between the two ROMS models are attributed to the weighting used to develop the standard density-Jacobian from the the higher-order scheme. The choice of weighting is shown in *Shchepetkin and McWilliams* [2003] to be similar to the standard Jacobian choice of pressure

gradient scheme (*OneFifth* = 0). However, the small difference shown here between ROMS-J and ROMS-H suggest the following:

1. The standard Jacobian choice of pressure gradient scheme in ROMS is not explicitly created by setting *OneFifth* equal to zero; that is, the pressure gradient force algorithm used for ROMS-J is not equivalent to that used for OzPOM-J; and
2. The error levels in the simulations are controlled by more general model factors than just the PGF, for example, the tracer advection scheme, forms of diffusivity, and viscosity operators.

The goal of this section, to evaluate the effectiveness of the ‘default’ ROMS-H pressure gradient scheme at an ice shelf front, has been achieved. Further tests of the effectiveness of the ROMS-H pressure gradient scheme are left to future studies.

3.3 Equation of State for Seawater in Polar Regions

Density driven flows in polar regions, such as the “ice-pump” mechanism, brine formation processes due to sea-ice growth and the flow of bottom water into the abyssal oceans, can be affected by the density computation. An increase in the temperature of an ice/seawater mixture will cause an increased rate of melting as the ice-seawater mixture responds to maintain the temperature near to the local freezing point. As the ice melts, the seawater becomes fresher, and thus buoyant as its density decreases due to the salinity decrease. The computation of density, which is important in the pressure gradient force calculation, for example, can lead to significant changes in circulation. Therefore, it is paramount that realistic ice-ocean modelling studies use an EOS that is as accurate as possible.

The ROMS EOS is only valid for temperatures in the range from -2 – 40°C . However, temperatures colder than -2°C can be found at depths in the polar regions. For example, the local freezing point temperature at a salinity of 34.4 is about -3.8°C for the deepest part of the Amery Ice Shelf, which has some of the deepest ice in contact with the oceans in Antarctica at about 2700 m below mean sea level [Galton-Fenzi *et al.*, 2008b]. In polar regions changes in salinity are the main component leading to changes in density, reflected in the near vertical lines of Fig. 3.6.

The formulation that is used in the Modular Ocean Model (MOM4.0) is adapted for inclusion into ROMS, which has the McDougall *et al.* [2003] EOS [Griffies *et al.*, 2004]. The EOS is updated by using the revised coefficients of Jackett *et al.* [2006]. This EOS is recommended for purposes of realistic ice-ocean simulations, where accuracy over a wide range of temperature, salinity, and pressure is crucial and has been fitted over the range:

$$0 \leq S \leq 120 \quad (3.18a)$$

$$-6^{\circ}\text{C} \leq \theta \leq 80^{\circ}\text{C} \quad (3.18b)$$

$$0 \text{ db} \leq P \leq 10000 \text{ db} \quad (3.18c)$$

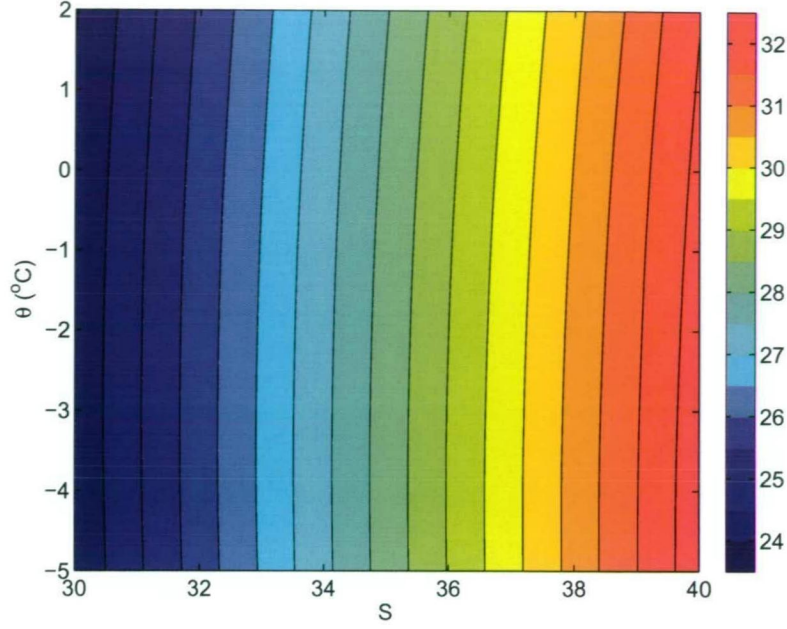


Figure 3.6: Density calculated at the surface for a range of salinities and potential temperatures that are common to the polar oceans from *McDougall et al.* [2003].

Feistel [1993], *Feistel and Hagen* [1995], and *Feistel* [2003] studied the equilibrium thermodynamics of seawater and produced a more accurate EOS than UNESCO by using more recent empirical data. *McDougall et al.* [2003] produced a fit to *Feistel and Hagen* [1995] to render an expression convenient for use in ocean models, and *Jackett et al.* [2006] updated this EOS based on *Feistel* [2003] and included some handy algorithms for the calculation of the freezing point temperature. The *standard* ROMSv3.0 EOS uses an approximated version of the *Jackett and McDougall* [1995] EOS. The polynomial functions and density partial derivatives in the *updated* form that is used here can be seen in Appendix 1.

3.4 Frazil Settling Scheme

From Chapter 2, eqn 2.10, the change in concentration of frazil crystals per model cell due to the vertical rising of buoyant frazil crystals is,

$$\frac{\partial \mathcal{C}_i}{\partial t} = w'_i \frac{\partial \mathcal{C}_i}{\partial z} \quad (3.19)$$

where the concentration of frazil \mathcal{C}_i for each size class, i is assessed at the ρ levels in the vertical model grid shown in Fig. 3.7. The vertical rise velocity w'_i for each size class is calculated at levels that are equidistant from the ρ levels in the vertical model grid.

The finite-difference approximation to eqn 3.19 calculates the transport of frazil through the

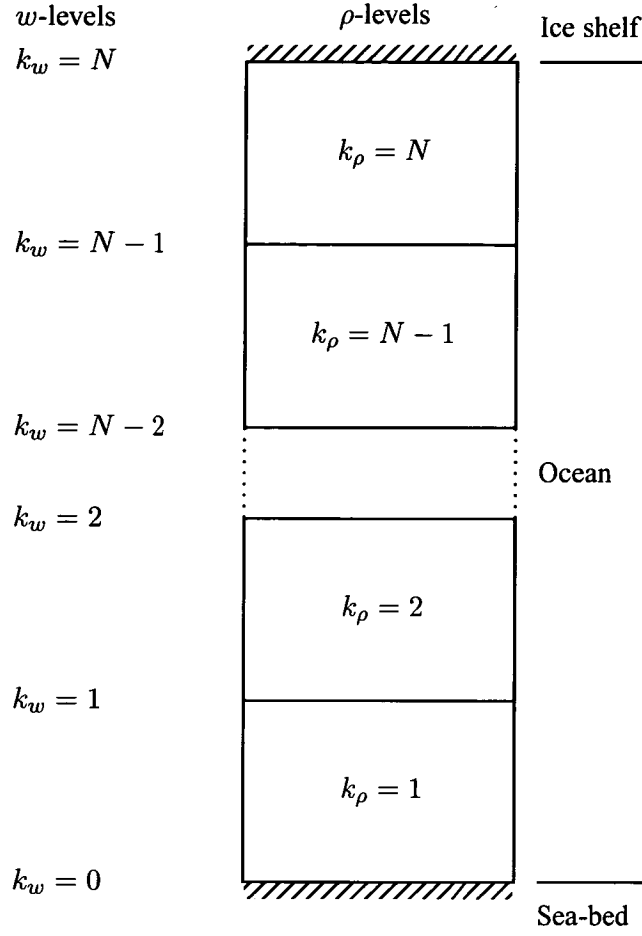


Figure 3.7: Stencil of the vertical levels showing the tracer points (ρ -levels) and velocity points (w -levels).

w -levels using the Forward Time, Centered Space (FTSC) scheme [Press *et al.*, 1987],

$$\frac{C_{\rho i, k}^{t+\Delta t} - \Delta C_{\rho i, k}^t}{\Delta t} = -w'_i \left(\frac{C_{w i, k_w}^t - C_{w i, k-1}^t}{2\Delta z} \right) \quad (3.20)$$

where the frazil concentration at each w -level, k_w , is calculated as:

$$C_{w i, k}^t = \frac{C_{\rho i, k}^t + C_{\rho i, k+1}^t}{2}, \text{ and} \quad (3.21a)$$

$$C_{w i, k-1}^t = \frac{C_{\rho i, k-1}^t + C_{\rho i, k}^t}{2} \quad (3.21b)$$

at an incremented time-step $t + \Delta t$ in terms of the concentration known at time-step, t . As w'_i is constant, the flux calculation is performed at the ρ -level. The advantage of this scheme is that it is

an explicit equation for C and is stable as long as:

$$\frac{|w'_i|\Delta t}{\Delta z} \leq \frac{1}{2} \quad (3.22)$$

This condition numerically places a constraint on the size of the time-step Δt relative to the vertical grid spacing Δz and frazil rise velocity w'_i . If this condition is violated physically unrealistic conditions could emerge. Instability in the FTCS scheme is avoided provided that the stability criterion is observed and the frazil rise velocity is constant over depth, z .

Fig. 3.8 shows a vertical one-dimensional implementation of the FTCS scheme for two frazil size classes with vertical velocities of 1 and 3 mm s⁻¹. The model has 16 vertical layers that are spaced to give higher resolution at the top and bottom of the domain, typical of all of the models runs shown in this thesis. A concentration of 1 kg m⁻³ for each of two frazil size classes was introduced initially at the deepest layer. The column of water is at rest and the frazil is thermodynamically inert. The model uses a time-step $\Delta t = 200$ s and is run for 70×10^3 s. The final amount of frazil in the top cell or the vertical integration of the frazil at any time, is equal to that of the initial amount. The scheme correctly transports the frazil as compared to the continuous theoretical rise velocity, shown as the thick black line. There is some numerical diffusion.

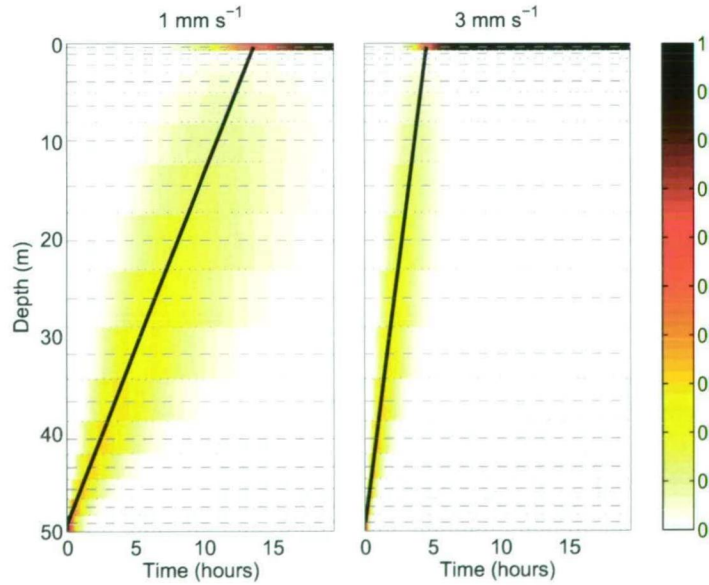


Figure 3.8: Showing the time evolution of two different frazil size classes with rise velocities of 1 mm s⁻¹ (left panel) and 3 mm s⁻¹ (right panel) from a one-dimensional, 16 layer stretched vertical coordinate model. The model was initially seeded at the deepest layer with 1 kg m⁻³ of frazil. The thickness of the ρ -levels (horizontal dashed lines) from top to bottom are: 0.72, 1.11, 1.71, 2.53, 3.57, 4.69, 5.595, 5.98, 5.68, 4.86, 3.85, 2.92, 2.24, 1.82 and 1.65 m. The model was run with $\Delta t = 200$ s. The thick black line is the analytical rise trajectory. The ρ -levels and w -levels are represented by the horizontal dashed and dotted lines, respectively.

Eqn 3.22 can be used, given the models time-step constraint to estimate the maximum permissible frazil rise velocity and hence size class. For a minimum vertical increment of, say 0.72m and a model time-step of 300 seconds, from Fig. 2.6, the largest frazil crystals have a radius of $\sim 0.5\text{mm}$.

3.5 Concluding Remarks

This chapter has presented modifications that have been made to terrain-following models for the study of the ocean cavity beneath ice shelves. In particular, the ROMS pressure gradient force algorithm was evaluated here against OzPOM and with other GCMs which was followed by a discussion of modifications that were made to the EOS and the implementation of a conservative vertical frazil advection scheme. ROMS has the necessary internal numerics capable of simulating the oceans beneath ice shelves. ROMS and modifications are used for the remainder of this thesis.

CHAPTER FOUR

SIMPLIFIED MODELS OF ICE-OCEAN INTERACTION

This chapter investigates the effects of the frazil ice/ocean and direct ice shelf-ocean thermodynamic processes that occur beneath ice shelves using two different simplified models. The first is a non-rotating overturning model that was first used for plume modelling studies by *Jenkins and Bombosch* [1995]. The second is a variation of *Grosfeld et al.* [1997], which includes rotation and uses the cavity geometry outlined in Chapter 3. It is shown that the inclusion of a frazil ice model dramatically alters the mechanism for refreezing and circulation beneath ice shelves.

4.1 The Plume Model of Jenkins & Bombosch (1995)

The essential feature of this model is that it is non-rotating. Previous studies of frazil ice dynamics beneath ice shelves that have used this configuration have been limited to plume models that rely on a buoyant plume originating at the grounding line [*Jenkins and Bombosch*, 1995; *Smedsrud and Jenkins*, 2004; *Holland and Feltham*, 2006]. The version presented here has an ice shelf that is uniform in the y-direction – the “linear ice shelf” where the shelf base rises linearly in the x-direction from a grounding line depth at 1400 m to an ice front at 285 m below mean sea level at a distance of 600 km away. The model here also includes a region of open ocean that is 600 km long. The sea floor is a constant depth at 1500 m below mean sea level.

The initial conditions of the ambient fluid has a salinity profile that decreases linearly from 34.71 psu at the grounding line depth to 34.5 psu at the surface and a temperature that rises linearly from -2.18°C at the grounding line to -1.85°C at the surface. Note that the temperature profile has been modified from that specified in *Jenkins and Bombosch* [1995] so that the surface temperature is above the surface freezing point using eqn 2.6: $T_f = -1.88^{\circ}\text{C}$ for $S = 34.5$. The model domain used here is 100 km wide and has closed free-slip side walls except for the furthest boundary from the grounding line which is open. The grid is uniform in both the x- and y-directions with a horizontal spacing of 5 km (20 x 240 horizontal cells) and has 21 vertical layers which increase in resolution at the top and bottom of the domain. The results shown here are all loosely grid independent. The model uses a 300 second baroclinic and a 10 second barotropic time-step.

Laplacian horizontal mixing of tracers is along horizontal (geopotential) surfaces with a diffusivity of $5\text{ m}^2\text{s}^{-1}$. The third-order upstream momentum advection scheme used in ROMS is naturally dissipative and therefore only a small background value ($0.1\text{ m}^2\text{s}^{-1}$) of explicit horizontal momentum mixing was required [*Shchepetkin and McWilliams*, 2005]. Quadratic bottom stress, with a coefficient of 2.5×10^{-3} (non-dimensional), was applied as a body force over the bottom layer and to the layer immediately below the ice shelf. The vertical momentum and tracer mixing were handled using the K profile parametrisation (KPP) mixing scheme [*Large et al.*, 1994]. No double diffusive mixing was included. The open boundaries were handled as:

- *Lateral open boundary:* Temperature and salinity were relaxed to the initial conditions

using a two-dimensional radiation scheme combined with adaptive nudging over 10 days [Marchesiello *et al.*, 2001]. No sponge layer, or region of increased horizontal viscosity near the open boundaries, was used.

- *Ocean-atmosphere boundary*: The temperature and salinity in the upper-layer in the open ocean were relaxed to the initial conditions using a relaxation time scale of 10 days. Frazil ice present in the upper-layer was removed from the domain at the rate proportional to its vertical terminal velocity. The assumption here is that the frazil ice precipitates onto the base of sea-ice which is then transported from the domain. Results of preliminary models without this upper boundary condition developed unrealistic concentrations of frazil that reached the density of ice.

4.1.1 Experiments

The ‘plume’ model cavity is used to investigate the effect of frazil on basal melting and freezing. Two models are compared: one model with frazil ice and the other without frazil ice. In both cases a plume is initiated at the grounding line in the upper sigma-layer ($\sim 1\text{--}2$ m) at the ice shelf base and a volume flux of $5 \times 10^{-5} \text{ m}^2\text{s}^{-1}$ per unit width. The inflow here is analogous to a small constant sub-glacial river that drains into the ocean cavity and mixes with some ambient seawater. Following [Holland and Feltham, 2006], the plume has an initial temperature of -2.95°C that corresponds to the freezing point temperature at a salinity of 34.42 [Gade, 1979].

The experiment includes frazil ice with 10 size classes having radii of 0.01, 0.05, 0.15, 0.3, 0.4, 0.5, 0.6, 0.8, 1 and 2 mm [Holland and Feltham, 2005]. The control was configured as closely as possible to experiments done in Jenkins and Bombosch [1995], Smedsrud and Jenkins [2004], and Holland and Feltham [2006] by setting $Nu = 1$ and using the terminal rise velocity calculation from White [1974]. A number of parameter sensitivities for the frazil model were also investigated:

1. Run “HF06- Nu ” uses eqn 2.15 for the calculation of the Nusselt number Nu [Holland *et al.*, 2007] instead of $Nu = 1$.
2. Run “Scaled- γ_T ” uses eqn 2.19 to scale the thermal exchange coefficient γ_T by Θ' .
3. Run “MR09- w' ” uses eqn 2.27 for the calculation of the vertical rise velocity [Morse and Richard, 2009] instead of White [1974].
4. Run “1/2-plume” is with the buoyancy input reduced by half.

4.1.2 Results

Fig. 4.1 compares the spin-up of the direct basal melting (positive) and freezing (negative) along the x-direction for the model without frazil (a) and the model with frazil (b). Note that the accretion shown in Fig. 4.1b is only the direct basal freezing component and does not include frazil precipitation.

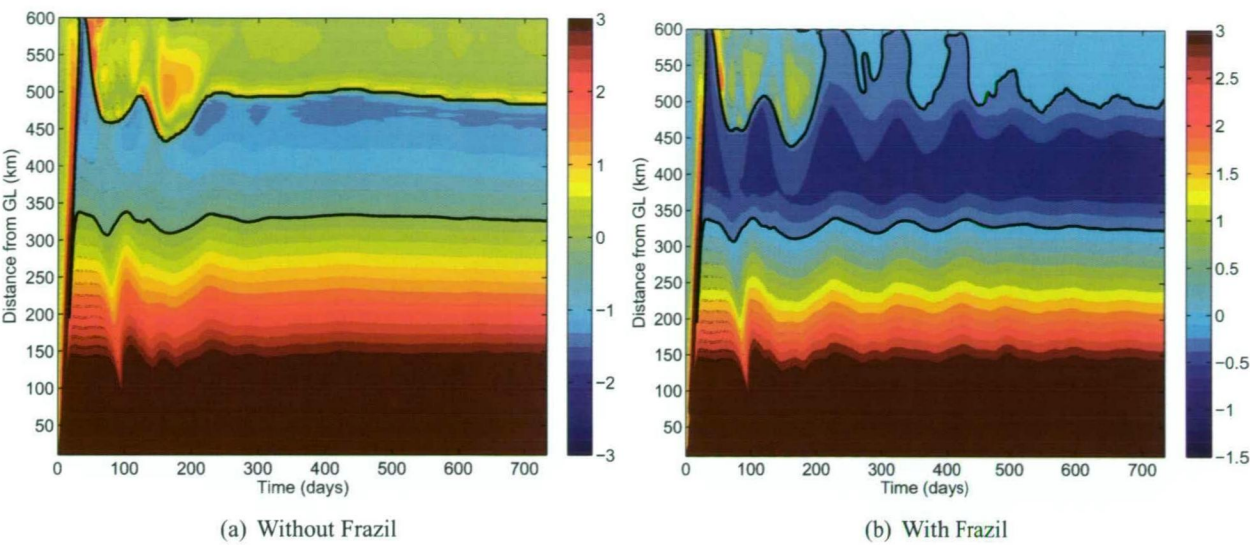


Figure 4.1: Comparing the spin-up of direct basal melt rate (m year^{-1}) along the ice shelf with (right) and without (left) frazil. The transition between melting and freezing (the zero melt rate contour) is indicated by the black line. Note that the colour scales are different.

For the model that contains frazil, the time that it takes for the melt/freeze at the ice shelf-ocean interface to reach approximate steady state is ~ 750 days (Fig. 4.1.b). The oscillations that can be seen in the zero melt rate contour are mostly due to spurious oscillations in the model due to spin-up which die out over time. However, the model that contains frazil maintains the spurious oscillations for longer. The introduction of the plume at the grounding line causes a divergence due to the buoyancy driven flow that can entrain ‘ambient’ seawater.

In response to supercooling, frazil ice is first seeded into the model after about 25 days at about 250 km from the grounding line. The level of supercooling then moves towards the front of the shelf over the next 25 days, whereby the plume then starts to separate from the base of the ice shelf after about 60 days, as shown in Fig. 4.2.c. After this time, the concentration of frazil ice in the upper layer becomes a poor indicator of the connection of the plume with the base of the ice shelf.

At steady state (at ~ 700 days), the supercooled plume of ISW is detached from the ice shelf base. The front 100 km of the ice shelf is not undergoing direct basal refreezing (Fig. 4.2.b). However, the presence of frazil in the uppermost grid cell (c) and the precipitation of frazil (a) in the region show that frazil is present in the model and is rising out of the supercooled plume and precipitating against the ice shelf base. This result highlights a key difference between including frazil dynamics in a three-dimensional ocean model compared to using a two-dimensional plume model.

The accretion process for frazil ice in the three-dimensional model is different to that for the plume models. Here, a plume of frazil laden seawater can detach from the base of the ice shelf

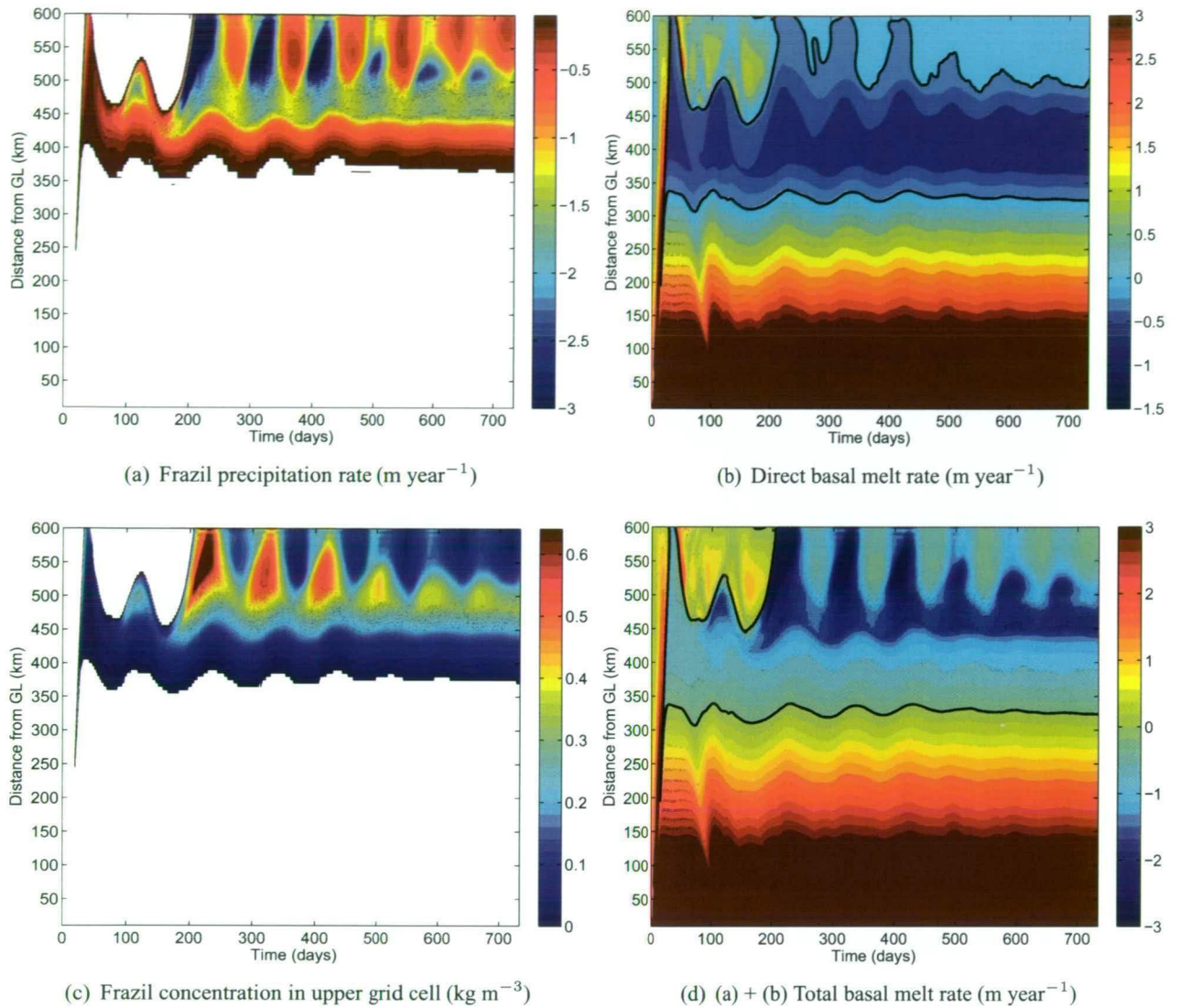


Figure 4.2: Spin-up of the model that contains frazil ice: (a) frazil precipitation; (b) direct basal melt/freezing; (d) the net basal melt rate; and (c) the amount of frazil present in the uppermost grid cell. Panel (b) is the same as Fig. 4.1b. The transition between melting and freezing is indicated by the black line. High accretion rates of frazil (a) corresponds to the times and locations where the frazil concentration is also highest (c). Frazil accretion is about 3 times more efficient than direct basal freezing.

and flow horizontally, at its neutral density. The ice crystals that are suspended in the plume can then rise further and settle against the base of the ice shelf.

The two-dimensional plume models cannot follow the evolution of frazil laden water after it detaches from the base of the ice shelf. Figs. 4.3 and 4.4 compare the results of the three-dimensional model here and the plume separation point used in the published results of earlier two-dimensional plume models. These figures show that the control model compares well with

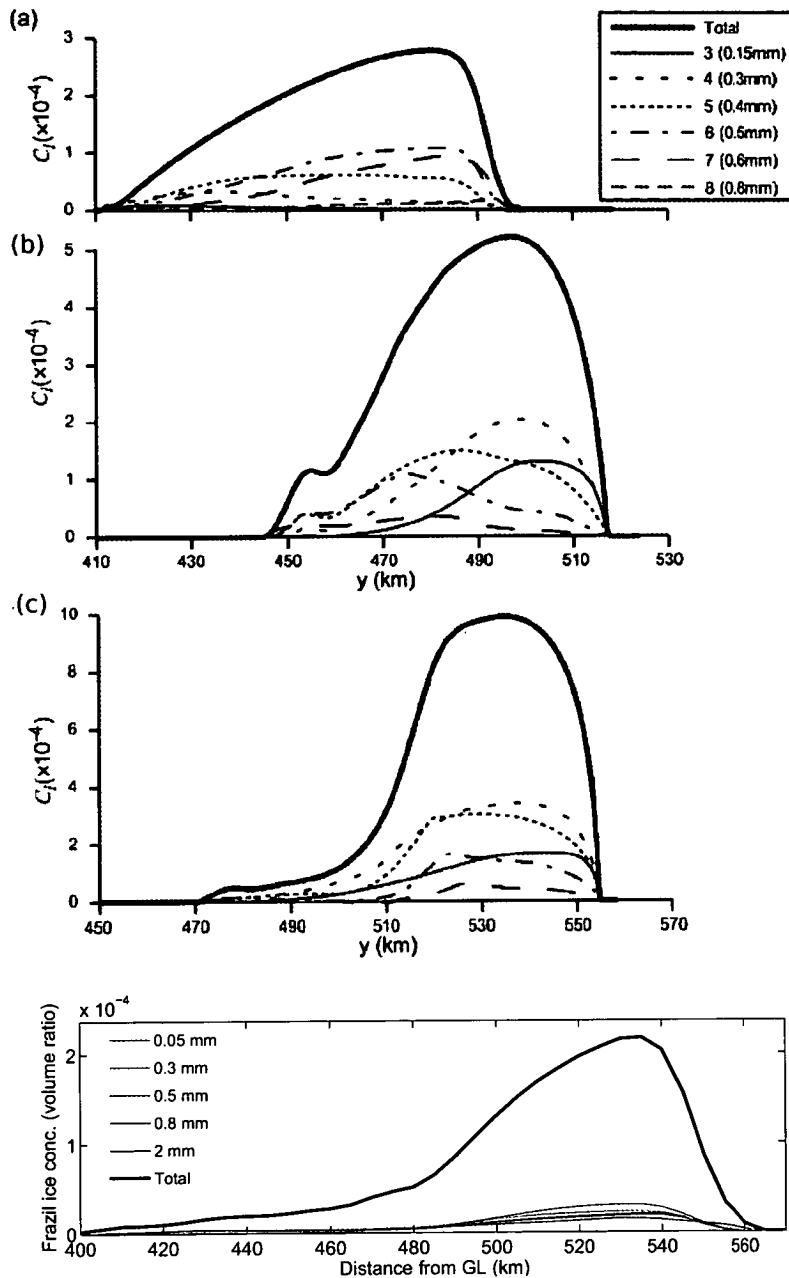


Figure 4.3: Frazil ice concentrations for a select number of size classes, resulting from various models in the overturning simulations. (a) *Smedsrud and Jenkins* [2004] after 76 days, (b) *Holland and Feltham* [2006] seeding strategy and model after 76 days (c) *Holland and Feltham* [2006] seeding strategy and model after 80 days, and (d) the control model when the plume first detaches from the base of the ice shelf. In each case the thick line also shows the extent of the plume.

the existing models. The total concentration of frazil increases with distance downstream because the crystals grow as they move through the region of supercooling. The distribution of the frazil precipitation is in general agreement with the results from the one-dimensional plume models.

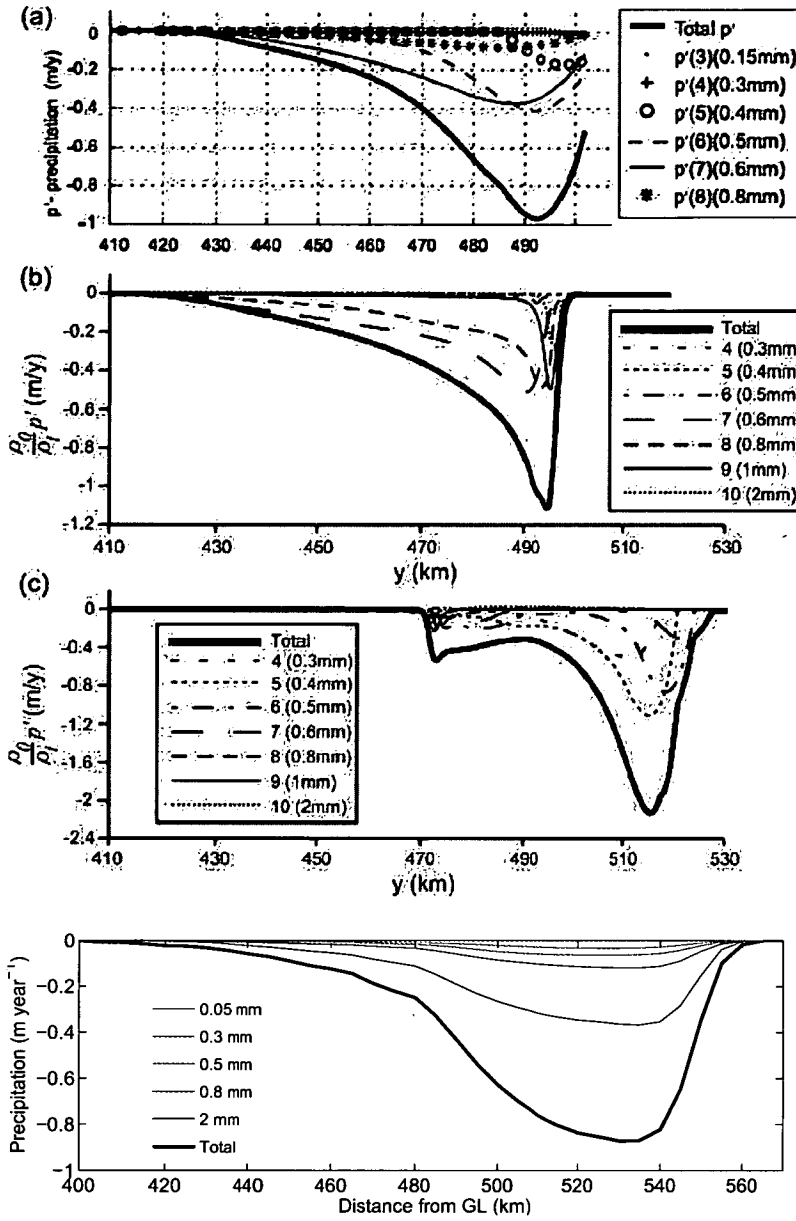


Figure 4.4: Frazil precipitation rates (m yr^{-1}) in the overturning simulations. (a) steady-state results from *Smedsrud and Jenkins* [2004], (b) transient results from *Holland and Feltham* [2006] after 76 days, (c) transient results from *Holland and Feltham* [2006] after 80 days, (d) the model used here, when the plume first detaches from the base of the ice shelf. Note the different scales.

The level of precipitation increases as the concentration of crystals increases. The amount and general distribution of the precipitation matches better to the steady state model of *Smedsrud and Jenkins* [2004] than to the transient model of *Holland and Feltham* [2006].

However, the evolution of the plume can be tracked after it has detached itself from the ice shelf base. This leads to an increase in the amount of precipitation that occurs at the ice shelf base as

frazil that moves away from the ice shelf base can still rise upwards through the water column and precipitate against the base of the ice shelf (Fig. 4.2). The separation of the plume at steady state can be seen in (b) where the direct basal re-freezing stops at about 500 km from the grounding line. Precipitation (c) is still maintained between 500 to 600 km from the grounding line (d). This result highlights a major difference between using a one- or two-dimensional plume model as compared to a three-dimensional ocean model.

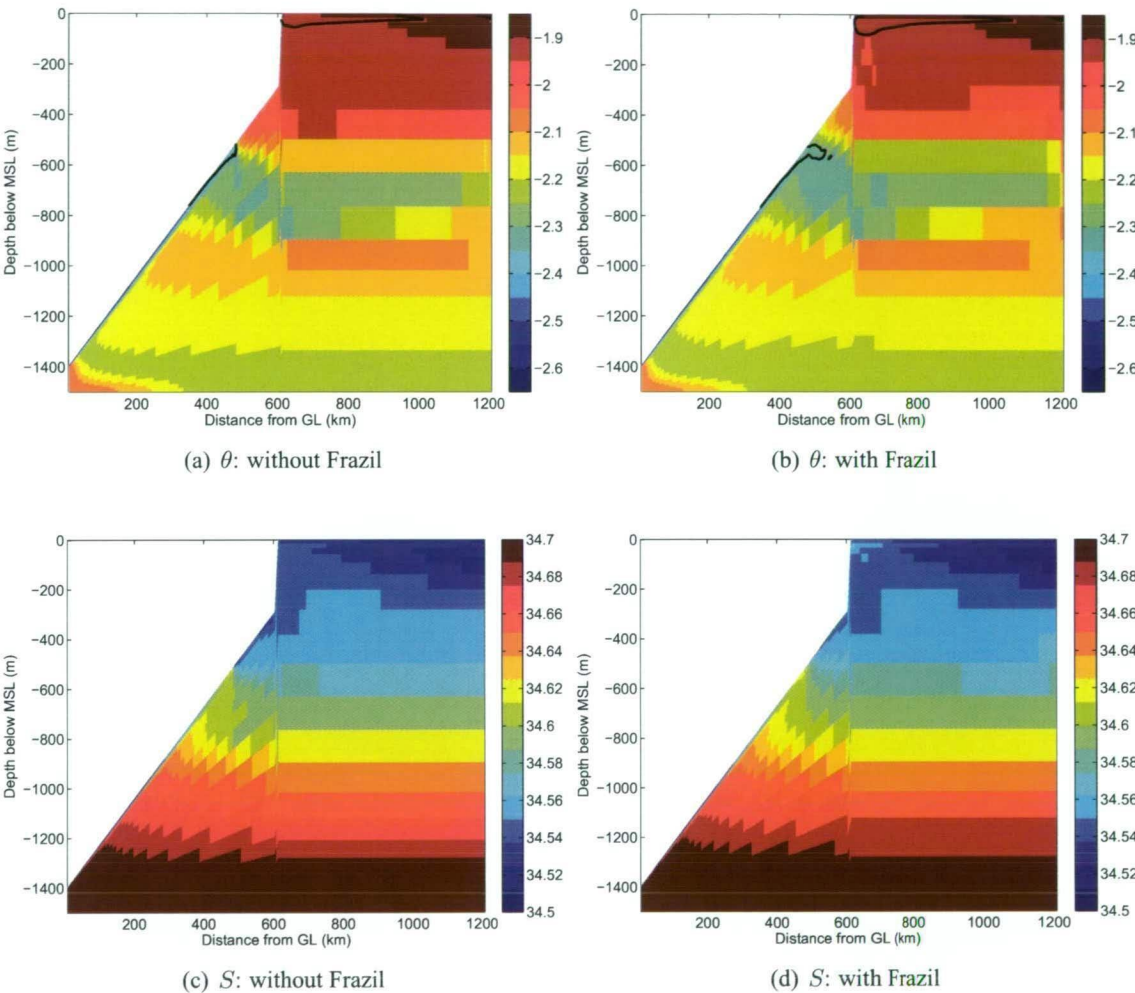


Figure 4.5: Comparing the potential temperature ($^{\circ}\text{C}$) and salinity between models with and without frazil. The tracers are averaged over the last 100 time-steps (~ 30 days). The black contour line in the temperature plots surrounds water that is supercooled.

An important side effect of the model used here is that frazil can also form in the surface layer of the open ocean. This can occur through two processes:

- By being transported out from underneath the ice shelf in a plume of supercooled water, where it can then settle to the surface. Frazil seeding initially takes place when newly formed cold water becomes supercooled as it rises suddenly over 285 m as it exits the ice

shelf cavity.

- By direct supercooling processes in the surface layer, such as latent heat processes that cause the ocean surface to cool below the surface freezing temperature. The formation of frazil at the ocean surface provides a downward salt flux and maintains the surface ocean at the surface freezing temperature.

The formation and then removal of frazil from the Ice Shelf Water (ISW) by upward precipitation means that saline water is left behind. The plume of supercooled ISW then has a higher density and flows horizontally, at its neutral density, and moves into a region of water that is warmer. The ISW can entrain surrounding ambient fluid and can become warmer. This process means that it loses supercooling and remains at its neutral density (Fig. 4.5).

4.1.3 Sensitivity to some frazil related parameters

Transects of the basal melt rate and frazil accretion are presented in 4.6. It becomes apparent that the supercooling that would normally be taken up via direct basal freezing goes to the production of frazil crystals (compare panels b and c). This is true across all variations that are tested here. The scaled version of γ_T removes less supercooling from the water due to frazil growth and so direct basal melting processes are more dominant when compared to models that use an unscaled γ_T . Overall, the formulation of the frazil rise velocity is a small effect when compared to the effect that reducing the plume speed or scaling γ_T has on accretion rates.

The production of supercooled water in the case where the plume speed is reduced is lower than that for the other cases. The effect here is that the growth of ice, and hence, the production of saltier water through brine rejection, is also slower. The buoyancy of the plume is therefore maintained and it then stays in contact with the base of the ice shelf for longer. Frazil laden water that remains in contact with the base of the ice shelf maintains a more consistent concentration of crystals which leads to higher precipitation rates overall. The effect is similar with the scaled γ_T simulation as this has the effect of slowing the frazil growth rate, again leading to less brine formation and higher accretion rates.

4.2 With Rotation: Variations on Grosfeld (1997)

The cavity used here has been outlined in Chapter 3. This cavity geometry has been used in previous simplified ice shelf-ocean modelling experiments and thus can be used as the basis for a comparisons between the numerics of the model used here and with other General Circulation Models (GCM). In this section we examine the various parametrisations of ice-ocean thermodynamics. The sub-ice shelf ocean cavity that is used here has been outlined in section 3.2.1. The extended *Grosfeld et al.* [1997] cavity that has been outlined in *Hunter* [2006] has been used in a number of recent papers to investigate various parameters [*Losch*, 2008; *Holland et al.*, 2008; *Little et al.*, 2008]

Experiments are used to test the formulations available for the ice-ocean thermodynamics. The experiments start with the simplest two-equation (2EQN) formulation of the ice-ocean boundary

conditions and finishes with the full three-equation (3EQN) formulation that includes the heat flux into the ice shelf (HF) and frazil ice (FRAZIL). The experiments are summarised as follows:

- Run “2EQN” uses a 2-eqn parametrisation of the basal ice-ocean fluxes (outlined in 3.2.1).
- Run “3EQN” uses a 3-eqn parametrisation of the basal ice-ocean fluxes.
- Run “3EQN+HF” is the 3EQN model but with an additional linear heat flux into the ice shelf only during melting.
- Run “3EQN+HF+FRAZIL” is the 3EQN+HF model that includes the control run frazil ice model used above.

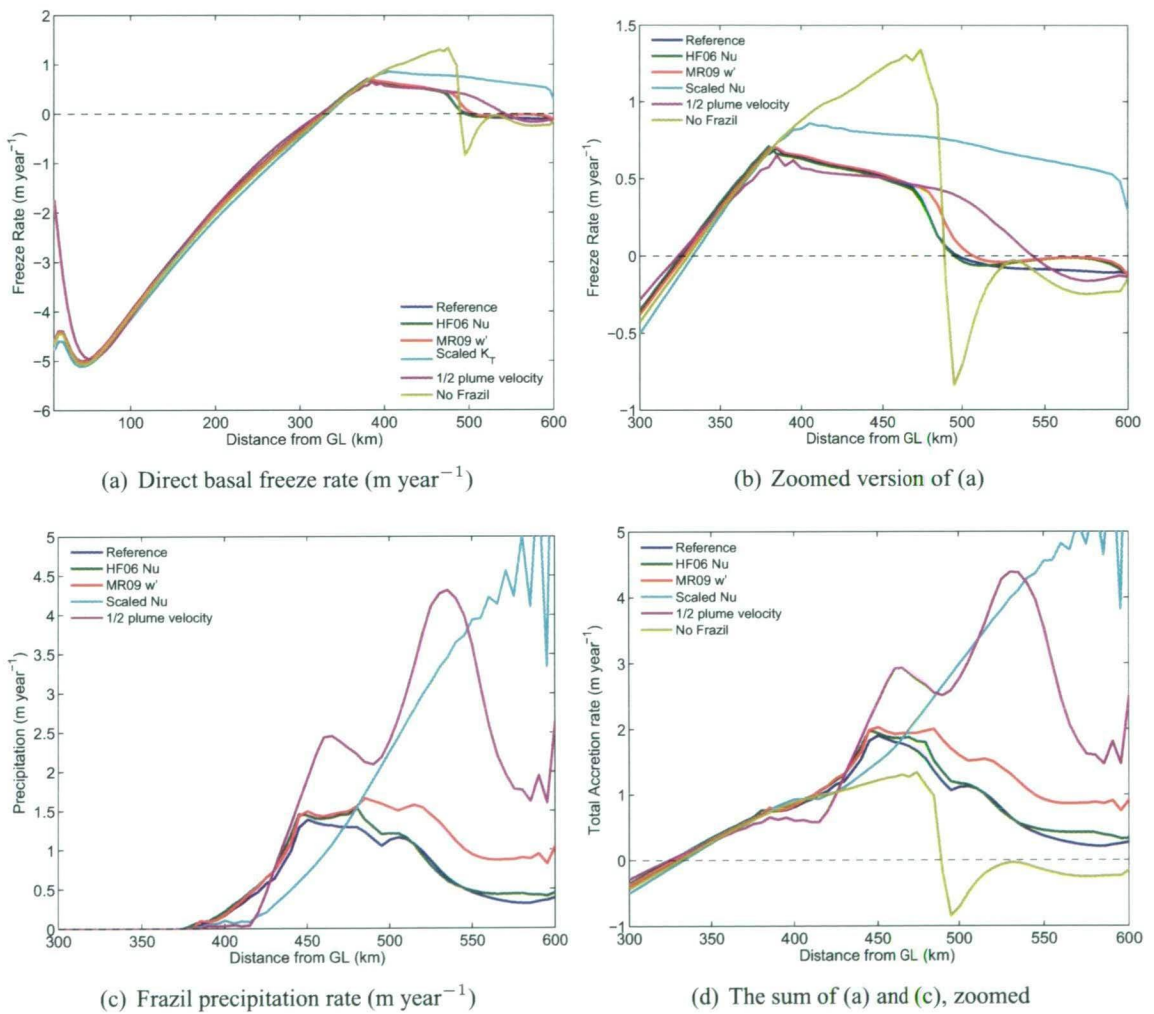


Figure 4.6: Results from an ensemble showing (a and b) direct basal freezing, (c) frazil precipitation rates summed over all size classes and (d) total accretion rate (i.e. (a) + (c)) for several different frazil models. The reference model is matched to that from Holland and Feltham (2006) where, $Nu = 1$ and $w' = \text{White}(1974)$. In all cases a point source has been added at the grounding line with (volume flux = $0.05\text{m}^3\text{s}^{-1}$, $T = -2.18$, $S = 34.4$)

4.2.1 Results and discussion

The essential feature of this cavity is that it includes rotation and that the forcing of the model comes from the prescribed thermodynamic surface boundary conditions. The most obvious effect of rotation on sub-ice shelf ocean circulation is that a strong area of marine ice accretion occurs at the western boundary of the cavities, consistent with an ice-pump mechanism that is deflected to the left (in the Southern Hemisphere) due to the Coriolis force (Fig. 4.7). The outflowing component of the ice-pump mechanism is shown as a narrow boundary current. The area of strongest melting occurs in the southeastern corner in all four models.

Table 4.1 summarises the area-averaged melt/freeze rates for each of the experiments. As expected, the net melt rate in models that use the three-equation (3EQN) basal ice-ocean thermodynamics is 8% lower than models that use only the two-equation (2EQN) formulation. This is because the basal melt rates in 2EQN are proportional only to the difference in temperature from the freezing point in the cell adjacent to the ice base. The model that uses a the 3EQN formulation with linear heat flux into the ice shelf is 15% lower than the model without the basal heat flux. The flux of heat into the ice shelf during melting means that less energy is therefore available to melt the ice. The results show that the additional heat flux term only affects the melt rates as during freezing it is assumed that the temperature gradient within the ice shelf is zero.

Table 4.1: Results for the four experiments for the area-averaged net melt/freeze rate $\langle m' \rangle$ (m year^{-1}), due only to Melt $m' > 0$ and due only to freeze $m' < 0$. Note that the freeze for experiment 3EQN+HF+FRAZIL is the sum of direct basal freeze and due to frazil ice accretion.

Model	$\langle m' \rangle$	Melt	Freeze
2EQN	0.131	0.160	-0.264
3EQN	0.120	0.140	-0.123
3EQN+HF	0.101	0.12	-0.124
3EQN+HF+FRAZIL	0.136	0.157	-0.756 [†]

[†] Sum of direct basal freezing (-0.012) and frazil accretion (-0.744)

The model that includes frazil ice processes (3EQN+HF+FRAZIL) shows the highest net melt rate, strong melting (similar to 2EQN) and the most refreezing. The freezing rates are dominated by the accretion of frazil. The enhanced melt rates can be explained as being because of the extra addition of heat from the ocean due to the growth, and subsequent deposition, of frazil. The Ice Shelf Water (ISW), that is formed in the ouflowing plume in all models, does not have time to come fully to equilibrium with the prescribed air-sea tracer fluxes before being subducted beneath the ice shelf again. However, the ISW created in 3EQN+HF+FRAZIL is warmer than the ISW created in 3EQN+HF due to the effectiveness of frazil in removing residual supercooling. The amount of residual supercooling is 0.002 °C for 3EQN+HF+FRAZIL compared to 0.039 °C for 3EQN+HF.

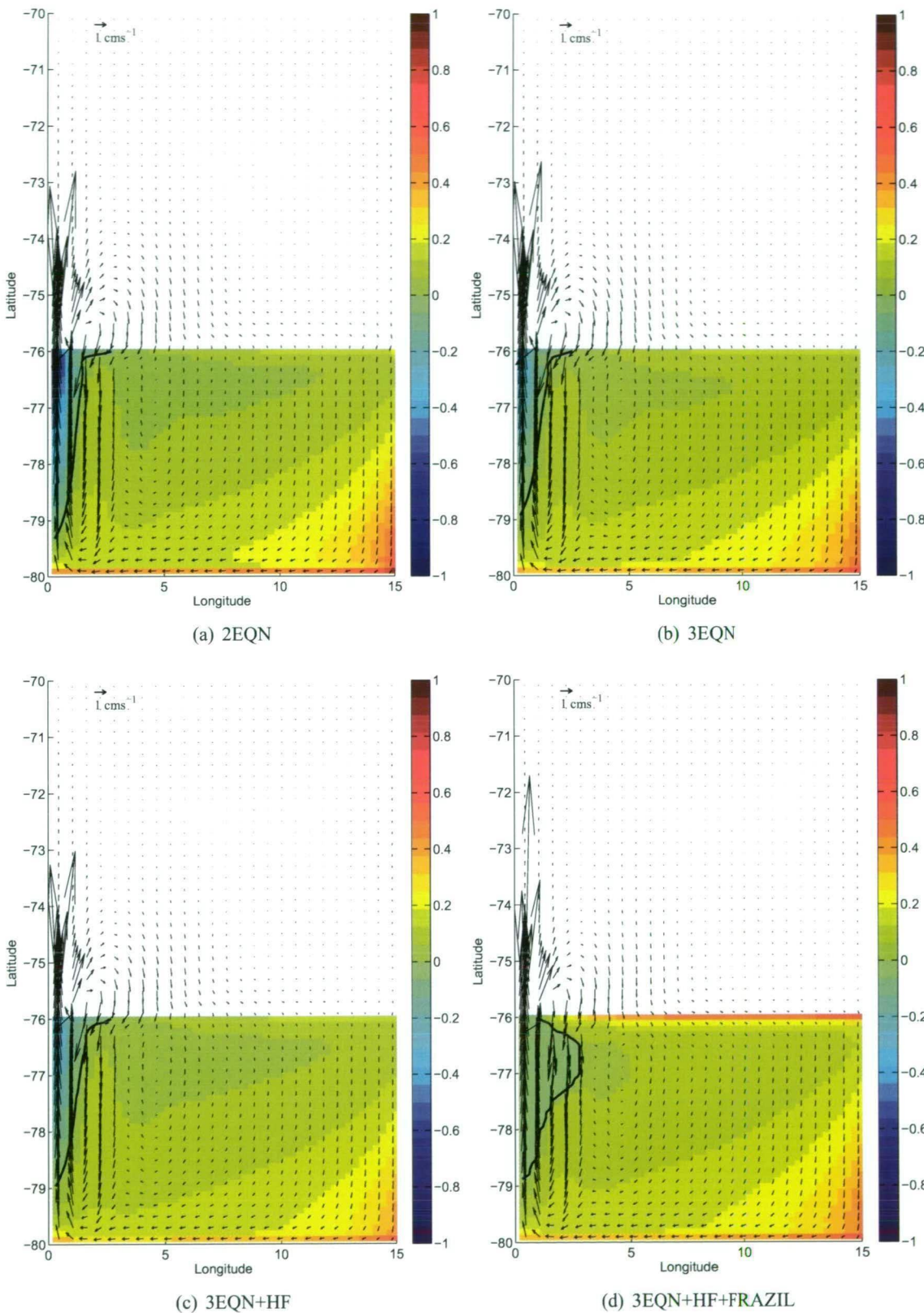


Figure 4.7: Direct basal melt/freezing rates (m/year) for the four models that include rotation. Depth average velocities are shown by the black arrows for every second grid cell.

Ultimately, waters that enter the ocean cavity beneath the ice shelf are *warmer* in 3EQN+HF+FRAZIL than in 3EQN+HF. Fig. 4.7.d shows enhanced melting across the front of the ice shelf compared to Fig. 4.7.c. Frazil is an efficient mechanism for removing supercooling from seawater that is created by the melting and buoyant rising of ISW. Note that the presence of supercooling in 3EQN+HF+FRAZIL shows that the frazil ice interactions are dynamic and not limited by the models time-step. If the frazil model was constrained by the time-step, then the frazil growth would also be limited to removing all of the residual supercooling, which is not the case.

The *net* freezing rate in the model with frazil is higher than models without frazil (Table 4.1). This is due to the enhanced ability of frazil to remove supercooling from seawater. The frazil can then precipitate upwards through the water column and accrete to the base of the ice shelf. Results show that the presence of frazil in the model increases the rate of basal accretion by sixfold. However, as discussed above, this also corresponds to an increased melt rate. So, compared to the 2EQN model, which has approximately equivalent melt rates, the total marine ice accretion is about 2.86 higher in 3EQN+HF+FRAZIL.

4.2.2 Conditional instability of frazil laden water

The three-dimensional studies show that frazil laden water can be conditionally unstable. This effect was explored earlier by *Foldvik and Kvinge* [1974] who discuss a thermohaline convection mechanism based on the relationship between the freezing point of seawater and pressure. Frazil crystals that do not accrete to the base of the ice shelf stay suspended within the ISW plume. The frazil laden parcel of water, at the local freezing point, that is displaced upward, leads to the further formation of frazil. The increase in ice mass causes the water/frazil parcel to become less dense than the density of surrounding water, and the parcel ascends further by itself. This mechanism is possible provided that supercooling occurs and the vertical rise velocity of the frazil crystals are small relative to the velocity of the ascending water parcel. The bulk of the ice crystals will stay within the original volume until reaching the surface or an internal stable (neutrally buoyant) level. Results from the simulations show that as the supercooling is quenched and no further frazil growth occurs, the ice/water mass can become neutrally stable. The ice/water mass then intrudes into a neutral level, whereby the suspended ice crystals can then precipitate upward, leaving the water with cold, saline properties behind. The remaining water mass is then heavier than the surrounding water and can sink.

However, frazil laden water can be forced deeper when vertical currents become stronger than the frazil rise velocity. Examples of processes that create strong downwelling are Ekman pumping and dense water created at the surface during sea ice formation. The downward transported frazil laden water at the surface freezing point then becomes warmer than the *in situ* freezing point, due to the pressure dependence, whereby the frazil melts. This causes both a cooling and freshening of the surrounding water making it lighter (due to the freshening) than the surrounding water causing it to rise, increasing the bulk density. The instability reaches a limit deeper in the water column by running out of frazil that can melt, and in the shallower part of the water column by reaching the

surface, causing a layer of very high concentration of frazil ice at the surface.

4.3 Concluding Remarks

- The studies shown here extend the conclusions of *Holland and Feltham* [2006] to three-dimensional representation of realistic frazil/ocean conditions. Dynamic frazil processes strongly affect local circulation and ice sheet mass balance. Models that contain frazil dynamics show lower residual supercooling and enhanced accretion rates, by up to 6 times more than in models without frazil.
- The results shown here also have implications for deep water formation processes. The presence of ice in the model causes the bulk density to be lower than the surrounding water. The mixture then rises until it reaches the surface or a neutrally buoyant layer. The frazil ice crystals then continue rising through the water column, or precipitate out at the surface leaving the denser saltier water behind. The heavy residual water will sink through the water and mixes with the surrounding water. Ultimately, this heavy salty and cold water formed by this process may reach the bottom and in turn contribute to the formation of deep water, such as Antarctic Bottom Water. Attempts to quantify the formation rates of bottom water in ice shelf-ocean models, without accounting for frazil ice processes, could underestimate formation rates.
- Models with ten frazil size classes take about three times more computing time than do models without frazil, due to the extra computations required for computing both the state of the additional frazil tracers and for the dynamic frazil model. The difference in computing time between the various basal ice shelf-ocean formulations are negligible.

CHAPTER FIVE

THE AMERY ICE SHELF OCEAN MODEL: SETUP

This chapter describes the set-up for a realistic simulation of the ocean cavity beneath the Amery Ice Shelf (AIS), including model geometry and forcing and boundary conditions. Attention is given to the development of the most up-to-date Amery Ice Shelf cavity geometry [Galton-Fenzi *et al.*, 2008b]. A description of the basic model configuration is given along with a discussion of aspects of the spin-up procedure used in later chapters.

5.1 Geometry and Location

5.1.1 Introduction

The Amery Ice Shelf (AIS) is the major embayed ice shelf of East Antarctica (Fig. 5.1) and drains about 16% of the grounded East Antarctic Ice Sheet through the Lambert and other tributary glaciers [Allison, 1979]. The geometry of the cavity beneath the AIS is thought to have a strong influence on the thermohaline circulation [Williams *et al.*, 1998a] and is important for studies of future climate and sediment studies [for example, Hemer and Harris, 2003], biological studies [for example, Riddle *et al.*, 2007] and paleo-climate studies of historic grounding line positions [for example, O'Brien *et al.*, 2007]

The AIS cavity geometry and grounding line has been redefined a number of times since early modelling studies by Williams *et al.* [1998a, b]. Fricker *et al.* [2002b] estimated that the southern limit of the grounding line was a further 240 km south than prior estimates [Budd *et al.*, 1982] and most recently Giovanna *et al.*¹ used observations from Moderate Resolution Imaging Spectroradiometer (MODIS) and Synthetic Aperture Radar (SAR) to infer grounding line positions from the break in the surface slope topography in agreement with independent estimates [Fricker *et al.*, 2009] (shown as the solid black line in Fig. 5.1).

Available bathymetry data beneath the AIS are restricted to regions that are easily accessed in the field and do not extend south of 71.6° S on the AIS, which is shown here to have a southern limit at ~73.3° S (see Fig. 1a for data locations). As a consequence, the shape of the AIS cavity south of 71.6° S is largely unknown. These reasons necessitate the use of an alternative method to achieve a bathymetry that is as accurate as possible for use in an ocean model.

In this section, a method that was first used by Hemer *et al.* [2006] – hereinafter referred to as H06 – is refined to determine the general cavity shape beneath the AIS. H06 showed that the water column thickness (WCT), which is the difference in depth between the ice shelf draft and bathymetry, in the unknown areas beneath an ice shelf can be inferred with the aid of a tidal model. The original sparse bathymetry data used in HE06 is supplemented with new seismic

¹ Giovanna, L., I. Allison and N. Young. Determining the Coastline of the Antarctic using Remote Sensing Techniques, *Polar Geography*, in review

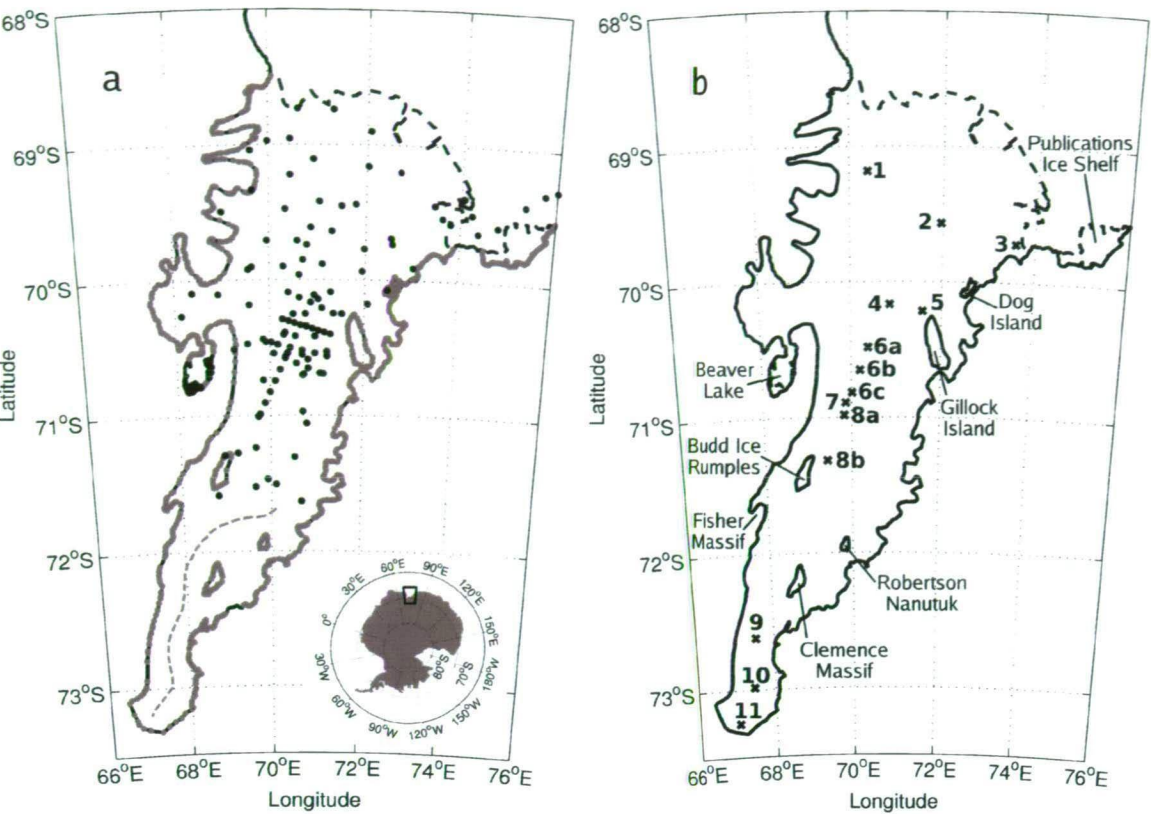


Figure 5.1: The location of the Amery Ice Shelf and Prydz Bay in East Antarctica (black box in inset). (a) The bathymetry data used in the interpolation: The black dots show the location of the seismic data, the grey line shows the ice-draft data taken at the grounding line and the dashed grey line in the southern region of the AIS is the prescribed channel centerline. (b) The locations of the 11 available GPS observation sites and major features of the Amery Ice Shelf region.

surveys, direct observations through boreholes in the floating ice shelf and ice-draft radar data, taken at the grounding line. The updated grounding line position of Giovanni and others (personal communications) is also used to provide the most up-to-date map of the AIS cavity geometry. An improved high resolution hydrodynamic tidal model [MOG2D, Maraldi et al., 2007] is used to produce tidal predictions for 10 different estimates of the WCT, with the values for WCT chosen to be within what we believe to be are plausible ranges. These tidal predictions are then compared with GPS observations of the tidal amplitude and phase measured at various locations on the AIS (see Fig. 5.1.b for GPS locations). The most appropriate WCT corresponds to the smallest difference of the complex sum of squares between the observed and predicted harmonics for the 4 main tidal constituents (K_1 , O_1 , S_2 , M_2), which represent about 80% of the total tidal variance in this region.

5.1.2 AIS geometry data

Bathymetry

Measurements of the cavity shape beneath ice shelves generally rely on data from seismic surveys and direct observations via boreholes through the ice. The largest single seismic study of the bathymetry covered $\sim 60\%$ of the northern region beneath the AIS (Ruddell and Popov, unpublished)². This survey provided 72 usable data points. Seismic surveys conducted from 2002/03 until 2005/06 [Tassell, 2004; McMahon and Lackie, 2006], over 5 Antarctic summer seasons, were confined to areas that were more easily accessed and operationally safer. These seismic profiles covered the central part of the AIS and added another 35 data points. The error associated with converting the seismic reflections into a depth below mean sea level is ~ 3 m, due to uncertainty with estimating the seismic velocity within the ice shelf [Tassell, 2004]. The surface height above mean sea level was estimated by subtracting the geoid height, using FZ/CNES's EIGEN-Grace02S geopotential model [Reigber *et al.*, 2005] from the GPS ellipsoidal height of the surface at the seismic site. Uncertainties in the geoid model introduces an error of about ± 1 m³.

Direct observations of the bathymetry and ice thickness came from 4 boreholes that were drilled through the AIS as part of the ongoing AMISOR project [Allison, 2003]. In addition, Bardin and Shmideberg [1990] obtained direct measurements of the Beaver Lake near-shore bathymetry, via holes drilled through the fast ice, from which we use 12 data points. Note that the agreement in the WCT data between different seismic surveys and direct observations made in the same area is within about 5 m.

Ice-draft

Surface elevations and ice thicknesses have been measured over much of the area using satellite radar altimeter and radio-echo sounding. The elevation and thickness estimates of [Fricker *et al.*, 2000, 2002b] using the ERS radar altimeter are used here. The ice-drafts were found by subtracting the elevation from the ice thickness data. The ice-draft data were then re-sampled onto a 2-km grid using nearest neighbour interpolation, which also removed gaps in the data-set. This resulted in a continuous ice-draft map for the entire area of the AIS, which is shown in Fig. 5.2.

The uncertainty in the observations was estimated by comparing the gridded ice draft with independent radio echo sounding measurements of ice thickness collected as part of the Prince Charles Mountains Expedition of Germany and Australia (PCMEGA) campaign during the 2002/03 Antarctic Summer. The PCMEGA derived ice draft values are calculated by subtracting the ice elevation data [Fricker *et al.*, 2000] from the PCMEGA ice thickness data. The resulting PCMEGA data derived ice draft, only available for the southernmost region of the AIS, is about 3% thicker than the gridded ice-draft data. This is about 75 m at the deepest part of the ice shelf which

² Ruddell, A and S. Popov. 2001. Maps of Seismic Surveys on the AIS. Antarctic CRC.

³ Personal communications with Rachael Hurd, Antarctic Climate and Ecosystems CRC, Hobart, Tasmania.

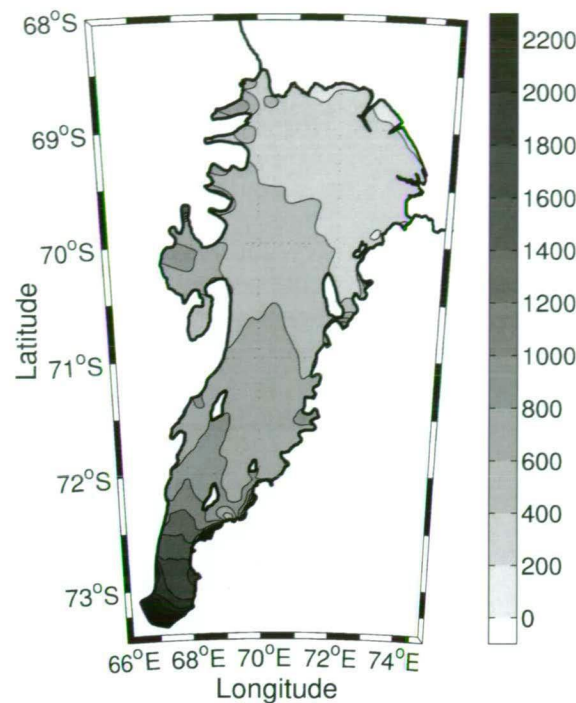


Figure 5.2: Ice-draft of the Amery Ice Shelf showing 200 m contour intervals.

is about 2500 m below mean sea level at its southern extremity. This error in the earlier gridded ice-draft data is probably due to underestimating the ice density in regions of higher ablation, which is typically where the ice shelf is thickest, as in the southern region of the AIS⁴. We have found that the southernmost grounding line depth is deeper than BEDMAP estimates by about 450 m [Lythe *et al.*, 2000] and is one of the deepest grounding lines of any ice shelf. The ice-draft at the deepest part of the cavity is 1600m deeper than that used in studies by Williams *et al.* [2002, 2001], which has major implications for the amount of melting that can occur.

Gridding method

Ice-draft data at the grounding line were extremely useful in the interpolation of the bathymetry. The grounding line is the place where the base of the ice shelf coincides with the sea floor. These data are important to include in the interpolation because they help to constrain the shape of the AIS cavity. The ice draft data were interpolated using nearest neighbour interpolation to each known grounding line location, which is made up of 1317 points. The grounding line locations are shown as the grey line in Fig. 5.1.a. Note that this is made up of individual inferences of the grounding line position. The combined data set, involving both bathymetry and grounding-line locations, contained 1436 data points compared with only 72 in H06.

The 2x2 km grid covered the Prydz Bay depression from 66° E to 79° E and from the southernmost extension of the AIS at 73.6° S to the shelf break at about 66° S. This created 120291 (397x303) interpolation sites. All available sub-ice shelf bed elevation data and Prydz Bay

⁴ Personal communications with Helen Fricker, Scripps Institute of Oceanography, La Jolla, California.

bathymetry data ⁵ were interpolated onto the model grid using a Universal Transverse Mercator projection (using the WGS84 ellipsoid). The bathymetry data were gridded using a kriging technique with an isotropic variogram which varied linearly within a correlation radius and zero outside. The correlation radius was set at a few grid cells (6 km), based on the average data density in the northern region of the AIS. The standard error that is introduced by the kriging technique can be calculated by comparing the elevation from the interpolated grid with the observations at each location. This yields a standard error in the bathymetry interpolation, excluding the ice-draft data taken at the grounding line, of about ± 6 m. The standard error in the bathymetry interpolation at the grounding line is about ± 2 m. The lower standard error at the grounding line is due to the higher data density in this region.

A range of ten possible choices of bathymetry was created by incorporating synthetic data into the interpolation from along the prescribed channel centerline, which is shown by the dashed grey line in Fig. 1a. Each of the 10 choices of bathymetry used a single prescribed value of WCT that was added to the value of the overlying ice-draft along the channel centerline. The values that were added to the ice-draft along the channel centerline were 170, 470, 770, 1070, 1370, 1670, 1970, 2270, 2570 and 2870 m. This effect can be seen in Fig. 5.3, which shows the range of South-North (a) and East-West (b) profiles that were created, following the two transects shown in the inset of Fig. 5.3.a. The WCT was constrained to a minimum of 10 m.

5.1.3 Tide model

Each choice of WCT was tested in MOG2D, which is a finite-element barotropic time-stepping and non-linear two-dimensional (vertically averaged) gravity wave model, based on Lynch and Gray (1979). In regions where there is an ice shelf cavity, the WCT (rather than the depth of the sea floor) is the appropriate ‘water depth’ to use in the model. MOG2D computes the sea-surface height and mean currents due to wind and tidal forcing by solving the shallow-water momentum and continuity equations on a finite-element mesh. This spatial discretisation allows the resolution to be coarser in the deep ocean and finer in coastal regions and those with strong topographic gradients, enabling good simulation of gravity waves. The spatial resolution is determined by the WCT, its gradient and the wavelength of the gravity waves [Le Provost and Vincent, 1986].

The model domain covers the southern area of the Indian Ocean with a grid ranging in size from a few kilometers on the continental shelf, including the AIS region, to 100 km in the deep ocean. Details of the finite element mesh can be found in Maraldi *et al.* [2007]. By calculating tides for a range of plausible WCTs in unsampled areas in the southern AIS, we can produce a map of WCT values that provide the optimum agreement between modelled and measured (GPS) tides.

The coefficient used for tidal bottom friction parametrization was taken to be 0.0025 and, following other studies, was doubled for the area that is covered by the ice shelf [for example, MacAyeal, 1984]. Dissipation due to ice shelf flexure caused by the tidal motion is not accounted

⁵ A combination of ship track measurements supplied by the Australian Antarctic Division Data Centre and the GEBCO 1-minute bathymetric data [IOC and BODCM, 2003]

for at the grounding line; the ice shelf is considered to be freely floating. The ice flexure zone is narrow, $\mathcal{O}(1\text{-}3\text{ km})$ and is related to the ratio of the ice thickness to the distance from the grounded ice. The open boundaries are forced using the harmonic constants (amplitude and phase) obtained from the FES2004 [Lyard *et al.*, 2006] global barotropic solution. Three semi-diurnal (M_2 , S_2 , N_2) and three diurnal (K_1 , O_1 , P_1) tidal constituents were modelled. The model was run for 40 days including a 3 day spin-up period. The harmonic analysis was performed on the last 30 days so that each of the constituents was well resolved.

5.1.4 Data analysis

GPS data from 11 records was used to validate the tide model (see Table 1). Tidal amplitude and phase for the 4 main constituents was found for each GPS record. GPS data from sites 1,2,3,5 and 11 (Fig. 5.1.b) have records long enough (i.e., greater than 15 days) so that tidal analysis may resolve M_2 from S_2 and K_1 from O_1 . Records shorter than this were analysed for M_2 and K_1 , where S_2 and O_1 were deduced by using amplitude and phase relationships from the longer tidal records from nearby Davis station. The errors in analysing specific constituents from short record lengths (i.e., less than $\sim 3\text{-}4$ days) can be large. We combined sites that had short records and were within 20 km of each other to make longer time series so that this error is reduced: record 6 is a concatenation of sites 6a, 6b and 6c and record 8 is a concatenation of sites 8a and 8b (see Fig 5.1.b and Table 5.1). Typical GPS measurement precisions are 1-5 cm for the AIS, representing

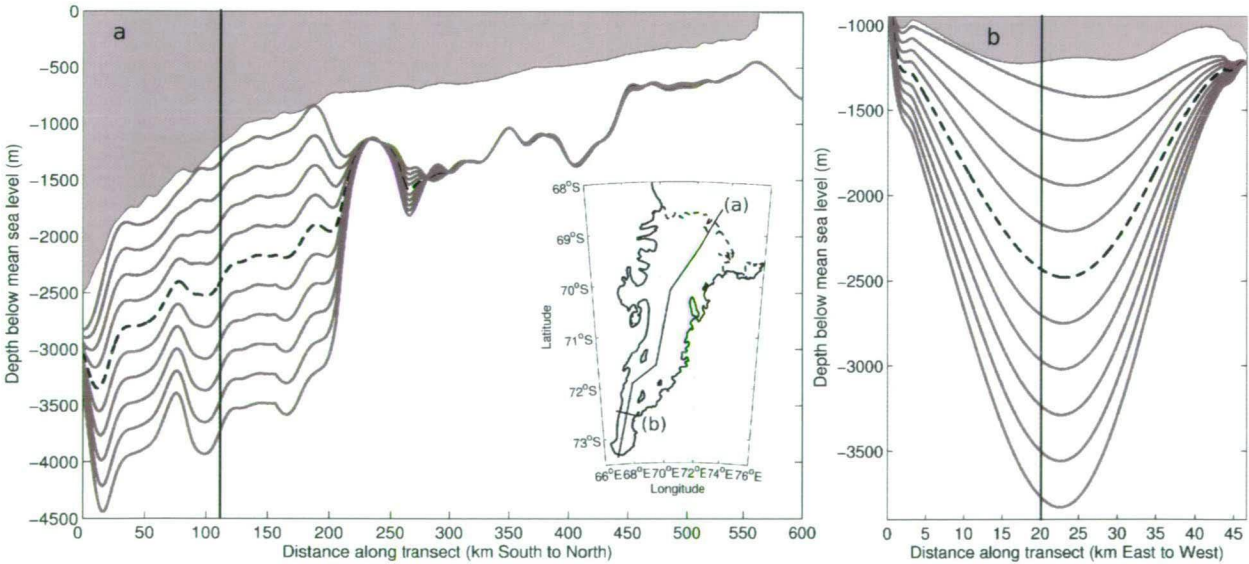


Figure 5.3: Vertical sections along transects (a) south-north and (b) east-west as shown in the inset. Ten possible choices of bathymetry are shown. The best estimate is the black dashed line. Each bathymetric choice was created by varying the thickness of the water column below the ice shelf along the dashed grey line shown in Fig. 1. The intersection point of the two transects is shown on each figure by a vertical black line.

about ~1-5% of the tidal range [King, 2006; Zhang and Andersen, 2006; King et al., 2007].

Table 5.1: The modulus of the complex error (ϵ cm) for the optimum WCT from this study (TS) and [Hemer et al., 2006] (H06) for GPS sites 1 to 11. The last row is the root mean square value calculated over sites 1 to 10. Site 11 is excluded in the RMS calculation as it lies in the ice shelf flexure zone.

Record	Length (days)	ID	M ₂		S ₂		K ₁		O ₁	
			TS	H06	TS	H06	TS	H06	TS	H06
1	48	TS03	0.6	2.1	0.7	2.2	0.9	4.1	0.5	8.2
2	68	TS01	1.3	2.4	0.9	0.5	1.9	6.1	0.4	5.5
3	26	HWDT	0.4	1.6	1.1	0.7	1.1	0.8	0.3	2.9
4	1.8	G2	0.1	5.5	1.6	2.2	1.3	6.1	2.3	5.3
5	65	TS04	1.4	2.1	0.8	2.1	0.8	6.8	0.8	8.0
6	3.3 ¹	C12,10,8	0.6	-	0.4	-	1.1	-	1.3	-
7	11	CAMP	0.9	1.5	1.1	4.5	0.6	3.5	1.1	2.1
8	2.3 ¹	C6,2	1.7	-	2.3	-	1.7	-	1.6	-
9	3.5	V3	2.6	12.1	3.0	10.2	3.2	3.7	2.4	3.8
10	3.8	V5	2.9	9.1	3.2	8.3	3.8	4.5	2.9	4.0
11	83	TS05	17.2	-	18.3	-	16.9	-	16.5	-
RMS(cm)			1.6	5.9	1.9	5.1	2.1	4.8	1.7	5.4

¹ Record 6 is combined from sites 6a (1.13), 6b (1.2) and 6c (0.96) and record 8 is combined from sites 8a (1.0) and 8b (1.3). See Fig. 1b for locations.

For each choice of WCT, the tidal solutions from MOG2D as a time series were compared to the GPS ellipsoidal height data that were measured over the AIS (see the crosses on Fig. 5.1.b for the locations). The sensitivity of the model to changes in the WCT are compared using the modulus of the complex difference between observations and model predictions (the 'complex error'), which is calculated as,

$$\epsilon = |z_{\text{observations}} - z_{\text{predictions}}| \tag{5.1}$$

where $z = Ae^{i\phi}$, A and ϕ being the amplitude (cm) and phase ($^{\circ}$), respectively, of each tidal constituent M_2 , S_2 , K_1 and O_1 . The root mean square (RMS) error was calculated using,

$$RMS^2 = \frac{1}{N} \sum_{i=1}^N \epsilon_i^2 \tag{5.2}$$

where, N is the total number of tidal constituents. The sensitivity of the model to changes in the WCT are shown in Fig.5.4.

5.1.5 Choosing the best cavity: results and discussion

A significant minimum can be seen in the RMS error for the simulations (Fig. 5.4). Summing over GPS records 1 to 10 shows that the smallest RMS between the observations and simulations

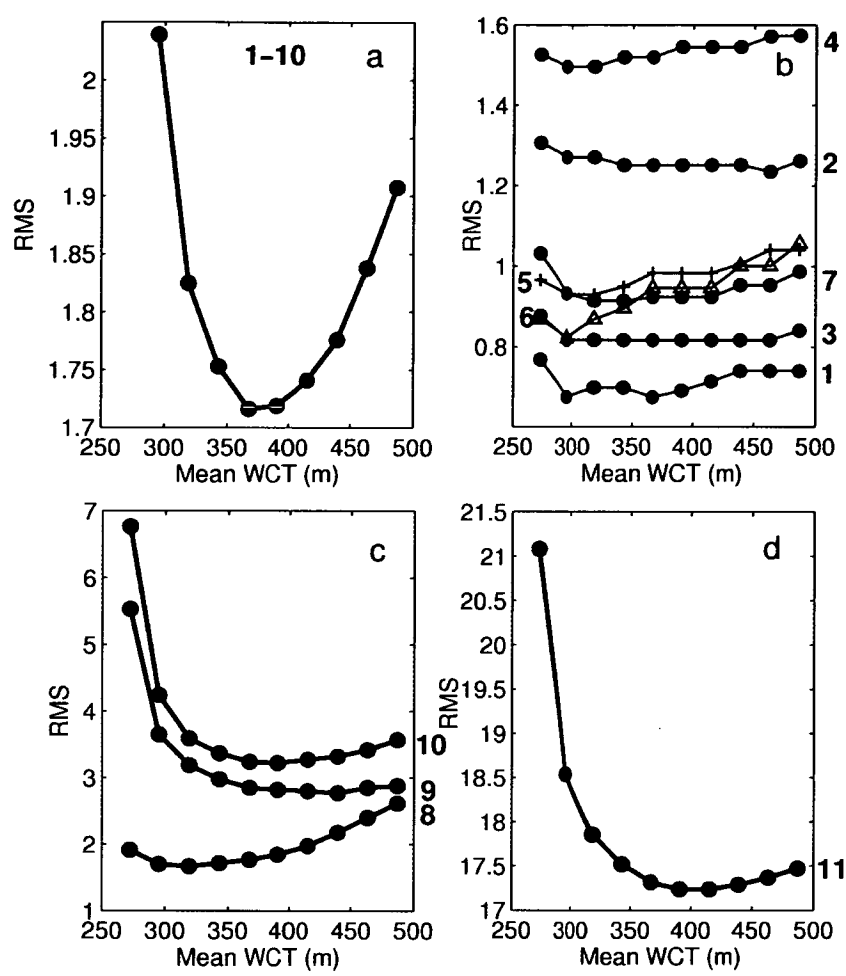


Figure 5.4: The sum of the RMS complex errors (cm) for the 4 major tides are compared against the mean WCT calculated over the AIS, for (a) the sum of records 1 to 10, (b) records 1 to 7, (c) records 8 to 10 and (d) record 11. Note that record 11 lies within the ice shelf flexure zone which acts to damp the tidal amplitude, thereby increasing the complex error and so was not included in (a).

is for a mean WCT of 367 m (a), which is about 35 m deeper than that estimated by H06. In this case, the WCT along the prescribed channel centreline was 1370 m, which is ~ 750 m deeper than H06. Record 11 (d) was excluded from (a) as it lies in the ice shelf flexure zone, which can act to damp the tidal amplitude. Ice shelf flexure is a physical process that is not modelled in MOG2D, which is reflected in the larger RMS for (d). The records in the adjusted southern region (records 8 to 11 in c and d) show an increase in the RMS toward the southern grounding line of the AIS. Records 8-10 (c) are clearly important contributors for the minimum RMS seen in Fig. 5.4.a. Otherwise, the records to the north of the cavity (b) are essentially constant and do not contribute significantly to the shape of (a).

Comparison of the RMS errors for the optimum WCT of 367 m with the RMS errors from H06

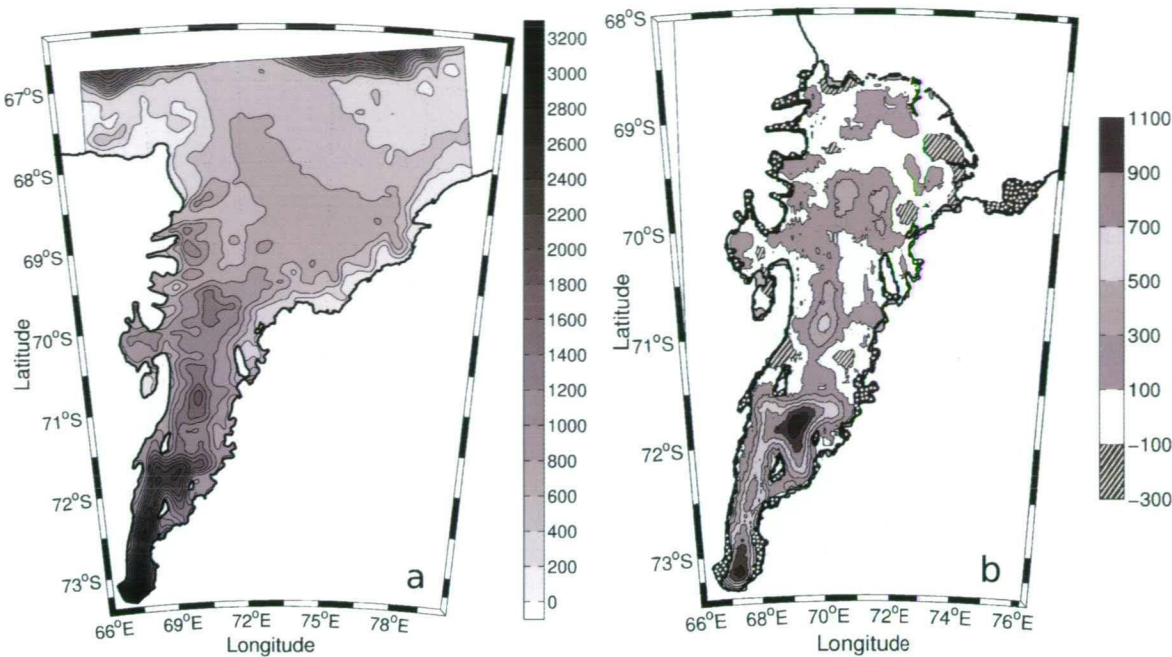


Figure 5.5: (a) The resulting bathymetry of the Amery Ice Shelf and Prydz Bay region showing 200 m contour intervals. (b) Difference between this bathymetry and that of H06, the extra area included in this study being indicated by the spotted dark grey, and the extra area used by H06 being indicated by light grey (i.e. in some regions near the grounding line such as in Beaver Lake).

shows a significant improvement over all of the GPS sites (Table 5.1). This is especially obvious in the southern region of the AIS for sites 9 and 10 where MOG2D shows large improvements. *Maraldi et al.* [2007] have shown that the performance of MOG2D with the best-fit WCT profile outperforms regional Antarctic models [CATS and CADA *Padman et al.*, 2002] and global tide models [for example, TPXO and FES2004 *Egbert et al.*, 1994; *Lyard et al.*, 2006]. These improvements are therefore due to both the higher resolution of the tide model and the improved ice draft and bathymetry.

Best-Fit Cavity Geometry

The refined bathymetry, shown in Fig. 5.5.a, was derived incorporating ice-draft data at the grounding line and a prescribed channel centerline. Sections through the best-fit bathymetry are shown by the dashed black line in Fig. 5.3. The differences between the bathymetry of H06 and this study are shown in Fig. 5.5.b. As expected, the main differences occur in the area south of 71.5°S. Most of the change seen in the northern part of the AIS can be attributed to the new grounding line position and the seismic and borehole data. The best fit continues the North-South trend in the bathymetry that can be seen in the northern part of the cavity (Fig. 5.3.a).

The total area of the AIS, less any area covered by Budd Ice Rumples, Clemence Massif, Robertson Nunatuk and Gillock and Dog Islands, is 58,380 km². This estimate is 5% larger than the area used by H06 (the differences between grounding line positions can be seen in the

dotted dark grey and light grey areas on Fig. 5.5.b) and 15% larger than suggested by [Fricker *et al.*, 2002b]. Most of the difference in area estimates is seen in the southern grounding line position. This estimate uses an ice front position from 2001 that is advancing at a rate of ~ 1200 m annum⁻¹ [Young and Hyland, 2002]. The total area of the AIS as of 2009 is therefore $\sim 60,000$ km². Obtaining a realistic description of the cavity shape is especially important for studies of the ocean circulation in the sub-ice shelf cavity.

5.2 General Model Configuration

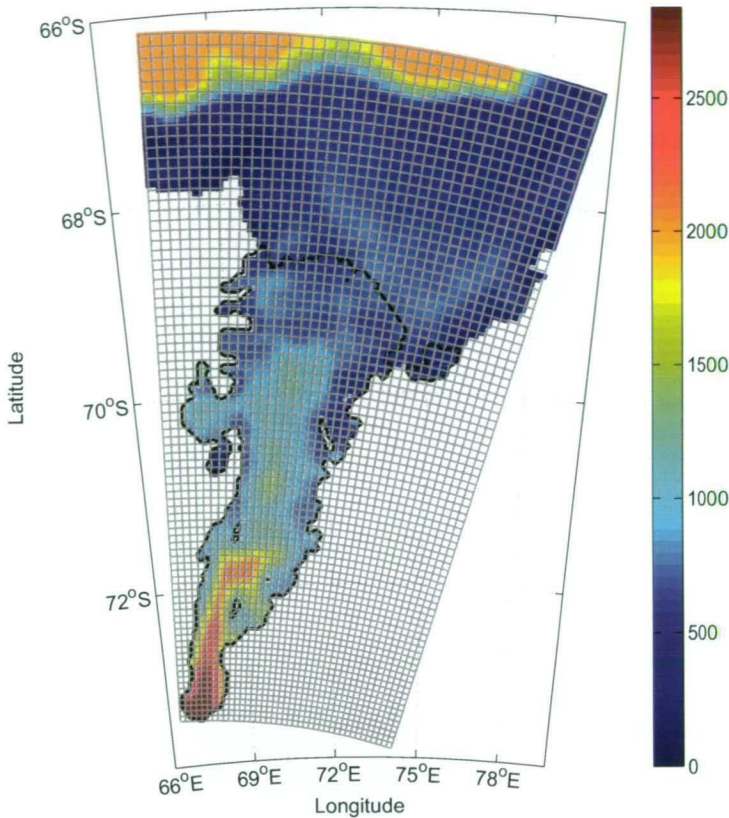
The three-dimensional model (ROMS) has a free surface and uses a vertical s (terrain-following) coordinate. The model domain (Fig. 5.6) covers the AIS and Prydz Bay, extending to an open northern boundary at 66°S at its northernmost extent. The southern boundary of the model is a closed solid free slip wall and the eastern and Western boundaries are partially open. The horizontal grid is an orthogonal polar projection that was developed to minimise wasted cells due to land masking, especially to the south. The horizontal grid resolution is between ~ 3 km near the southern boundary to ~ 7 km near the northern boundary.

There are 16 vertical levels that are concentrated towards the top and bottom of the model domain (see Fig. 5.6). The thickness of the top model layer is between 0.72 m over the shallows to 28.69 m over the deep ocean. The interpolated bathymetry from section 5.1 [Galton-Fenzi *et al.*, 2008b] was smoothed with a modified Shapiro filter that was designed to selectively smooth areas where the changes in bathymetry are large with respect to the total depth [Wilkin and Hedström, 1998]. A similar filter was used for the ice draft. Most of the smoothing was on the sea floor and there was less smoothing required for the ice draft and over the shelf break. The mean slope over the entire model domain was reduced from 1.1% to 0.9%.

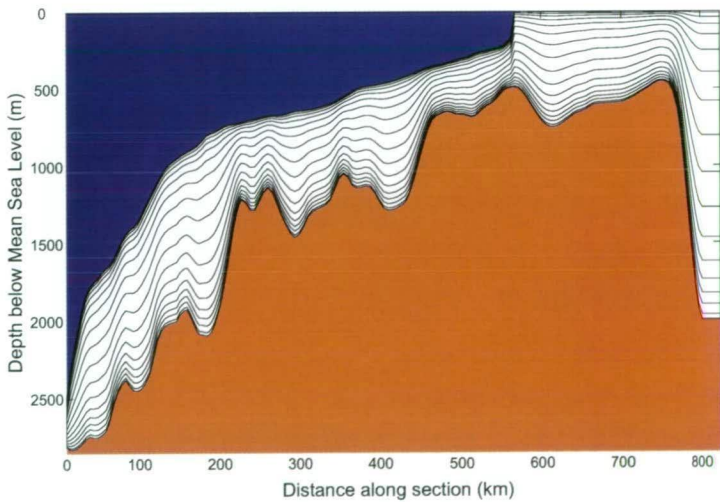
The choice of mixing and advection schemes follows the choices that were successfully used by Dinniman *et al.* [2007, 2003] for studies of the shelf seas near the Ross Ice Shelf. The Laplacian horizontal mixing of tracers uses a diffusivity of $5 \text{ m}^2 \text{ s}^{-1}$. A background value $100 \text{ m}^2 \text{ s}^{-1}$ of explicit horizontal momentum mixing was required for stability. Quadratic boundary stress, with a coefficient of 2.5×10^{-3} (non-dimensional), was applied as a body force over the bottom layer and surface layer in contact with the ice shelf. The vertical momentum and tracer mixing used the K profile parametrisation (KPP) mixing scheme [Large *et al.*, 1994], including the use of a surface mixed layer. No double diffusive mixing was included [Dinniman *et al.*, 2007].

5.3 Forcing and Initial Conditions

The model forcing was different from that used in Dinniman *et al.* [2007]. The non-linear equation of state discussed in Chapter 3.3 and Appendix 1 is used. The initial conditions of the seawater are horizontally-uniform temperature and salinity with a vertical profile that increases linearly from 34.35 psu at the surface to 34.65 psu at the bottom and a temperature that decreases linearly from -1.85 °C at the surface to -2.05 °C at the bottom. The model uses 300 seconds for the baroclinic time-step and 7.5 seconds for the barotropic time-step.



(a)



(b)

Figure 5.6: (a) Horizontal grid showing every second grid cell. Resolution is 3.1 km at the southern boundary and 6.9 km at the northern boundary. (b) Vertical profile along the channel centerline shown in the inset of Fig. 5.3 showing the spacing of the 16 vertical layers.

5.3.1 Ice-ocean conditions

The melting and freezing formulation uses the full three-equation formulation outlined in Chapter 2 and used in the simplified studies of Chapter 4. In all experiments, the same five frazil size classes are considered. These have diameters of: 0.1, 0.3, 0.6, 0.8 and 1.0 mm. Using the smaller number of size classes reduces the computational effort and complexity of the analysis, but retains information about differences depending on rise velocity, precipitation and effects of deposition. All experiments are initialized with a zero concentration of frazil.

The seeding distribution of the frazil deposits equal amounts across all size classes. The growth rate depends on Nu [Chapter 2, eqn 2.15 based on *Holland and Feltham*, 2006] and is scaled to consider the effects of salt exchange (Chapter 2, eqn 2.19). The frazil rise velocity is calculated using the piecewise function [*Morse and Richard*, 2009, Chapter 2, eqn 2.27]. Preliminary studies showed the stability limits imposed on the frazil ice growth (melt) rate (i.e. not to exceed the amount of supercooling (heating) during a single time-step) are important only during the initial spin-up of the model, otherwise the frazil model behaves dynamically and allows interactions between size classes to occur within the model time-step. To minimise the shock of high frazil ice growth during the initial spin-up stage, the frazil growth rate was ramped up over one year.

5.3.2 Open ocean surface boundary conditions

Brine rejection during the formation of ice in polynyas is considered to be very important in the creation of bottom water [*Zwally et al.*, 1998]. The polynya has been attributed to many processes, including southerly katabatic winds [*Bromwich et al.*, 1998] and upwelling of warm Circumpolar Deep Water (CDW) [*Jacobs and Comiso*, 1989]. The dense High Salinity Shelf Water (HSSW) that is created as a result of these processes also has the potential to lead to the production of Antarctic Bottom Water [*Williams et al.*, 2008] and drain underneath the ice shelf, melting the underside. The response of the ocean to coastal polynyas has been investigated with ocean models that include sea-ice dynamics [*Marsland et al.*, 2004; *Stössel et al.*, 2007].

An alternative method uses ice concentrations from a climatology derived model from the Special Sensor Microwave Imager (SSM/I) [Fig. 5.7 and *Tamura et al.*, 2008]. These estimates are valuable during the time of active sea-ice growth and represent the brine formation from polynyas especially well.

The surface salt flux in *Tamura et al.* [2008] is calculated from the estimated ice production rates over the freezing period from March to October by assuming that all of the heat loss at the surface is used for ice formation. Specifically, the volume of ice production per unit area \mathcal{V}_i is given by:

$$\mathcal{V}_i = \frac{Q}{\rho_i L} \quad (5.3)$$

where Q is the heat loss at the thin ice surface, ρ_i (900 kg m^{-3}) is the ice density, and L is the latent heat of fusion of sea-ice ($3.02 \times 10^5 \text{ J kg}^{-1}$). The ice production rate is converted to a surface salinity flux: an annual ice production of 1 m corresponds to salinity flux of $21.7 \text{ kg m}^{-2} \text{ year}^{-1}$,

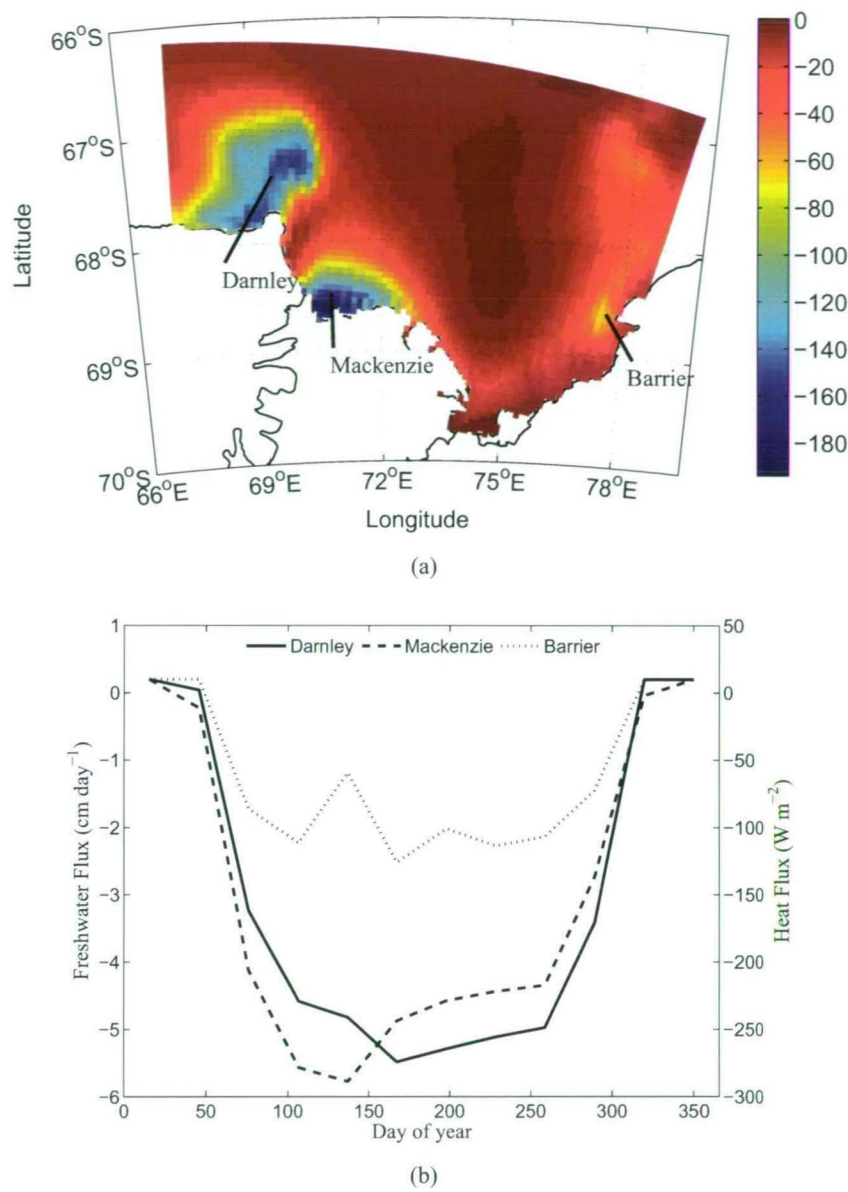


Figure 5.7: (a) Winter snapshot of the surface heat flux showing the strong effect of the Darnley, Mackenzie and Barrier polynyas. (b) Monthly heat and Salt fluxes for each of the three polynyas. The values come from the cell indicated by the lines in panel (a). The salt and heat fluxes during active sea-ice formation are derived from the Special Sensor Microwave Imager (SSM/I) [Tamura *et al.*, 2008] which, during the summer months, are supplemented with fluxes from NCEP-2 [Kanamitsu *et al.*, 2002].

assuming a water and thin ice salinity of 35 and 10.85, respectively [Martin and Kauffman, 1981]. During summer, the Tamura *et al.* [2008] data are supplemented with open-water heat and salt fluxes using the monthly climatologies from the NCEP-2 [Kanamitsu *et al.*, 2002].

The timing of the heat flux in winter is closely associated with the maximum wind strength from

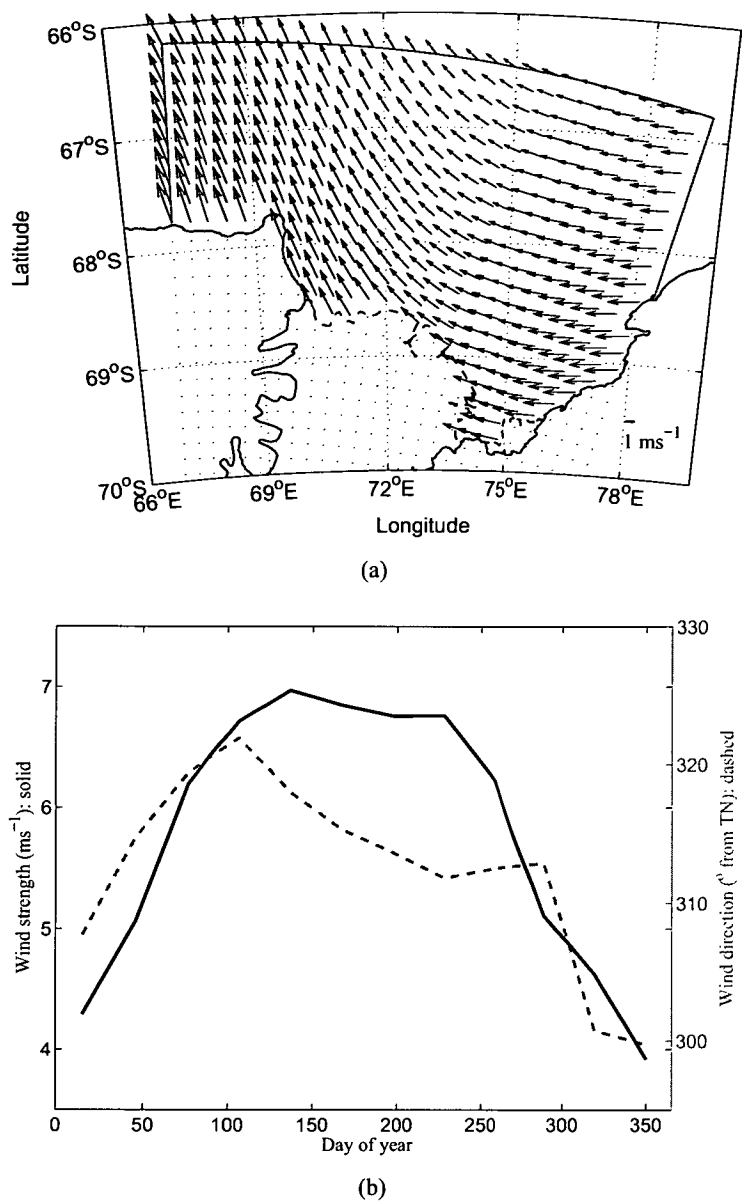


Figure 5.8: (a) Time-average wind fields for every third grid cell and (b) monthly area-average wind velocity (solid line) and direction (dashed line) from NCEP-2 [Kanamitsu et al., 2002].

NCEP-2. The maximum brine production from the Darnley and MacKenzie polynyas corresponds to the maximum strength shown in the coastal katabatic winds (see Fig.5.8.a). The wind fields, shown in Figs 5.8, are typical of the prevailing wind direction.

A wintertime snapshot of the open ocean region shows the strong heat flux due to the Darnley, the Mackenzie and to a lesser extent the Barrier polynyas, located within the domain of the model (see Fig.5.7(a)). The Darnley and Barrier polynyas may be enhanced by the position of

blocking grounded icebergs in the region. Together, these three polynyas produce a volume of ice comparable to the Ross polynya ⁶. The large variation due to the active polynyas over a seasonal cycle are shown in Fig. 5.7(b).

The formation rate of ice due to the coastal polynyas reaches a maximum near the middle of the year and then slows down leading into summer, where the fluxes of heat and salt reverse sign (i.e. the surface ocean warms and freshens) during the summer months, which is typical then of most of the open ocean region within the model domain (see Figure 5.7). The heat and wind forcing from NCEP-2 [Kanamitsu *et al.*, 2002] closely matches the ERA-40 reanalysis in the region of the AIS [Uppala *et al.*, 2005].

Wind fields are taken from NCEP-2. The magnitude and direction are in general agreement with available Automatic Weather Station records from sites AM01 and AM02 on the AIS ⁷. The surface kinematic wind stress, τ is calculated in the i and j -direction from the velocity field \mathbf{u} , as:

$$\tau_{i,j} = \rho_a c_a \mathbf{u}_{i,j} |\mathbf{u}_{i,j}| \quad (5.4)$$

where, ρ_a is the air density (1.3 kg m^{-3}) and c_a is the dimensionless air-sea friction coefficient (1.4×10^{-3}).

Lateral (open ocean) boundary conditions (tracers, velocities and tides)

The computational overhead required for modelling ice shelf cavities at a resolution that resolves the narrow boundary currents necessitates the use of a regional model and hence open boundaries. Having open boundaries requires the specification of the conditions that represent the transfer processes between the modelled ocean and the excluded portion of the global ocean. The regional model described here has open boundaries to the East, North and West of the domain to represent exchange with the global ocean. Tracers and velocities in the model are relaxed to conditions at the boundaries over a constant time scale. The time scale of the “nudging” is based on inward or outward advection velocity of properties at the boundary and is 30 days on the incoming and 2 days on the outgoing. Frazil ice is relaxed over 10 days, which prevents unwanted concentrations from building up within the model domain. No sponge layer, or region of increased horizontal viscosity near the open boundaries, was used.

A common climatology used for this purpose is from the World Ocean Atlas [Locarnini *et al.*, 2006; Antonov *et al.*, 2006]. Preliminary simulations using the World Ocean Atlas climatology showed that it is inadequate for regional application of the coastal oceans surrounding Antarctica. The sparse observations included in the data set, especially for winter, mean that tracer properties are biased to summer conditions. Furthermore, the coarse resolution (1°) data does not represent the coastal water column structure adequately. Instead, in the region of the Antarctic coastal margin, climatology from ECCO was used [Menemenlis *et al.*, 2008; Wunsch *et al.*, 2009].

⁶ The Darnley polynya ($181 \pm 19 \text{ km}^3$) is the second highest active polynya around Antarctica, the Barrier ($80 \pm 19 \text{ km}^3$) is seventh and the Mackenzie ($68.2 \pm 5.8 \text{ km}^3$) is tenth [Tamura *et al.*, 2008].

⁷ These data are available online at, <http://aws.acecrc.org.au/background.html>

ECCO2, which is a data assimilating global model with realistic air-sea interactions and sea processes, has been used in a form to simulate the circum-Antarctic ice shelves [Losch, 2008]. Lateral boundary fields (potential temperature, salinity and currents) on the open boundaries are relaxed to monthly climatologies⁸.

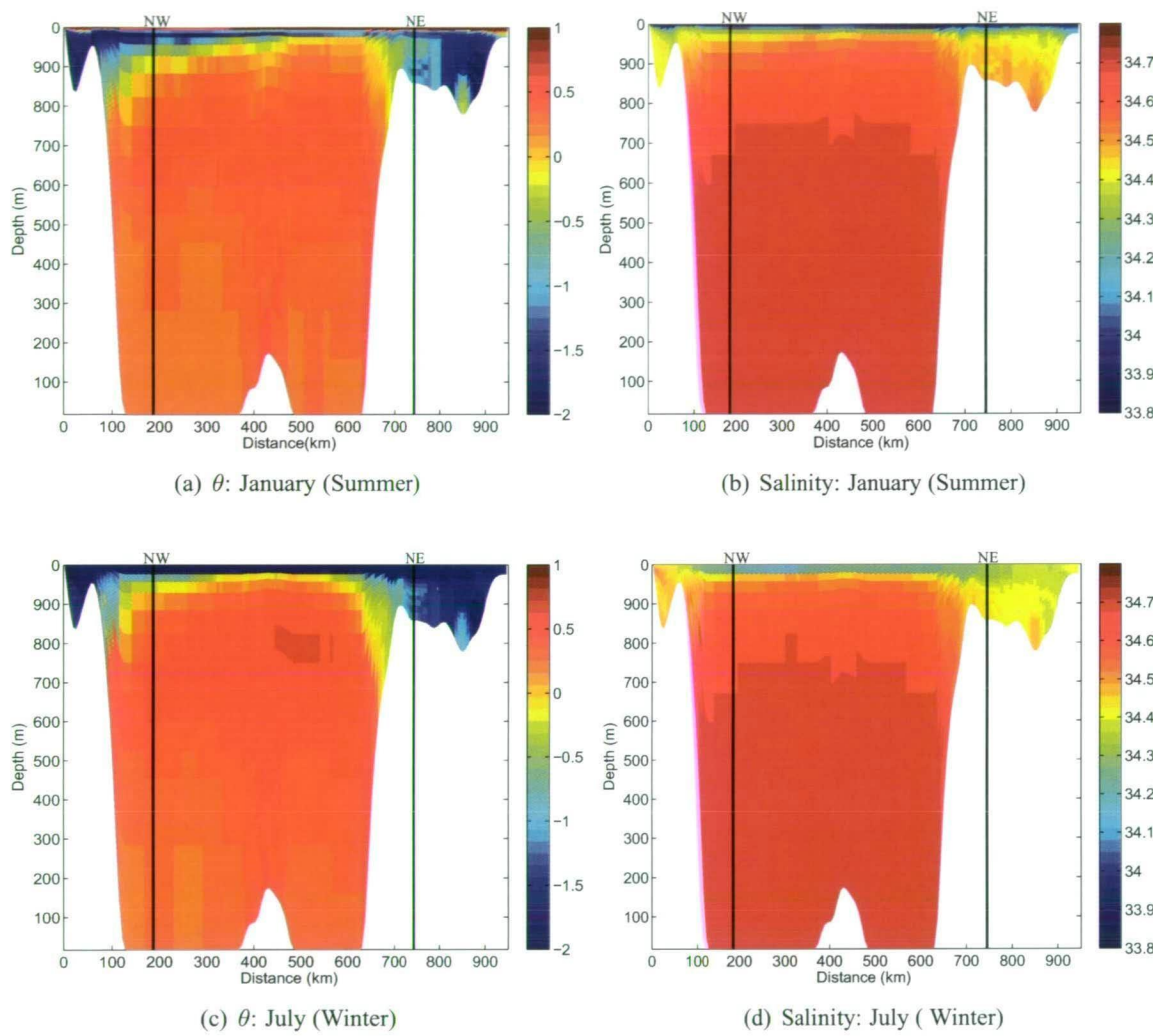


Figure 5.9: The θ and S fields on the open boundaries. Each panel follows the open boundary clockwise from West to East. The domain vertices for the northeast (NE) and northwest (NW) are indicated by the vertical black lines. The fields, representative of Summer (top row) and Winter (bottom row) conditions, show variability in the upper few hundred meters due to the seasonal cycle.

Fig. 5.9 shows summer and winter snapshots of the potential temperature and salinity fields used to force the model. The fields, representative of Summer (top row) and Winter (bottom row) conditions, show variability in the upper few hundred meters due to the seasonal cycle. It is clear that the ECCO2 model is able to reproduce the strong seasonal forcing in the coastal

⁸ Personal communication: Michael Schodlok, NASA, JPL.

seas environment, due to its coupling with a dynamic sea-ice model. The plots show regions of HSSW on the continental shelf seas. The dominant water mass on the northern boundary below the surface seasonal mixed layer is CDW.

The ECCO2 boundary currents do not include tidal forcing, so tides were added as a free surface forcing. The combination Flather/Chapman sea surface conditions were used with the barotropic tidal currents added to the boundary currents. The tidal amplitudes and phase are calculated using a non-standard ROMS subroutine⁹ based on tidal information from the Proudman Oceanographic Laboratory [Murray, 1964] and modified to be included within ROMS, yielding a standard tidal prediction.

5.3.3 Spin-up procedure

The time over which initial transients disappear in ice shelf-ocean modelling studies are varied. The published descriptions of model spin-up procedures often lacks the level of detail required to reveal the rate of the convergence of the solution. Simplified studies by Holland *et al.* [2008] use 10 years. Models of the open ocean region of the Ross Sea used 5 years [Dinniman *et al.*, 2007]. Realistic ice shelf-ocean interaction studies choose 10 years as an appropriate spin-up time [for example, Darelius *et al.*, 2009; Holland, 2001]. Chapters 3 and 4, show that for a closed model domain, temporal changes are present in the models state variables, above numerical error, even after 30 year integration.

During model spin-up, bulk measures such as basin-average kinetic energy, are common methods to monitor the approach of the model simulation to an approximate steady state. For the model outlined above, the kinetic energy is measured using eqn 3.10 and is shown in Fig. 5.10. The average time history of kinetic energy shows that the model has reached approximate steady state after about 4 years of integration, in agreement with modelling studies by Dinniman *et al.* [2007] using ROMS with similar grid resolution and boundary forcing characteristics.

However, because the model used here is primarily designed to investigate ice-ocean interactions, then diagnosing an appropriate integration timescale should also include analysis of evolution of the tracer fields. The time history evolution of the ocean heat content \mathcal{HC} is given as,

$$\mathcal{HC} = \sum_{i,j,k} [\Delta\mathcal{V}_{i,j,k} T_{i,j,k}^K c_p \rho_{i,j,k}]; \quad (5.5)$$

where $\Delta\mathcal{V}$ is the tracer control volume, T^K is the temperature in °Kelvin, c_p is the specific heat of polar seawater ($3974 \text{ J kg}^{-1} \text{ K}^{-1}$) and ρ is the density (kg m^{-3}) for each cell, i, j and k . Fig. 5.11 shows the time history of heat content for the total model and for the ocean cavity below the AIS, relative to the initial heat content.

The open ocean quickly adjusts to the boundary conditions. The change in the total model heat content from steady state (see Fig. 5.11 a.) suggests the tracers reach approximate steady state on

⁹ Available online at staff.acecrc.org.au/johunter/tides.html

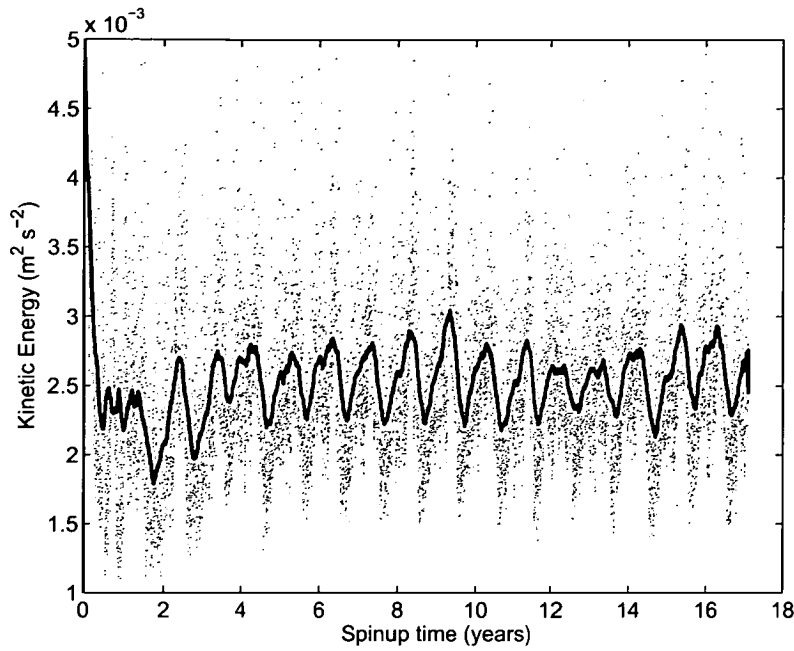


Figure 5.10: Time history of the average model kinetic energy. The large variability (grey dots) are predominately due to tidal oscillations. The time history also shows a strong seasonal cycle and inter-annual variability (black line). The grey dots are 4.2 hourly model output and the black line is a smoothed version using a 30 day moving average.

about the same time scale as the momentum, over about 5 years. However, Fig. 5.11 b. shows that the total heat content beneath the AIS requires much longer to reach approximate steady state. The waters that reside beneath the ice shelf have a longer time between exchanging with the open ocean boundaries than do waters in the open ocean.

The mean residence time is estimated by dividing the volume of the ocean cavity ($2.6115 \times 10^{13} \text{ m}^3$) by the volumetric flow rate of seawater which either enters or exits the cavity, based on the assumption that the volume of seawater beneath the cavity is approximately constant. So, neglecting tidal currents and relying on mooring observations taken near the front of the Amery Ice Shelf [Lefranue and Craven, 2004], the volumetric transfer rate can be calculated over the area of the exiting ISW plume ($\sim 5 \times 10^6 \text{ m}^2$) multiplied by its exit velocity ($\sim 0.1 \text{ ms}^{-1}$), to give a volumetric flow rate of $5 \times 10^5 \text{ m}^3 \text{ s}^{-1}$ and a residence time of ~ 1.7 years.

The long residence time suggests that much of the Amery Ice Shelf cavity is isolated from the effects of the open ocean seasonal cycles. This is evident by the weak seasonal cycle in Fig. 5.11.b when compared to the strong seasonal cycle present in Fig. 5.11.a. The dominant mechanism driving changes in the ocean heat content are primarily correlated with the tidal oscillations. As the prescribed heat transfer primarily depends on the velocity of the water adjacent to the base of the ice shelf, tidal currents enhance the melting/freezing rates, leading to the large fluctuations in ocean heat content (seen as the grey line in Fig. 5.11). A preliminary examination shows that the

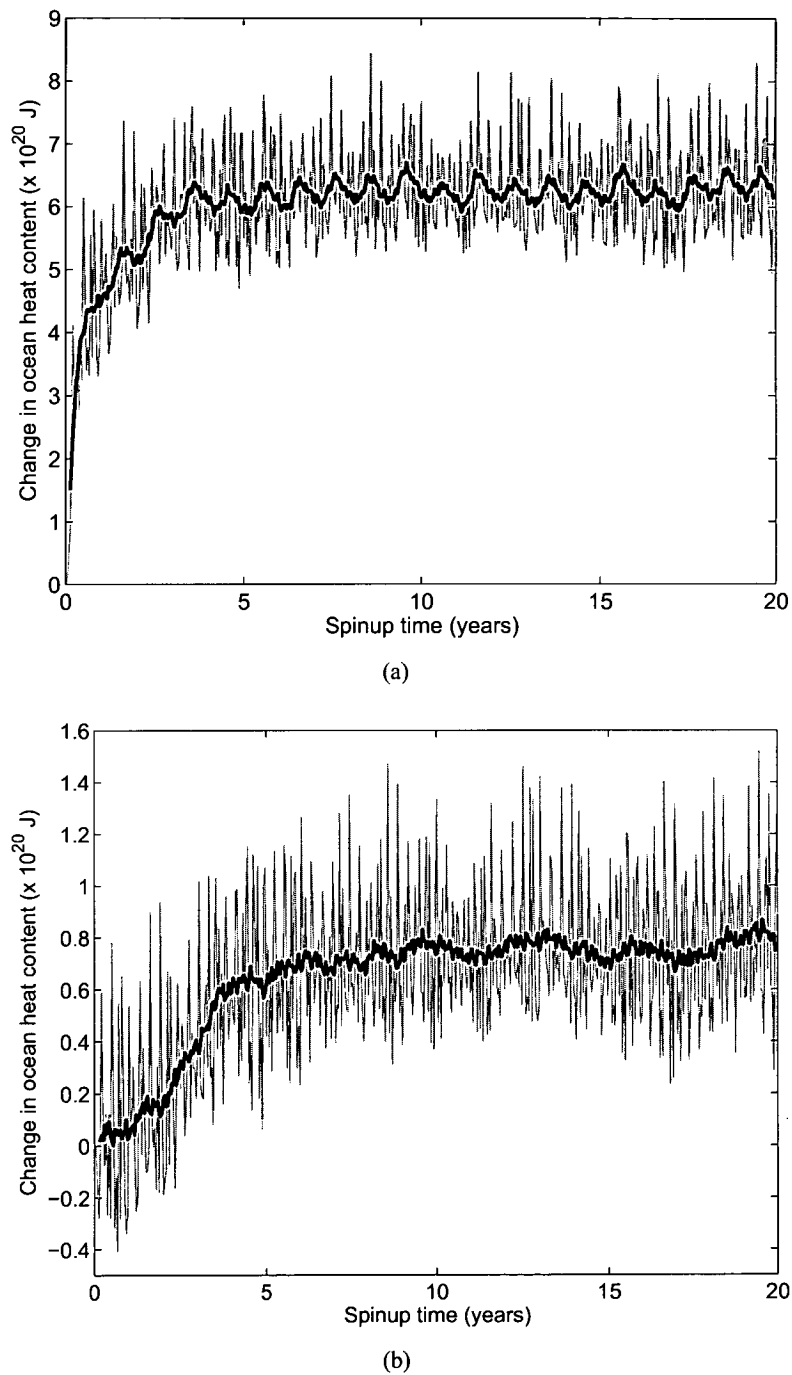


Figure 5.11: Change in heat content for (a) entire model domain and (b) ocean cavity beneath the Amery Ice Shelf, both relative to the initial state. The grey line is calculated using 15 day model output and the black line is a smoothed version, using a 3 point moving average. Note that between 10 and 20 years there is still a slight increase in the total heat content beneath the ice shelf of $2.4 \times 10^{17} \text{ J year}^{-1}$.

influence of the seasonal cycle is strongest beneath the ice shelf near the front and diminishes with distance towards the southernmost part of the cavity. The influence of the open ocean seasonal cycle on the basal melting and freezing are discussed in Chapter 6.

As the state of the ocean beneath ice shelves are often poorly known the initial conditions are also poorly attributed and not near the equilibrium condition. As such, the use of inaccurate initial conditions can lead to long integration times to approach approximate steady state. If a model is near to steady state and comparisons between models utilise similar integrations then the offsets from complete equilibrium are not usually problematic. However, for meaningful comparison with observations, the model state variables should be at, or as near to, steady state as achievable. In many cases, the length of time that a model can be run also depends on being able to complete runs within a reasonable time-frame and access to sufficient numbers of cpu-hours.

5.4 Concluding Remarks

This chapter has outlined the ocean model that will be used in the following two chapters with the aims:

Chapter 6: To evaluate the response of the Amery Ice Shelf ocean system to present day forcing.

Chapter 7: To test the sensitivity of the Amery Ice Shelf ocean system to climate change.

The level of detail given to the development of the cavity geometry is justified because previous modelling studies suggest that the geometry of the cavity beneath the AIS is thought to have a strong influence on the thermohaline circulation [Hemer *et al.*, 2006; Williams *et al.*, 1998b]. Also, simplified studies show that the geometry of the cavity can have a strong effect on the response of basal melt rate to ocean thermal forcing [Holland *et al.*, 2008; Little *et al.*, 2008].

The residence time of seawater in the cavities beneath ice shelves is important when considering the spin-up of an ice shelf ocean model. As such, simulations of the Amery Ice Shelf-Ocean model cover 15 years. Analyses are performed on monthly averages of the final 3 years of model output. Within the context of the thesis, time scales shorter than months, are not considered.

CHAPTER SIX

THE AMERY ICE SHELF-OCEAN MODEL

This chapter extends the conclusions of the simplified studies (Chapters 3 and 4) by presenting the results of the sophisticated Amery Ice Shelf/Prydz Bay model that was described in Chapter 5. The chapter evaluates the ability of the model to reproduce and extend our understanding of some key features of the region, namely,

- The general circulation in the region of Prydz Bay; and,
- The magnitude and spatial patterns of basal melting and freezing on the underside of the Amery Ice Shelf (AIS).

Three model simulations are discussed in this chapter, assessing the impact of frazil dynamics on marine ice accretion and assessing the impact of ISW on the production of Antarctic Bottom water in the vicinity of the AIS:

1. “Reference”: the reference simulation uses the most sophisticated treatment of both the basal ice-ocean thermodynamics and frazil ice dynamics.
2. “Without Frazil”: the reference simulation but without frazil dynamics.
3. “Without Ice Shelf”: the reference simulation without any ice/ocean thermodynamics.

6.1 General Circulation and Water Mass Properties

The distribution of potential temperature and salinity from the observations and model data are used to define appropriate water masses for discussion in the chapter. The locations of the observations are shown in Fig.6.1. The observations are from moorings via four access holes melted through the ice shelf [*Allison*, 2003; *Craven et al.*, 2003a, b, red circles], from seven moorings deployed along the ice shelf front [*Leffanue and Craven*, 2004, blue circles], and from two legs from the BROKE-West oceanographic survey undertaken during the Austral summer of 2006 [blue squares *Meijers et al.*, 2009].

Definitions of coastal Antarctic water masses typically rely on the constraints published in *Whitworth et al.* [1998, Fig. 1a]. These constraints define water masses according to their neutral density, potential temperature and salinity. However, neutral density is poorly defined in the polar regions due to the high helicity in the Southern Ocean [*Klocker et al.*, 2009; *Jackett and McDougall*, 1997]. This is indicated by the converging neutral densities near the freezing point used in *Whitworth et al.* [1998] and *Meijers et al.* [2009]. As such, we rely on potential density, potential temperature and salinity to place bounds, when required, on the water masses defined here (Table 6.1).

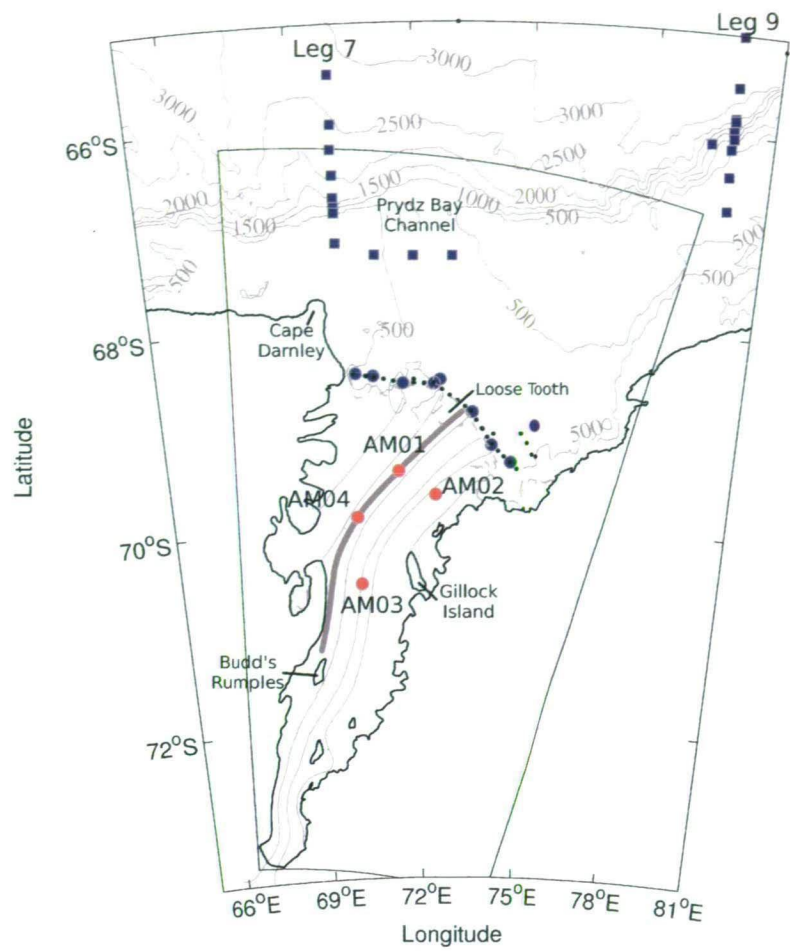


Figure 6.1: Locations of the oceanographic observations used to evaluate the model, from Legs 7 and 9 of the BROKE-West Survey (blue squares), AMISOR moorings from 2002/03-present (blue circles), CTD survey (black dots) and 4 long term moorings located beneath the AIS (red circles). Two of the long term boreholes (AM01 and AM04) lie on a glacier flowline (thick grey line). Also shown are bathymetry contours (in m) in the open ocean and the perimeter of the model domain.

The lateral potential temperature (θ) and salinity (S) fields used to force the model are superimposed on the observational data (grey dots) in Fig. 6.2.a and b. The distribution of the $\theta - S$ data used to force the lateral boundaries from ECCO2 show good agreement with the observations. The warmer regions of Circumpolar Deep Water (CDW) shown in the observations are from far offshore on Legs 7 and 9 taken during the BROKE-West cruise. The near shore temperatures are consistent with the ECCO2 fields that force the northern model boundary, which have $\theta - S$ characteristics of Modified Circumpolar Deep Water (MCDW).

Fig. 6.2.b shows monthly $\theta - S$ output for all grid cells for the reference model. Each point is a monthly average of the last 3 years worth of model output. The model creates both Antarctic Bottom Water (AABW) and Ice Shelf Water (ISW) that are not contained in either the initial

Table 6.1: Water mass definitions based on the potential temperature (θ), salinity (S) and potential density (ρ_0) characteristics. SSW is Summer Surface Water, CDW is Circumpolar Deep Water, MCDW is modified Circumpolar Deep Water, HSSW is High Salinity Shelf Water, LSSW is Low Salinity Shelf Water, ISW is Ice Shelf Water, and AABW is Antarctic Bottom Water. The freezing point at the surface (θ_{fp}) is defined for each water mass for the appropriate salinity range.

Water	θ ($^{\circ}\text{C}$)	S (psu)	ρ (kg m^{-3} -1000)
SSW	$\theta_{fp} < \theta < 2$	$S < 34$	$\rho < 27.75$
CDW	$\theta > 1$	$S < 34.7$	$27.75 < \rho < 27.83$
MCDW	$\theta < 1$	$S < 34.7$	$27.75 < \rho < 27.83$
HSSW	$\theta_{fp} \leq \theta < -1.75$	$S > 34.5$	–
LSSW	$\theta_{fp} \leq \theta < -1.75$	$S \leq 34.5$	–
ISW	$\theta < \theta_{fp}$	–	–
AABW	$-1.75 \leq \theta < 0$	$S > 34.5$	$\rho > 27.83$

conditions or the boundary conditions. The model reproduces the main distribution of Summer Surface Water (SSW) but fails to reproduce the extreme cool/fresh waters that are seen in the observations. These water masses are not seen in the upper layers of the ECCO2 data either and suggest that the prescribed surface forcing during the summer months does not account correctly for the summer melting of residual sea-ice that can be present, which would both cool and freshen the surface layers.

The distribution of $\theta - S$ below 200m is shown in Fig. 6.3. The plot shows every second cell from the model for the open ocean (squares) and the ocean cavity (circles). The profiles of $\theta - S$ in the AIS cavity follow a classic melt/freeze dilution line, first proposed by Gade [1979]. The dashed line assumes no heat is required for warming the glacial ice to the local freezing point before melting can occur and the solid line assumes that the glacial ice is first warmed (from $\sim -6^{\circ}\text{C}$) to the local freezing point before it is melted. The parent water masses driving the melting at the deepest parts of the ocean cavity beneath the AIS originate from winter sea-ice formation processes. The Gade line relationship between $\theta - S$ shows that the waters driving the melting in the deeper parts of the cavity beneath the AIS are saltier than the waters that drive melting at the shallower parts of the cavity. However, these water masses, although still classified as HSSW, have been both warmed and freshened by mixing with MCDW.

Fig. 6.4 shows the spatial patterns of model currents and θ (left panels) and S (right panels) for the s-layer below the surface layer (top panels) and the bottom s-layer (bottom panels). The general summertime circulation seen in the model agrees with the results of previously published work. The large-scale circulation in Prydz Bay is characterised by a strong inflow of MCDW into Prydz Bay from the eastward flowing offshore current [Nunes Vaz and Lennon, 1996]. A narrow westward flow along the continental shelf break has also been observed [Wong *et al.*, 1998] and offshore, just to the north of the shelf break is characterised by eastward flow, which

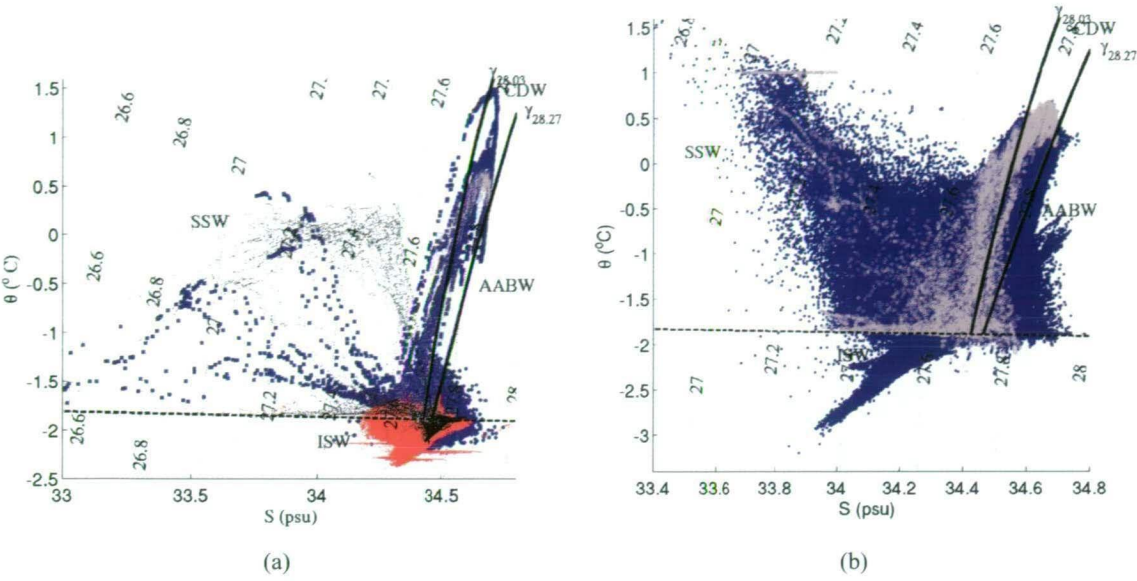


Figure 6.2: (a) Distribution of potential temperature (θ $^{\circ}\text{C}$) and salinity (S psu) for the observation sites shown in Fig. 6.1. The blue and black dots are primarily from summer and the red dots are from long term moorings in the ocean below the AIS. The grey dots are the lateral ocean boundary conditions used to force the model. (b) Distribution of potential temperature (θ $^{\circ}\text{C}$) and salinity (S psu) for the model (blue dots) compared to the same lateral ocean boundary forcing shown in (a) (grey dots). The dotted lines are potential density contours; the almost horizontal dashed line is the surface freezing relationship with salinity; and the solid lines are neutral density contours 28.03 and 28.27 ($\text{kg m}^{-3}-1000$).

has been associated with the southern extent of the Antarctic Circumpolar Current [Wong *et al.*, 1998; Meijers *et al.*, 2009].

The MCDW is recirculated across the front of the AIS as part of the Prydz Bay gyre. The subsurface layer shows that ISW is following the coastline as part of a barotropic circulation, in agreement with observations done during the BROKE-west survey that showed a signal of outflowing ISW to the western side of the Prydz depression (the locations are shown in Fig 6.2 as the blue squares crossing east-west across the Prydz Bay channel). The water exiting the domain to the west occurs in 2 regions: 1) along the coast, as a coastal current; and 2) as a strong current along the continental slope, after exiting from the Prydz Bay channel.

The dominant circulation beneath the AIS ($\sim 10 \text{ cm s}^{-1}$) is a clockwise circulation pattern under the influence of the Coriolis force. The main inflow is near the centre of the front of the AIS, near the Loose Tooth region, and comprises water that is recirculated from within the McKenzie gyre and the coastal current. The coastal current exits the model domain carrying HSSW that has been modified by the ISW outflow. The outflowing ISW bifurcates approximately 100 km from the open ocean, leading to two plumes of ISW, that rejoin in Prydz Bay when encountering the coastal current that flows across the front of the AIS. The coherent plumes of ISW are laden with frazil at

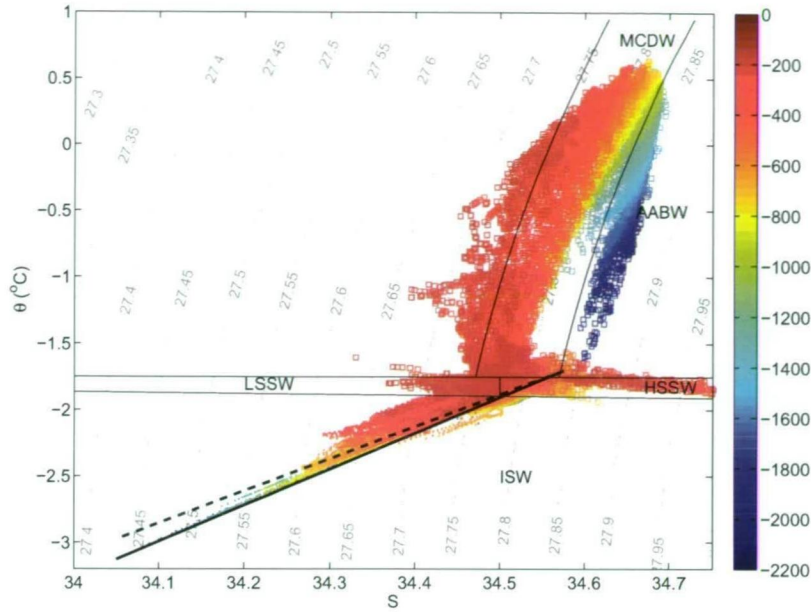


Figure 6.3: Summertime distribution of potential temperature (θ °C) and salinity (S psu) for every second model grid cell in the open ocean (squares) and for the ocean cavity (circles) below 200 m beneath the ocean surface. The colour scale shows the depth for each cell. The grey dotted lines are potential density contours; the thin solid lines define the water masses from Table 6.1. The thick lines in the ISW show the dilution relation when ice melts/freezes in seawater, without considering the heat flux into the ice shelf (dashed solid line) and with the heat flux into the ice shelf (thick solid line) [Gade, 1979].

concentrations as high as $\sim 1 \text{ kg m}^{-3}$. The circulation in the bottom layer shows a recirculation feature that is constrained by the position of Budd's Rumples (see Fig. 6.1 for location). The upper layer shows that the northward flowing ISW is not connected with the bottom flow and is diverted to the west of Budd's Rumples before again continuing northward along the western boundary.

The summertime profiles of temperature and salinity seen in the model agree with the results of previously published work [Leffanue and Craven, 2004]. The CTD temperature and salinity profiles taken during the austral summers of 2001 and 2002 are the highest resolution observations across the front of the AIS to-date (see Fig. 6.5). There is large variability between the summer CTD casts of 2001 and 2002 in the upper 200 metres of the water column. During the 2002 cruise there was persistent sea-ice which contrasts with 2001 conditions when there was more open water [Leffanue and Craven, 2004]. Below 200 metres, the observations are generally consistent between years. There are two major regions of ISW that are visible in the potential temperature field (Fig. 6.5.a) and a sloping east-west salinity profile that shows HSSW in the deeper waters to the eastern side of the AIS (Fig. 6.5.b).

The θ and S fields from the reference simulation were interpolated onto the CTD transect

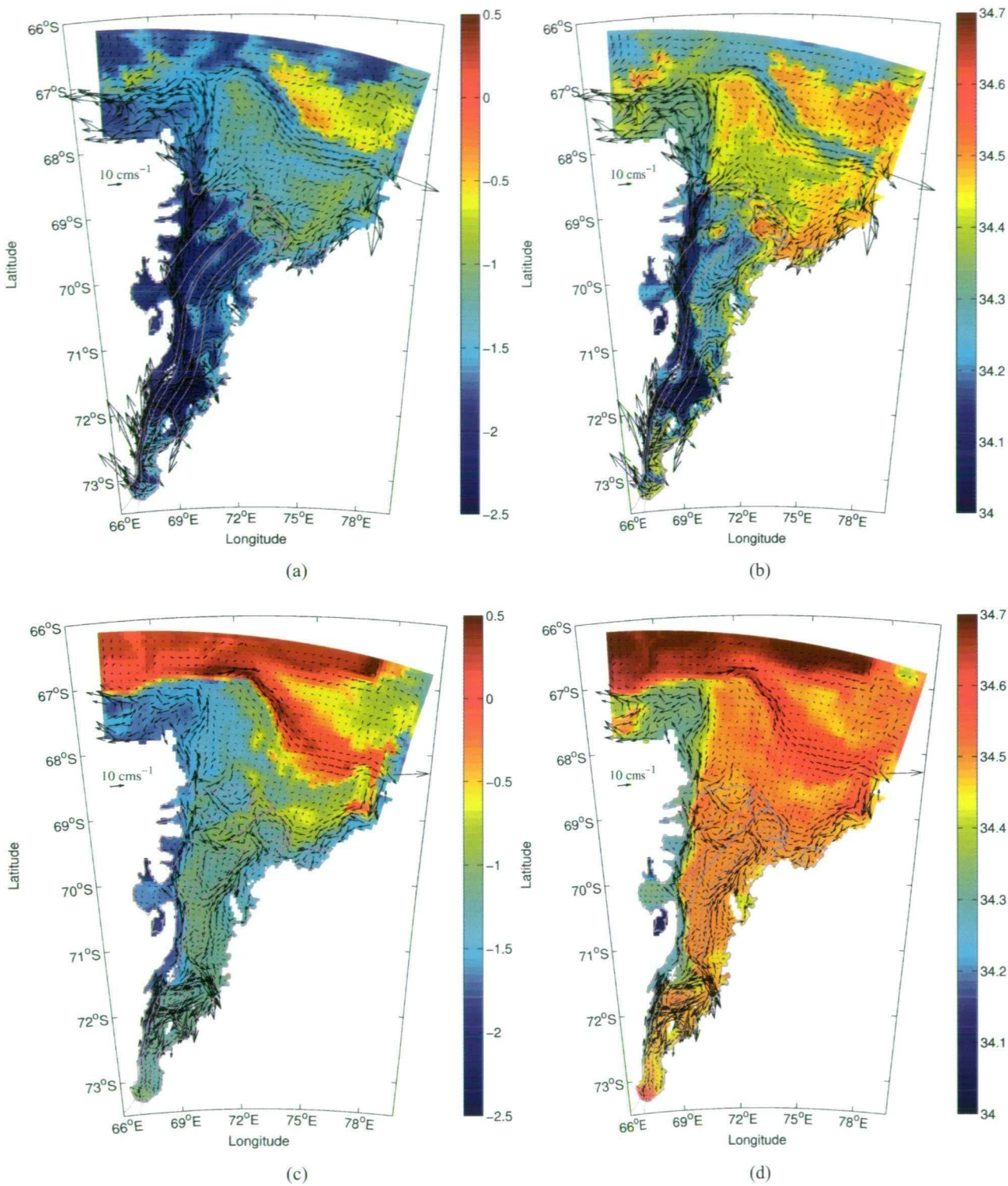


Figure 6.4: Annual average potential temperature (θ °C , left panels) and salinity (S psu, right panels) for the sigma layer below the surface layer (top panels) and the bottom layers (bottom panels).

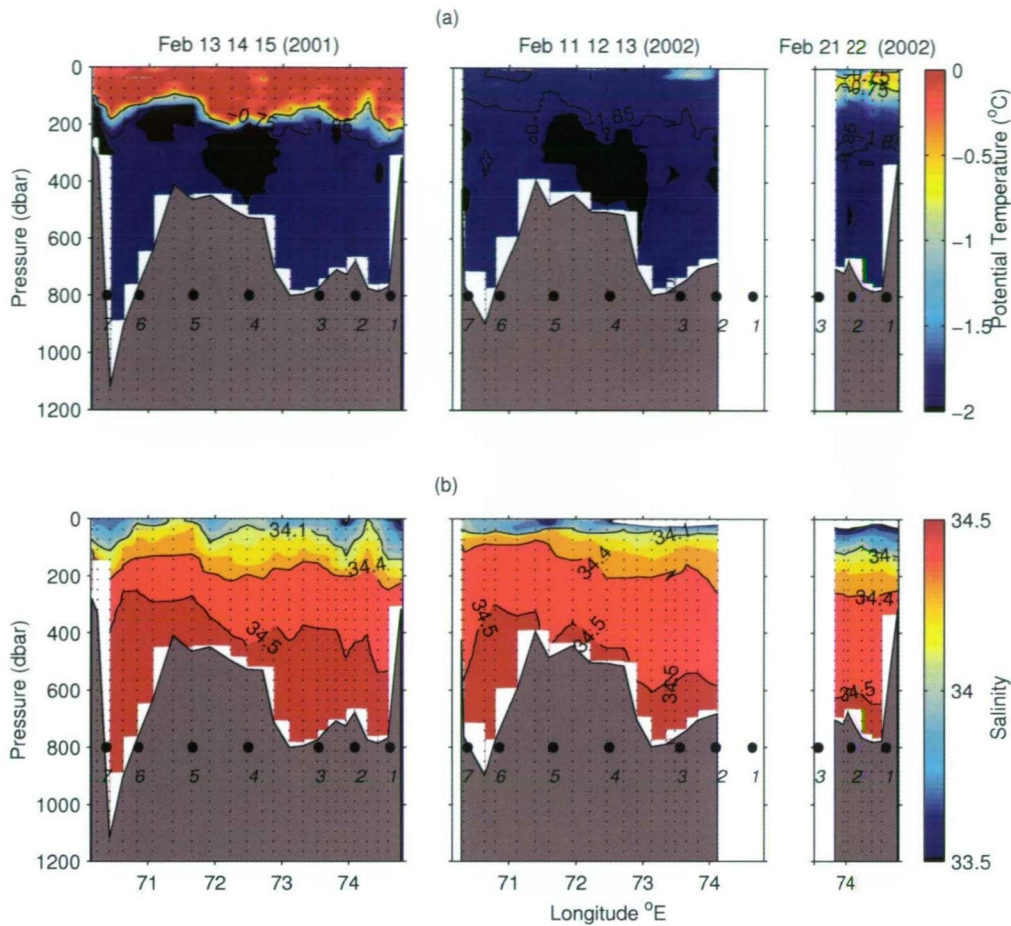


Figure 6.5: Summertime profiles of potential temperature (upper panels) and salinity (lower panels) from the CTD transect shown in Fig. 6.1 for February 2001 and 2002 [taken from *Leffanue and Craven, 2004*]. Extensive open water was present during Feb 2001, shown by the much warmer surface waters, when compared to Feb 2002. Both years show a strong region of ISW outflow to the western boundary and in the mid-shelf region ($\sim 72^{\circ}\text{E}$).

for comparison. The vertical profiles of temperature and salinity generally agree with the CTD observations (see Fig. 6.6). Importantly, the reference simulation broadly reproduces the main observed cores of outflowing ISW (compare Fig. 6.6.a. with Fig. 6.5.a). The profiles of potential temperature and salinity are generally consistent with the CTD observations below 200 metres. However, the vertical profiles in the reference simulation are smoothed when compared to the observations. The models homogenised vertical profiles, when compared to observations, suggest that the vertical mixing enhancement is too strong in the scheme of *Large et al. [1994]*.

6.2 Antarctic Bottom Water Formation

The initial and boundary conditions used in the model do not contain any bottom water. As such, any bottom water present in the reference model has been created as a result of mixing

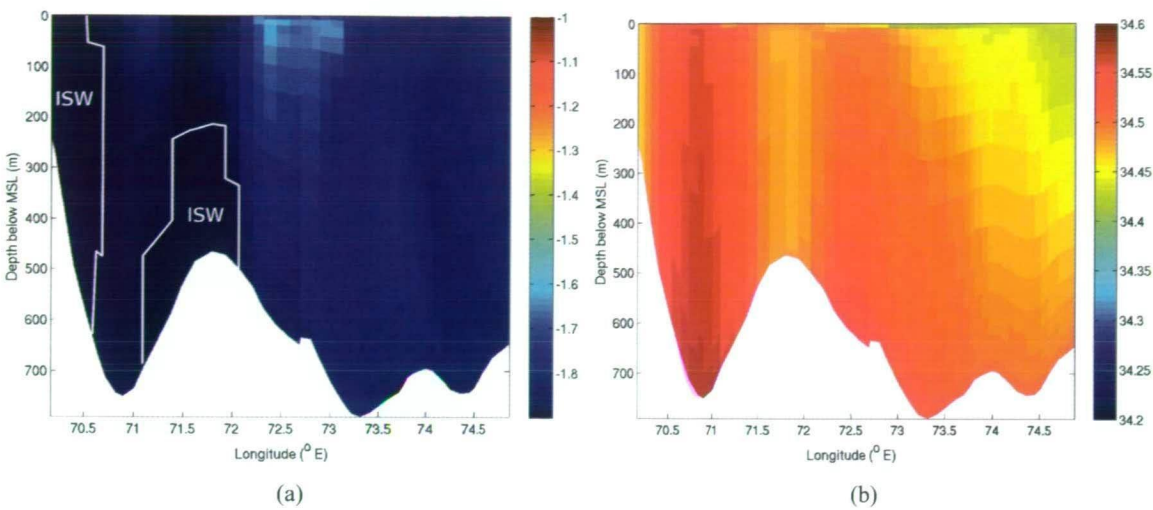


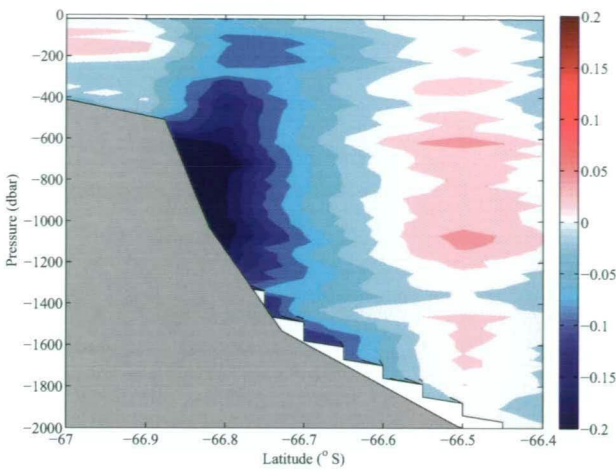
Figure 6.6: Summertime profiles of potential temperature (θ °C , left) and salinity (S psu, right) from the reference simulation, following the CTD transect from Fig. 6.1.

the parent water masses of AABW, namely HSSW, ISW and MCDW, within the domain. In the Section above, AABW has been identified in the reference simulation to be present on the shelf front region of the open ocean. The goal of this Section is to evaluate the origins of AABW within the reference model in comparison with observations.

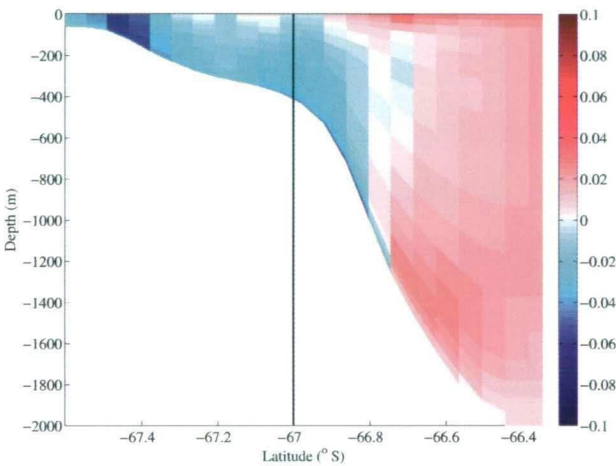
The strong westward flowing continental slope current shown in the reference model agrees with recent summertime ship based observations [Meijers *et al.*, 2009]. Fig. 6.7 compares model currents against the Leg 7 of the ship based observations from the BROKE-West cruise during the Austral summer of 2005/06. Both the ship observations and the model show a strong transition zone between the westward flowing slope currents and the southern boundary of the Antarctic circumpolar current (ACC) (Fig. 6.7.a). The transition zone in the observations (a) occurs at the foot of the continental slope. The model section interpolated along Leg 7 (b) shows the transition zone occurs at the mid slope region and the westward flowing currents are weaker than the observations. However, the model shows further west (c) that the transition zone occurs at the foot of the continental slope with currents of similar magnitude as the observations.

The magnitude and spatial pattern of the westward currents from the model agree well with the BROKE-West observations along 70°E (see Fig. 6.7.b). The model shows strong eastward flow in the open ocean and westward transport along the continental slope. Further to the east at ~69°E, the model shows a tongue of westward flowing water intruding beneath the eastward flowing southern extent of the ACC. This water has characteristics of AABW (see Table 6.1). This westward flow at the bottom is found progressively deeper (further north) to the west and occupies the abyssal floor suggesting AABW is produced in the region of the AIS, moves down the slope, and is deflected westward due to the Coriolis force.

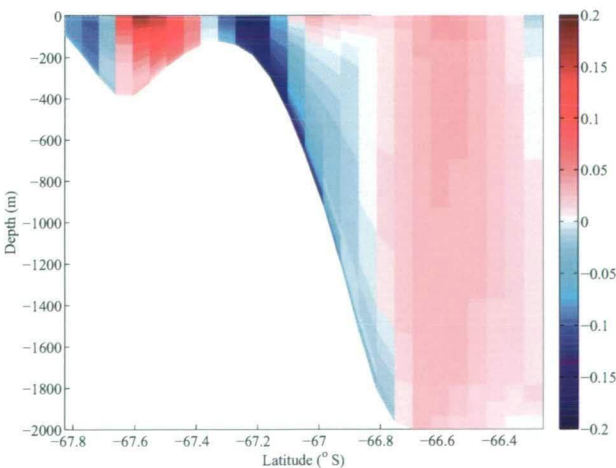
The results presented here confirm the results of Meijers *et al.* [2009] who suggested that the



(a)



(b)



(c)

Figure 6.7: Vertical section of annual averaged model zonal currents (positive is eastward) for (a) observations from BROKE-West leg 7, (b) model output along the BROKE-West leg 7 at 70°E and (c) model output at the western boundary. The vertical line in (b) shows the southern limit of (a).

export of newly formed AABW at Leg 7 does not recirculate in the Prydz Bay gyre, and is instead exported to the west. Observations show that high oxygen concentration values (over 255 mol l^{-1}) indicate a newly formed water mass, recently exposed to the atmosphere [Meijers *et al.*, 2009]. Combined with the presence of SW and ISW close to Leg 7 suggests seasonal AABW production in this region. Additionally the bottom water properties close to Cape Darnley suggest AABW production is influenced by the SW and ISW originating from the AIS, as suggested by Yabuki *et al.* [2006].

The westward transport along the shelf slope was calculated from the reference simulation for AABW, ISW and HSSW (Fig. 6.8). The westward transport is the annual average integration starting from $\sim 77^\circ\text{E}$ and finishing at the western model boundary. The strength of the total westward flowing current is $\sim 1.6 \text{ Sv}$ near the western model boundary, of which $\sim 1.2 \text{ Sv}$ is comprised of AABW. The majority of the remaining transport is comprised of HSSW. The initial pulse of the westward transport of water masses at $\sim 72.5^\circ\text{E}$ along the shelf slope corresponds to the bottom transport of MCDW (not shown) and HSSW created from the eastern parts of the model domain. The net transport of AABW increases approximately linearly from the Prydz Bay outflow region until it reaches the longitude of Cape Darnley. After Cape Darnley, the net transport of AABW increases non-linearly until reaching the western boundary.

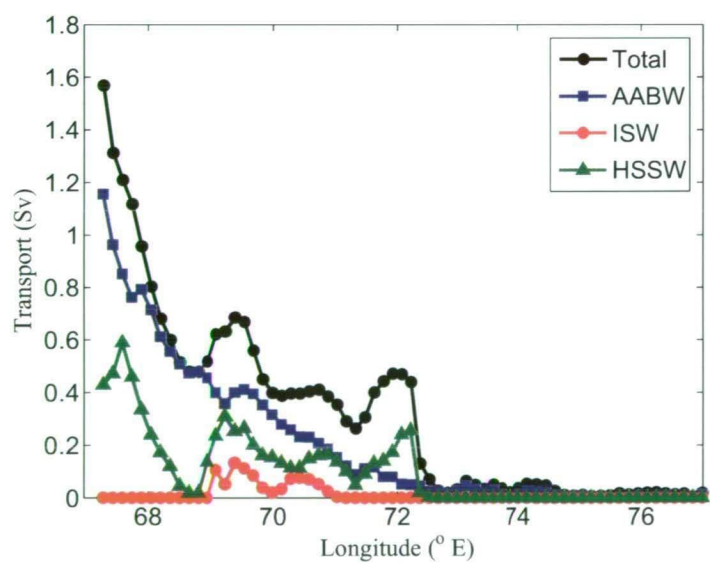


Figure 6.8: Total westward transport (black) along the continental slope, from the reference simulation, compared to the watermass components for AABW (blue), ISW (red) and HSSW (green).

In summary, the results presented here show that AABW is primarily exported from high on the continental slope near Cape Darnley. The mixing of HSSW with intruding MCDW, SSW and ISW occurs further inside Prydz Bay, where the origins of HSSW are the Barrier and McKenzie polynyas. The production of HSSW from the Cape Darnley region more than doubles the net

transport of AABW from the reference model domain.

6.3 Mass Balance of the Amery Ice Shelf

An important component of this study is to estimate the mass balance of the AIS (see Fig. 1.3, Chapter 1). The major components of the mass balance, discussed in Chapter 1, are the flux of ice from the feed glaciers across the grounding line, snowfall and ablation on the upper surface, basal melting and freezing, and the calving of icebergs. The purpose of this Section is to evaluate the net basal melt and spatial patterns of melting and freezing shown in the reference simulation against the available observations. The net basal mass loss estimates derived from glaciological and oceanographic studies are first discussed before discussion of the results from the reference simulation are compared with previous modelling studies.

6.3.1 Glaciological estimates

The AIS is assumed to be in approximate mass balance [King *et al.*, 2009; Allison, 1979]. The major mass balance components of the AIS are summarised in Table 6.2.

Table 6.2: Observational estimates of the various mass balance components for the AIS. The Net Melt = Glacier inflow + Net accumulation - Calving.

Component	Gt ice year ⁻¹	Study
Glacier inflow rate	88.9 ± 8.9	Wen <i>et al.</i> [2008]
Net accumulation rate	11.3 ± 0.7	Arthern <i>et al.</i> [2006]
Calving rate	44.6 ± 9.3	See text
Net melt rate	55.6 ± 12.6	

The net basal mass loss can be found by subtracting the mass loss due to calving from the total mass additions due to both glaciers that contribute to the AIS and surface accumulation (see Fig. 1.3). Estimates of the Lambert basin drainage area, which agree with independent estimates using flux gates across the grounding line, show that approximately 88.9 Gt ice year⁻¹ enter the AIS across the grounding line[Wen *et al.*, 2008]. Much of this ice mass is comprised of the Mellor, Lambert and Fisher glaciers which enter the AIS fjord across the southern grounding line. Tributary glacier flow into the AIS region, across the western and eastern boundaries contributes about 38% of the mass of ice that makes up the AIS.

The major uncertainty with the mass balance estimates of the AIS, aside from the basal melt/freeze, are with the calving rate. Here, the calving rate has been estimated using both velocity information and ice thickness at the front of the AIS, to provide an ice flux. The average velocity across the front of the AIS (about 150 km wide) is about 1100 ± 200 m ice year⁻¹[Young and Hyland, 2002]. The average ice thickness is 0.3 ± 0.03 km that when multiplied by the product of average velocity and width, yields an ice volume flux of 49.5 ± 10.3 km³ that is ‘added’ to the front of the AIS every year. The mass of ice that is added yearly is therefore 44.6 ± 9.3 Gt, assuming

a density at the calving front of $\sim 900 \text{ kg m}^3$ [Fricker *et al.*, 2000]. Note that near to the front of the AIS, the flow rate fields of Young and Hyland [2002] exclude parts of the margins. As such, the total transport across the front of the AIS using the Young and Hyland [2002] velocity fields may well underestimate the transport of ice due to fast flowing tributary glaciers to the eastern and western side of the AIS by an additional 5%.

An independent assessment of the calving rate can be determined using historical observations of the position of the calving front. Historic records of the AIS front position suggest that it calves every 65 ± 5 years [Fricker *et al.*, 2002a]. The last major calving event occurred in 1963/64 which liberated an iceberg with an area of about $10 \times 10^3 \text{ km}^2$. The current position of the front is about half the northward extent of the last calving position and has an average thickness of $0.3 \pm 0.03 \text{ km}$. The average volume of ice that is calved is $3 \pm 0.3 \times 10^3 \text{ km}^3$. The ice mass that is advanced from the front is $41.5 \pm 5.2 \text{ Gt year}^{-1}$, in agreement within the error estimates of the flux derived calving rate.

In conclusion, the net melt rate from glaciological estimates derived from observations is 55.6 ± 12.65 (see Table 6.2; Total Inflow + Net Accumulation - Iceberg Calving). The area-average net basal melt rate is $1.1 \pm 0.3 \text{ m ice year}^{-1}$, found by dividing the net mass loss from the AIS due to basal melt by the area of the ice shelf [$60 \times 10^3 \text{ km}^2$; Galton-Fenzi *et al.*, 2008a].

6.3.2 Oceanographic estimates

Oceanographic estimates of basal melting have been made for the AIS using temperature and salinity fields from oceanographic observations from a cruise undertaken in the austral summer of 1991 [Wong *et al.*, 1998]. Following Foldvik *et al.* [2001], the observations of temperature and salinity were used to estimate the net heat transport into the ocean cavity beneath the AIS to obtain an estimate of the melting and heating of glacial ice in contact with seawater. The CTD observations estimated the average net melt rate from the temperature data at $26.4 \pm 8.6 \text{ Gt year}^{-1}$ and from the salinity data at $14.7 \pm 4.6 \text{ Gt year}^{-1}$ [Wong *et al.*, 1998]. However, the same melting rate should be obtained from calculations based on either temperature or salinity. The fact they do not suggests that Wong *et al.* [1998] incorrectly estimated the currents across the front of the AIS. More recent calculations of the basal melt rate from CTD observations done at a higher resolution than Wong *et al.* [1998] suggest a melt rate of $\sim 46 \text{ Gt year}^{-1}$ ¹, when accounting for heat required to warm the glacial ice from its interior temperature [$\theta_{ice} = -20^\circ \text{C}$ Jenkins, 1991], to the local melt temperature.

It is clear that the oceanographic estimates are sensitive to sample resolution that can be obtained across the front of ice shelves. CTD sections can potentially miss part of the narrow outflowing ISW and inflowing HSSW, leading to underestimate the net basal melting, when compared to the glaciological derived estimates. Net basal melting estimates derived from salinity can also be corrupt because salinity sensors are prone to fouling with frazil crystals. There are direct observations of frazil at depths from the surface to 125 m at the west side of the front of the

¹ Leffanue (unpublished) from 2000/01 Aurora Australis cruise data.

AIS [Penrose *et al.*, 1994]. From the amount of supercooling present in the water, Penrose *et al.* [1994] calculated a frazil ice volume fraction of 1.3×10^{-3} , or about ~ 1.2 kg per m^3 of seawater (assuming an ice density of 920 kg m^{-3}). Depth sounding measurements during the 2000/01 cruise also showed a strong return echo at about 200-300 metres below the surface, in a region where the bathymetry is known to be deeper than 500 m^2 . The strong return echo was attributed to a density contrast that is created between water without frazil overlying water with frazil.

However, in light of the simulations presented in Chapter 4, the difference between glaciological and oceanographic derived estimates of net basal melting can be reinterpreted to be due to the export of frazil from beneath the ice shelf. The glaciological estimates can be explained to be higher because the component of refreezing that actually remains as suspended frazil crystals will not be 'seen'. The difference between the glaciological and the most recent oceanographic derived estimates is $\sim 5 \text{ Gt year}^{-1}$. The average frazil concentration can be found by dividing the mass estimate of frazil by the volumetric flow rate of ISW, which assumes that the ISW plume is laden with frazil crystals. Given that the volumetric flow rate of ISW, estimated in Chapter 5, is $\sim 5 \times 10^5 \text{ m}^3 \text{ s}^{-1}$, then the concentration of frazil crystals would be 0.33 kg m^{-3} . This simple calculation, in light of the direct observations of frazil, show that the total frazil flux from beneath the ice shelf is a major component worth considering when calculating net melting using glaciological observations. The estimates of net basal melting using salinity and potential temperature can also be improved by considering the heat required for warming ice to the *in situ* melting temperature. The difference in mass loss between the glaciological and oceanographic derived estimates is primarily due to a combination of frazil ice transport and latent heat flux into the ice shelf base.

6.3.3 Model estimates

The annual averaged net loss of ice due to basal melting from the reference model is $\sim 45.63 \text{ Gt year}^{-1}$. The simulated net mass loss agrees within the uncertainty of the glaciological estimate of $55.6 \pm 12.6 \text{ Gt year}^{-1}$. The results are summarised in Table 6.3 and compared with previous modelling studies.

The simplest model used a two-dimensional overturning model with several configurations representative of the AIS cavity [Hellmer and Jacobs, 1992]. Results from this study indicated a mean melting rate as high as $0.65 \text{ m ice year}^{-1}$, equal to the removal of 23 Gt year^{-1} of basal ice using the much smaller ice shelf area utilised in their model. Williams *et al.* [2001] used a three-dimensional numerical ocean model to simulate the ocean cavity beneath the AIS with two different boundary conditions. The two simulations gave net melt rates of 5.8 Gt year^{-1} and $18.0 \text{ Gt year}^{-1}$, respectively. Both models showed basal freezing of several Gt year^{-1} . Hellmer [2004] also reported a spatial average basal melting rate of $0.35 \text{ m ice year}^{-1}$, and the total basal mass loss of $17.65 \text{ Gt year}^{-1}$ beneath the AIS, using a coupled ice-ocean model. Studies by Hunter *et al.* [2004] showed, using OzPOM that tides enhanced the net basal mass loss rate from 11.4 to $21.9 \text{ Gt year}^{-1}$. However, this model used the default pressure gradient algorithm that, as was

² personal communication: Mark Rosenberg, ACE CRC, 2007

Table 6.3: Comparing the observed and simulated annual averages of Freshwater Flux (FWF), Total Basal Mass Loss (BML) from ocean models used to simulate the cavity beneath the AIS. An ice density of 916 kg m^{-3} is assumed. $1 \text{ mSv} = 1000 \text{ m}^3 \text{ s}^{-1}$.

Study	Area ($\times 10^4 \text{ km}^2$)	m' (m ice year^{-1})	FWF (mSv)	BML (Gt year^{-1})
Observations	6.1	0.91 ± 0.21	1.76 ± 0.4	55.6 ± 12.6
Reference Model	6.2	0.74	1.45	45.63
<i>Hunter et al.</i> [2004]	6.0	0.19–35.6	0.36–0.69	11.4–21.9
<i>Hellmer</i> [2004] [†]	5.6	0.35	0.55	17.65
<i>Williams et al.</i> [2001]	5.6	0.11–0.35	0.20–0.62	5.6–18
<i>Hellmer and Jacobs</i> [1992]	3.5	0.65	0.73	23

[†] Results are from a circum-Antarctic ocean model using an assumed ice density of 917 kg m^{-3} .

shown in Chapter 3, leads to spurious circulation and melt/freeze.

Previous simulations varied widely from the reference simulation on the choice of model type, cavity geometries, and forcing fields. The models are all similar in that the ice-ocean boundary conditions are variations of the three-equation basal ice-ocean boundary conditions outlined in Chapter 2, with the exception of *Hunter et al.* [2004] who used a two-equation parametrisation. In all cases, the previous models are all much lower than the net basal mass loss estimates suggested by the observations. The good performance of the reference model is attributed to cavity geometry, the inclusion of realistic seasonally varying boundary conditions, and the inclusion of tides.

6.3.4 Local melt/freeze rates

The annual averaged spatial pattern of melting and freezing for the reference simulation is shown in Fig. 6.9. The freeze rates are the sum of the contributions from both direct basal refreezing and frazil accretion. Consistent with understanding of the circulation patterns beneath the AIS, areas of melting occur primarily along the east and south of the AIS and areas of refreezing primarily occur along the west. The inflow causes areas of melting adjacent to Gillock Island that correspond to a rise of the sea floor. The strongest regions of freezing are located in regions where the ice draft contains depressions such as north of Budd’s ice Rumples, near Jetty Peninsula and near to the outflow region of the ice shelf.

The melting rate for each model cell beneath the AIS is shown in Fig.6.9.b and shows that the strongest melt occurs where the ice is deepest. A comparison of the model melt/freeze with observational estimates is shown in Table . The maximum amount of melt that can occur in this region exceeds $30 \text{ m ice year}^{-1}$. These results are in strong agreement with a study of local basal melting and freezing rates, using glaciological flux gate estimates, that show the mean melting rate near the southern grounding line is $23 \pm 4 \text{ m ice year}^{-1}$ [*Wen et al.*, 2007]. That study also showed that melting decreased rapidly downstream, and transitioned to refreezing at around 300 km from

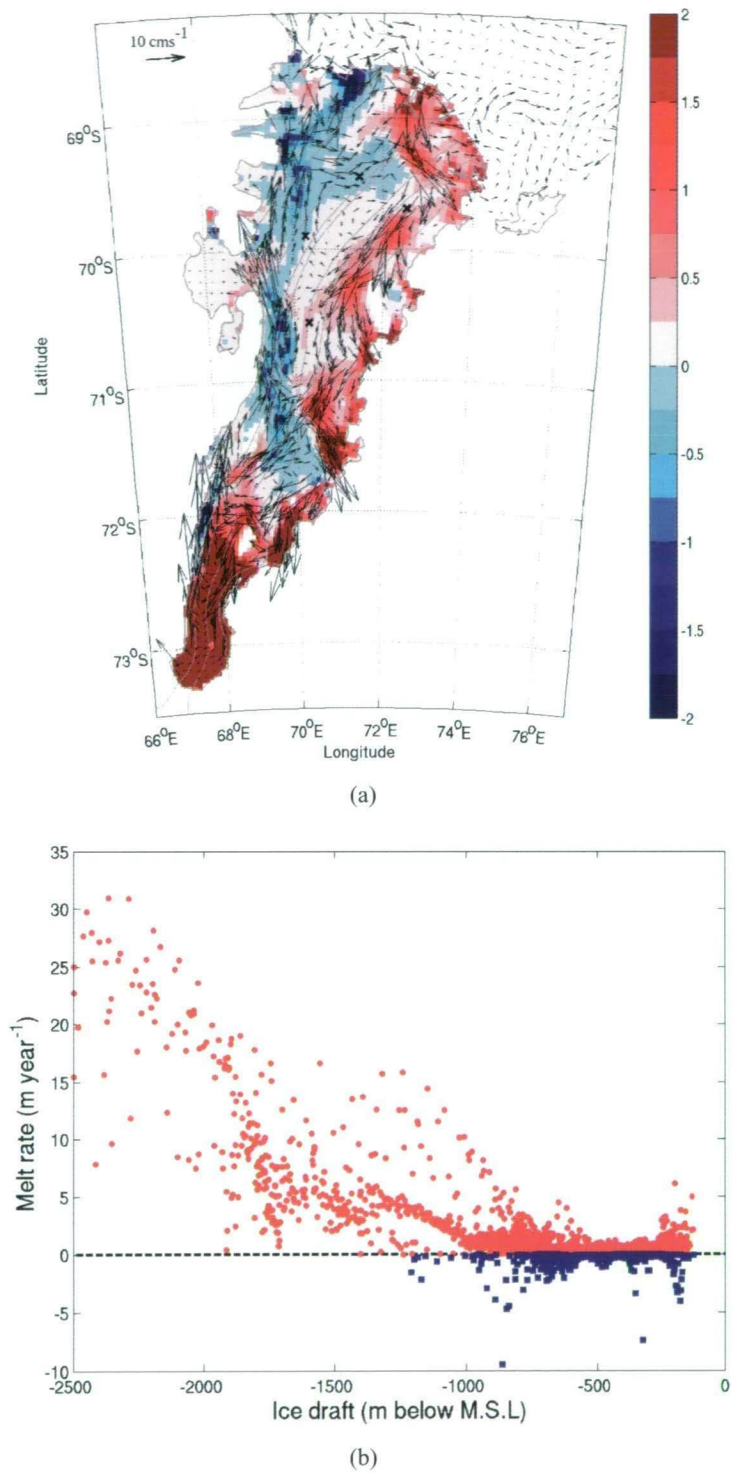


Figure 6.9: (a) The annual averaged pattern of melting (positive) and freezing (negative) superimposed with depth average currents, and (b) the melt rate from (a) plotted against ice draft thickness.

Table 6.4: Summary of local estimates of melt/freeze compared to the model results (m ice year^{-1}). The model values are an area average with size similar to that used in previous studies. The bracketed values are the highest rates observed in the region.6.3.4

Melt rate near southern grounding zone		
<i>Wen et al.</i> [2007]	Mass balance	23.5 ± 3.5
<i>Rignot</i> [2002a]	InSAR	31 ± 5
Reference model	Modelling	23 (32)
Freeze rate near $70^\circ\text{E}, 70^\circ\text{S}$		
<i>Wen et al.</i> [2007]	Mass balance	1 ± 0.5
<i>Craven et al.</i> [2009]	Drilling/Boreholes	1.1-1.3
Reference model	Modelling	1.2 (4)

the southern extremity of the AIS in agreement with the reference model results. Freezing rates along the Mellor, Lambert and Fisher flowbands ranged from $0.5\text{--}1.5 \pm 0.2 \text{ m ice year}^{-1}$. Estimates based on InSAR data yielded local melt rates of $31\text{--}32 \pm 5 \text{ m ice year}^{-1}$ near the southern grounding line [*Rignot and Jacobs*, 2002; *Rignot*, 2002b]. Recent results from direct observations showed that local freezing between Jetty Peninsula and AM04 must be $\sim 1.3 \pm 0.2 \text{ m ice year}^{-1}$ to account for the amount of marine ice encountered at AM04 [*Craven et al.*, 2009]. Similarly, the average rate of accretion between AM04 and AM01 that is required to account for the observed marine ice at AM01 must be $\sim 1.1 \pm 0.2 \text{ m ice year}^{-1}$.

The area of refreezing to the south of Budd's Rumples against the western model boundary does not exist in the observations of marine ice thickness [*Fricker et al.*, 2001]. East-west cross sections of the ice draft across the refreezing zone (not shown) show that the ice draft shoals towards the western boundary. This would mean that ISW that is flowing along the western boundary can become supercooled as it rises into the shallow artefact in the ice draft, causing refreezing to occur. The artefact in the ice draft along the western boundary is likely due to the grounding line position being misplaced too far west in the interpolation of the ice draft. Future studies can investigate the robustness of the grounding line placement.

Marine ice accretion

It has been shown that the reference model's ability to simulate the net basal mass loss rates and local estimates of melting and freezing compare favourably with the available observations. However, the ability to simulate marine ice thickness in rough agreement with observations has been suggested to be a strong test of a model's ability to simulate the basal melting and freezing rates [*Holland*, 2002]. The aim of this Section is to calculate the thickness of the marine-ice layer by utilising the total thickness, horizontal flow field and basal accumulation rate. This technique, based on the principle of conservation of mass, has been previously described by *Budd et al.* [1982], and applied to Antarctic ice shelves [for example, *Determann*, 1991; *Williams et al.*, 2001]

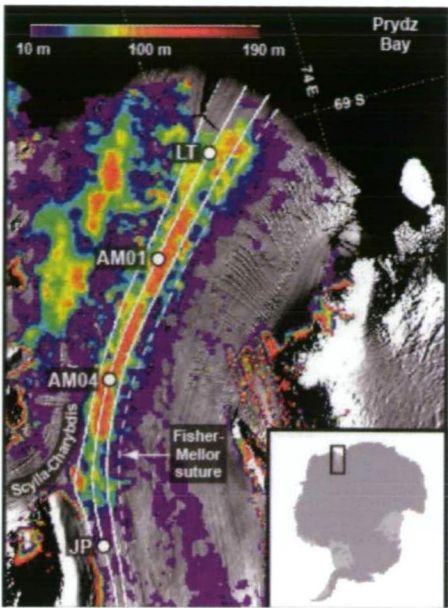


Figure 6.10: The AIS from the MODIS Mosaic of Antarctica [Scambos *et al.*, 2007] showing sites discussed in the text. From upstream: Jetty Peninsula point (JP), where marine ice band accretion begins; AM04 and AM01 boreholes; and the Loose Tooth point (LT). Also shown are flowbands from tributary glaciers, the location of the Fisher-Mellor ice shelf profile flowline shown in Fig. 2 (dotted), and colour shading (scale top left) of the estimated marine ice thickness [Fricker *et al.*, 2001]. For scale the boreholes AM01-AM04 are approximately 68 km apart. The Budd Ice Rumples are south of the lower extremity of the area shown 140 km upstream along the flowline from JP. Taken from Craven *et al.* [2009]

and simplified studies [Holland, 2002].

Glaciological derived estimates of velocity and strain thinning from Young and Hyland [2002] are used to calculate the marine ice accretion along a flowline. The flowline used for the comparison is shown in Fig. 6.1 as the thick grey line. The southernmost point along the flowline where the ice shelf shows zero ice accretion is at the point north of Budd’s Rumples and was used as the starting point for the integration. Two boreholes were drilled along approximately the same glacier flowline, which allows direct observations of marine ice thickness to evaluate the integration. The direct observations of marine ice thickness were converted to a consolidated ice equivalent using the appropriate marine ice porosity for each site as reported in Craven *et al.* [2009]. The marine ice thickness along the flowline from Fricker *et al.* [2001] with error bars of ± 30 m are also compared with both the direct observations and the reference model results. The map of marine ice, labelled with relevant features, is shown in Fig.6.10.

The marine ice thickness estimates along the flowline, derived from the model’s pattern of basal melting and freezing, are shown in Fig. 6.11. The majority of the marine ice accretion is due to the precipitation of frazil. Generally, the reference model deposits marine ice glacially further upstream than is suggested by the marine ice map of Fricker *et al.* [2001]. At AM04, the reference

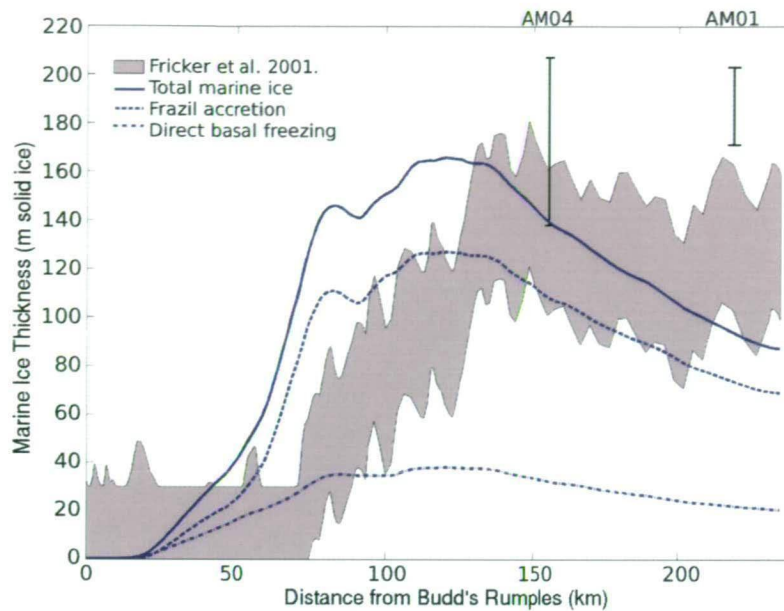


Figure 6.11: Estimate of marine ice thickness for the reference simulation for the ice shelf flowline that passes through boreholes at AM04 and AM01. The vertical solid line at about 100 km from JP is from direct observations through a borehole drilled at site AM04. The error in the borehole measurements represents conversion from the measured thickness to metres of solid ice equivalent. The error bars are measures of the uncertainty in estimates of the marine ice porosity. The thick shaded area is from *Fricker et al.* [2001].

model shows marine ice thicknesses comparable to both the estimates from remote sensing and direct observation. At AM01, the reference model shows ~ 80 m of marine ice compared to $\sim 141 \pm 30$ m of ice from *Fricker et al.* [2001] and a solid ice equivalent of 187 ± 16 m of consolidated ice.

As the glacial flowlines run roughly parallel with the direction of the frazil laden ISW, most of the offset can be explained by frazil being deposited from the water column about 40-50 km too far south along the flowline. Even considering the offset, the model still underestimates the marine ice at AM01 by about 50 m. Overall, the amount of marine ice accretion in the reference simulation is about right. It is remarkable that a frazil model with only 5 size classes can lead to approximately both the right spatial pattern and magnitude of accretion. However, the low deposition in the northern part of the flowline may be due to a number of reasons, such as the inability to model flow through marine ice. Observations have shown that up to 100 m of the lower part of the marine ice beneath the AIS can be in hydraulic connection with the ocean [*Craven et al.*, 2009].

6.4 Seasonal Cycles of Melt/Freeze and Circulation

The area averaged seasonal cycle of net basal melt rate is shown in Fig. 6.12. The net melt rate exhibits a strong seasonal cycle with the highest rates, of ~ 0.8 m ice year $^{-1}$, occurring in the middle of the year. The high inter-annual area averaged melt rate variability of $\sim \pm 0.1$ m ice

year^{-1} , shown by the grey dots, is due to tidal oscillations.

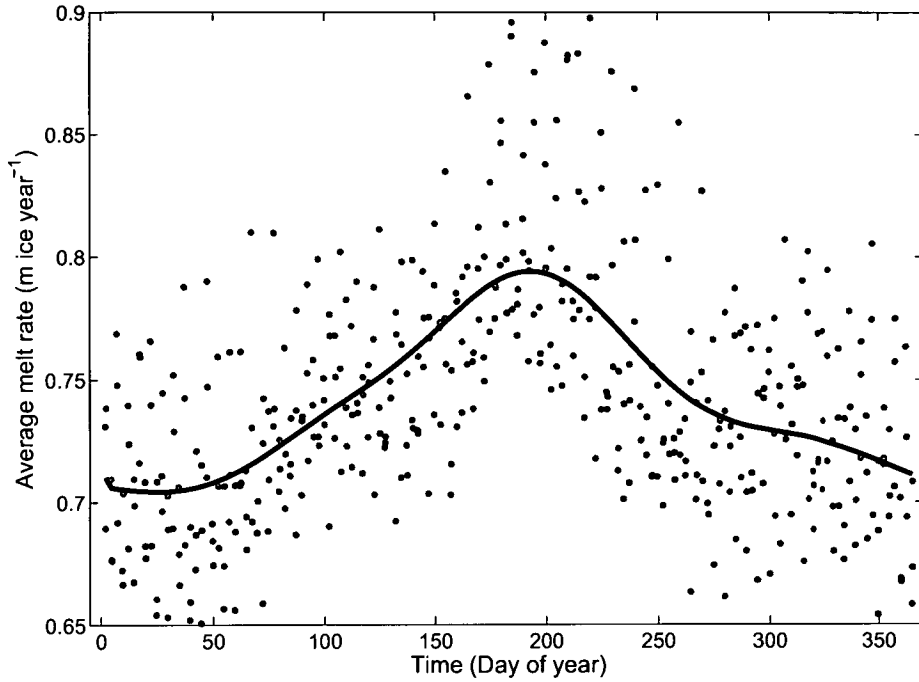


Figure 6.12: The seasonal variation of the area averaged melt rate (m ice year^{-1}), averaged for each month (black line). The raw 2.5 day model output shows tidal aliasing (grey dots).

Beneath the ice shelf, a strong seasonal cycle is characteristic of both the observations and the model and is stronger towards the open ocean. Fig. 6.13 shows the melt/freeze variance and variance ellipses. The boundary current of ISW is largely a stable feature on seasonal time scales. The variability of the basal melt rates are $\sim \pm 2 \text{ m ice year}^{-1}$ in regions along the front of the AIS and at regions along the eastern boundary. The major variability in the currents occur beneath the ice shelf within 100 km of the open ocean. Borehole sites AM01 and AM02 are within the region of high current variability, which is reflected in the seasonal cycles of temperature and salinity, compared to sites AM03 and AM04. The north-west to south-east orientation of the semi-major axis of the variance ellipses indicates that the response of the u and v components are negatively correlated.

The residual velocities are calculated using velocity variances that were calculated using the final 3 years output of 2.5 days resolution for the residual depth averaged velocities, $\overline{u'}$ and $\overline{v'}$. From these data the north/east velocity variance ($\overline{u'^2}, \overline{v'^2}$) and the covariance ($\overline{u'v'^2}$) are calculated. The magnitude and direction of the variability are represented using variance ellipses [see Preisendorfer, 1988]. The direction α of the axis of principal variability, measured

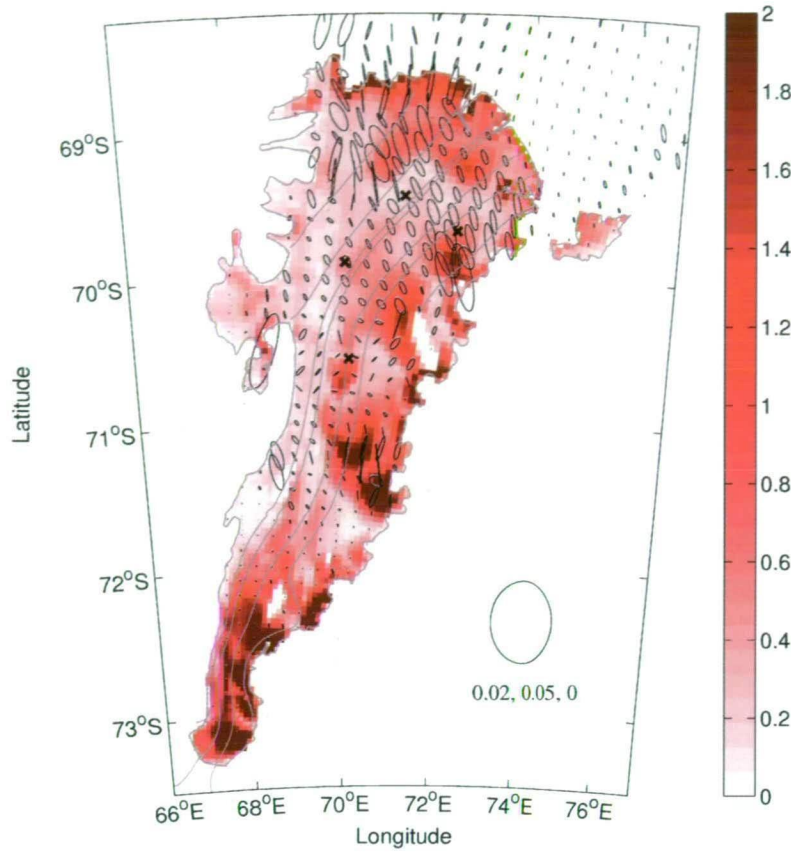


Figure 6.13: Melt/freeze variance (m ice year^{-1}) and velocity variance ellipses over 3 years of simulation. The variance ellipses of the depth averaged velocity for every 3rd grid cell are also shown. The scale ellipse has a semi-major axis of $0.02 \text{ m}^2 \text{ s}^{-2}$, a semi-minor axis of $0.05 \text{ m}^2 \text{ s}^{-2}$ and is orientated north.

anticlockwise from east is,

$$\tan \alpha = \frac{\sigma_{maj} - \overline{u'^2}}{\overline{u'v'^2}} \quad (6.1)$$

where the variance along the major axis, σ_{maj} , is

$$\sigma_{maj} = \frac{\overline{u'^2} + \overline{v'^2} + \sqrt{(\overline{u'^2} - \overline{v'^2})^2 + 4(\overline{u'v'^2})^2}}{2} \quad (6.2)$$

and along the minor axis, σ_{min} , is

$$\sigma_{min} = \overline{u'^2} + \overline{v'^2} - \sigma_{maj} \quad (6.3)$$

Anisotropic flow is represented by an elongated ellipse with the principal direction of the velocity variance aligned with the direction of the major axis. The orientation of the ellipse depends on the covariance ($\overline{u'v'^2}$); the major and minor ellipse axes define the coordinate system in which $\overline{u'}$ and $\overline{v'}$ are uncorrelated. Ellipses with a major axis orientated in the north-east/south-west are

positively correlated and ellipses orientated to the north-west/south-east are negatively correlated [Wilkin and Morrow, 1994; Morrow *et al.*, 1994].

The AM01 borehole is located at a region of primarily inflowing waters that exhibit high seasonal variability. Smoothed potential temperatures and salinities in the ice shelf cavity are roughly out of phase over a seasonal cycle at AM01, with temperature falling as salinity rises, and *vice versa*. This is an indicator that inflow of HSSW dominates the average properties of the ocean near the front of the AIS. The exchange with the open ocean is stronger during the summer months when the average temperature of the cavity rises and the average salinity falls. The water masses beneath the AIS are rarely warmer than the surface freezing point. Instrumentation from boreholes AM01 and AM02 show the largest seasonal variability in both potential temperatures and salinities.

This signature reflects the mixture of LSSW, MCDW and some surface water that enters the cavity along with HSSW during the summer period. Although the less dense water masses do not penetrate far into the cavity, a large proportion of the cavity volume lies close to the ice front where seasonal variations are strong.

6.4.1 Prydz Bay gyre

From the reference model, the seasonal cycle of the circulation in Prydz Bay can be described as follows: in the austral summer, the circulation in the region is characterised by a strong westwards flowing coastal current, with temperature and salinity properties of LSSW in bottom layers and SSW characteristic in the upper part of the water column. The inflow from the open ocean to the Prydz Bay depression follows the bathymetric contours, whereby they deflect westward and become part of the coastal current. The circulation associated with this current forms a cyclonic gyre in Prydz Bay. Some of the waters contained in the gyre exit through the Prydz Bay channel and becomes part of a westward flowing slope front current. The northward flowing component of the gyre, in the west of Prydz Bay contains ISW that has exited the cavity along the western boundary.

However, in the late austral winter, the coastal current, which now has properties associated with winter water formation is diverted from the coast, in the vicinity of the Barrier polynya, and flows north-westward through the Prydz Bay channel and becomes a westward flowing slope front current. There is some recirculation of these water masses which entrain dense water formed from both the Barrier and McKenzie polynyas that can enter the cavity beneath the AIS. It is clear that the primary driver of melting beneath the ice shelf is the HSSW formed during winter sea-ice growth. The shutdown of the gyre circulation may be important to allow the southward migration of HSSW to drain beneath the cavity, rather than be advected offshore.

This change in the circulation in Prydz Bay is highlighted by the time history of eastward velocities shown in Fig. 6.14. The sections shown are the time evolving zonal velocity field along $\sim 76^\circ\text{E}$ for the mid-depth layer (b) and the bottom layer (c). The bathymetry along the transect is shown in (a). The strong coastal current at 69.5°S , can be seen in both (b) and (c) to be active

during the summer months, where negative values of velocity indicate flow along the coastline from east to west. In early winter, the coastal current, along the same latitude, changes direction.

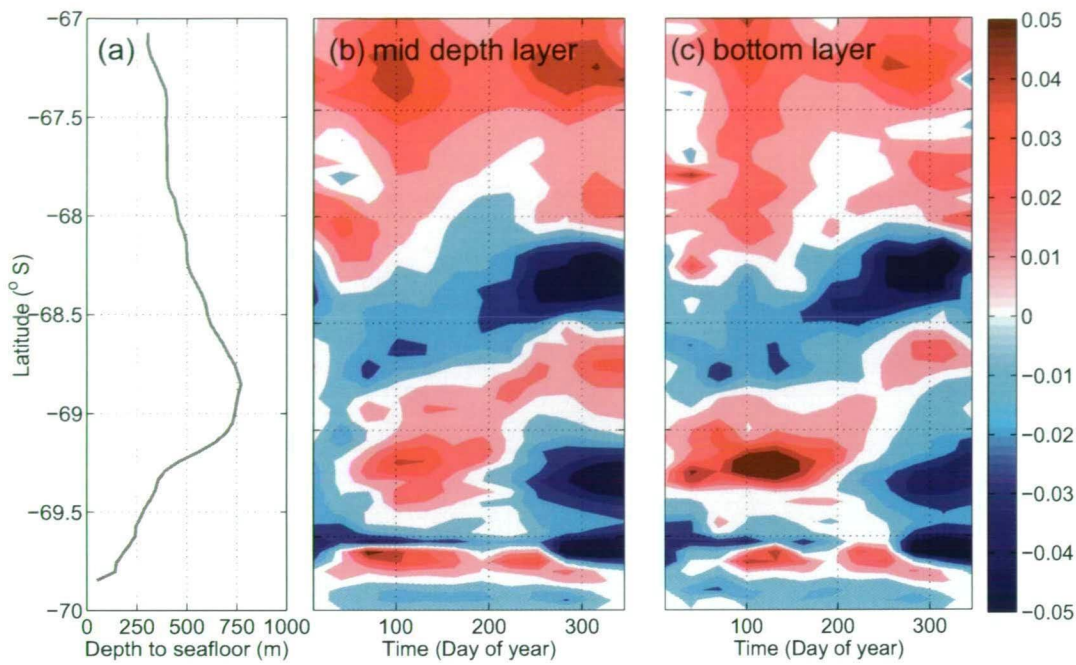
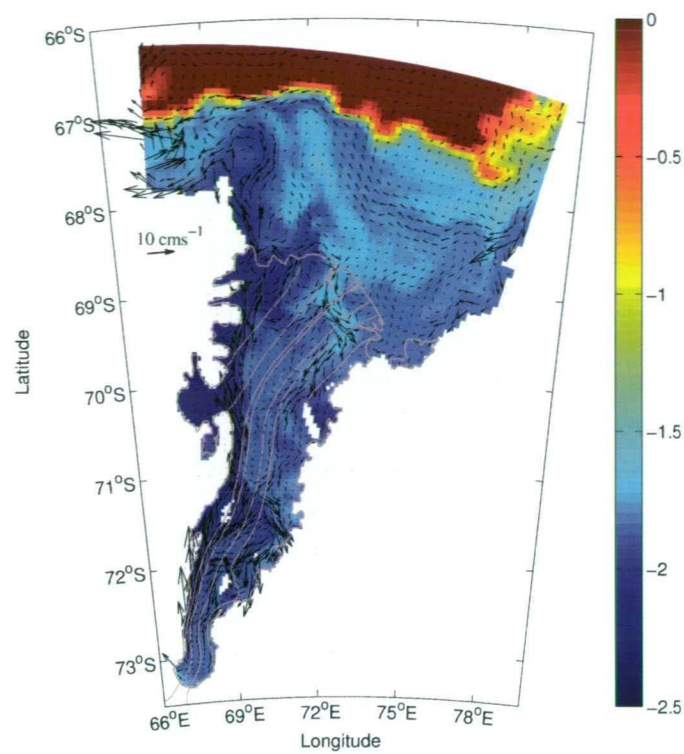


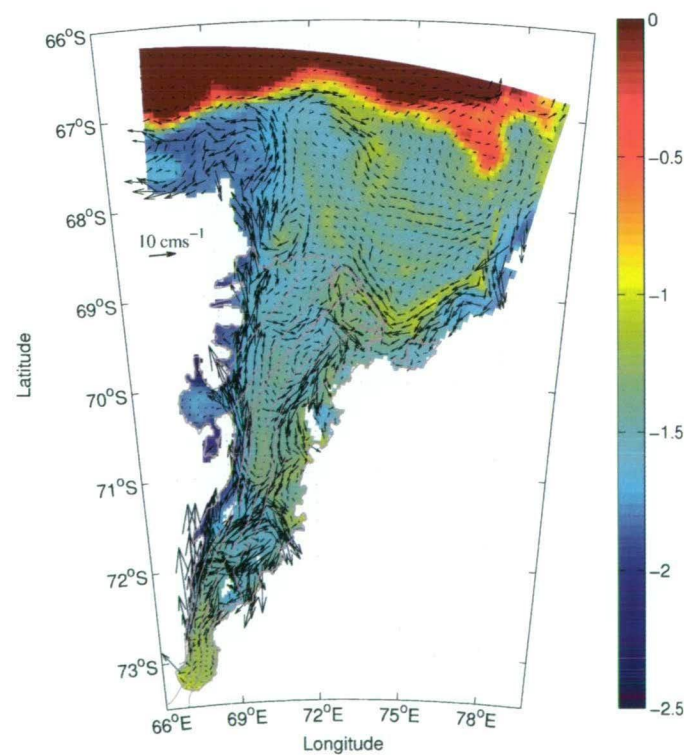
Figure 6.14: Time evolving velocity fields (m s^{-1}) along $\sim 76^\circ\text{E}$ for the mid-depth (b) and bottom (c) model layers. The model bathymetry along the transect is shown in (a). Positive features indicate flow from west to east.

Evidence from a simulation to test the control of the Barrier polynya on the general circulation within Prydz Bay is shown in Fig. 6.15. The simulation (b) was modified by decreasing the surface fluxes associated with the region of the Barrier polynya by 90%. The model with reduced Barrier polynya activity shows that the Prydz Bay gyre is maintained during the winter months compared to the reference simulation (compare Fig. 6.15.a and b). The more realistic scenario (a) shows that the effect of the shutdown of the Prydz Bay gyre is to reduce the advection of warmer MCDW onto the shelf region.

The fact that the gyre is only present when the Barrier polynya is inactive suggests that the seasonal circulation change is not wind driven. Simulations with the wind field turned off (not shown) did not change the main characteristics of the seasonal circulation structure present in the reference simulation. Furthermore, observations of the clockwise circulation of sea-ice in early summer using drifter buoys could not be reproduced using an atmospheric circulation model [Watterson *et al.*, 1995], with the conclusion that the ice flow in the vicinity of Prydz Bay is primarily driven by oceanographic currents rather than winds [Heil and Allison, 1999]. However, the polynya activity is closely related to the strength and direction of the winds. The results of the simulations suggest that the activity of the Prydz Bay gyre is primarily controlled by the negative



(a) Reference simulation



(b) Reference without Barrier polynya

Figure 6.15: Comparing the late winter temperature of the mid-depth sigma layer overlain with depth averaged currents between the reference simulation and a simulation that has had the fluxes associated with the Barrier polynya reduced by 90%.

buoyancy associated with dense water production from polynyas.

Dense water created in the polynya acts to block the main inflow from the Prydz Bay channel. Specifically, the Barrier polynya is located at the junction where waters flowing into Prydz Bay during summer meet the westward flowing coastal current. The activity of the Prydz Bay polynyas during winter actually shields the ice shelf from the main brunt of warm MCDW. The maximum melt rates of the AIS are still primarily correlated with the formation of dense waters in the sea-ice region at the eastern side of Prydz Bay. MCDW that is allowed into the Prydz Bay region during summer does not have the requisite density to be able to sink into the deeper parts of the cavity. It is not until the Prydz Bay gyre shuts off in early winter, combined with dense water production from sea-ice growth in the region, that MCDW mixes with HSSW and becomes dense enough to sink into the cavity beneath the AIS. The dense waters then have the capacity to melt the underside of the ice shelf, primarily in the inflow regions to the eastern side of the cavity. The lag between the shutdown of the Prydz Bay circulation and the time of maximum averaged melt rates is approximately 2 months.

The model results are confirmed in composite images developed over various times of the year from the thermal infra-red images from the MODerate resolution Imaging Spectroradiometer (MODIS) satellite instrument. The composite images are comprised of suitable images measured in the thermal infra-red wavelength ($11.03\ \mu\text{m}$) [Parkinson, 2003]. The images are quality controlled to yield up to 36 images for each composite image shown in Fig. 6.16.

The analysis technique was initially developed for the detection of fast ice. Due to the relatively static nature of fast ice and the accurate geo-location of MODIS data, the compositing process preserves the sharp edges at the shear zone between pack ice, open water and fast ice. Thus, edge detection algorithms or other change detection methods should be easily applicable to fast ice and polynya detection using composite images generated this way [Fraser *et al.*, 2009]. Fast ice is shown as areas with relatively low levels of surface brightness and polynyas are shown as areas with high levels of surface brightness in Fig. 6.16.

Importantly, it was seen that this technique also allows the detection of ice motion. The images generated for the Prydz Bay region show a blurred circular pattern during the early time of sea-ice growth, as seen in Figs. 6.16a and b. Tracking features in the individual images that make up the composite images when the gyre is present shows that the sea-ice is rotating clockwise about a point located at $\sim 75^\circ\text{E}$, 68°S . The clockwise circulation of sea-ice decreases as the Barrier polynya increases in activity until it completely stops later in the year (see Fig. 6.16.b and d).

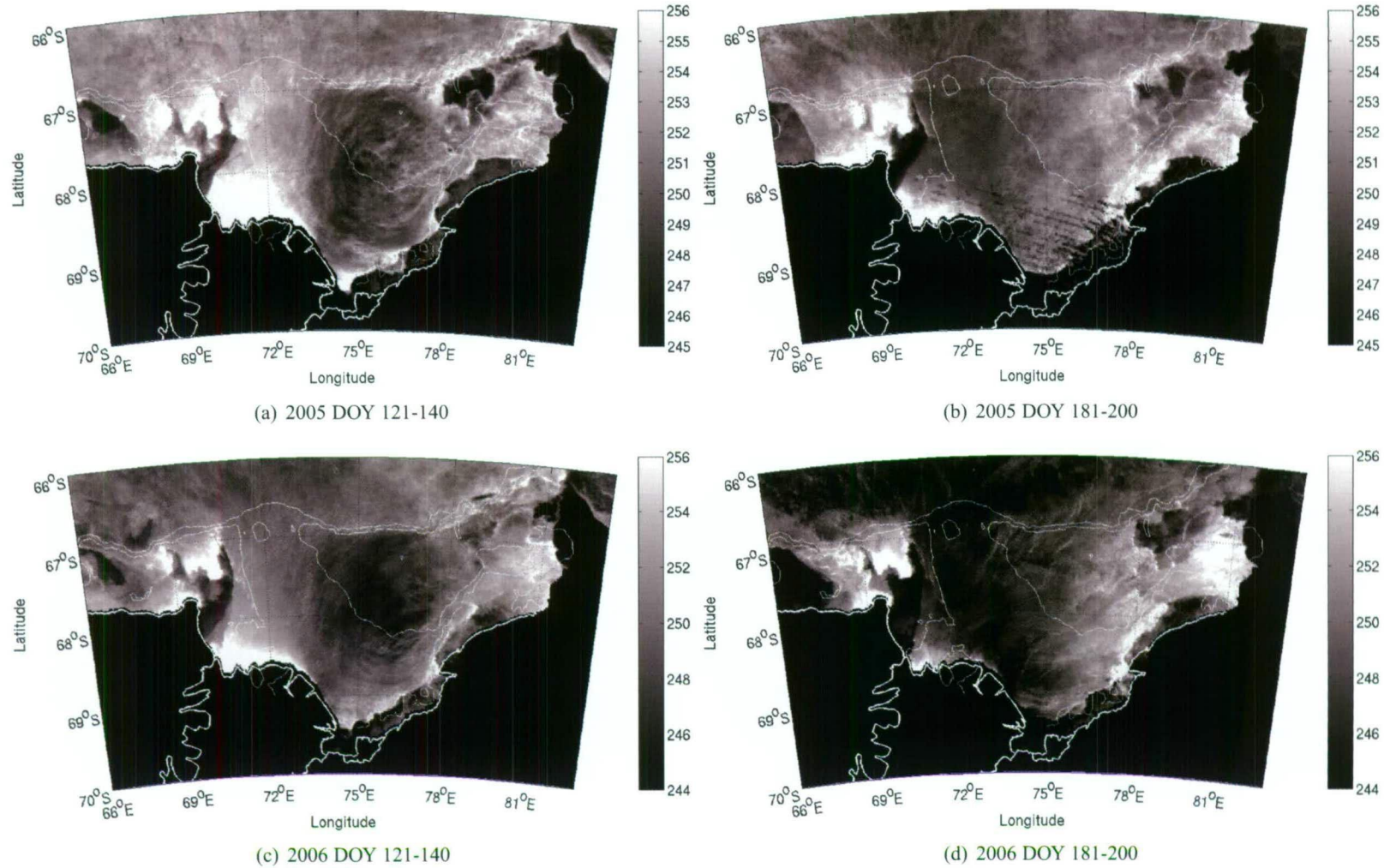


Figure 6.16: Examples of sea-ice circulation patterns when the Barrier polynya is strong (right panels) and weak (left panels) during two periods in the year 2005 (top panels) and two periods in the year 2006 (bottom panels). Each composite image was created by averaging viable thermal infra-red satellite images from the MODIS instrument (Channel 31, wavelength= $11.03\mu\text{m}$) during the 20 day of year (DOY) period [Fraser *et al.*, 2009]. The colour scales represents the brightness temperature ($^{\circ}\text{K}$). The 500 and 1000 m bathymetry contours are marked.

It is not clear from the images if it is the advection of newly formed sea-ice, created in the Barrier polynya, that disrupts the surface expression of the circulation feature. However, interpreting the circulation features visible in the composite images in light of the conclusions of *Heil and Allison* [1999] and the results of the simulations presented here suggests that the sea-ice is responding to the ocean circulation in the region that is driven by dense water production from polynyas. In summary, the model results show that the direction and strength of the Prydz Bay gyre is only effected by the strength of the Barrier polynya. However, the comparison of composite MODIS images suggest that it is the relative strength between the McKenzie and Barrier polynyas that drive the circulation in Prydz Bay.

6.4.2 Dense water export

The strong seasonality of the westward transport of AABW, ISW and HSSW is shown in Fig. 6.17. The transport of water masses is calculated using the θ, S and ρ properties shown in Table 6.1. The AABW water production only accounts for flow that has made it off the continental shelf and onto the continental slope. The westward transport of dense water with AABW characteristics along the slope front varies strongly over the season.

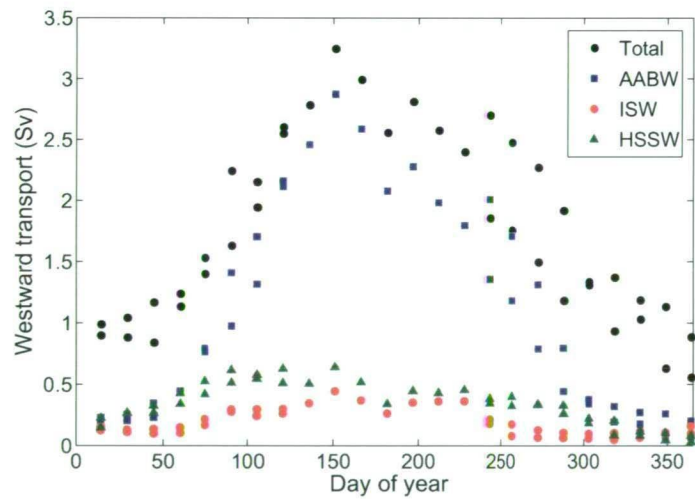


Figure 6.17: The annual-averaged westward transport (sv) of watermasses on the continental slope, for AABW (blue), ISW (red), HSSW (green) and the Total (black).

6.5 Sensitivity Studies

The use of the three-equation parametrisation of the ice shelf-ocean interface is becoming commonplace in regional polar ocean model applications. However, to the knowledge of the author, there is only one global climate model which includes the effects of glacial ice-ocean interaction *Losch* [2008]. Furthermore, models that include frazil are limited to plume studies [for example, *Holland and Feltham*, 2006]. However, it is clear that including the processes involved in

ice shelf-ocean interaction is important for providing robust projections of the evolution of the ice sheet and its impact on sea level and freshwater budgets under different global and regional climate scenarios. There are still many processes at the ice-ocean boundary that need further examination before climate predictions can become more reliable. Two key processes are investigated here:

- The total freezing process, as has been shown, depends on the parametrisation of frazil. In Chapter 4, frazil was also shown to affect circulation due to the modifications on the water properties. In Chapter 4 it was also shown that the removal of supercooling by frazil formation can actually lead to a melting enhancement. These simplified studies are tested here using the AIS model.
- Heat exchange at the ice/ocean interface has a major impact on the global ocean heat and freshwater budget as water masses are formed and modified in the sub-ice shelf cavity [Wong *et al.*, 1998; Williams *et al.*, 2001]. Mixing of modified Circumpolar Deep Water (CDW) near the continental shelf break with locally-formed High Salinity Shelf Water (HSSW) may contribute to the formation of Antarctic Bottom Water (AABW) which is a key driver in the global thermohaline circulation [Jacobs, 2004].

6.5.1 AABW formation

The net seasonal transport of AABW from the westernmost boundary of the model domain was calculated for each simulation of the model. The results are shown in Fig. 6.18. The production of bottom waters by coastal polynyas is strongly moderated by proximity to the ice shelves (see Fig. 6.18). In particular, it is shown here that models that do not include ice shelf ocean interaction will overestimate AABW production by as much as 280%. The production of AABW in the simulation without ice shelves (dashed line) continues throughout the year, whereas, the reference model (solid line) and the model without frazil (dot-dashed line) both show that the production of AABW is significantly reduced during the summer months.

The results confirm the hypothesis suggested in the conclusions of Chapter 4: that ice shelf-ocean models containing frazil dynamics will lead to an enhancement of dense water production. Fig. 6.18 shows that ice shelf-ocean models that do not include frazil ice dynamics can underestimate bottom water formation by 14%. ISW originating from the AIS has an important influence on AABW production in the region.

The potential temperature and salinity relationship along $\sim 69^\circ\text{E}$ is shown in Fig. 6.19. It is clear that the model without ice shelves (red) has a higher formation of dense water masses, both HSSW and AABW, compared to the reference simulation (blue). The model without frazil (green) underestimates the dense water production compared to the reference simulation.

The basal melt rates can be indirectly affected by the presence of frazil due to the modifications on the water properties, particularly the temperature. In Chapter 4 it was shown that the removal of supercooling by frazil formation can actually lead to a melting enhancement. In this application of the AIS model, it is found that the net melting rate in the model with frazil is decreased (see Table 6.5).

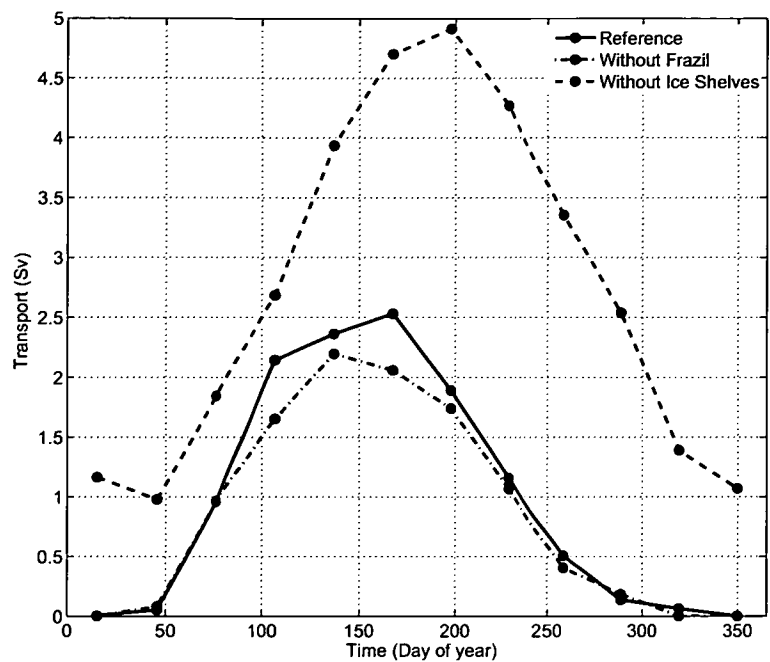


Figure 6.18: Seasonal transport of AABW (Sv) for the reference model (solid line), the model without frazil ice (dot-dashed line) and the model without ice shelf thermodynamics (dashed line).

Table 6.5: Model estimates of the various basal mass balance components for the AIS. Net = Melt-Freeze (Gt year^{-1}). The total refreezing for the reference experiment is comprised of $1.64 \text{ Gt year}^{-1}$ of direct basal refreezing and $3.62 \text{ Gt year}^{-1}$ of frazil accretion.)

Model	Net	Melt	Freeze
Reference	45.63	50.89	5.26
Without Frazil	50.9	52.97	2.07
Glaciological Observations	55.6 ± 12.6	61.6 ± 12.6	$\sim 6^\dagger$

[†] Personal communication: Roland Warner, ACE CRC (2009)

The lower melting rate in the AIS model simulations is attributed to the strong difference in the basal melting and freezing patterns (see Fig. 6.20). The model with frazil (a) has much higher regions of net accumulation than the model without frazil (b). Hence, the enhanced melting presented in Chapter 4 was due to the ability of frazil to remove supercooling from the recirculated ISW. In the simplified studies it was found that the water masses exiting the cavity did not fully equilibrate with the surface forcing before being moved into the ice shelf cavity. In the simplified models with frazil, the water masses entering the cavity were warmer than the models without frazil.

Here, the circulation pattern of the domain means that outflowing waters from beneath the ice

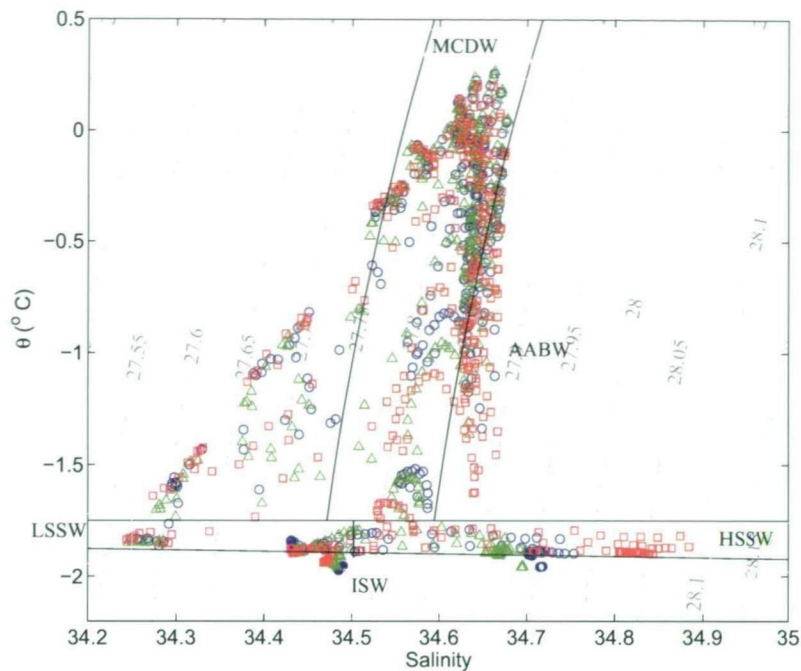


Figure 6.19: Distribution of July average potential temperature and salinity for the reference model (blue circles), the model without frazil (green triangles) and the model without ice-ocean thermodynamics (red squares) along a latitudinal transect located at $\sim 69^{\circ}\text{E}$. The black lines divide the water masses using the constraints in Table 6.1.

shelf exit the domain. The water masses that enter beneath the cavity in both the reference model and the model without frazil have about the same amount of heat. As such, the lower melting rate shown in the reference model is attributed to the enhanced vertical mixing of supercooled water with the ambient water due to the associated brine rejection process during frazil formation. Subsequently, the water masses that move into the deeper parts of the cavity under gravity are slightly cooler than the same water masses in the model without frazil. The reduction that this effect has on the basal melting processes is shown in Fig. 6.21.a. The model without frazil has higher rates of melting near the southernmost parts of the AIS.

6.6 Concluding Remarks

Using realistic surface forcing fields has been shown to be of paramount importance for simulating the ocean in the shelf seas around Antarctica. Presently, polar ocean models and global climate models do not include these sub-grid scale features. The model developed in earlier chapters was applied to a realistic scenario and evaluated against some available observations. The analysis was extended to include some sensitivity studies. The major conclusions from this chapter are as follows:

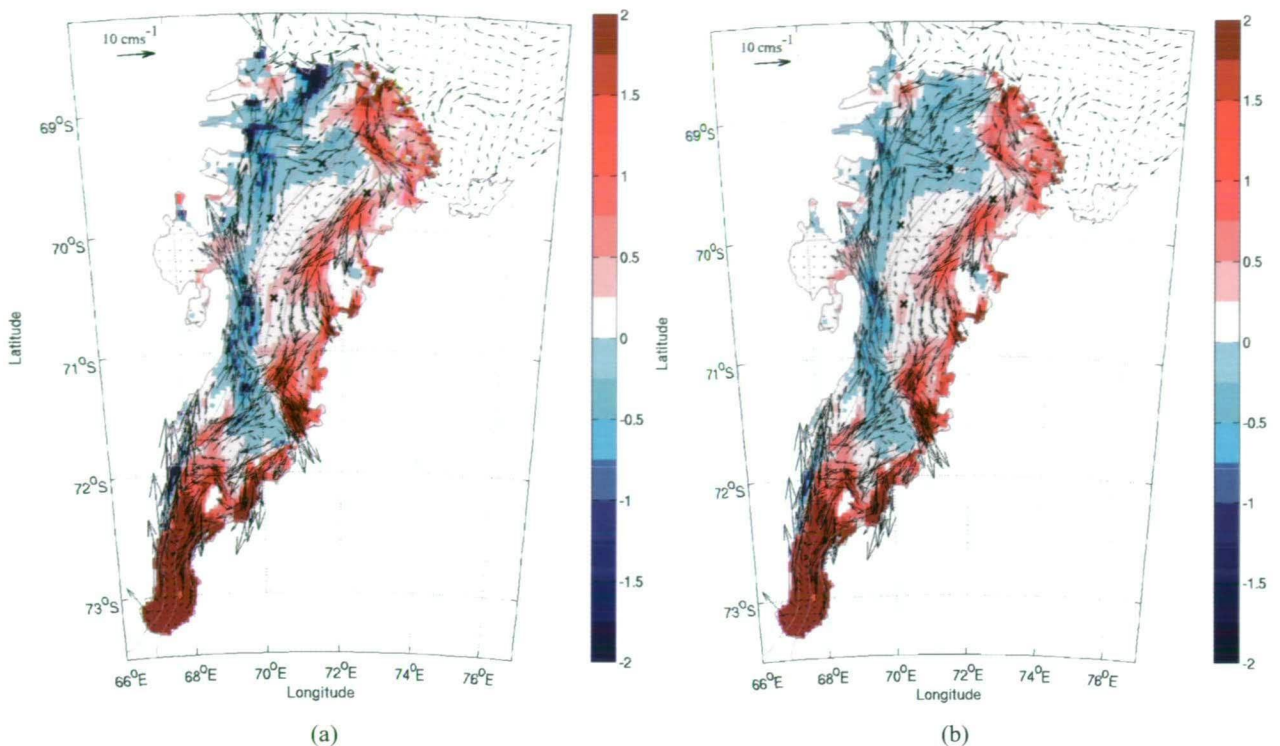


Figure 6.20: Comparing (a) the model with frazil and (b) the model without frazil for the annual averaged depth averaged currents (cm s^{-1}) and basal melting (m year^{-1} , positive) and freezing (negative).

- The basic model is supplemented with fluxes following the literature: tidal, wind and polynya forcings come from independent models and without any data assimilation and with very little tuning show encouraging results. The analysis presented in this chapter shows that the Reference model performs well when compared to available oceanographic and glaciological observations. The dense shelf water formation in coastal polynyas is important for both the mass balance of the ice shelf and for AABW formation. The sensitivity studies also show that including frazil ice dynamics is important to correctly estimate the mass balance of the ice shelf.
- The melting at the base of the ice shelf is primarily due to interaction with HSSW created from the surface sea-ice formation in winter. Although the AIS is smaller than both the Ross Ice Shelf and Ronne-Filchner Ice Shelf, the amount of meltwater production is comparable. This is due to the larger thermal driving at the deep ice shelf regions of the AIS compared to the shallower ice of the Ross and Filchner-Ronne, where the majority of the melt is thought to occur. The temperature difference between the coldest waters created in the open ocean and the *in situ* freezing point of ocean water in contact with the deepest part of the AIS is $\sim 2^\circ\text{C}$, leading to a melt rate that can exceed $30 \text{ m ice year}^{-1}$.
- The circulation in Prydz Bay is seasonally variable: the Prydz Bay gyre is primarily a

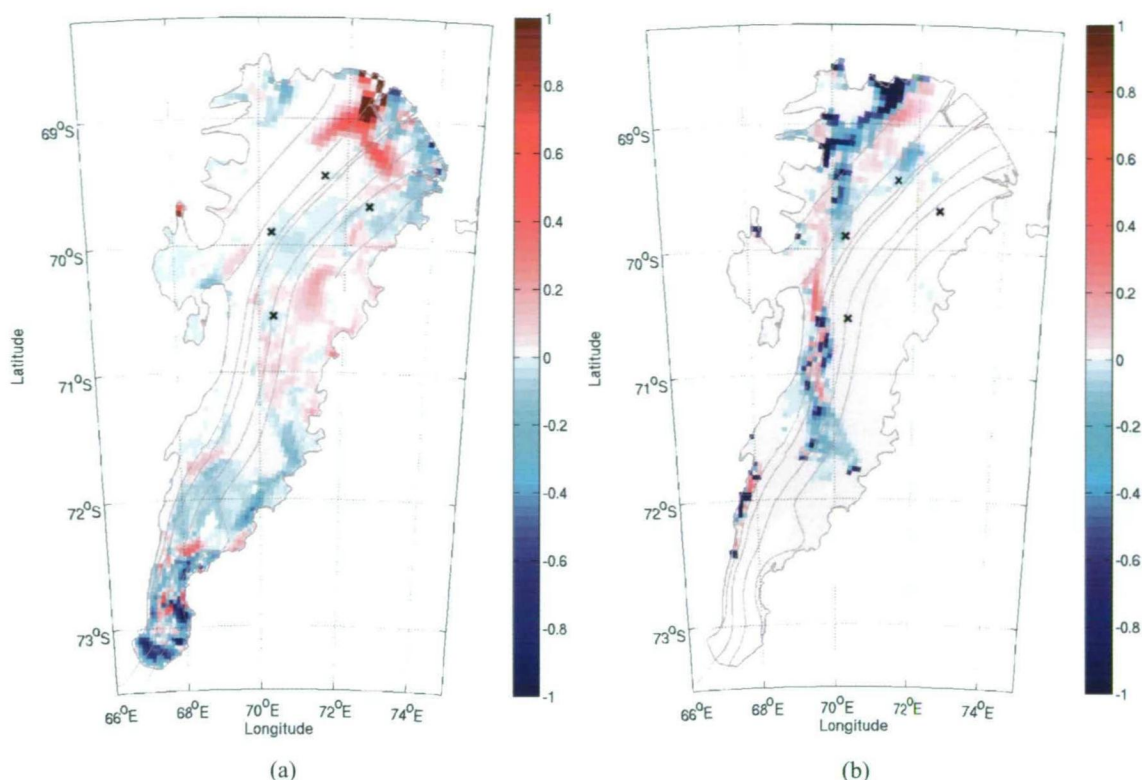


Figure 6.21: Showing the effect that frazil ice dynamics has on (a) basal melting and (b) freezing on the underside of the AIS from the differences between the reference model and the model without frazil ice dynamics. The colours should be interpreted as (a) positive indicates the reference model melts more than the model without frazil and (b) positive indicates the reference model has higher rates of accretion than the model without frazil.

summertime feature. Both the strength and direction of the gyre is controlled by the strength of the Barrier polynya. When the Barrier polynya is active, the Prydz Bay gyre is not and *vice versa*. When the polynya is active the westward flowing coastal current is diverted away from the coast and flows as a barotropic current out of the Prydz Bay channel and westward along the slope front. In periods of low polynya activity, during summer, the inflowing MCDW is entrained by the westward flowing coastal current as part of the gyre circulation.

- The position of grounded iceberg on the Cape Darnley coast has been suggested to enhance the formation of HSSW in the Cape Darnley polynya and the subsequent export of AABW from the region [Ohshima *et al.*, 2009]. Grounded icebergs in the vicinity of the barrier polynya region may also lead to enhanced production of HSSW. From MODIS imagery, it is clear that the Barrier polynya is a collection of smaller polynyas that form in the lee of grounded icebergs.
- Simulations that include a dynamic sea-ice model, without accounting for the effect of sub-grid scale features, such as grounded icebergs will underestimate the production of HSSW

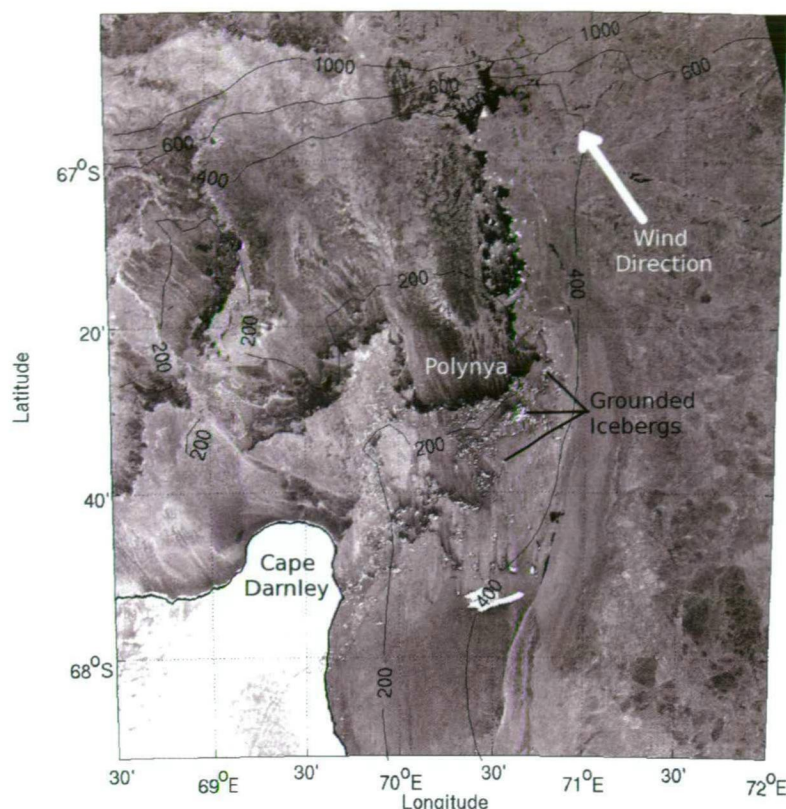


Figure 6.22: The Cape Darnley polynya is comprised of many polynyas created in the lee of small icebergs grounded around the 300-400 m bathymetry contours. The image has a pixel resolution of 200x200m [Jezek and Team, 2002].

and the subsequent production of AABW. As an example, Fig. 6.22 shows small icebergs near Cape Darnley that are grounded near the 300-400 m bathymetric contours. Many of the dotted icebergs are less than a few pixels across (1 pixel = 200x200 m)

- As with the simplified studies shown in Chapter 4, frazil ice initially forms in the supercooled water layer adjacent to the base of the ice shelf. Frazil moderates the maximum amount of supercooling found beneath the ice shelf, in agreement with the conclusions presented in Chapter 4. Importantly, the reduced level of supercooling manifests as enhanced basal refreezing through the precipitation of frazil. The frazil formation process leads to enhanced salt formation and modifies both the horizontal and vertical circulation patterns of the sub-ice shelf cavity when compared to models without frazil. Implementing a full dynamic frazil model has been shown to be important for marine ice accretion. However, a simpler approach for models that only aim to model deep water formation on climate time scales can be to simply remove excess supercooling beneath the ice shelf, modifying both the temperature and salinity fields, and depositing the mass directly against the base of the ice shelf.

- A limitation of the reference model is that the polynya activity is forced separately from the wind and surface temperature fields and that the distribution of icebergs and formation of sea-ice are important to get the absolute details correct. *Massom et al.* [1998] note that 26 of the 28 East Antarctic polynyas that they consider form in the lee of protruding coastal features, iceberg tongues, or grounded icebergs. However, the fields used for the polynya are derived from observations and hence do contain information about the processes that lead to their formation, such as winds and sub-grid scale sized icebergs. The use of a dynamic sea-ice model, potentially including the frazil model outline here would be appropriate for better representing the heat exchange and ice growth rate within the polynyas. However, this would require some parametrisation of the small polynyas that can form in the lee of sub grid scale sized icebergs.
- The present choice of 5 frazil size classes is due to the limitations of available computing power. This has shown remarkable agreement with observations but cannot be a full representation of the wide frazil size variation beneath the AIS. The parametrisation of the frazil physics and marine ice accretion contains a large number of assumptions and represents one of the major sources of uncertainty in the model.
- Vertical mixing is a difficult parameter to correctly tune in ocean models. Model results presented here show that the vertical mixing beneath regions of strong salt production is too high (shown as the vertically homogeneous tracer fields (Fig. 6.5) when compared with the observations). Stratification of the water properties was slightly improved by placing an artificial upper bound on the vertical mixing coefficient ($K_v = 0.2 \text{ m}^2 \text{ s}^{-1}$). However, sensitivity showed that the upper bound helped to reduce the vertical mixing and did indeed increase the stratification of the water column, particularly beneath the polynyas.

The testing of mixing schemes in the literature show that KPP, when bound, reproduced observations better than other schemes. However, recent attempts parameterise convective plumes by placing negative buoyancy, in the form of temperature and salinity, directly at its neutral depth. Appropriate convective adjustment schemes are a topic of development in the ocean modelling community [for example, *Timmermann and Beckmann*, 2004; *Timmermann and Losch*, 2005]. Future ROMS applications should consider such schemes as a parametrisation of sub-grid scale convective transport.

- The forcing applied to the model boundaries are about 10 years more recent than the observations made for the ice sheet mass balance. As our ocean boundary conditions are monthly averages over the observing time, which also show recent climate change, then they are likely to be biased towards a system that has already been affected by climate change when compared with pre-industrial forcing. The full effect of climate change on the mass balance of the AIS and AABW formation are tested in Chapter 7. Two-way coupling to a larger global model would provide more realistic boundary conditions. A logical next step is to extend the present model to be forced with timeseries that overlap the satellite era.

CHAPTER SEVEN

COASTAL ANTARCTIC RESPONSE TO CLIMATE CHANGE

As was discussed in Chapter 1, enhanced ocean warming has been suggested as the cause for the increased thinning of glaciers and accelerated rise of sea level from western Antarctica [Rignot *et al.*, 2004; Thomas *et al.*, 2004; Rignot, 1998]. However, the influence of ocean warming on the melting of ice shelves is uncertain due to the lack of long term oceanographic records in the regions beneath ice shelves. Furthermore, the mechanisms whereby the ocean waters near to ice shelves can warm is even less well known. As such, this chapter aims to understand the effect of climate change on the mass balance of ice shelves and deep water formation.

In this chapter, the steady state response of the reference model to changes in ocean forcing due to climate change is investigated. The ability of the Amery Ice Shelf (AIS) ocean model to simulate present day conditions was evaluated in Chapter 6. The response of the ice shelf-ocean system is investigated by perturbing the reference model with representative global warming forcing scenarios. The chapter begins by outlining recent observations of climate change. Linear observational trends in air-sea and lateral ocean forcing are used to define appropriate experiments to investigate the effect of climate change on ice shelf-ocean interaction. The response of net basal melting to an increase in surface warming is quadratic.

7.1 Recent Climate Change

There is limited scientific consensus as to the potential magnitudes of climate change over the Antarctic coastal regions. The IPCC [2007] concludes that for the majority of Antarctica, present and projected surface temperatures during the 21st century are too cold for significant melting to occur and precipitation is balanced by glacier flow into the ocean. In climate change scenarios for the 21st century, climate models project an increase in snowfall, resulting in increased storage of ice in Antarctica, partially offsetting other contributions to sea level rise. However, an increase in precipitation has not been observed to date [Lemke *et al.*, 2007].

Observations suggest that presently the response of the Antarctic coastal environment to climate change does not follow the observations for the rest of the Earth. This is attributed to the polar vortex that acts to insulate the Antarctic continent from the majority of change and, in fact, offsets “polar amplification”. Polar amplification of global mean temperatures is a feature of multi-model mean global climate projections using atmosphere-ocean coupled general circulation models [IPCC, 2007]. Polar amplification and the corresponding reduction of sea-ice extent in northern high latitudes has been observed. However, observations of climate change in Antarctica are less certain. The southern high latitudes have experienced less warming, with the exception of the Antarctic Peninsula. This has been proposed to be predominantly due to a contraction of the Antarctic polar vortex. However, there is still much uncertainty about the impacts of global

warming on the coastal regions of Antarctica.

Determining the effects of climate change on ice shelves using regional ocean models requires knowledge about the changes in mid-depth ocean temperature and changes in surface forcing. The relationship between changing ocean temperatures and basal melt rates has been investigated using a number of different ocean models [reviewed in, *Holland et al.*, 2008]. To the author's knowledge, this study is the first to investigate the response of ice shelf basal melting and subsequent bottom water formation, to changes in both surface and lateral forcing.

The impact of this ocean warming on the Amery Ice Shelf has not been directly observed. Observations of the AIS surface elevation show significant changes, suggested to be due to unexplained basal processes [*King et al.*, 2009]. However, it is not clear which physical mechanism can account for these changes. Strong decadal variability in HSSW production could be a likely mechanism for the observed signal in surface elevation. Meandering of the ACC can bring warmer ocean waters from the north into Prydz Bay. Furthermore, as suggested in Chapter 6, the repositioning of icebergs can influence the polynya activity in the region causing changes in the local circulation with significant consequences for basal melting.

Reconstructions of historical air temperature records from around Antarctica combined with satellite observations show a significant warming trend of the surface of Antarctica by $0.1\text{ }^{\circ}\text{C decade}^{-1}$, since the 1960s [*Jacka and Budd*, 1998]. More recent climate reconstructions show a $0.1\text{ }^{\circ}\text{C decade}^{-1}$ (1957–2006) warming over East Antarctica [*Steig et al.*, 2009], in agreement with the observed warming of $0.1\text{--}0.2\text{ }^{\circ}\text{C decade}^{-1}$ [*Monaghan et al.*, 2008].

A $0.027\text{ }^{\circ}\text{C year}^{-1}$ warming of surface air temperature over the sea-ice covered regions of the southern ocean [*Zhang*, 2007] has been discerned using NCEP-2 reanalysis, with a $0.02\text{ }^{\circ}\text{C year}^{-1}$ warming in air temperatures in the region of the Amery Ice Shelf, during the period from 1979 to 2004. Modelling studies show that the warming is primarily due to regional changes in atmospheric circulation and associated changes in sea surface temperature and sea-ice [*Steig et al.*, 2009]. A general warming has also occurred in the surface temperature of the peripheral seas [*Kwok and Comiso*, 2002].

An increase in precipitation for Antarctic and the Southern Ocean is predicted in more than 90 % of the simulations presented in the *IPCC* [2007] for the 20 coupled climate models using the A1B level forcing. Research by *Held and Soden* [2006] shows that troposphere saturated vapour pressure increases by $\sim 7\%$ for every $1\text{ }^{\circ}\text{C}$ of air temperature warming. As such, a doubling of atmospheric carbon dioxide, leading to an increase of $3\text{ }^{\circ}\text{C}$ in average surface air temperatures *IPCC* [2007], will increase rainfall by $20\%^1$. However, observations of ocean salinity show a decrease in the rate of change of surface salinity that is greater than that predicted by theory. The precipitation increase has led to a decrease of the surface salinity of the Southern Ocean by up to $0.02\text{ psu decade}^{-1}$. This change in surface salinity can be attributed to a $\sim 10\%$ increase in precipitation for every $1\text{ }^{\circ}\text{C}$ increase in surface air temperature².

¹ The analysis uses the well known Clausius-Clapeyron relationship

² P. Durack and S. Wijffels, Diagnosing rates of climate change using ocean hydrographic data. in-preparation. 2009,

The relationships between surface air temperature, polynya activity and lateral ocean warming are uncertain. For example, polynya ice production rates are influenced by a number of factors, other than iceberg position, including surface air temperature and wind forcing. Studies by *Marsland et al.* [2007] show that most of the reduction in polynya sea-ice formation, due to a 2 °C warming of surface air temperatures can be offset by a 20 % increase in wind strength. Including representative changes in both lateral and surface forcing to assess the response of the Amery Ice Shelf to climatic change is difficult.

7.1.1 Lateral ocean forcing

Long term observations of ocean warming near the Antarctic margin can be inferred with the aid of regional observations. Mid-depth ocean waters in the Southern Ocean are warming faster than other oceans in the world. Ocean temperatures have increased by 0.17 °C between 1955 and 1995 [*Gille*, 2002] compared to a 0.1 °C average temperature increase over the global ocean in the upper 1000 m [*Levitus et al.*, 2000]. The strongest warming rates are seen in the southern region of the ACC [*Böning et al.*, 2008]. The inclusion of ARGO float data show that ocean temperatures south of the ACC (south of 65 °S) are warming faster than previous observations suggest, at a rate of 0.17 °C decade⁻¹ [*Böning et al.*, 2008].

7.1.2 Ocean-atmosphere forcing

The production of brine in polynyas has been shown in Chapter 6 to have a strong effect on the basal melt rates beneath the AIS. Within the model domain there are three polynyas; the Cape Darnley, the McKenzie and the Barrier. Activity for the two main polynyas shows a decrease of 7.2% per decade for the Cape Darnley polynya and 11.4 % per decade for the MacKenzie polynya [*Tamura et al.*, 2008] (shown in Fig. 5.7(a)). The remaining polynya in the model domain is the Barrier polynya which shows a 55% increase in productivity. The impact of such a change in Barrier polynya activity was extensively discussed in Chapter 6.

Further investigation into the observed increased trend in ice production from the Barrier polynya shows that the production was biased due to low production rates pre-1994³. The increase in ice production rates after 1994 can be attributed to an increase in the number of grounded icebergs in the region. The bathymetry in the vicinity of the polynya is shallow (< 350 m) enough for icebergs to ground in this region.

As evidenced from the results shown in Chapter 6, low activity from the Barrier polynya is strongly correlated with increased persistence of the Prydz Bay gyre. And, as polynyas can form in the lee of icebergs, an increase in the number of icebergs can therefore lead to an increase in ice production. The impact of climate change on the number of icebergs is unclear. However, if the rate of ice shelf collapse increases due to climate change then it can be supposed that the number of grounded icebergs will also increase.

CSIRO Marine and Atmospheric Research, Hobart, Australia.

³ Personal communications with Takeshi Tamura, Low Temperature Institute, Hokaido, Japan.

Table 7.1: 10 model runs and approximate predictions of changes in surface air-temperature in the Amery Ice Shelf region, based on linear trends from observations since the 1960s. The runs include a set of lateral ocean warming runs (L1–L3), a set of air-sea flux runs (A1–A3) and combined runs (+0.5–+2). The lateral ocean warming runs is applied to MCDW from the reference simulation (R). The response of the air-sea flux is calculated as the difference from the annual mean used in R, shown in Fig. 7.1.

Air-Sea flux change (%)	Lateral warming (°C)			
	0	0.25	0.5	1
0	R	L1	L2	L3
-10	A1	+0.5		
-20	A2		+1	
-40	A3			+2

However, by assuming that the area of polynya activity remains constant into the future then climate change scenarios in the vicinity of the AIS can rely on the mean reduction in polynya activity between Darnley and McKenzie. The ice production rate from these two polynyas has decreased by 8.3% per decade over the satellite period [Tamura *et al.*, 2008].

7.2 Experiments

The experiments are designed to isolate the effect of the polynyas from lateral warming to measure their respective importance under climate change. In the vicinity of the Amery Ice Shelf the decrease in polynya activity over the last decade has been 8.3 %, which corresponds with an increase in air temperature of about 0.2–0.3 °C [Zhang, 2007; Johanson and Fu, 2007] and an increase in warming of mid-ocean waters (CDW) of 0.17 °C [Böning *et al.*, 2008]. Within the uncertainty of the linear trend, 10 scenarios are investigated that can realistically be expected within the next ~100 years (see Table 7.1).

The impact of surface air warming has been observed in reduced sea-ice extent [Cavalieri and Parkinson, 2008] and polynya productivity [Tamura *et al.*, 2008]. Atmospheric processes since the 1960s have led to a decrease in the ice production rates from the two largest polynyas in the vicinity of the AIS by ~8 % decade⁻¹. Part of the observed reduction in ice production has been suggested to be because of reduced convective overturning in the ocean beneath the ice, and hence reduced ocean heat flux available to melt ice, resulting in an overall increase in ice extent and volume [Zhang, 2007]. Studies by Marsland *et al.* [2007] have shown that a 2 °C surface air temperature warming (the maximum investigated here) leads to a 6% reduction in the ocean heat flux, which is smaller than that suggested by observations.

The adjustment used to force the model reduces the heat and salt fluxes proportionally to the annual mean change over a year, shown in Fig. 7.1. The change in the air-sea fluxes are calculated by subtracting the percent reduction annual mean value (Column 1 in Table 7.1), giving both a freshening and warming of the ocean surface waters. The use of climatological derived air-sea

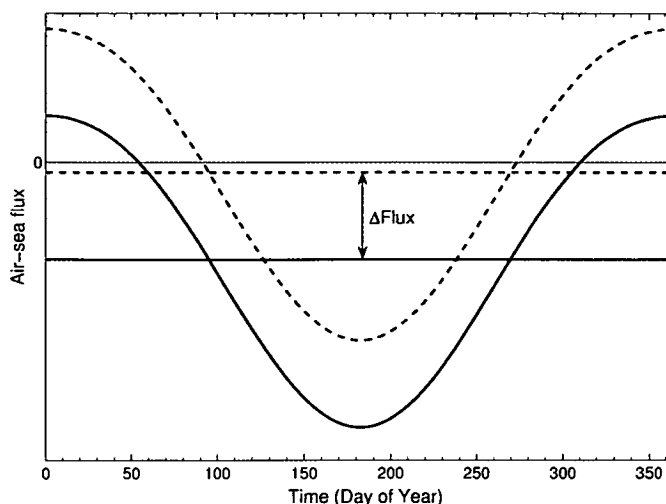


Figure 7.1: Idealised seasonal cycles of either heat and/or freshwater air-sea fluxes in the Southern Hemisphere. The change in surface air-sea fluxes (ΔFlux) is applied to the annual mean. The mean is calculated separately for each grid cell

fluxes includes the effect of wind on ice (and hence brine) production rates.

The wind stress and lateral currents are held constant, which is justified, because observations of transport in the ACC and meridional overturning in the Southern Ocean are insensitive to decadal changes in wind stress [Böning *et al.*, 2008]. Furthermore, warming trends around Antarctica are driven by changes in sea surface temperature and sea ice and not by changes in winds [Steig *et al.*, 2009]. The open boundaries were handled as outlined in Chapter 5, with the exception for the perturbation experiments outlined in Table 7.1.

The lateral forcing was modified by increasing the temperature of the MCDW (defined using Table 6.2) by the values from the top row of Table 7.1. Simulations that test the combination of both air-sea forcing and lateral forcing are referred to as changes in surface air temperature, above the present are shown in the Table 7.1 as “+0.5”, “+1” and “+2”. The combined forcing simulations are based on approximate linear trends from the observations. Each of the 10 experiments are run to approximate steady state under constant forcing.

It is expected that increased melting will lead to a slowdown in the production of AABW due to the dilution of HSSW with extra ice shelf melt. However, it is not clear if a reduction in polynya activity will partially offset the increased melt caused by ocean warming. The reduction in polynya activity will also lead to a reduction in AABW formation but this rate is unknown.

7.3 Results and Discussion

The response of the Amery Ice Shelf and the Prydz Bay region to the various climate change scenarios are interpreted by comparison with the reference model outlined in Chapter 5. The effect on the melt rate is shown as an enhancement above the reference simulation by dividing the melt

response to the climate change forcing scenarios by the reference model response. Similarly, the effect on the formation of AABW is shown as an enhancement above the reference simulation by dividing the AABW formation response to the climate change forcing scenarios by the reference model response. The deep water (AABW) production is calculated for the model's western boundary, as discussed in Chapter 6, and is defined by the water mass properties defined in Table 6.1. As in Chapter 6, the definition of the production rate of AABW used here requires that AABW has been transported off the continental shelf and onto the slope front. The main transport site of AABW across all simulations is from the Cape Darnley region, which remains unchanged from the simulations shown in Chapter 6.

7.3.1 Lateral warming

The lateral warming experiments (L1, L2 and L3) have changes as shown in Table 7.1 while the surface air-sea forcing is the same as the reference simulation (R). The enhancement of basal melting and AABW production as a function of lateral ocean warming is shown in Fig. 7.2.

The enhancement of basal melting and deep water production due to lateral ocean forcing over the reference simulation, which represents a steady state, both show a strong quadratic relationship to lateral thermal forcing. A $1\text{ }^{\circ}\text{C}$ increase in CDW temperatures will enhance the basal melt rates by a factor of 1.3 and reduce deep water formation by a factor of 4. Obviously, negative deep water formation rates are unrealistic; however, deep water formation is projected to completely shut-off at $\sim 1.1\text{ }^{\circ}\text{C}$ increase in CDW temperatures.

The enhancement of AABW production, for CDW warming $< 0.5\text{ }^{\circ}\text{C}$, is because the relative densities between the warmer CDW and AABW allows greater downslope movement of AABW. The subsequent decrease in AABW export for CDW warming higher than $0.5\text{ }^{\circ}\text{C}$ above present is attributed to enhanced basal melting. As shown in Chapter 6, the presence of meltwater from ice shelves can strongly moderate the export of dense water from the Antarctic continental shelf region. As such, a CDW warming of $\sim 0.5\text{ }^{\circ}\text{C}$ represents a threshold where the reduced density of AABW because of dilution with ISW is equal to the relative density differences between CDW and AABW.

The climate change studies of *Williams et al.* [2002], that also investigate a lateral ocean warming enhancement for the AIS, show that a $\sim 1\text{ }^{\circ}\text{C}$ increase in warming applied directly at the front of the ice shelf led to a melt rate enhancement of 2.8 times their present day simulation. The comparison estimate from the model presented here has a melt rate enhancement of 1.3 times the present. *Williams et al.* [2002] also found a linear response in basal melting to lateral ocean warming, contrary to the results presented here. However, their model contains a number of limitations. Primarily, the front of the cavity is at the northern boundary. Barotropic flow into and out of the cavity is fixed throughout to values determined from summertime temperature and salinity conditions, neglecting any variations in exchange that may occur under warming scenarios. Furthermore, any lateral ocean warming is applied directly at the front of the ice shelf cavity and does not need to traverse the continental shelf seas.

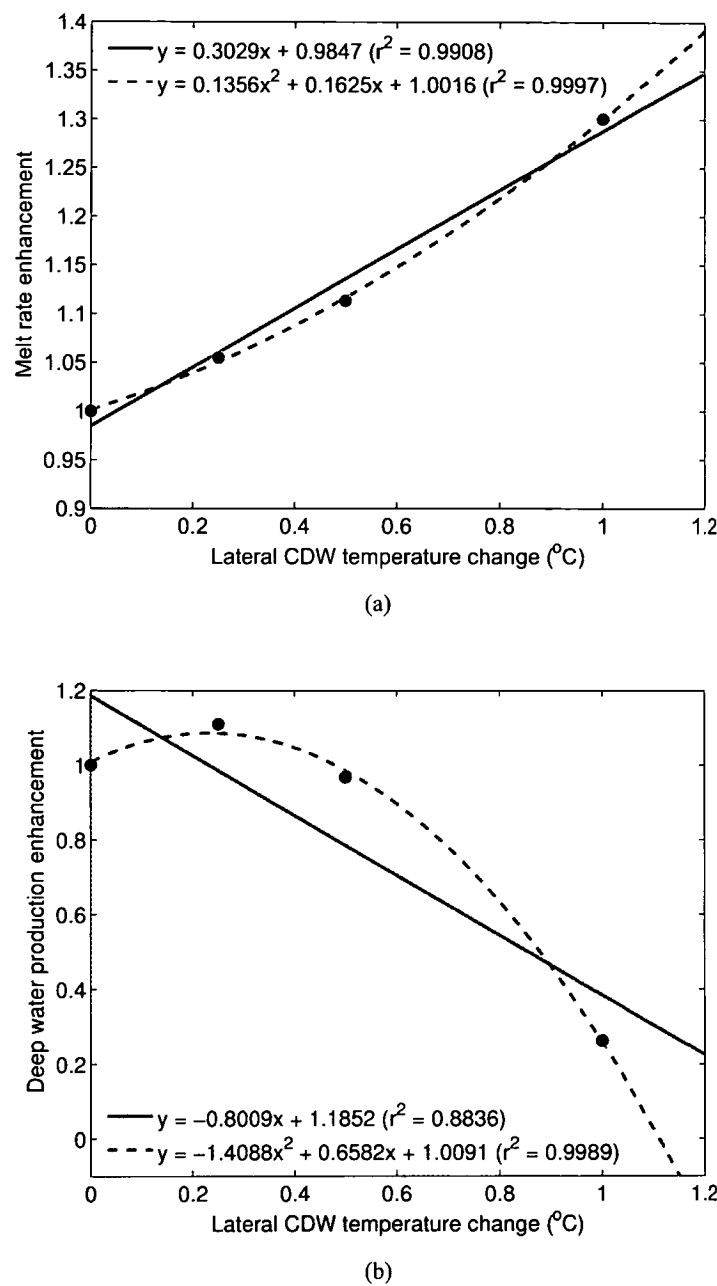


Figure 7.2: Relationship between lateral boundary thermal forcing due to warming of Circumpolar Deep Water and (a) area-averaged melt rate enhancement of the Amery Ice Shelf, and (b) deep water production rate enhancement, measured across slope near the western boundary. The enhancements are relative to the reference model, that uses the set-up outlined in Chapter 5.

7.3.2 Surface warming

The air-sea flux experiments (A1, A2 and A3) have changes as shown in Table 7.1, while the CDW temperature is held fixed at the present day. The surface warming manifests as both an

increased summer surface warming and decreased winter sea-ice activity over the surface of the open ocean. Fig. 7.3 shows that the response of both the deep water formation and melt rate is linear.

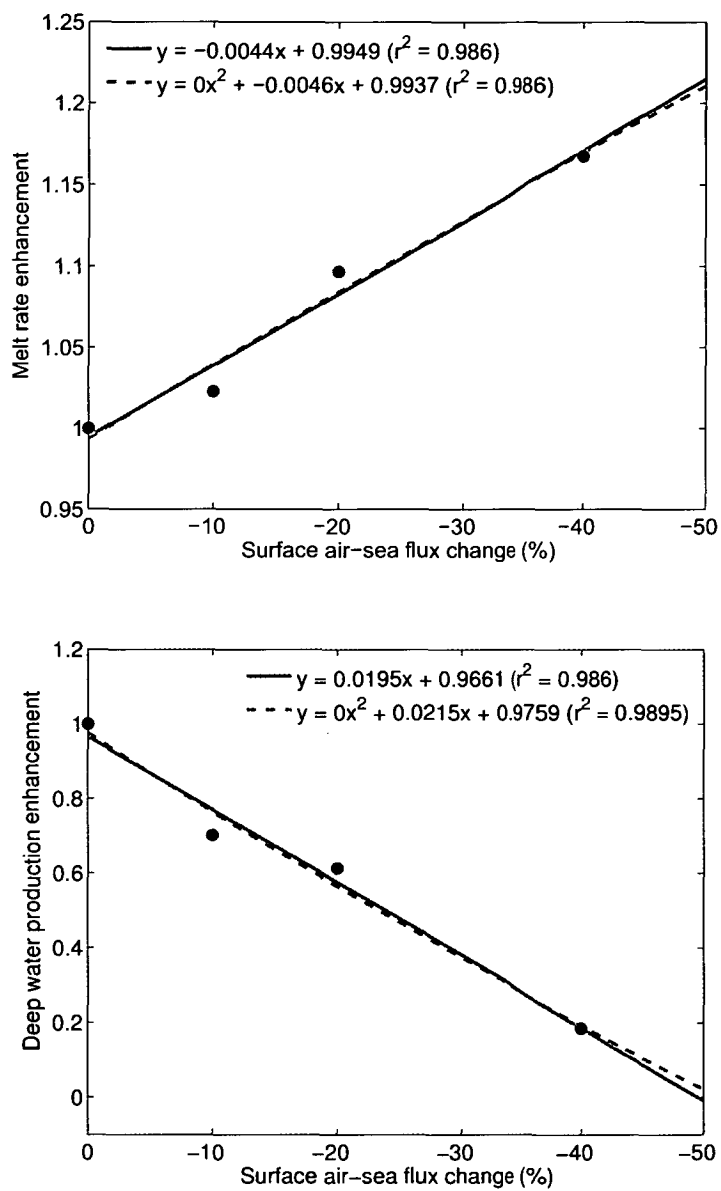


Figure 7.3: Relationship between decrease in air-sea fluxes due to reduced polynya activity and (a) area-averaged melt rate enhancement of the Amery Ice Shelf, and (b) deep water production rate enhancement, measured across slope near the western boundary. The enhancements are relative to the reference model, that uses the set-up outlined in Chapter 5. Note that the x-axis is reversed.

The surface warming scenarios act directly on the ocean cavity beneath the AIS compared to the lateral ocean warming, which must move onto the continental shelf before interacting with the

AIS. The surface warming scenarios, in this case are more akin to the experiments of *Williams et al.* [2001] who applied the forcing directly at the front of the cavity. However, the linear melt rate enhancement, shown here, is much smaller than suggested by *Williams et al.* [2002].

7.3.3 Combined lateral and surface warming

These experiments (+0.5, +1 and +2 shown in Table 7.1) are the most likely climate change scenario. They rely on extending present trends forward to simulate changes in both lateral ocean forcing and changes to the air-sea fluxes, when considering the linear trends shown in the observations. The combined effect of lateral ocean warming and decreased surface forcing are shown in Fig. 7.4. The enhancement of the melt rates follows a quadratic relationship with combined surface and lateral warming ($r^2 = 0.998$). The response of deep water production is also quadratic. The global warming scenarios suggest that the production of deep water in the vicinity of the Amery Ice Shelf will completely shutdown for a combined forcing of a 40 % reduction in air-sea fluxes and a 1 °C warming of CDW (shown in Fig. 7.4 as an effective 2 °C increase in surface air temperatures).

The effect of enhanced ocean warming due to both a 1 °C increase in the lateral temperature of the CDW and a 40 % reduction in polynya activity is shown in Fig. 7.5. The figure shows the difference in basal melt rates and the averaged velocities from the reference simulation. The enhanced melting due to increased surface warming is highest at the deepest parts of the Amery Ice Shelf. The maximum increase in the melt rate is $\sim 4 \text{ m year}^{-1}$, near the southern grounding line. Analysis of ocean temperatures and precipitation over East Antarctica suggest an increase in precipitation over the region of the Amery Ice Shelf. Much of the precipitation occurs at the front of the Amery Ice Shelf. The southern region has high surface ablation which means any increased melting of the southern part of the ice shelf will not be offset by an increase in precipitation.

The spatial pattern of melting and freezing shows little change; however, the melt rate is increased and freeze rate is decreased. The basal melt rates near the front and western boundary of the ice shelf show an overall increase of up to 1 m year^{-1} . The increased rates are of the same magnitude as the seasonal variability in these parts of the shelf. The variability shown here is of the same magnitude as observed changes in equivalent surface elevation [*King et al.*, 2009].

The modification of the strength and direction of the circulation beneath the ice shelf due to climate change is negligible. The strength of the coastal current is enhanced, although this is also a small effect and is likely only due to the decreased buoyancy driven flow from the Barrier polynya. However, the result of the reduced polynya activity is to bring warmer water into the cavity beneath the ice shelf. The variance ellipses between the reference simulation and the +2 equivalent surface air temperature simulation show almost no variability beneath the ice shelf, with the exception of the north-west region. The position of the variance ellipses in this region shows that the change in currents can be attributed to a change in the region of outflowing ISW.

Fig.7.6 compares the sub surface distribution of potential temperature and salinity ($\theta - S$) for the strongest cases compared to the reference model. The properties of the water masses beneath

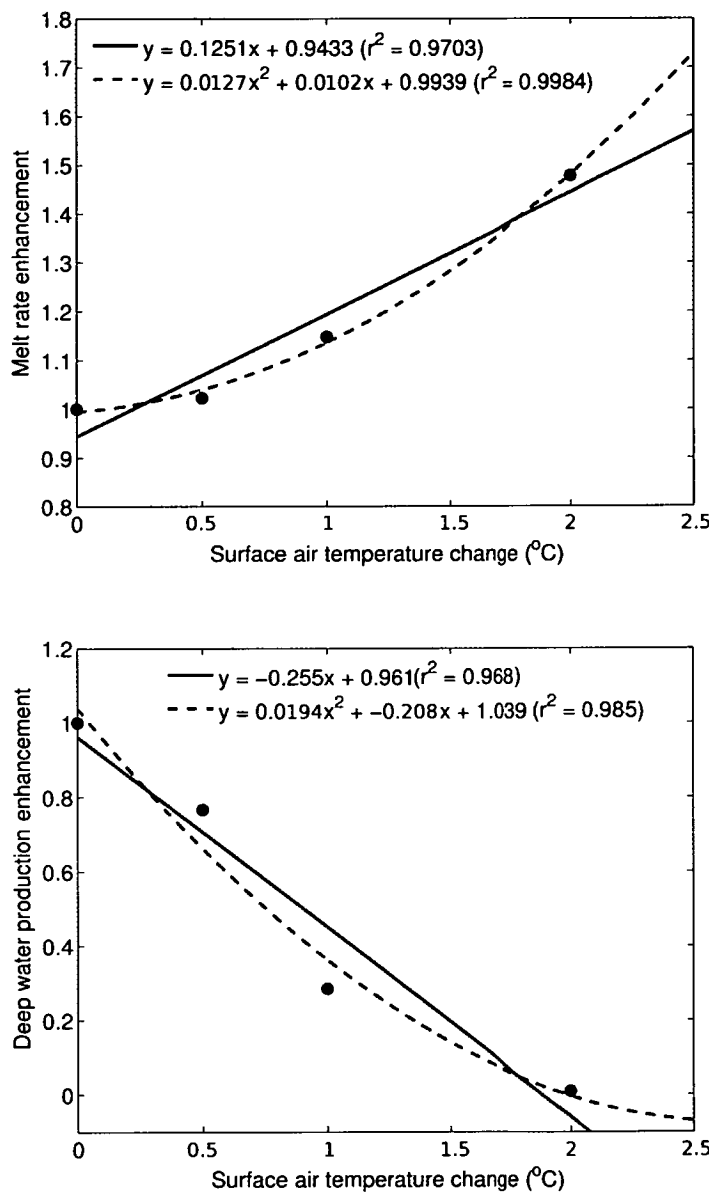


Figure 7.4: Relationship between climate change and (a) basal melt rates and (b) deep water formation. The model data are shown as the dots. The climate change scenarios are a combination of lateral warming of circumpolar deep water and reduced sea-ice growth conditions as outlined in Table 7.1. The runs are plotted relative to changes in surface air temperature, which are approximate estimates from the available literature.

the ice shelf are fresher in the perturbation simulations compared to the reference simulation, as shown by the position of the Gade line [Gade, 1979]. It is clear that the decreased air-sea flux leads to decreased production of HSSW and subsequently inhibits the production of AABW (Fig. 7.6 b and d). However, lateral warming (c) shows the production of HSSW with water mass properties similar to the reference simulation with a distribution of modified AABW. The properties of dense

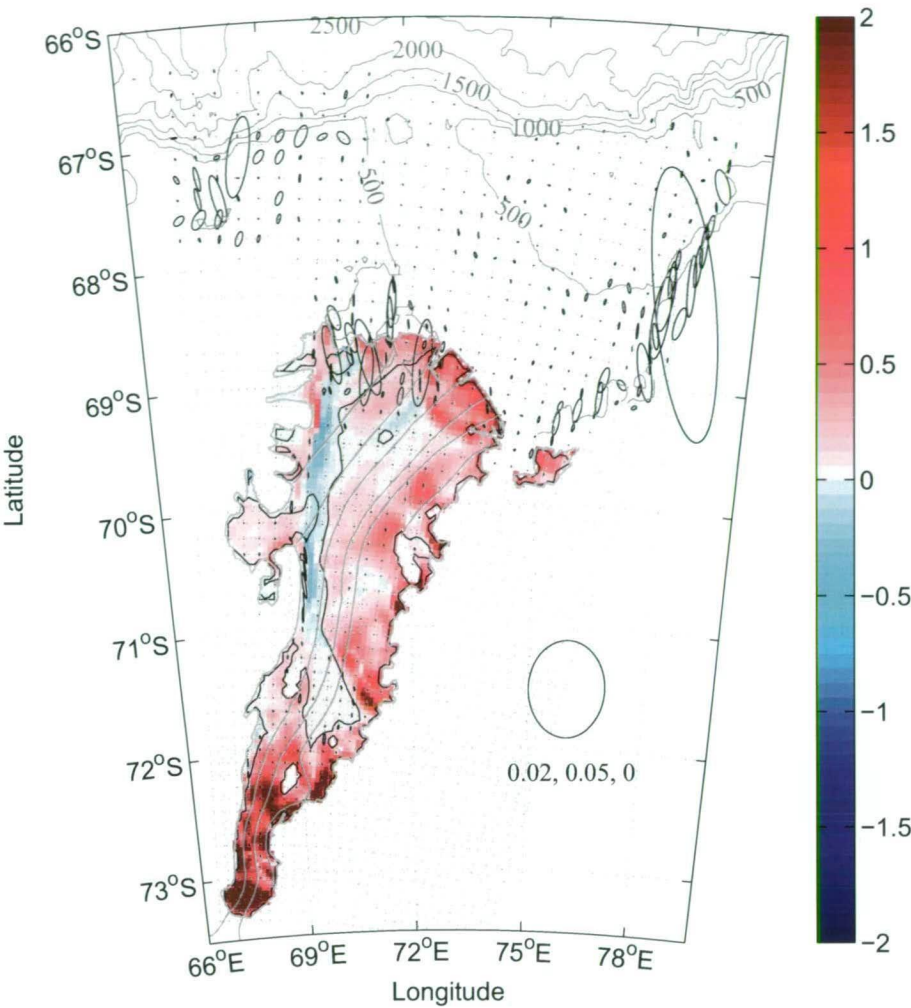


Figure 7.5: Change in the spatial pattern of melt/freeze (m year^{-1}), calculated by subtracting the results from the “+2” $^{\circ}\text{C}$ combined surface and lateral warming from the reference (R). The zero contour melt rate from the reference simulation is shown as the thin black line. The variance ellipses of the depth averaged velocity for every 3rd grid cell are also shown. The scale ellipse has a semi-major axis of $0.02 \text{ m}^2 \text{ s}^{-2}$, a semi-minor axis of $0.05 \text{ m}^2 \text{ s}^{-2}$ and is orientated north.

water in (c) are both fresher (by 0.05) and lighter (by 0.05 kg m^{-3}) than the reference simulation. Interestingly, the total volume transport of dense water present on the slope front (deeper than 800 m), when considering the changed water mass properties, is greater in (c) than in (a). This is consistent with the enhanced production of dense waters shown at moderate CDW warming, discussed above.

The increase considered in the surface air temperature simulations fall within the estimates of

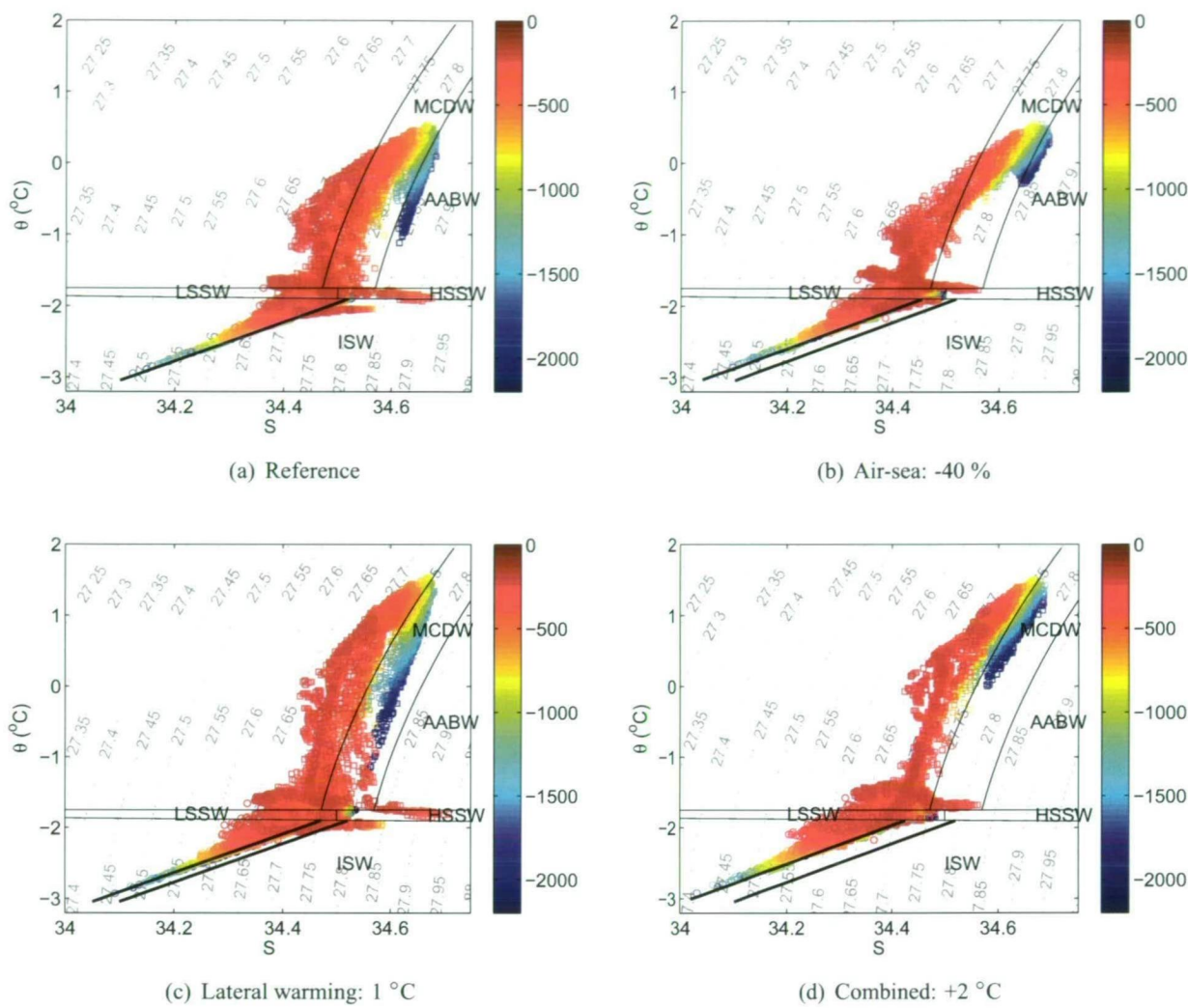


Figure 7.6: Comparing the distribution of potential temperature (θ $^{\circ}\text{C}$) and salinity (S psu) for (a) the reference simulation, (b) the strongest surface warming, (c) the strongest lateral warming and (d) the strongest combined forcing. The $\theta - S$ diagrams show every second model grid cell beneath the open ocean (squares) and for the ocean cavity (circles) below 200 m beneath the ocean surface. The colour scale shows the depth for each cell. The grey dotted lines are potential density contours; the thin solid lines define the water masses from Table 6.1. The thick lines in the ISW show the dilution relation when ice melts/freezes in seawater that considers heat flux into the ice shelf (thick solid line) [Gade, 1979].

surface Antarctic warming from the IPCC emissions scenarios. The corresponding changes in air-sea flux and ocean temperatures is within the range of model predictions for a range of scenarios. The “+1” scenario (Table 7.1) is the multi-model mean prediction of surface air warming over East Antarctica [IPCC, 2007] and fits within the A1B emissions scenario. The “+2” is approximately within the predictions for surface air warming over East Antarctica coastal oceans for the A2

emission scenario.

7.4 Concluding Remarks

Very little effort has been spent to model the future climate of coastal Antarctica at a spatial scale finer than that of GCMs [IPCC, 2007]. As such, the results presented here represent a significant contribution to understanding of the response of ice shelf-ocean systems to climate change. Results suggest that the warming signal does not necessarily need to propagate from the open ocean and that changes in air-sea forcing can also lead to significant changes in the melt regimes of ice shelves. For the Amery Ice Shelf, the warming signal can be expected to be driven by both changes in air-sea interaction and lateral ocean warming.

The relative robustness of the Amery Ice Shelf to lateral and surface warming can be due to the deep embayed and wide continental shelf region that isolates the deepest parts of the ice from the main warming from the deep ocean. The summer surface waters do not find their way into the cavity easily. The initial surface fluxes of heat and salinity during summer act to reduce the density of the surface waters. The effect of this is that the warmed surface waters are not able to mix downwards into the water column until winter. The primary mechanism from the surface forcing for waters to enter the deepest parts of the cavity is by mixing with dense HSSW.

The response to lateral ocean warming is enhanced by the linear response to a reduction in surface air-sea fluxes. This suggests the production of HSSW from surface sea-ice formation processes partially buffers the effects of lateral ocean warming. The primary water masses that drive melting (HSSW) under the lateral warming scenarios are fresher (by 0.02). The results shown here agree with the findings of *Holland et al.* [2008] that the basal melt response to lateral ocean warming and the combined response to both lateral and surface warming is quadratic. However, linear response to surface warming alone is a new finding that explains the linear results of *Williams et al.* [2002]. Enhanced melting does not necessarily require a heat input to the ocean and can be influenced by changes in ocean circulation. In the case of the surface forcing scenarios, warmer waters reach the base of the ice shelves because of the influence of another mechanism, namely the strength of the Prydz Bay gyre, that brings heat into the cavity from the open ocean.

The mass imbalance under a 2°C increase in surface air temperature scenario would lead to a loss of the Amery Ice Shelf in ~500 years, solely due to increased basal melting. However, the results presented here rely on steady state solutions using the present day ice shelf geometry. Assuming that the reference simulation is in steady state then any perturbation will melt more ice than can be replaced by the inflowing glacier. An approximate estimate of the state of the ice shelf under the strongest climate change scenario will melt the inflowing column of ice (~2500 m thick) within 500 years. This assumes that mass fluxes, due to glacier flow, accumulation and iceberg calving stay constant.

The dynamic response of the ice shelf due to the enhanced basal melting still remains a major uncertainty in projections of the effects of climate change. For example, there are suggestions of a potential dynamical response (sliding of the outlet glaciers over the bedrock) of the Greenland

and Antarctic ice sheets [Lemke *et al.*, 2007]. In Greenland, there was a significant increase in the flow rate of many of the outlet glaciers during the early 21st century . One potential reason for this is increasing surface melt making its way to the base of the glaciers, lubricating their flow over the bed rock, consistent with increased glacier flow rates [Zwally *et al.*, 2002]. This is a significant outstanding uncertainty that remains to be investigated using numerical models.

As the model does not contain a dynamic sea-ice/polynya model, the effects of climate change are implemented by adjusting the surface salt/heat fluxes. This is justified partially because the modelled response of projected Antarctic sea-ice trends due to global warming are not well known. Individual models show large differences in simulated Antarctic temperature trends over the past century. Since this model imposes the sea-ice, it is difficult to compute explicitly the relative importance of wind effects versus upwelling of warm water on the maintenance of the polynya.

CHAPTER EIGHT

CONCLUSIONS

8.1 Summary and Main Findings

Our understanding of ice shelf-ocean systems is poorly constrained by observations, due to the inaccessibility of these areas. Knowledge of these systems for the present and under future climate change scenarios relies almost exclusively on the use of numerical simulations. This thesis has developed a terrain following numerical ocean model for the application to the oceans beneath ice shelves. The model developed for the purpose of this thesis represents the state-of-the-art in ice shelf-ocean modelling. In the process of development a number of key advances were made. Terrain following models have been shown to be suitable for the study of ice shelf/ocean interaction. The inclusion of frazil dynamics with depth dependent supercooling into a three-dimensional ocean model represents a significant advance in international modelling efforts to simulate ice shelf-ocean interaction. The equation of state was also updated and a simple vertical rise model used for the frazil was also presented.

The development of a set of realistic boundary conditions was found to reproduce the main circulation and mass balance features of the Amery Ice Shelf and Prydz Bay region. The Amery Ice Shelf-ocean model is forced with tides, seasonal winds and relaxation to seasonal lateral boundary climatologies. The open ocean surface fluxes are modified by an imposed climatological sea-ice cover that includes the seasonal effect of polynyas. The numerical model has been shown to produce results that are consistent when compared against other simplified cavity models and when compared against observations. The sigma model here has shown that bottom water formation and transport process can be modelled with a high degree of realism (in comparison with observations). This research contributes to understanding how interaction between ice shelves and various forcing mechanisms can lead to changes in basal melt/freeze and dense water formation, which has major implications for the stability of ice shelves, sea level rise, and the salt budget of the global oceans.

Each of the aims of this thesis, listed in Chapter 1, has been achieved. The main conclusions from this study are as follows:

1. Frazil ice both enhances marine ice accretion and limits the supercooling present in the model domain with implications for net melting of ice shelves and dense water formation. Frazil also acts to destabilise the ISW plume, due to brine rejection processes during growth, that cause local changes in circulation and the spatial pattern of melt/freeze. Direct comparison with glaciological observations shows that ice shelf models that include frazil processes dramatically improve the simulated pattern of marine ice accretion.
2. The circulation and basal melting and freezing show good agreement with glaciological and oceanographic observations that have been collected from beneath the Amery Ice Shelf via

boreholes through the ice and in the adjacent area of Prydz Bay. Strong horizontal and thermohaline (“ice-pump”) circulation is primarily driven by melting and refreezing of the ice shelf. The net basal melt rate is $\sim 45 \text{ Gt year}^{-1}$ ($\sim 0.7 \text{ m year}^{-1}$), which represents 67 % of the total mass loss of the Amery Ice Shelf. The total amount of refreezing is $\sim 5.3 \text{ Gt year}^{-1}$, of which 70 % is due to frazil accretion. The seasonal variability of the basal melt/freeze (up to $\pm 1 \text{ m year}^{-1}$) within 100 km of the open ocean is the same magnitude as the area-averaged melt rates.

3. Freshwater from the basal melting of ice shelves inhibits the formation of AABW. For the Amery Ice Shelf region, simulations without ice shelf-ocean thermodynamic processes overestimate bottom water formation by up to 2.8 times as much as simulations with ice shelf-ocean thermodynamic processes, due to the missing buoyant freshwater from the melting ice shelf. The most realistic model shows annual averaged bottom water formation rates are $\sim 1 \text{ Sv}$ to the west of the Amery Ice Shelf, in the vicinity of Cape Darnley. The production has a strong seasonal cycle with a winter maximum of $\sim 3 \text{ Sv}$. There is also a significant dense water transport along the continental shelf out of the models western boundary that has not exported off the shelf as AABW. This dense water could also lead to significant bottom water formation further along the coast.
4. The dense water production from coastal polynyas can strongly modify local circulation patterns with implications for both net basal melting of ice shelves and AABW formation. Polynyas that form in the lee of grounded icebergs are important for Antarctic coastal oceanographic processes. Icebergs that have grounded offshore contribute to enhanced regional ice production rates and thus brine input into the underlying ocean within lee polynyas [Massom, 2003]. Studies of iceberg distribution in East Antarctic showed that 705 icebergs grounded in the vicinity of Cape Darnley had a mean area of 0.17 km^2 and near the Barrier polynya region, the 1378 icebergs that were counted had a mean area of 0.4 km^2 [Young *et al.*, 1998].
5. The Prydz Bay gyre was found to be primarily a summertime feature. Both the strength and direction of the gyre is controlled by the production of dense water from the Barrier polynya – when the Barrier polynya is active the gyre is not and *vice versa*. The production of dense water, primarily during late winter, blocks the westward flowing coastal current and diverts it northward away from the coast. The coastal current then bypasses the Amery Ice Shelf and flows as a barotropic current out of the Prydz Bay channel and westward along the slope front. In periods of low polynya activity, during summer, the inflowing MCDW is entrained with the eastward flowing coastal current as part of the gyre circulation.
6. Climate change sensitivity studies show that the enhanced melt response of the AIS is quadratic, driven by both lateral warming and a linear response to surface warming. A diabatic warming of CDW $< 0.5 \text{ }^\circ\text{C}$ can lead to enhanced AABW production due to the increased density contrast between the AABW and CDW. For CDW warming $> 0.5^\circ\text{C}$ the

formation of AABW is ultimately controlled by the air-sea flux driven production of HSSW and the freshwater contributions from the enhanced basal melt of ice shelves.

7. A CDW warming of 1°C above present day temperatures can potentially remove the Amery Ice Shelf in ~ 500 years, solely due to increased basal melting, and can also lead to a significant decrease in the formation of bottom water. Given the current rates of warming, collapse of the Amery Ice Shelf through enhanced basal melting processes seems unlikely in the next 100-200 years. However, the production of AABW in the vicinity of the AIS will shutdown with a combined 40% decrease of polynya activity and 1°C warming of CDW.

8.2 Caveats and Future Work

- The model presented here has been developed to simulate the under ice shelf circulation and dynamics due to a parametrisation of the melt/freeze. The inclusion of frazil ice dynamics extends the capabilities of the model to correctly represent the transport of heat and mass in the ocean. However, the assumption made here is that the ice shelf reacts instantaneously to melting and/or accretion and is maintained in the initial state. For an ice shelf in steady state, the convergence of the ice flux is exactly balanced by the sum of the surface and basal accumulation. Under the steady state assumption, increasing the rate of basal melting due to climate change (Chapter 7), must be balanced by an increase in the mass flux convergence and/or surface accumulation rate. The increased mass flux convergence is achieved by either increasing the flow of ice to, or decreasing the outflow of ice from, the ice shelf.
- The newly-defined Amery Ice Shelf cavity geometry represents a significant advance over previous cavity geometries and contains a significant number of new observations of bathymetry and ice draft data. However, regions of high freezing which are not apparent in the observations suggest that the ice draft is in places unrealistically shallow. The shallow ice draft then allows water near to the freezing point to become supercooled leading to marine ice accretion.
- A limitation of the model for climate change simulations is that the polynya activity is forced separately from the wind and surface temperature fields. The use of a dynamic sea-ice/polynya model, potentially including the frazil model outlined here, would improve the estimates of heat exchange and ice growth rates under future climate change scenarios. However, this would require some parametrisation of the winter water production that can form in sub grid scale “lee” polynyas.
- The present choice of 5 frazil size classes is due to the available computing power. This has shown remarkable agreement with observations but cannot be a full representation of the wide size variation of frazil crystals beneath the AIS. The parametrisation of the frazil ice physics contains a large number of assumptions and represents one of the major sources of uncertainty in the model. Future research should include some mechanism whereby frazil crystals can cohesively interact. The frazil model shown here has particular applicability

to use in a sea-ice/polynya model. The implementation method used for the frazil model means that any process that creates supercooling in the frazil domain can create frazil and dense water.

- Models without appropriate freshwater fluxes from ice shelves can overestimate bottom water production by 2.8 times more than models with ice shelves. Accurate estimation of water mass budgets and the transformation rates are important in terms of assessing their importance for the larger scale thermohaline circulation and how it may be affected by climatic changes in the local and global scale. Simulating AABW formation and circulation in a global ocean climate model is a significant challenge, requiring accurate representations of a number of individual processes including shelf water production, overflow and entrainment, and abyssal circulation. In models that do manage to simulate sea-ice in agreement with observations it is found that coupled ocean/sea-ice models tend to have too much ventilation of the deep Southern Ocean [Dutay *et al.*, 2002]. Climate models should incorporate both some basic parametrisation of basal ice-ocean interaction and frazil dynamics. However, as the dynamic frazil model is computationally expensive it is recommended that simulations of ice shelf-ocean interaction, for the purpose of bottom water formation, can parameterise the effect of frazil. The parameterisation can be achieved by simply warming (cooling) the appropriate amount of supercooling (heating) at each time-step by the amount that corresponds to growing (melting) of the available ice.
- The model developed here has application to other ice shelves and Earth systems where ice-water interactions are important, such as both surface and sub-glacial lakes and tide water glaciers. Preliminary studies of the Mertz Glacier tongue show results that are in agreement with observations. The model, with its curvilinear coordinate system, would be particularly amenable to circum-Antarctic and circum-Greenland applications. Such an application would be useful for a number of reasons. Dense shelf water, with sufficient negative buoyancy and an export pathway to the continental slope, can mix downslope and supply the deep and bottom layers of the global ocean with nutrients and oxygen, as well as with indicators of recent anthropogenic activity, such as chlorofluorocarbons [Meredith *et al.*, 2001] and increased concentrations of carbon dioxide [Sabine *et al.*, 2004]. As observations of AABW rely on constraints that can be provided by anthropogenic tracer (such as CFCs) studies, the addition of CFC and CO₂ tracers to the model would make an important contribution towards constrained estimates of the production rates of AABW and estimating the impacts of anthropogenic climate change on deep ocean properties.
- With respect to modelling Antarctic coastal oceans, icebergs are sub-grid scale in size but have an influence that can extend to the entire model domain. Estimates suggest that there are 200 000–300 000 icebergs in the Southern Ocean [Orheim, 1988] with sizes ranging from a linear dimension of 50 m to tens of kilometres and occasionally in excess of 100 km. Many icebergs become grounded in coastal regions where the bathymetry becomes

shallower than $\sim 300\text{--}400$ m. The size of grounded icebergs is significantly less than the horizontal grid dimensions of most regional models, $\mathcal{O}(1\text{--}5)$ km and significantly smaller than the grid scale of contemporary global climate models. Future work should consider a parametrisation of the effect of such sub-grid scale features as they have been shown here to be crucial for ice-ocean interaction studies.

- The experiments presented here use a diabatic alteration of MCDW temperature. However, the signal of warming of the mid-depth waters around Antarctic has been observed to contain a component of adiabatic change. That is, a warming/salinisation on density surfaces due to a poleward migration of the ACC fronts [Böning *et al.*, 2008]. The ice shelf response to warming using a diabatic warming may well underestimate the melt rate enhancement.
- The frazil model included here has extended the ability of ocean models to simulate marine ice accretion. This represents a significant improvement of the current two-dimensional plume studies. However, there is still a significant amount of development that can be done to improve the simulations of marine ice accretion. The porous features of marine ice layers observed beneath the Amery Ice Shelf are not included in the model but must significantly alter the interaction of the ice shelf with the ocean [Craven *et al.*, 2009]. Furthermore, the denser character of marine ice should prompt a re-evaluation of estimates of ice shelf draft significant for sub-ice ocean circulation studies. Since the deepest marine ice is highly permeable it may be more vulnerable to melt by intrusions of warmer seawater, and/or more vigorous circulation in the ice shelf cavity. Loss of these substantial marine ice layers could have a significant influence on ice shelf flow and sub-ice ocean circulation.
- Vertical mixing is a difficult parameter to correctly tune in ocean models. The testing of mixing schemes in the literature show that KPP, when bound, reproduced observations better than other schemes. This approach was used here. However, recent attempts to parametrise the convective plumes have placed negative buoyancy in the form of temperature and salinity directly at its neutral depth. Appropriate convective adjustment schemes are a topic of development in the ocean modelling community [for example, Timmermann and Beckmann, 2004; Timmermann and Losch, 2005]. Future ROMS applications in polar regions should consider such schemes for the parametrisation of sub-grid scale convective transport.

APPENDIX ONE

EQUATION OF STATE POLYNOMIALS

The EOS has 25 terms, which can be found in *Jackett et al.* [2006]. Its general form is motivated by that of *Wright* [1997]. Appendix B to *McDougall et al.* [2003] provides the following equation for local density written in terms of pressure, salinity, and potential temperature

$$\rho(s, \theta, p) = \frac{P_1(s, \theta, p)}{P_2(s, \theta, p)} \quad (1.1)$$

where p is the gauge pressure in units of decibars, θ is the potential temperature referenced to zero pressure in units of Celsius, and s is salinity as a practical salinity unit (psu). The salinity variable in ROMSv3.0 is interpreted as psu salinity, since this facilitates a more direct comparison with observations.

The polynomial functions P_1 and P_2 are given by

$$P_1 = a_0 + a_1\theta + a_2\theta^2 + a_3\theta^3 + a_4s + a_5s\theta + a_6s^2 + a_7p + a_8p\theta^2 + a_9ps + a_{10}p^2 + a_{11}p^2\theta^2 \quad (1.2a)$$

$$P_2 = b_0 + b_1\theta + b_2\theta^2 + b_3\theta^3 + b_4\theta^4 + b_5s + b_6s\theta + b_7s\theta^3 + b_8s^{3/2} + b_9s^{3/2}\theta^2 + b_{10}p + b_{11}p^2\theta^3 + b_{12}p^3\theta \quad (1.2b)$$

The coefficients a_n and b_n are tabulated in Appendix B of *Jackett et al.* [2006]. Rearrangement in order to reduce multiplications leads to

$$P_1 = a_0 + \theta(a_1 + \theta(a_2 + a_3\theta)) + s(a_4 + a_5\theta + a_6s) + p(a_7 + a_8\theta^2 + a_9s + p(a_{10} + a_{11}\theta^2)) \quad (1.3a)$$

$$P_2 = b_0 + \theta(b_1 + \theta(b_2 + \theta(b_3 + \theta b_4))) + s(b_5 + \theta(b_6 + b_7\theta^2) + s^{1/2}(b_8 + b_9\theta^2)) + p(b_{10} + p\theta(b_{11}\theta^2 + b_{12}p)) \quad (1.3b)$$

The density partial derivatives are

$$\left(\frac{\partial \rho}{\partial \theta}\right)_{s,p} = (P_2)^{-1} \left[\left(\frac{\partial P_1}{\partial \theta}\right)_{s,p} - \rho \left(\frac{\partial P_2}{\partial \theta}\right)_{s,p} \right] \quad (1.4a)$$

$$\left(\frac{\partial \rho}{\partial s}\right)_{\theta,p} = (P_2)^{-1} \left[\left(\frac{\partial P_1}{\partial s}\right)_{\theta,p} - \rho \left(\frac{\partial P_2}{\partial s}\right)_{\theta,p} \right] \quad (1.4b)$$

where $(P_2)^{-1}$ can be saved in a temporary array, thus reducing the number of divisions from four to one. The partial derivatives are given by

$$\left(\frac{\partial P_1}{\partial \theta}\right)_{s,p} = a_1 + 2a_2\theta + 3a_3\theta^2 + a_5s + 2a_8p\theta + 2a_{11}p^2\theta \quad (1.5a)$$

$$\left(\frac{\partial P_1}{\partial \theta}\right)_{\theta,p} = a_4 + a_5\theta + 2a_6s + a_9p \quad (1.5b)$$

$$\begin{aligned} \left(\frac{\partial P_2}{\partial \theta}\right)_{s,p} &= b_1 + 2b_2\theta + 3b_3\theta^2 + 4b_4\theta^3 + b_6s + 3b_7s\theta^2 + 2b_9s^{3/2}\theta \\ &\quad + 3b_{11}p^2\theta^2 + b_{12}p^3 \end{aligned} \quad (1.5c)$$

$$\left(\frac{\partial P_2}{\partial \theta}\right)_{\theta,p} = b_5 + b_6\theta + b_7\theta^3 + \frac{3}{2}b_8s^{1/2} + \frac{3}{2}b_9s^{1/2}\theta^2 \quad (1.5d)$$

with rearrangement leading to

$$\left(\frac{\partial P_1}{\partial \theta}\right)_{s,p} = a_1 + \theta(2a_2 + 3a_3\theta) + a_5s + 2p\theta(a_8 + a_{11}p) \quad (1.6a)$$

$$\left(\frac{\partial P_1}{\partial \theta}\right)_{\theta,p} = a_4 + a_5\theta + 2a_6s + a_9p \quad (1.6b)$$

$$\begin{aligned} \left(\frac{\partial P_2}{\partial \theta}\right)_{s,p} &= b_1 + \theta(2b_2 + \theta(3b_3 + 4b_4\theta)) + s(b_6 + \theta(3b_7\theta + 2b_9s^{1/2})) \\ &\quad + p^2(3b_{11}\theta^2 + b_{12}p) \end{aligned} \quad (1.6c)$$

$$\left(\frac{\partial P_2}{\partial \theta}\right)_{\theta,p} = b_5 + \theta(b_6 + b_7\theta^2 + \frac{3}{2}s^{1/2}(b_8 + b_9\theta^2)) \quad (1.6d)$$

Fig. 1.1 shows a comparison between the *in situ* density calculated using the original ROMS algorithm *Shchepetkin and McWilliams* [2003] and the EOS that was implemented as part of this study, from *Jackett et al.* [2006]. The errors between the truncated EOS used in ROMS are especially apparent at low temperatures for a range of salinities.

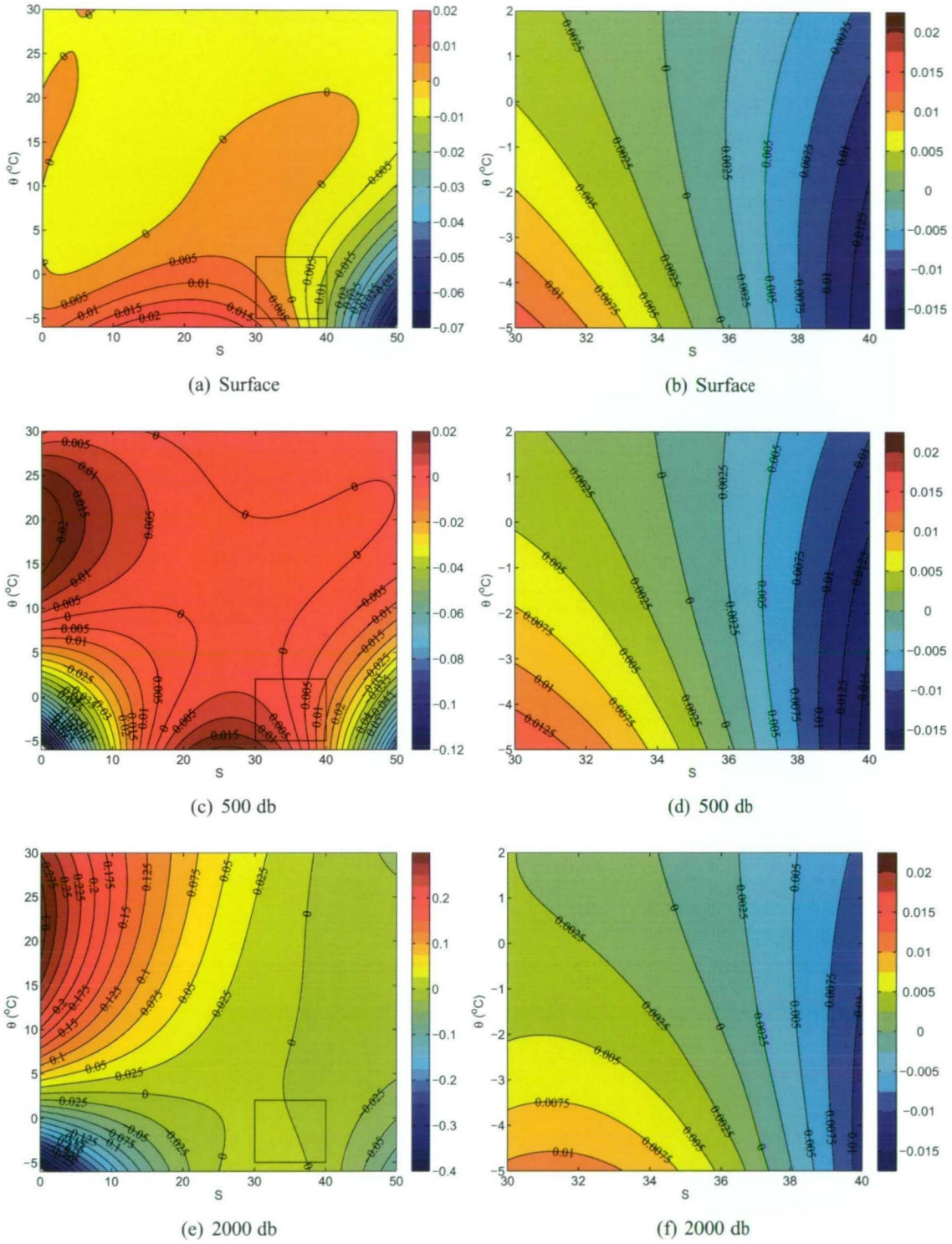


Figure 1.1: Errors in the evaluation of the *in situ* density at three different depths (0, 500 and 2000 db) over a range of potential temperatures and salinities for the global ocean (left column panels), the black boxes are shown for a range of potential temperature and salinities that reside in the polar oceans (right column panels). Following *Shchepetkin and McWilliams* [2003], the errors are defined as deviations of ρ_{insitu} that are calculated using the original ROMS EOS from the most up-to-date EOS *Jackett et al.* [2006], which are considered ‘exact’ in this comparison

REFERENCES

- Adcroft, A., and J. M. Campin, Rescaled height coordinates for accurate representation of free-surface flows in Ocean Circulation Models, *Ocean Modelling*, pp. 269–284, 2004.
- Adcroft, A., R. Hallberg, and M. Harrison, A finite volume discretization of the pressure gradient force using analytic integration, *Ocean Modelling*, 22, 106–113, 2008.
- Allison, I., The mass budget of the Lambert Glacier drainage basin, Antarctica, *Journal of Glaciology*, 22, 223–235, 1979.
- Allison, I., The AMISOR project: Ice shelf dynamics and ice-ocean interaction of the Amery Ice Shelf, *Report 14*, FRISP, 2003.
- Allison, I., R. Alley, H. Fricker, R. Thomas, and R. Warner, Ice sheet mass balance and sea level, *Antarctic Science*, *Forthcoming*, 1–14, 2006.
- Antonov, J. I., R. A. Locarnini, T. P. Boyer, A. V. Mishonov, and H. E. Garcia, World Ocean Atlas 2005, Volume 2: Salinity, S. Levitus, Ed. NOAA Atlas NESDIS 62, U.S. Government Printing Office, Washington, D.C., 182 pp., 2006.
- Aoki, S., S. R. Rintoul, S. Ushio, S. Watanabe, and N. L. Bindoff, Freshening of the Adélie Land Bottom Water near 140° E, *Geophysical Research Letters*, 32, 2005.
- Arakawa, A., and V. R. Lamb, Computational design of the basic dynamical process of the UCLA General Circulation Model, *Methods in Computational Physics*, pp. 173–265, 1977.
- Arthern, R. J., D. P. Winebrenner, and D. G. Vaughan, Antarctic snow accumulation mapped using polarization of 4.3-cm wavelength microwave emission, *Journal of Geophysical Research*, 111, 2006.
- Bardin, A. A. P., V. I., and N. A. Shmideberg, Hydrological and hydrochemical characteristics of deep water basins in Prince Charles Mountains, *Antarktika; doklady komisii*, 29, 97–112. [Russian with English summary], 1990.
- Beckmann, A., and D. B. Haidvogel, Numerical Simulation of Flow around a Tall Isolated Seamount. Part I: Problem Formulation and Model Accuracy, *Ocean Modelling*, 23, 1736–1753, 1993.
- Beckmann, A., H. H. Hellmer, and R. Timmermann, A numerical model of the Weddell Sea: Large-scale circulation and water mass distribution, *Journal of Geophysical Research*, 104, 23,375–23,391, 1999.
- Blumberg, A. F., and G. L. Mellor, *Three Dimensional Coastal Ocean Models*, vol. 4 of *Coastal and Estuarine Sciences*, chap. A description of a three-dimensional coastal circulation model, pp. 1–16, American Geophysical Union, 1987.

- Böning, C. W., A. Dispert, M. Visbeck, S. Rintoul, and F. U. Schwarzkopf, The response of the Antarctic Circumpolar Current to recent climate change, *Nature Geoscience*, 1, 864–869, 2008.
- Bromwich, D., Z. Liu, M. L. V. Woert, and A. N. Rogers, *Ocean, Ice, and Atmospheres: Interactions at the Antarctic Continental Margin*, vol. 75 of *Antarctic Research Series*, chap. Winter Atmospheric Forcing of the Ross Sea Polynya, pp. 1–27, American Geophysical Union, 1998.
- Budd, W. F., M. J. Corry, and T. H. Jacka, Results from the Amery Ice Shelf project, *Annals of Glaciology*, 3, 36–41, 1982.
- Cavalieri, D. J., and C. L. Parkinson, Antarctic sea ice variability and trends, 1979–2006, *Journal of Geophysical Research (Oceans)*, 113, 2008.
- Chu, P. C., and C. Fan, Sixth-order difference scheme for sigma coordinate ocean models, *Journal of Physical Oceanography*, 27, 2064–2071, 1997.
- Ciappa, A. C., An operational comparative test of z-level PGF schemes to reduce pressure gradient errors of the ocean model POM, *Ocean Modelling*, 12, 80–100, 2006.
- Craven, M., I. Allison, R. Brand, A. Elcheikh, J. Hunter, M. Hemer, and S. Donoghue, Initial borehole results from the Amery Ice Shelf hot water drilling project, in *Seventh International Symposium on Antarctic Glaciology*, 39A042, 2003a.
- Craven, M., A. Elcheikh, R. Brand, and I. Allison, Hot water drilling on the Amery Ice Shelf, East Antarctica, *Tech. Rep. 14*, FRISP Report, 2003b.
- Craven, M., F. Carsey, and S. Nicol, Ice krill under the Amery Ice Shelf, East Antarctica, *Antarctic Science*, 18, 81–82, 2006.
- Craven, M., I. Allison, H. Fricker, and R. Warner, Properties of a marine ice layer under the Amery Ice Shelf, East Antarctica, *Journal of Glaciology*, 55, 717–728, 2009.
- Daly, S. F., Frazil ice dynamics, *CRREL monograph 84(1)*, USA Cold Regions Research and Engineering Laboratory, 1984.
- Darelius, E., L. Smedsrud, S. Østerhus, A. Foldvik, and T. Gammelsrød, Structure and Variability of the Filchner Overflow Plume, *Tellus A*, 61A, 446–464, 2009.
- De Angelis, H., and P. Skvarca, Glacier Surge After Ice Shelf Collapse, *Science*, 299, 1560–1563, 2003.
- Determann, J., Numerical modelling of ice shelf dynamics, *Antarctic Science*, 3, 187–195, 1991.
- Determann, J., and R. Gerdes, Melting and freezing beneath ice shelves: Implications from a three-dimensional ocean-circulation model, *Annals of Glaciology*, 20, 413–419, 1994.
- Dinniman, M. S., J. M. Klinck, and W. O. S. Jr., Cross-shelf exchange in a model of the Ross Sea circulation and biogeochemistry, *Deep Sea Research II*, 50, 3103–312, 2003.
- Dinniman, M. S., J. M. Klinck, and W. O. S. Jr., Influence of sea ice cover and icebergs

- on circulation and water mass formation in a numerical circulation model of the Ross Sea, Antarctica, *Journal of Geophysical Research*, 112, 2007.
- Domingues, C. M., J. A. Church, N. J. White, P. J. Gleckler, S. E. Wijffels, P. M. Barker, and J. R. Dunn, Improved estimates of upper-ocean warming and multi-decadal sea-level rise, *Nature*, 453, 1090–1093, 2008.
- Drazin, P. G., and W. H. Reid, *Fundamentals of Heat and Mass Transfer*, 2nd Ed., Cambridge University Press, 605 p., Second Edition, 2004.
- Dupont, T. K., and R. B. Alley, Assessment of the importance of ice-shelf buttressing to ice-sheet flow, *Geophysical Research Letters*, 32, 2005.
- Dutay, J., et al., Evaluation of ocean model ventilation with CFC-11: comparison of 13 global ocean models, *Ocean Modelling*, 4, 89–120, 2002.
- Egbert, G., A. Bennett, and M. Foreman, TOPEX/Poseidon tides estimated using a global inverse model, *Journal of Geophysical Research*, 99, 821–852, 1994.
- Ezer, T., H. Arango, and A. F. Shchepetkin, Developments in terrain-following ocean models: Intercomparisons of numerical aspects, *Ocean Modelling*, 4, 249–267, 2002.
- Feistel, R., Equilibrium thermodynamics of seawater revisited, *Progress in Oceanography*, 31, 101–179, 1993.
- Feistel, R., A new extended Gibbs thermodynamic potential of seawater, *Progress in Oceanography*, 58, 43–114, 2003.
- Feistel, R., and E. Hagen, On the Gibbs thermodynamic potential of seawater, *Progress in Oceanography*, 36, 249–327, 1995.
- Foldvik, A., and T. Kvinge, Conditional instability of sea water at the freezing point, *Deep Sea Research*, 21, 229–243, 1974.
- Foldvik, A., T. Gammelsrød, E. Nygaard, and S. Østerhus, Current measurements near Ronne Ice Shelf: Implications for circulation and melting, *Journal of Geophysical Research*, 106, 4463–4478, 2001.
- Fortunato, A. B., and A. M. Baptista, Evaluation of horizontal gradients in sigma-coordinate shallow water models, *Atmosphere and Ocean*, 34, 489–514, 1996.
- Fox, A. J., and A. P. R. Cooper, Measured properties of the Antarctic ice sheet derived from the SCAR Antarctic digital database, *Polar Record*, 30, 201–206, 1994.
- Fraser, A. D., R. A. Massom, and K. J. Michael, A Method for Compositing Polar MODIS Satellite Images to Remove Cloud Cover for Landfast Sea-Ice Detection, *IEEE Transactions on Geoscience and Remote Sensing*, 47, 2009.
- Fricker, H., R. Coleman, L. Padman, T. Scambos, and J. Bohlander, Mapping the grounding zone of the Amery Ice Shelf, East Antarctica, using InSAR, MODIS, and ICESat, *Antarctic Science*,

in press, 2009.

- Fricker, H. A., G. Hyland, R. Coleman, and N. W. Young, Digital elevation models for the Lambert Glacier-Amery Ice Shelf system, East Antarctica, from ERS-1 satellite radar altimetry, *Journal of Glaciology*, 46, 553–560, 2000.
- Fricker, H. A., S. Popov, I. Allison, and N. Young, Distribution of marine ice beneath the Amery Ice Shelf, *Geophysical Research Letters*, 28, 2241–2244, 2001.
- Fricker, H. A., N. W. Young, I. Allison, and R. Coleman, Iceberg calving from the Amery Ice Shelf, East Antarctica, *Annals of Glaciology*, 34, 241–246, 2002a.
- Fricker, H. A., et al., Redefinition of the Amery Ice Shelf, East Antarctica, grounding zone, *Journal of Geophysical Research*, 107, ECV, 2002b.
- Gade, H. G., Melting of Ice in Sea Water: A Primitive Model with Application to the Antarctic Ice Shelf and Icebergs, *Journal of Physical Oceanography*, 9, 189–198, 1979.
- Galton-Fenzi, B. K., J. Hunter, and R. Coleman, Frazil ice beneath ice shelves in a three-dimensional ocean model, in *FRISP/WAIS report*, edited by L. Smedrud, Forum for Research into Ice Shelf Processes, 2008a.
- Galton-Fenzi, B. K., C. Maraldi, R. Coleman, and J. Hunter, The cavity under the Amery Ice Shelf, East Antarctica, *Journal of Glaciology*, 54, 2008b.
- Gerdes, R., J. Determann, and K. Grosfeld, Ocean circulation beneath Filchner-Ronne Ice Shelf from three-dimensional model results, *Journal of Geophysical Research*, 104, 15,827–15,842, 1999.
- Gibson, J. A. E., and T. W. Trull, Annual cycle of fCO₂ under sea-ice and in open water in Prydz Bay, East Antarctica, *Marine Chemistry*, 66, 187–200, 1999.
- Gill, A. E., Circulation and bottom water production in the Weddell Sea, *Modern Concepts of Oceanography*, 1982.
- Gille, S. T., Warming of the Southern Ocean Since the 1950s, *Science*, 295, 1275–1278, 2002.
- Gosink, J. P., and T. E. Osterkamp, Measurements and analyses of velocity profiles and frazil ice-crystal rise velocities during periods of frazil-ice formation in rivers, *Annals of Glaciology*, 4, 79–84, 1983.
- Griffies, S. M., M. J. Harrison, R. C. Pacanowski, and A. Rosati, A Technical Guide to MOM4, *Tech. Rep. 5*, NOAA/Geophysical Fluid Dynamics Laboratory, www.gfdl.noaa.gov, 2004.
- Grosfeld, K., and H. Sandhager, The evolution of a coupled ice shelf-ocean system under different climate states, *Global and Planetary Change*, 42, 107–132, 2004.
- Grosfeld, K., R. Gerdes, and J. Determann, Thermohaline circulation and interaction between ice shelf cavities and the adjacent open ocean, *Journal of Geophysical Research*, 102, 15,595–15,610, 1997.

- Grosfeld, K., H. Sandager, and M. A. Lange, Sensitivity of a coupled ice-shelf/ocean system to changed oceanographic boundary conditions, *Tech. Rep. 14*, FRISP Report, 2001.
- Hallberg, R., A thermobaric instability of Lagrangian vertical coordinate ocean models, *Ocean Modelling*, 8, 279–300, 2005.
- Hammar, L., and H. T. Shen, Frazil evolution in channels, *Journal of Hydraulic Research*, 33, 291–306, 1995.
- Haney, R. L., On the pressure gradient force over steep topography in sigma coordinate ocean models, *Journal of Physical Oceanography*, 21, 610–619, 1991.
- Hedstrom, K. S., *User's manual for an S-Coordinate Primitive Equation Ocean Circulation Model (SCRUM) Version 3.0*, Institute of Marine and Coastal Sciences, Rutgers University, 1997.
- Heil, P., and I. Allison, The pattern and variability of Antarctic sea-ice drift in the Indian Ocean and western Pacific sectors, *Journal of Geophysical Research*, 104, 15,789–15,802, 1999.
- Held, I. M., and B. J. Soden, Robust Responses of the Hydrological Cycle to Global Warming, *Journal of Climate*, 19, 2006.
- Hellmer, H. H., Impact of Antarctic ice shelf basal melting on sea ice and deep ocean properties, *Geophysical Research Letters*, 31, 2004.
- Hellmer, H. H., and S. S. Jacobs, Ocean interactions with the base of the Amery Ice Shelf, Antarctica, *Journal of Geophysical Research*, 97, 20,305–20,317, 1992.
- Hellmer, H. H., and D. Olbers, A two-dimensional model for the thermohaline circulation under an ice shelf, *Antarctic Science*, 1, 325–33, 1989.
- Hellmer, H. H., S. S. Jacobs, and A. Jenkins, *Ocean, Ice and Atmosphere Interactions at the Continental Margin*, vol. 75 of *Antarctic Research Series*, chap. Oceanic erosion of a floating Antarctic glacier in the Amundsen Sea, American Geophysical Union, Washington, United States, 1998.
- Helm, K. P., Decadal ocean water mass changes: global observations and interpretation, Phd, Institute for Antarctic and Southern Ocean Studies, University of Tasmania, 2008.
- Hemer, M., and P. T. Harris, Sediment core from beneath the Amery Ice Shelf, East Antarctica, suggests mid-Holocene ice-shelf retreat, *Geology*, 312, 127–130, 2003.
- Hemer, M., J. Hunter, and R. Coleman, Barotropic tides beneath the Amery Ice Shelf, *Journal of Geophysical Research*, 111, doi: 10.1029/2006JGRC.11111,008H, 2006.
- Holland, D. M., An impact of sub-grid-scale ice-ocean dynamics on sea-ice cover, *Journal of Climate*, 14, 1585–1601, 2001.
- Holland, D. M., Computing marine-ice thickness at an ice-shelf base, *Journal of Glaciology*, 48, 9–19, 2002.
- Holland, D. M., and A. Jenkins, Modeling thermodynamic ice-ocean interactions at the base of an

- ice shelf, *Journal of Physical Oceanography*, 29, 1787–1800, 1999.
- Holland, D. M., and A. Jenkins, Adaptation of an isopycnic coordinate ocean model for the study of circulation beneath ice shelves, *Monthly Weather Review*, 129, 1905–1927, 2001.
- Holland, D. M., S. S. Jacobs, and A. Jenkins, Modelling the ocean circulation beneath the Ross Ice Shelf, *Antarctic Science*, 15, 13–23, 2003.
- Holland, P. R., and D. L. Feltham, Frazil dynamics and precipitation in a water column with depth-dependent supercooling, *Journal of Fluid Mechanics*, 530, 101–124, 2005.
- Holland, P. R., and D. L. Feltham, The effects of rotation and ice shelf topography on frazil-laden ice shelf water plumes, *Journal of Physical Oceanography*, 36, 2312–2327, 2006.
- Holland, P. R., D. L. Feltham, and S. Daly, On the Nusselt number for frazil ice growth a correction to Frazil evolution in channels by Lars Hhammar and Hung-Tao Shen, *Journal of Hydraulic Research*, 45, 421–424, 2007.
- Holland, P. R., A. Jenkins, and D. M. Holland, The response of ice shelf basal melting to variation in ocean temperature, *Journal of Climate*, in press, 2008.
- Holland, P. R., H. F. J. Corr, D. G. Vaughan, A. Jenkins, and P. Skvarca, Marine ice in Larsen Ice Shelf, *Geophysical Research Letters*, 36, 2009.
- Hunter, J., M. Hemer, and M. Craven, Modelling the circulation under the Amery Ice Shelf, *Tech. Rep. 15*, FRISP, 2004.
- Hunter, J. R., *Specification for test models of ice shelf cavities*, Antarctic Climate and Ecosystems Cooperative Research Centre, Hobart, Australia, available at http://staff.acecrc.org.au/johunter/isomip/test_cavities.pdf ed., 2006.
- Incropera, F. P., and D. P. DeWitt, *Fundamentals of Heat and Mass Transfer*, John Wiley & Sons, New York. p. 919 + appendices, 1990.
- IOC, I., and BODCM, Centenary Edition of the GEBCO Digital Atlas, published on CD-ROM on behalf of the Intergovernmental Oceanographic Commission and the International Hydrographic Organization as part of the General Bathymetric Chart of the Oceans, British Oceanographic Data Centre, Liverpool, U.K., 2003.
- IPCC, *Climate Change 2001: The Scientific Basis*, Cambridge University Press, Cambridge, England, 2001.
- IPCC, *Climate Change 2007: The Physical Science Basis. Contribution of Working Group I to the Fourth Assessment Report of the Intergovernmental Panel on Climate Change*, Cambridge University Press, Cambridge, United Kingdom and New York, NY, USA, 966 pp., 2007.
- Jacka, T. H., and W. F. Budd, Detection of temperature and sea-ice-extent changes in the Antarctic and Southern Ocean, 1949–96, *Annals of Glaciology*, 27, 553–559, 1998.
- Jackett, D. R., and T. J. McDougall, Minimal adjustment of hydrographic profiles to achieve static

- stability, *Journal of Atmospheric and Oceanic Technology*, 12, 381–389, 1995.
- Jackett, D. R., and T. J. McDougall, A Neutral Density Variable for the World's Oceans, *Journal of Physical Oceanography*, 27, 237–263, 1997.
- Jackett, D. R., T. J. McDougall, R. Feistel, S. G. Wright, and S. M. Griffies, Algorithms of Density, Potential Temperature, Conservative Temperature, and the Freezing Temperature of Seawater, *Journal of Atmospheric and Oceanic Technology*, 23, 1709–1728, 2006.
- Jacobs, S. S., Bottom water production and its link with the thermohaline circulation, *Antarctic Science*, 16, 427–437, 2004.
- Jacobs, S. S., and J. C. Comiso, Sea ice and oceanic process on the Ross Sea continental shelf, *Journal of Geophysical Research*, 94, 18,195–18,211, 1989.
- Jacobs, S. S., H. H. Helmer, C. S. M. Doake, A. Jenkins, and R. M. Frolich, Melting of ice shelves and the mass balance of Antarctica, *Journal of Climate*, 38, 375–387, 1992.
- Jacobs, S. S., C. F. Giulivi, and P. A. Mele, Freshening of the Ross Sea during the late 20th century, *Science*, 297, 386–389, 2002.
- Jenkins, A., A one-dimensional model of ice shelf-ocean interaction, *Journal of Geophysical Research*, 96, 20,671–20,677, 1991.
- Jenkins, A., and A. Bombosch, Modelling the effects of frazil ice crystals on the dynamics and thermodynamics of Ice Shelf Water plumes, *Journal of Geophysical Research*, 100, 6,967–6,981, 1995.
- Jenkins, A., and D. Holland, Melting of floating ice and sea level rise, *Geophysical Research Letters*, 34, 2007.
- Jenkins, A., and D. M. Holland, A model study of ocean circulation beneath Filchner-Ronne Ice Shelf, Antarctica: Implications for bottom water formation, *Geophysical Research Letters*, 29, 34–1–34–4, 2002.
- Jenkins, A., H. H. Hellmer, and D. M. Holland, The role of meltwater advection in the formulation of conservative Boundary Conditions at an Ice-Ocean Interface, *Journal of Physical Oceanography*, 31, 285–296, 2001.
- Jenkins, A., D. M. Holland, K. W. Nicholls, M. Schroder, and S. Osterhus, Seasonal ventilation of the cavity beneath Filchner-Ronne Ice Shelf simulated with an isopycnic coordinate ocean model, *Journal of Geophysical Research*, 109, 1–12, 2004.
- Jezek, K., and R. P. Team, RAMP AMM-1 SAR Image Mosaic of Antarctica, Fairbanks, AK: Alaska SAR Facility, in association with the National Snow and Ice Data Center, Boulder, CO. Digital media, 2002.
- Johanson, C. M., and Q. Fu, Antarctic atmospheric temperature trend patterns from satellite observations, *Geophysical Research Letters*, 34, 2007.

- Joughin, I., E. Rignot, C. E. Rosanova, B. K. Lucchitta, and J. Bohlander, Timing of Recent Accelerations of Pine Island Glacier, Antarctica, *Geophysical Research Letters*, 30, 2003.
- Kanamitsu, M., W. Ebisuzaki, J. Woollen, S. Yang, J. J. Hnilo, M. Fiorino, and G. L. Potter, NCEP-DOE AMIP-II Reanalysis (R-2), *Bulletin of the American Meteorological Society*, 83, 1631–1643, 2002.
- King, M., Kinematic and static GPS techniques for estimating tidal displacements with application to Antarctica, *Journal of Geophysical Research*, 41, 77–86, 2006.
- King, M. A., R. Coleman, P. J. Morgan, and R. S. Hurd, Velocity change of the Amery Ice Shelf, East Antarctica, during the period 1968-1999, *Journal of Geophysical Research (Earth Surface)*, 112, 2007.
- King, M. A., R. Coleman, A.-J. Freemantle, H. A. Fricker, R. S. Hurd, B. Legrésy, L. Padman, and R. Warner, A 4-decade record of elevation change of the Amery Ice Shelf, East Antarctica, *Journal of Geophysical Research (Earth Surface)*, 114, 2009.
- Klocker, A., T. McDougall, and D. R. Jackett, A new method for forming approximately neutral surfaces, *Ocean Science*, in press, 2009.
- Kwok, R., and J. C. Comiso, Spatial patterns of variability in Antarctic surface temperature: Connections to the Southern Hemisphere Annular Mode and the Southern Oscillation, *Geophysical Research Letters*, 29, 50–1–50–4, 2002.
- Large, W. G., J. C. McWilliams, and S. C. Doney, Oceanic vertical mixing: A review and model with a nonlocal boundary layer parameterization, *Reviews of geophysics*, 32, 363–403, 1994.
- Le Provost, C., and P. Vincent, Some tests of precision for a finite element model of ocean tides, *Journal of Computational Physics*, 65, 273–291, 1986.
- Leffanue, H., and M. Craven, Circulation and water masses from current meter and T/S measurements at the Amery Ice Shelf, *Tech. Rep. 15*, FRISP, 2004.
- Lemke, P., et al., *Climate Change 2007: The Physical Science Basis. Contribution of Working Group I to the Fourth Assessment Report of the Intergovernmental Panel on Climate Change*, chap. Observations: Changes in snow, ice and frozen ground, pp. 337–383, Cambridge Univ. Press, New York, 2007.
- Levitus, S., J. I. Antonov, T. P. Boyer, and C. Stephens, Warming of the World Ocean, *Science*, 287, 2225–2229, 2000.
- Lewis, E. L., *Effect of a CO₂-Induced Climate Change*, vol. 43 of Rep. DOE/EV/60235-1, chap. The Ice Pump; a mechanism for ice-shelf melting, glaciers, ice sheets, and sea level, pp. 275–278, U.S. Dept. of Energy, 1985.
- Little, C. M., A. Gnanadesikan, and R. Hallberg, Large-Scale Oceanographic Constraints on the Distribution of Melting and Freezing under Ice Shelves, *Journal of Physical Oceanography*, 38, 2008.

- Locarnini, R. A., A. V. Mishonov, J. I. Antonov, T. P. Boyer, and H. E. Garcia, World Ocean Atlas 2005, Volume 1: Temperature, S. Levitus, Ed. NOAA Atlas NESDIS 61, U.S. Government Printing Office, Washington, D.C., 182 pp., 2006.
- Losch, M., Modeling Ice Shelf Cavities in a z-Coordinate Ocean General Circulation Model, *Journal of Geophysical Research*, 2008.
- Lyard, F., F. Lefebvre, T. Letellier, and O. Francis, Modelling the global ocean tides: modern insights from FES2004., *56*, 394–415, 2006.
- Lythe, M. B., D. G. Vaughan, and the Bedmap Consortium, Bedmap - bed topography of the Antarctic, 1:10000000 scale map., BAS (misc) 9, Cambridge, British Antarctic Survey., 2000.
- MacAyeal, D. R., Numerical simulations of the Ross Sea tides, *Journal of Geophysical Research*, *89*, 607–615, 1984.
- MacAyeal, D. R., *Oceanology of the Antarctic Continental Shelves*, vol. 43 of *Antarctic Research Series*, chap. Evolution of tidally triggered meltwater plumes below ice shelves, pp. 109–132, 1985.
- Maraldi, C., B. Galton-Fenzi, F. Lyard, L. Testut, and R. Coleman, Barotropic tides of the Southern Indian Ocean and the Amery Ice Shelf cavity, *Geophysical Research Letters*, *34*, 2007.
- Marchesiello, P., J. C. McWilliams, and A. Shchepetkin, Open boundary conditions for long-term integration of regional ocean models, *Ocean Modelling*, *3*, 1–20, 2001.
- Marsland, S. J., N. L. Bindoff, G. D. Williams, and W. F. Budd, Modeling water mass formation in the Mertz Glacier Polynya and Adelie Depression, East Antarctica, *Journal of Geophysical Research*, *109*, 2004.
- Marsland, S. J., J. A. Church, N. L. Bindoff, and G. D. Williams, Antarctic coastal polynya response to climate change, *Journal of Geophysical Research (Oceans)*, *112*, 2007.
- Martin, S., and P. Kauffman, A field and laboratory study of wave damping by grease ice, *Journal of Glaciology*, *27*, 283–313, 1981.
- Massom, R., Recent iceberg calving events in the Ninnis Glacier region, East Antarctica, *Antarctic Science*, *15*, 2003.
- Massom, R. A., P. T. Harris, K. J. Michael, and M. J. Potter, The distribution and formative processes of latent-heat polynyas in East Antarctica, *Annals of Glaciology*, *27*, 420–426, 1998.
- McCave, I. N., and S. A. Swift, A physical model for the rate of deposition of fine-grained sediments in the deep sea, *GSA Bulletin*, *87(4)*, 541–546, 1976.
- McDougall, T. J., D. R. Jackett, D. G. Wright, and R. Feistel, Accurate and computationally efficient algorithms for potential temperature and density of seawater, *Journal of Atmospheric and Oceanic Technology*, *20*, 730–741, 2003.
- McMahon, L., and M. A. Lackie, Seismic reflection studies of the Amery Ice Shelf, East

- Antarctica: delineating meteoric and marine ice, *Geophys. J. Int.*, 166, 757–766, 2006.
- Meijers, A., A. Klocker, N. L. Bindoff, G. D. Williams, and S. J. Marsland, The circulation and water masses of the Antarctic shelf and continental slope between 30 and 80°E, *Deep Sea Research Part II*, in press, 2009.
- Mellor, G. L., L. Y. Oey, and T. Ezer, Sigma coordinate pressure gradient errors and the seamount problem, *Journal of Atmospheric and Oceanic Technology*, 6, 1122–1131, 1998.
- Mellor, G. L., S. Hakkinen, T. Ezer, and R. Patchen, *A generalization of a sigma coordinate ocean model and an intercomparison of model vertical grids*, vol. Ocean forecasting: Conceptual basis and applications, chap. 4, pp. 55–72, Springer, Berlin, 2002.
- Menemenlis, D., J.-M. Campin, P. Heimbach, C. Hill, T. Lee, A. Nguyen, M. Schodlock, and H. Zhang, ECCO2: High resolution global ocean and sea ice data synthesis., *Mercator Ocean Quarterly Newsletter*, 31, 13–21, 2008.
- Meredith, M. P., A. J. Watson, K. A. Van Scoy, and T. W. N. Haine, Chlorofluorocarbon-derived formation rates of the deep and bottom waters of the Weddell Sea, *Journal of Geophysical Research*, 106, 2899–2919, 2001.
- Monaghan, A. J., D. H. Bromwich, W. Chapman, and J. C. Comiso, Recent variability and trends of Antarctic near-surface temperature, *Journal of Geophysical Research (Atmospheres)*, 113, 2008.
- Morrow, R., R. Coleman, J. Church, and D. Chelton, Surface Eddy Momentum Flux and Velocity Variances in the Southern Ocean from Geosat Altimetry, *Journal of Physical Oceanography*, 24, 2050–2071, 1994.
- Morse, B., and M. Richard, A field study of suspended frazil ice particles, *Cold Regions Science and Technology*, 55, 86–102, 2009.
- Murray, M. T., A general method for the analysis of hourly heights of the tide, *International Hydrographic Review*, 41, 91–101, 1964.
- Noerdlinger, P. D., and K. R. Brower, The melting of floating ice raises the ocean level, *Geophysical Journal International*, 170, 145–150, 2007.
- Nunes Vaz, R. A., and G. W. Lennon, Physical Oceanography of the Prydz Bay region of Antarctic waters, *Deep Sea Research Part I*, 43, 603–641, 1996.
- O'Brien, P. E., I. Goodwin, C. F. Forsberg, A. K. Cooper, and J. Whitehead, Late Neogene ice drainage changes in Prydz Bay, East Antarctica and the interaction of Antarctic ice sheet evolution and climate, *Paleogeography*, 245, 390–410, 2007.
- Ohshima, K. I., T. Tamura, Y. Fukamachi, and S. Aoki., Sea ice production in the polynya and the associated bottom water formation off the Cape Damley, East Antarctica, Abstract volume of 9th International Conference on Southern Hemisphere Meteorology and Oceanography, Melbourne, Australia, 2009.

- Oreskes, N., K. Shrader-Frechette, and K. Belitz, Verification, Validation, and Confirmation of Numerical Models in the Earth Sciences, *Science*, 263, 641–646, 1994.
- Orheim, O., Antarctic icebergs—production, distribution and disintegration, *Annals of Glaciology*, 11, 205–205, 1988.
- Pacanowski, R., and A. Gnanadesikan, Transient response in a z-level ocean model that resolves topography with partial-cells, *Monthly Weather Review*, 126, 3248–3270, 1998.
- Padman, L., H. A. Fricker, R. Coleman, S. Howard, and L. Erofeeva, A new tide model for the Antarctic ice shelves and seas, *Annals of Glaciology*, 34, 2002.
- Parkinson, C. L., Aqua: an earth-observing satellite mission to examine water and other climate variables, *IEEE Transactions on Geoscience and Remote Sensing*, 41, 173–183, 2003.
- Penrose, J. D., M. Conde, and T. J. Pauly, Acoustic detection of ice crystals in Antarctic waters, *Journal of Geophysical Research*, 99, 12,373–12,380, 1994.
- Pitts, D. R., and L. E. Sissom, *Schaum's Outline of theory and problems of heat transfer*, McGraw-Hill, p.325, 1977.
- Preisendorfer, R. W., *Principal Component Analysis in Meteorology and Oceanography*, Elsevier, Amsterdam, pp.924., 1988.
- Press, W. H., B. P. Flannery, S. A. Teukolsky, W. T. Vetterling, and P. B. Kramer, *Numerical Recipes: The Art of Scientific Computing*, Cambridge University Press, Cambridge, United Kingdom and New York, NY, USA, 818 pp., 1987.
- Reigber, C., R. Schmidt, F. Flechtner, R. Knig, U. Meyer, K.-H. Neumayer, P. Schwintzer, and S. Y. Zhu, An Earth gravity field model complete to degree and order 150 from GRACE: EIGEN-GRACE02S, *Journal of Geodynamics*, 39, 2005.
- Riddle, M. J., M. Craven, P. M. Goldsworthy, and F. Carsey, A diverse benthic assemblage 100 km from open water under the Amery Ice Shelf, Antarctica, *Paleoceanography*, 22, 2007.
- Rignot, E., Fast recession of a West Antarctic glacier, *Science*, 281, 549–551, 1998.
- Rignot, E., Mass balance of East-Antarctic glaciers and ice shelves from satellite data, *Annals of Glaciology*, 34, 217–168, 2002a.
- Rignot, E., East Antarctic glaciers and ice shelves mass balance from satellite data, *Annals of Glaciology*, 34, 228–234, 2002b.
- Rignot, E., and S. S. Jacobs, Rapid bottom melting widespread near Antarctic ice sheet grounding lines, *Science*, 296, 2020–2023, 2002.
- Rignot, E., G. Casassa, P. Gogineni, W. Krabill, A. Rivera, and R. Thomas, Accelerated discharge from the Antarctic Peninsula following the collapse of Larsen B ice shelf, *Geophysical Research Letters*, 31, 2004.
- Rintoul, S., Rapid freshening of Antarctic Bottom Water formed in the Indian and Pacific oceans,

- Geophysical Research Letters*, 34, 2007.
- Sabine, C. L., et al., The Oceanic Sink for Anthropogenic CO₂, *Science*, 305, 367–371, 2004.
- Scambos, T. A., J. A. Bohlander, C. A. Shuman, and P. Skvarca, Glacier acceleration and thinning after ice sheet collapse in the Larsen B embayment, Antarctica, *Geophysical Research Letters*, 31, 2004.
- Scambos, T. A., T. M. Haran, M. A. Fahnestock, T. H. Painter, and J. Bohlander, MODIS-based Mosaic of Antarctica (MOA) data sets: Continent-wide surface morphology and snow grain size, *Remote Sensing of Environment*, 111, 242–257, 2007.
- Scheduikat, M., and D. J. Olbers, A one-dimensional mixed layer model beneath the Ross Ice Shelf with tidally induced vertical mixing, *Antarctic Science*, 2(1), 29–42, 1990.
- Schmidt, G. A., C. M. Bitz, U. Mikolajewicz, and L. B. Tremblay, Ice-ocean boundary conditions for coupled models, *Ocean Modelling*, 7, 59–74, 2004.
- Shchepetkin, A. F., and J. C. McWilliams, Quasi-Monotone Advection Schemes Based on Explicit Locally Adaptive Dissipation, *Monthly Weather Review*, 126, 1998.
- Shchepetkin, A. F., and J. C. McWilliams, A method for computing horizontal pressure-gradient force in an oceanic model with a non-aligned vertical coordinate, *Journal of Geophysical Research*, 108, 2003.
- Shchepetkin, A. F., and J. C. McWilliams, The regional oceanic modeling system (ROMS): A split-explicit, free-surface, topography-following-coordinate oceanic model, *Ocean Modelling*, 9, 347–404, 2005.
- Shepherd, A., D. Wingham, T. Payne, and P. Skvarca, Larsen Ice Shelf has progressively thinned, *Science*, 302, 856–859, 2003.
- Shepherd, A., D. Wingham, and E. Rignot, Warm ocean is eroding West Antarctic Ice Sheet, *Geophysical Research Letters*, 31, 2004.
- Sherwood, C. R., Numerical model of frazil ice and suspended sediment concentrations and formation of sediment laden ice in the Kara Sea, *Journal of Geophysical Research*, 105, 14,061–14,080, 2000.
- Smedsrud, L. H., A model for entrainment of sediment into sea ice by aggregation between frazil-ice crystals and sediment grains, *Journal of Climate*, 48, 51–61, 2002.
- Smedsrud, L. H., and A. Jenkins, Frazil ice formation in an ice shelf water plume, *Journal of Geophysical Research*, 109, 1–15, 2004.
- Steig, E. J., D. P. Schneider, S. D. Rutherford, M. E. Mann, J. C. Comiso, and D. T. Shindell, Warming of the Antarctic ice-sheet surface since the 1957 International Geophysical Year, *Nature*, 457, 459–462, 2009.
- Stössel, A., M. M. Stössel, and J.-T. Kim, High-resolution sea ice in long-term global ocean GCM

- integrations, *Ocean Modelling*, 16, 206–223, 2007.
- Tamura, T., K. I. Ohshima, and S. Nihashi, Mapping of sea ice production for Antarctic coastal polynyas, *Geophysical Research Letters*, 35, 7606–+, 2008.
- Tassell, H., Seismic investigations into the ice thickness and seabed topography beneath the Amery Ice Shelf, East Antarctica, Honours thesis, Maths and Physics, University of Tasmania, Hobart, Tasmania, Australia., 2004.
- Thiem, O., and J. Bernsten, Internal pressure errors in sigma-coordinate ocean models due to anistropy, *Ocean Modelling*, 12, 140–156, 2006.
- Thomas, R., et al., Accelerated sea-level rise from West Antarctica, *Science*, 306, 255–258, 2004.
- Thomas, R. H., Ice shelves: A review, *Journal of Glaciology*, 24, 273–286, 1979.
- Tiem, O., and J. Berntsen, Internal pressure errors in sigma-coordinate ocean models due to anisotropy, *Ocean Modelling*, 12(1-2), 140–156, 2006.
- Timmermann, R., and A. Beckmann, Parameterization of vertical mixing in the Weddell Sea, *Ocean Modelling*, 6(1), 83–100, 2004.
- Timmermann, R., and M. Losch, Using the MellorYamada mixing scheme in seasonally ice-covered seas – Corrigendum to: Parameterization of vertical mixing in the Weddell Sea, *Ocean Modelling*, 10(3–4), 369–372, 2005.
- Timmermann, R., A. Beckmann, and H. H. Hellmer, Simulations of ice-ocean dynamics in the Weddell Sea 1. Model configuration and validation, *Journal of Geophysical Research*, C, doi:10.1029/2000JC000,741, 2002.
- Uppala, S. M., et al., The ERA-40 re-analysis, *Quarterly Journal of the Royal Meteorological Society*, 131, 2961–3012, 2005.
- Vaughan, D. G., J. L. Bamber, M. Giovinetto, J. Russell, and A. P. R. Cooper, Reassessment of Net Surface Mass Balance in Antarctica., *Journal of Climate*, 12, 933–946, 1999.
- Watterson, I. G., M. Dix, H. Gordon, and J. McGregor, The CSIRO nine-level atmospheric general circulation model and its equilibrium present and double CO₂ climates, *Aust. Meteorol. Mag.*, pp. 111–125, 1995.
- Wen, J., K. C. Jezek, B. M. Csatho, U. C. Herzfeld, K. L. Farness, and P. Huybrechts, Mass budgets of the Lambert, Mellor and Fisher Glaciers and basal fluxes beneath their flowbands on Amery Ice Shelf, *Science in China D*, 50, 1693–1706, 2007.
- Wen, J., Y. Wang, J. Liu, K. C. Jezek, P. Huybrechts, B. M. Csatho, K. L. Farness, and B. Sun, Mass budget of the grounded ice in the Lambert Glacier-Amery Ice Shelf system, *Annals of Glaciology*, 48, 2008.
- White, F. M., *Viscous Fluid Flows*, McCraw–Hill Book Company, 1974.
- Whitworth, T., A. H. Orsi, J. Kim, W. D. N. Jr., and R. A. Locarnini, *Ocean, Ice, and Atmospheres:*

- Interactions at the Antarctic Continental Margin*, vol. 75 of *Antarctic Research Series*, chap. Water masses and mixing near the Antarctic Slope Front, pp. 1–27, American Geophysical Union, 1998.
- Wilkin, J., and K. S. Hedström, Users manual for an orthogonal curvilinear grid-generation package., *Report*, Institute of Marine and Coastal Sciences, Rutgers University, 31pp, 1998.
- Wilkin, J. L., and R. A. Morrow, Eddy kinetic energy and momentum flux in the Southern Ocean: Comparison of a global eddy-resolving model with altimeter, drifter, and current-meter data, *Journal of Geophysical Research*, 99, 7903–7916, 1994.
- Williams, G. D., N. L. Bindoff, S. J. Marsland, and S. R. Rintoul, Formation and export of dense shelf water from the Adélie Depression, East Antarctica, *Journal of Geophysical Research (Oceans)*, 113, 4039–+, 2008.
- Williams, M. J. M., A. Jenkins, and J. Determann, *Ocean, Ice and Atmosphere: Interactions at the Antarctic Continental Margin*, vol. 75 of *Antarctic Research Series*, chap. Physical controls on ocean circulation beneath ice shelves revealed by numerical models, pp. 285–299, American Geophysical Union, 1998a.
- Williams, M. J. M., R. C. Warner, and W. F. Budd, The effects of ocean warming on melting and ocean circulation under the Amery Ice Shelf, East Antarctica, *Annals of Glaciology*, 27, 75–80, 1998b.
- Williams, M. J. M., K. Grosfeld, R. C. Warner, R. Gerdes, and J. Determann, Ocean circulation and ice-ocean interaction beneath the Amery Ice Shelf, Antarctica, *Journal of Geophysical Research*, 106, 22,383–22,399, 2001.
- Williams, M. J. M., R. C. Warner, and W. F. Budd, Sensitivity of the Amery Ice Shelf, Antarctica, to changes in the climate of the Southern Ocean, *Journal of Climate*, 15, 2740–2757, 2002.
- Wingham, D. J., A. Shepherd, A. Muir, and et al., Mass balance of the Antarctic ice sheet, *Royal Society of London Philosophical Transactions Series A*, 364, 1627–1635, 2006.
- Wong, A. P. S., N. L. Bindoff, and A. Forbes, *Ocean, Ice, and Atmospheres: Interactions at the Antarctic Continental Margin*, vol. 75, chap. Ocean-ice interaction and possible bottom water formation in Prydz Bay, Antarctica, pp. 173–187, American Geophysical Union, 1998.
- Wright, D. G., An Equation of State for Use in Ocean Models: Eckart's Formula Revisited, *Journal of Atmospheric and Oceanic Technology*, 14, 735–+, 1997.
- Wunsch, C., P. Heimbach, R. Ponte, I. Fukumori, and the ECCO-GODAE Consortium members, The global general circulation of the ocean estimated by the ECCO Consortium, *Oceanography*, in-press, 2009.
- Yabuki, T., T. Suga, K. Hanawa, K. Matsuoka, H. Jiwada, and T. Watanabe, Possible Source of Antarctic Bottom Water in Prydz Bay Region, *Journal of Oceanography*, 62, 649–655, 2006.
- Yanenko, N. N., *The method of fractional steps : The solution of problems of mathematical physics*

in several variables, Springer-Verlag, 160 p., 1971.

Young, N. W., and G. Hyland, Velocity and strain rates derived from InSAR analysis over the Amery Ice Shelf, East Antarctica, *Annals of Glaciology*, 34, 228–234, 2002.

Young, N. W., D. Turner, G. Hyland, and R. N. Williams, Near coastal iceberg distributions in East Antarctica, 50°E - 145°E, *Annals of Glaciology*, 27, 68–74, 1998.

Zhang, J., Increasing Antarctic Sea Ice under Warming Atmospheric and Oceanic Conditions, *Journal of Climate*, 20, 2515–+, 2007.

Zhang, X., and O. B. Andersen, Surface Ice Flow Velocity and Tide Retrieval of the Amery Ice Shelf using Precise Point Positioning, *Journal of Geodesy*, 80, 171–176, 2006.

Zwally, H. J., J. C. Comiso, and A. L. Gordon, *Oceanology of the Antarctic Continental Shelf*, vol. 43, chap. Antarctic offshore leads and polynyas and oceanographic effects, pp. 203–226, American Geophysical Union, 1998.

Zwally, H. J., W. Abdalati, T. Herring, K. Larson, J. Saba, and K. Steffen, Surface Melt-Induced Acceleration of Greenland Ice-Sheet Flow, *Science*, 297, 218–222, 2002.